Higher order and CP-violating effects in the neutralino and Higgs boson sectors of the MSSM

FOWLER, ALISON,CLARE

Higher order and CP-violating effects in the neutralino and Higgs boson sectors of the MSSM

Alison C. Fowler

September, 2010

Institute for Particle Physics Phenomenology

Department of Physics

A thesis submitted to Durham University
for the degree of Doctor of Philosophy

Abstract

Complete one-loop results are presented for neutralino and Higgs decay processes of the form $\tilde{\chi}_i^0 \to \tilde{\chi}_j^0 h_a$ and $h_a \to \tilde{\chi}_i^0 \tilde{\chi}_j^0$ in the MSSM with $\mathcal{CP}$-violating parameters. An on-shell renormalisation scheme is developed for the chargino–neutralino sector that consistently takes into account imaginary parts arising from complex parameters and absorptive parts of loop integrals. The genuine vertex contributions are combined with two-loop Higgs propagator-type corrections to obtain the most precise prediction currently available for this class of processes. In the $\mathcal{CP}$-violating CPX benchmark scenario, the corrections to the neutralino decay width are found to be particularly large – of order 45% for a Higgs mass of 40 GeV. We find that in this unexcluded parameter region, which will be difficult to cover by standard Higgs search channels at the LHC, the branching ratio for the decay $\tilde{\chi}_2^0 \to \tilde{\chi}_1^0 h_1$ is large. This may offer good prospects of detecting such a light Higgs boson in cascade decays of supersymmetric particles. We also study the full Higgs production and decay processes in scenarios where the intermediate Higgs bosons are nearly mass degenerate and interference effects can have a significant impact. We find that an on-shell approximation gives results in good numerical agreement with the full momentum-dependent Higgs propagator matrix calculation and we develop a generalised narrow width approximation to be used in such a situation. We use these methods to study the asymmetry between the production of left-handed and right-handed neutralinos in Higgs decays at the LHC in the presence of $\mathcal{CP}$-violating phases. Large asymmetries are found to be possible for large $M_{H^\pm} \gtrsim 500\,\text{GeV}$ and $\tan\beta \lesssim 10$, where the decay into neutralinos may be the only possibility to detect the heavy Higgs bosons.

Declaration

This thesis has not been submitted for another qualification to this or any other university and it contains my own work. Chapters 4-7 are partially based on the following publications:

A. C. Fowler and G. Weiglein, "Precise Predictions for Higgs Production in Neutralino Decays in the Complex MSSM," JHEP **1001** (2010) 108 arXiv:0909.5165 [hep-ph].

A. C. Fowler, "Precise Predictions for Higgs Production in Neutralino Decays," AIP Conf. Proc. **1200** (2010) 390 arXiv:0909.5633 [hep-ph].

Chapters 8, 9 and 10 are partially based on work done towards a collaboration with Krzysztof Rolbiecki and Georg Weiglein. The Tevatron limits used for Figures 9.7(e), 9.7(f), 9.8(e) and 9.8(f) were provided by Karina Williams.

This thesis was completed with the support of a Commonwealth Scholarship and a Durham University Postgraduate Teaching Fellowship.

Alison Fowler
September 2010

Acknowledgements

First of all, I would like to thank my fantastic supervisor, Georg Weiglein, for his valuable guidance, patience and encouragement throughout my PhD. Special thanks also go to Nigel Glover, Gudi Moortgat-Pick and Mike Pennington for their kind support.

I am very grateful to Krzysztof Rolbiecki for many fruitful discussions and useful suggestions. I also gratefully acknowledge helpful discussions with Sven Heinemeyer, Markus Schumacher and Jamie Tattersall. I am eternally indebted to Karina Williams for patiently helping me understand so many things, reading parts of the thesis draft and for providing the Tevatron exclusion limits. I also give my heartfelt thanks to Sophy Palmer for numerous checks, countless useful discussions and for tirelessly reading through parts of the thesis draft.

My time in Durham has been unforgettable and I would like to thank everyone at the IPPP for providing such a great place to do research. Special thanks go to all of my office mates over the years for being a pleasure to work alongside, and to all of my lunch mates, for their friendship and for keeping me sane. I would also like to take this opportunity to thank all of the staff and students at Bishop Barrington School for further enriching my time in Durham with wonderful experiences and lots of fun.

This thesis could not have been done without the tremendous support of my friends and family, all of whom deserve my heartfelt thanks. To all my friends here in Durham and Newcastle for so many fun times – I will miss you all. To Aoife, for her special friendship and constant encouragement. To all my Australian friends and relatives, for their encouragement from afar. To my Nanna for her wonderful letters. To my dear family, Mum, Dad and Cath, for all their love and support in everything I do. Most of all, I would like to thank Scott, for everything.

Contents

List of figures

List of tables

Chapter 1

Introduction

1.1 The Standard Model

The Standard Model (SM) of Particle Physics is one of the most successful theories of the 20th Century. It elegantly describes the elementary particles and their strong, weak and electromagnetic interactions in terms of the gauge group $\mathrm{SU(3)_C \times SU(2)_L \times U(1)_Y}$, and has led to solid experimental predictions, which have been confirmed with extraordinary and ever-increasing precision over the last few decades.[1]

So far the only particle of the SM that has not been seen at colliders is the Higgs boson. This hypothetical scalar particle is a prediction of the Higgs mechanism, incorporated into the SM as a way of spontaneously breaking electroweak symmetry. The Large Electron Positron Collider (LEP), in operation at CERN until 2000, excluded the existence of a SM Higgs boson with a mass, M_H, of up to 114.4 GeV at the 95% confidence level [2]. The Tevatron at Fermilab has since excluded the mass region of $158 < M_H < 175\,\mathrm{GeV}$ [3–5]. One of the major goals of the new Large Hadron Collider (LHC) at CERN, which began colliding proton beams in late 2009, and is designed to eventually reach a centre of mass energy of 14 TeV, is to shed light on the mechanism of electroweak symmetry breaking (EWSB), for which many popular models contain one or more Higgs boson(s). It has been shown that searches at the LHC for a SM Higgs boson should be sensitive to the whole theoretically motivated mass region [6]. We discuss the Higgs mechanism in more detail in the next section.

[1] Many excellent books have been written on the SM and gauge theories. See eg. Ref. [1] for a review.

1.1.1 The Higgs Mechanism in the Standard Model

The Higgs Mechanism was proposed in the 1960s as a way of explaining the gauge boson masses through spontaneous electroweak symmetry breaking [7–11]. If one explicitly introduces mass terms for the W and Z bosons into the SM Lagrangian, the Lagrangian is no longer gauge invariant under the electroweak symmetry group $\mathrm{SU(2)_L} \times \mathrm{U(1)_Y}$, and the renormalisability of the SM is no longer guaranteed. In the Higgs mechanism, mass terms are generated by spontaneously breaking the symmetry of the vacuum, while the underlying Lagrangian remains gauge invariant. There are many excellent books and reviews about the Higgs Mechanism (see eg. Refs. [1, 12, 13]). Below we give a brief overview as a means of introducing notation.

One introduces a scalar $\mathrm{SU(2)_L}$ doublet, written as

$$\phi(x) = \begin{pmatrix} \phi^+(x) \\ \phi^0(x) \end{pmatrix}. \tag{1.1}$$

The Lagrangian for this scalar is chosen to be

$$\mathcal{L}_S = (D_\mu \phi)^\dagger D^\mu \phi - \mu^2 \phi^\dagger \phi - \lambda(\phi^\dagger \phi)^2. \tag{1.2}$$

The gauge invariance of the kinetic term is ensured by using the covariant derivative,

$$D_\mu \equiv \partial_\mu - ig\widetilde{W}_\mu - ig' y_\phi B_\mu, \tag{1.3}$$

instead of ∂_μ.[2] Here, $g = e/s_W$ and $g' = e/c_W$ are the $\mathrm{SU(2)_L}$ and $\mathrm{U(1)_Y}$ couplings respectively, e is the electromagnetic coupling, and we have adopted the abbreviations s_W and c_W for the sine and cosine of the weak mixing angle, θ_W. The $\mathrm{U(1)_Y}$ charge of the scalar is given by $y_\phi = Q_\phi - T^3_\phi$, where Q_ϕ is its electromagnetic charge and T^3_ϕ is the third component of its weak isospin. B_μ is the $\mathrm{U(1)_Y}$ gauge field and W^i_μ $(i = 1, 2, 3)$ are the $\mathrm{SU(2)_L}$ gauge fields, where $\widetilde{W}_\mu = \sigma_i W^i_\mu / 2$, and σ_i are the Pauli matrices. The physical

[2] Note that this formula assumes the SM sign convention for the covariant derivative. Later in this thesis, we will use the MSSM convention, where $D_\mu \equiv \partial_\mu + ig\widetilde{W}_\mu + ig' y_\phi B_\mu$.

gauge boson fields, $W_\mu^\pm$, Z_μ and A_μ, are then derived from $W_\mu^\pm = (W_\mu^1 \mp iW_\mu^2)/\sqrt{2}$ and

$$\begin{pmatrix} W_\mu^3 \\ B_\mu \end{pmatrix} = \begin{pmatrix} c_W & s_W \\ -s_W & c_W \end{pmatrix} \begin{pmatrix} Z_\mu \\ A_\mu \end{pmatrix}. \tag{1.4}$$

For $\lambda > 0$ and $\mu^2 < 0$, the second and third terms of Equation (1.2) make up the "Mexican Hat" Higgs potential, V, which has an infinite set of degenerate minima, $\phi_0(x)$, all with energy $V_0 = -\lambda v^4/4$ and non-zero vacuum expectation value,

$$|\langle 0|\phi_0|0\rangle| = \sqrt{\frac{-\mu^2}{2\lambda}} = \frac{v}{\sqrt{2}}. \tag{1.5}$$

Once a particular ground state is chosen, such as

$$\phi_0(x) = \frac{1}{\sqrt{2}} \begin{pmatrix} 0 \\ v \end{pmatrix}, \tag{1.6}$$

the electroweak $\mathrm{SU(2)_L} \times \mathrm{U(1)_Y}$ symmetry is spontaneously broken to the electromagnetic subgroup $\mathrm{U(1)_{em}}$. This means that while the underlying Lagrangian is fully gauge symmetric, the vacuum ground state is not. We parameterise $\phi(x)$ in terms of excitations with respect to this non-trivial vacuum, as,

$$\phi(x) = \frac{e^{i\frac{\sigma_i}{2}\theta^i(x)}}{\sqrt{2}} \begin{pmatrix} 0 \\ v + H(x) \end{pmatrix}. \tag{1.7}$$

Here, the four degrees of freedom of the complex scalar doublet have been written in terms of four real scalar fields, $\theta_i(x)$ (i $= 1, 2, 3$) and $H(x)$. Since the Lagrangian is locally SU(2) gauge invariant, $\theta_i(x)$ can be rotated away by a gauge transformation, without loss of generality. These three fields are the would-be massless Goldstone bosons which provide the longitudinal degrees of freedom for the $W^\pm$ and Z bosons.

Expanding the kinetic term of the Lagrangian in terms of the physical fields we obtain,

$$\begin{aligned} (D_\mu\phi)^\dagger D^\mu\phi &= \frac{1}{2}\partial_\mu H \partial^\mu H + M_W^2 W_\mu^- W^{+\mu} + \frac{1}{2}M_Z^2 Z_\mu Z^\mu + g M_W H W_\mu^- W^{+\mu} \\ &\quad + \frac{g}{2c_W} M_Z H Z_\mu Z^\mu + \frac{g^2}{4} H^2 W_\mu^- W^{+\mu} + \frac{g^2}{8c_W^2} H^2 Z_\mu Z^\mu. \end{aligned} \tag{1.8}$$

The first term in Equation (1.8) is a kinetic term for the scalar $H(x)$, the Higgs boson. The second and third terms are mass terms for the $W^{\pm}$ and Z bosons, where

$$M_W = \frac{vg}{2}, \quad M_Z = \frac{vg}{2c_W}. \tag{1.9}$$

We see that it is the non-zero vacuum expectation value, v, of the neutral component of the Higgs doublet which gives rise to the gauge boson masses. The values of v and c_W are fixed by the experimental values of M_W and M_Z. Note that the electromagnetic symmetry $\mathrm{U}(1)_{\mathrm{em}}$ remains intact; the photon, A_μ, is exactly massless. The remaining terms of Equation (1.8) contain three- and four-point interactions between the Higgs boson and the massive gauge bosons. Expanding the Higgs potential in terms of the physical fields results in the following,

$$V = -\frac{\lambda v^4}{4} + v^2\lambda H^2 + \lambda v H^3 + \frac{\lambda}{4}H^4. \tag{1.10}$$

The first term in Equation (1.10) is the minimum energy, V_0. The third and fourth terms are Higgs cubic and quartic self-interactions. The second term is the mass term for the scalar Higgs boson, where,

$$M_H = \sqrt{2\lambda}v = \sqrt{-2\mu^2}. \tag{1.11}$$

Thus, the two parameters of the Higgs potential, μ and λ, can be conveniently reparameterised in terms of M_H and v, where M_H is, as yet, undetermined by experiment.[3]

Note that the fermion masses can also be generated by allowing Yukawa interactions between the fermions and the Higgs doublet, $\phi(x)$, described by Lagrangian,

$$\mathcal{L}_Y = -y_d\,(\bar{u}, \bar{d})_L\;\phi(x)\;d_R - y_u\,(\bar{u}, \bar{d})_L\;\phi^C(x)\;u_R - y_e\,(\bar{\nu}_e, \bar{e})_L\;\phi(x)\;e_R + h.c. \tag{1.12}$$

for each generation of fermions, where $\phi^C(x) \equiv i\sigma_2\phi^*(x)$ and $h.c.$ denotes the Hermitian conjugate. Here y_d, y_u and y_e are Yukawa couplings, $(\bar{u}, \bar{d})_L$ and $(\bar{\nu}_e, \bar{e})_L$ are the quark and lepton SU(2) doublets respectively and f_R are the SU(2) singlets. Once Equation

[3]Nevertheless, there are theoretical reasons to expect the Higgs mass to be at the electroweak scale. Requiring the SM to remain valid up to the grand unification scale, $\Lambda \sim 10^{16}\,\mathrm{GeV}$, without the introduction of new physics, results in a theoretically motivated mass region of $130\,\mathrm{GeV} \lesssim M_H \lesssim 180\,\mathrm{GeV}$ (see Refs. [13,14] for details). We shall see in the next section, however, that there are indeed theoretical motivations for introducing new physics below this scale which can alter this prediction. Some new physics models predict a Higgs mass of even less than 130 GeV (see Section 2.2). Electroweak precision data also favours a light Higgs boson (see eg. Refs. [15, 16]).

(1.12) is rewritten in terms of the physical fields after spontaneous symmetry breaking, fermion mass terms arise, with $m_f = y_f v/\sqrt{2}$, along with fermion interactions with the physical Higgs field, $H(x)$.

1.1.2 Limitations of the Standard Model

Despite the tremendous successes of the SM, it is well known that it cannot be the ultimate theory of everything. Perhaps most notably, it only contains three of the four fundamental interactions, making no attempt at a quantum theory of gravity. For interactions at the electroweak energy scale, $M_{\mathrm{W}} \sim \mathcal{O}(10^2)\,\mathrm{GeV}$, which is the scale probed by current particle physics experiments, gravity is many orders of magnitude weaker than the other forces and does not play a significant role. However, at much higher energies, near the Planck scale, $M_{\mathrm{Pl}} \sim \mathcal{O}(10^{19})\,\mathrm{GeV}$, gravitational and quantum effects become equally important. Therefore, the SM is widely viewed as a low-energy effective theory, which can only be valid up to M_{Pl}. At or below this energy scale, a more complete and fundamental theory is expected to replace the effective theory. Discussed below are further motivations for physics beyond the SM (BSM), which may manifest at energies much lower than M_{Pl}, perhaps accessible at the LHC.

Perhaps the most often discussed motivation is the so called Hierarchy Problem of the SM. This is a question concerning the naturalness of the coexistence of the electroweak and Planck scales, where $M_W \ll M_{\mathrm{Pl}}$. If there is no new physics between these scales then one must consider the cut-off scale, Λ, of the SM to be M_{Pl}. This becomes a problem, in particular, when quantum corrections to the Higgs mass are considered. These corrections turn out to be quadratically divergent, so that $\delta M_H^2 \sim \Lambda^2 \sim M_{\mathrm{Pl}}^2$. Divergences in quantum field theories are routinely dealt with using a procedure known as renormalisation, which we will discuss in detail in Chapter 3. So long as the Higgs mass is a free parameter, as it is in the SM, its bare value can be chosen to cancel with the quadratic divergences to give a finite physical value. However, in order to achieve a physical Higgs mass at the electroweak scale, an extreme, perhaps "unnatural" fine tuning of some 30 orders of magnitude is required between the bare Higgs mass and the quadratically divergent corrections, and different amounts of fine tuning are required at different orders of perturbation theory. This means that the Higgs mass is extremely unstable and sensitive to quantum corrections. The only way to stabilise the Higgs mass seems to be to introduce new physics at a scale well below this.

This instability problem is unique for scalar masses – the corresponding mass corrections for fermions and gauge bosons in the SM turn out to be protected from quadratic divergences by symmetries. However, corrections to the Higgs mass driven by Planck scale physics are indeed a problem for the entire theory, since all sectors of the SM are affected by elecroweak symmetry breaking. The discovery of a Higgs boson would hence instantly beg the question of what new physics allows its mass to be stabilised.

Another problem of the SM is that it contains no viable candidate for Dark Matter (DM), which astrophysical and cosmological data suggest makes up about 23% of the Universe (see Ref. [17] for a review). Many BSM models predict hypothetical particles which may help to explain DM.

Furthermore, the SM does not allow the unification of its three fundamental forces into one single interaction, in the form of a Grand Unified Theory (GUT). If one uses the renormalisation group equations to extrapolate the behaviour of the three fundamental coupling constants, α_{EM}, α_W and α_S, up to high energy scales, they cannot be made to coincide without the introduction of some new physics between the electroweak and GUT scales [18].

Another compelling motivation for BSM physics is the observed baryon asymmetry of the Universe. Big Bang Cosmology gives rise to the prediction that matter and anti-matter should have been created in equal amounts in the early Universe. Yet today the Universe is mostly made of matter. In order to explain this observation, the Sakharov conditions require the existence of interactions which are not symmetric under the combination of charge conjugation ($\mathcal{C}$) and parity inversion ($\mathcal{P}$), at least at the extreme energies after the Big Bang [19]. Yet there is not enough $\mathcal{CP}$-violation in the SM to explain such a large asymmetry.

The above motivations, together with many other shortcomings of the SM which we will not discuss further here, illustrate that, while the discovery of a SM-like Higgs boson at the LHC could complete the so far remarkably successful SM, there are many reasons to believe this will not be the whole story. One popular BSM physics model is supersymmetry, which will be our focus for the remainder of this thesis.

1.2 Supersymmetry

1.2.1 A symmetry between fermions and bosons

Supersymmetry is a symmetry between bosons and fermions, whereby a group generator, Q, transforms fermions into bosons, $Q|f\rangle = |b\rangle$, and bosons into fermions, $Q|b\rangle = |f\rangle$.[4] If exact supersymmetry existed in Nature, then every SM particle would have a supersymmetric partner with all the same properties except its spin, which would differ by half an integer. The scalar partners of SM fermions are known as sfermions, while the fermionic partners of the gauge bosons and Higgs bosons are known as gauginos and higgsinos respectively. Since no supersymmetric partners have ever been seen at colliders, we know that if supersymmetry exists in Nature, it must be a broken symmetry, so that the masses of the partners are, in general, much larger than their SM counterparts.

In the context of developing a more fundamental theory of Nature, supersymmetry is interesting because it is the unique extension of the direct product of a gauge symmetry with the Poincare group [24]. Also in this context, demanding local gauge invariance of supersymmetry transformations can lead to (non-renormalisable) theories involving gravity. Indeed, many attempts to unify gravity with the SM involve string theories, which may even demand supersymmetry, but experimental hints of these theories are not required until energies close to $M_{\rm Pl}$ [25]. However, there are several motivations for finding supersymmetry at the TeV energy scale explored by the LHC, as we discuss in the next section.

1.2.2 Motivations for low-energy supersymmetry

In order to explain why many believe that supersymmetry may be found at the energies accessible at the LHC, we first return to the Hierarchy Problem. The quadratically divergent quantum corrections to the Higgs mass in the SM arise from self-energy loops containing fermions. The offending term[5] takes the following form in the limit $p^2 \to \Lambda^2$, where p is the loop momentum;

$$\Sigma_f^{\phi\phi} \sim -\lambda_f^2 \Lambda^2 \tag{1.13}$$

[4] There are many excellent books and reviews on the topic of supersymmetry. See eg. Refs. [20–23].
[5] See Ref. [20] for its derivation.

where λ_f is the coupling. In supersymmetric extensions of the SM, for every such fermion loop diagram, there is a corresponding sfermion diagram, with coupling $\tilde{\lambda}_f$, which results in a quadratically divergent term of the form

$$\Sigma_{\tilde{f}}^{\phi\phi} \sim \tilde{\lambda}_f \Lambda^2. \tag{1.14}$$

Notice that the sfermion terms come with a plus sign while the fermion terms come with a minus sign. Thus the quadratic divergences cancel if the coupling factors are equal;

$$\lambda_f^2 = \tilde{\lambda}_f \tag{1.15}$$

as they are in a supersymmetric theory. In fact, the complete quantum correction to the Higgs self-energy from fermion and sfermion loops cancels if the masses of the fermion and its superpartner exactly coincide;

$$m_{\tilde{f}}^2 = m_f^2. \tag{1.16}$$

This would only be true for exact supersymmetry. As discussed in the previous section, if supersymmetry exists in Nature, then it is broken, and we assume

$$m_{\tilde{f}}^2 = m_f^2 + \Delta^2. \tag{1.17}$$

In order not to introduce any new sources of quadratic divergences, we assume "soft" supersymmetry breaking, in which the relations between dimensionless couplings remain unchanged. Moreover, the remaining corrections can be kept "acceptably small" if we assume $\Delta \sim \mathcal{O}(\text{TeV})$. There are further reasons to expect the masses of the superpartners to be at the TeV scale, as we will discuss below.

Realistic realisations of supersymmetric theories often contain the assumption of R-parity conservation, in order to avoid rapid proton decay. SM particles and Higgs bosons are assigned an R-parity of 1, while their supersymmetric partners are assigned an R-parity of -1. If R-parity is conserved, then an even number of supersymmetric particles must always appear at a vertex. Thus a given supersymmetric particle cannot decay into purely SM particles, rendering the lightest supersymmetric particle (LSP) stable and hence a natural DM candidate. Furthermore it has been shown that the LSP relic density can be made to coincide with the favoured range for the cold DM relic density if the mass of the LSP, M_{LSP}, is less than around 1 TeV (see eg. Ref. [26]).

It has also been shown that the unification of the strong, weak and electromagnetic couplings is possible if the masses of the supersymmetric particles are close to the TeV scale [18]. Thus, each of the above motivations for BSM physics is consistent with supersymmetry being present at the energy scales accessible at the LHC.

1.2.3 Supersymmetry and Higgs physics at colliders

In the previous sections we have provided motivations for why Higgs bosons and supersymmetric particles are prime candidates for new physics that could be discovered at the LHC. In this thesis we will explore cases where the searches for Higgs bosons and supersymmetric particles are very much linked and should go hand-in-hand.

While in the SM, Higgs physics is determined by a single parameter, M_H, we will see in the next chapter that Higgs phenomenology is very much enriched in supersymmetric theories. In the Minimal Supersymmetric Standard Model (MSSM), the spectrum contains five physical Higgs bosons, the properties of which may differ significantly from those of a SM Higgs boson. At lowest order the neutral Higgs bosons of the MSSM are $\mathcal{CP}$-eigenstates, so that there are two $\mathcal{CP}$-even Higgs bosons, h and H, a $\mathcal{CP}$-odd Higgs boson, A, and two charged Higgs bosons, $H^{\pm}$. Higher-order contributions in the MSSM Higgs sector yield large corrections to the masses and couplings, and can also induce $\mathcal{CP}$-violation, so that mixing can occur between h, H and A in the general case of complex parameters.

If the mixing between the three neutral mass eigenstates, denoted h_1, h_2 and h_3, is such that the coupling of the lightest Higgs boson, h_1, to gauge bosons is significantly suppressed, this state can be very light without being in conflict with the exclusion bounds from the Higgs searches at LEP [2, 27] and the Tevatron [28]. In the CPX benchmark scenario [29] an unexcluded region remains in which $M_{h_1} \approx 45$ GeV and $\tan\beta \approx 7$ [27] (see also Ref. [30] for a recent reevaluation with improved theoretical predictions). This unexcluded parameter region with a very light Higgs boson will also be difficult to cover at the LHC with the standard search channels [31–33]. We will show in this thesis, however, that there may be good prospects to detect such a light Higgs boson in cascade decays of supersymmetric particles such as neutralinos.

Decays of Higgs bosons into supersymmetric particles can also be phenomenologically important at the LHC, and may extend the discovery reach for heavy Higgs bosons [34–37]

(see eg. Refs. [38, 39] for a discussion of the parameter region in which only the light $\mathcal{CP}$-even MSSM Higgs boson can be discovered with the standard search channels). The decay processes of heavy Higgs bosons into supersymmetric particles, if accessible, can provide important information about the properties of the decaying particles. We will explore the possibility of measuring an asymmetry in the polarisation of the supersymmetric particles produced in the decay of Higgs bosons, in order to determine the existence of $\mathcal{CP}$-violation in the MSSM. In this study, we will come across scenarios where two or more of the three neutral Higgs bosons are nearly mass degenerate. This can lead to an enhancement or suppression of the Higgs production and decay processes due to interference between the Higgs bosons, a phenomenon which obviously does not occur in the SM where there is only one Higgs boson.

For most of this thesis, we will focus on the Higgs and neutralino–chargino sectors of the complex MSSM. We will obtain complete one-loop corrections to the processes where a neutralino decays into a Higgs boson, $\tilde{\chi}_i^0 \to \tilde{\chi}_j^0 h_a$, and where a Higgs boson decays into two neutralinos, $h_a \to \tilde{\chi}_i^0 \tilde{\chi}_j^0$, and explore the phenomenology of these decays in the context of Higgs physics at the LHC.

1.3 Thesis Outline

In Chapter 2 we lay out our notation for the MSSM with complex parameters. In Chapter 3 we explain how higher-order corrections involve divergent loop integrals which must be dealt with using renormalisation. We describe in detail our renormalisation prescription for the gauge and Higgs sectors and the electric charge. In Chapter 4 we develop an on-shell renormalisation scheme for the chargino–neutralino sector that consistently takes into account imaginary parts arising from complex parameters and absorptive parts of loop integrals. In Chapter 5 we evaluate the one-loop corrections to the $\tilde{\chi}_i^0 \tilde{\chi}_j^0 h_a$ vertex and combine these with two-loop Higgs propagator-type corrections to obtain precise predictions for the processes $\tilde{\chi}_i^0 \to \tilde{\chi}_j^0 h_a$ and $h_a \to \tilde{\chi}_i^0 \tilde{\chi}_j^0$. In Chapter 6 we show numerical results for the decay of a neutralino into a light Higgs boson, $\tilde{\chi}_i^0 \to \tilde{\chi}_j^0 h_a$, focusing in particular on the CPX scenario. In Chapter 7 we compute the branching ratios for this process and discuss the prospects for covering the "CPX hole" using the decay $\tilde{\chi}_2^0 \to \tilde{\chi}_1^0 h_1$. In Chapter 8 we show numerical results for the decay of a heavy Higgs boson into a pair of neutralinos, focusing in particular on the effect of $\mathcal{CP}$-violating phases on the decays into polarised neutralinos. In Chapter 9 we study interference

effects in the production and decay of nearly mass degenerate Higgs bosons, developing a generalised narrow width approximation. In Chapter 10 we study asymmetries in the polarisation of neutralinos produced in the processes $b\bar{b}, gg, WW \to h_i \to \tilde{\chi}_2^0\tilde{\chi}_2^0$ at the LHC. In Chapter 11 we will conclude.

Chapter 2

The Complex MSSM

2.1 The Minimal Supersymmetric Standard Model

In this thesis, we will consider the Minimal Supersymmetric Standard Model (MSSM), the simplest supersymmetric extension of the SM with R-parity conservation and soft SUSY breaking. Table 2.1 shows the field content of the MSSM. Each SM field is placed in a supermultiplet with a superpartner, indicated by a tilde, which differs in spin from the SM particle by a half. The spin-1/2 fermions (quarks and leptons) each have spin-0 scalar partners (squarks and sleptons), and the spin-1 gauge bosons (gluons, W and B bosons) each have spin-1/2 gaugino partners (gluinos, winos and binos). There are also spin-1/2 higgsino partners for the spin-0 Higgs doublets.

While the SM has only one Higgs doublet, the MSSM requires two Higgs doublets, $\mathcal{H}_1$ and $\mathcal{H}_2$, in order to give masses to both the down- and up-type quarks without the use of the Hermitian conjugate of the Higgs field as in Equation (1.12), which would break supersymmetry. In addition, having two Higgs doublets ensures the cancellation of gauge anomalies and quadratic divergences. As in the SM, EWSB uses up three degrees of freedom, so the eight degrees of freedom contained in the two complex Higgs doublets result in five physical Higgs bosons. The supersymmetric partners to the Higgs fields are the four spin-1/2 higgsinos, $\tilde{h}_u^+$, $\tilde{h}_u^0$, $\tilde{h}_d^0$ and $\tilde{h}_d^-$, contained in the two corresponding SU(2) doublets. In terms of the physical particle content of the MSSM, EWSB allows particles with different quantum numbers to mix with each other. For example, the charged winos and charged higgsinos mix, resulting in two "charginos", labelled $\tilde{\chi}_{1,2}^{\pm}$. Similarly, the neutral bino, wino and higgsinos mix, resulting in four "neutralinos", labelled $\tilde{\chi}_{1,2,3,4}^0$.

Chiral supermultiplets:		spin 0	spin $\frac{1}{2}$	$(\mathrm{SU}(3)_\mathrm{C}, \mathrm{SU}(2)_\mathrm{L}, \mathrm{U}(1)_\mathrm{Y})$
squarks and quarks	Q	$(\tilde{u}_L, \tilde{d}_L)$	(u_L, d_L)	$(3, 2, \frac{1}{6})$
	U	$\tilde{u}_R^*$	$u_R^\dagger$	$(\bar{3}, 1, -\frac{2}{3})$
	D	$\tilde{d}_R^*$	$d_R^\dagger$	$(\bar{3}, 1, \frac{1}{3})$
sleptons and leptons	L	$(\tilde{\nu}, \tilde{e}_L)$	(ν, e_L)	$(1, 2, -\frac{1}{2})$
	E	$\tilde{e}_R^*$	$e_R^\dagger$	$(1, 1, 1)$
higgs and higgsinos	$\mathcal{H}_1$	(h_d^0, h_d^-)	$(\tilde{h}_d^0, \tilde{h}_d^-)$	$(1, 2, -\frac{1}{2})$
	$\mathcal{H}_2$	(h_u^+, h_u^0)	$(\tilde{h}_u^+, \tilde{h}_u^0)$	$(1, 2, \frac{1}{2})$
Vector supermultiplets:		spin $\frac{1}{2}$	spin 1	$(\mathrm{SU}(3)_\mathrm{C}, \mathrm{SU}(2)_\mathrm{L}, \mathrm{U}(1)_\mathrm{Y})$
gluinos and gluons		$\tilde{g}$	g	$(8, 1, 0)$
winos and W-bosons		$\widetilde{W}^\pm, \widetilde{W}^0$	$W^\pm, W^0$	$(1, 3, 0)$
binos and B-boson		$\tilde{B}$	B	$(1, 1, 0)$

Table 2.1: The field content of the MSSM

The MSSM Lagrangian consists of the following main parts;

$$\mathcal{L}_\mathrm{MSSM} = \mathcal{L}_\mathrm{kin.} + \mathcal{L}_\mathrm{superpot.} + \mathcal{L}_\mathrm{soft} + \mathcal{L}_\mathrm{gauge-fix.} + \mathcal{L}_\mathrm{ghost}. \tag{2.1}$$

The kinetic terms for each of the fields are contained in $\mathcal{L}_\mathrm{kin.}$, while $\mathcal{L}_\mathrm{gauge-fix.}$ and $\mathcal{L}_\mathrm{ghost}$ are the terms involving gauge-fixing and Faddeev-Popov ghosts respectively. The superpotential terms contained in $\mathcal{L}_\mathrm{superpot.}$ are the mass terms and interaction terms which respect supersymmetry. The terms which break supersymmetry are contained in $\mathcal{L}_\mathrm{soft}$. There has been much discussion in the literature about possible mechanisms for supersymmetry breaking. However, in the MSSM, no particular supersymmetry breaking model is assumed. Rather, $\mathcal{L}_\mathrm{soft}$ is the most general parameterisation of the supersymmetry breaking terms which keep relations between dimensionless couplings unchanged so that no quadratic divergences result.

A careful count reveals that the MSSM has 105 new parameters, in addition to the 19 of the SM, which appear as masses, mixing angles and $\mathcal{CP}$-violating phases [40]. A large number of these parameters arise from allowing intergenerational mixing in the sfermion sectors. In this work, we assume minimal flavour violation, setting these parameters to zero so that the only flavour violation comes from the Cabibbo-Kobayashi-Maskawa (CKM) matrix in the SM. This leaves us with 41 independent parameters (see Equation

(2.43)), 12 of which are $\mathcal{CP}$-violating phases. We discuss these phases in more detail in Section 2.6. In the following sections, we lay out our notation for the various sectors of the MSSM at tree level.

2.2 The Higgs sector at tree level

For the Higgs sector of the complex MSSM, we follow the notation of Ref. [41]. The Higgs potential is written as

$$\begin{aligned} V_H &= m_1^2 H_{1i}^* H_{1i} + m_2^2 H_{2i}^* H_{2i} - \epsilon^{ij}(m_{12}^2 H_{1i} H_{2j} + m_{12}^{2\,*} H_{1i}^* H_{2j}^*) \\ &\quad + \frac{1}{8}(g^2 + g'^2)(H_{1i}^* H_{1i} - H_{2i}^* H_{2i})^2 + \frac{1}{2} g'^2 |H_{1i}^* H_{2i}|^2. \end{aligned} \tag{2.2}$$

This potential contains all the terms from $\mathcal{L}_{\text{superpot.}}$ and $\mathcal{L}_{\text{soft}}$ which involve Higgs fields only, where $\mathcal{H}_i = (H_{i1}\ H_{i2})^T$, $i, j = 1, 2$ are summed over and $\epsilon^{12} = 1$. Here, m_i^2 is defined by $m_i^2 = \widetilde{m}_i^2 + |\mu|^2$, where $\widetilde{m}_i^2$ are real coefficients from $\mathcal{L}_{\text{soft}}$. $m_{12}^2 \equiv |m_{12}^2| e^{i\phi_{m_{12}^2}}$ is a potentially complex coefficient from $\mathcal{L}_{\text{soft}}$. As we show in Section 2.6 that the $\mathcal{CP}$-violating phase, $\phi_{m_{12}^2}$, can be rotated away, we treat m_{12}^2 as real in the following.

It can be shown that one can choose a minimum for the Higgs potential for which the vacuum expectation values, $\langle 0|h_u^+|0\rangle$ and $\langle 0|h_d^-|0\rangle$, are both zero, while $\langle 0|h_d^0|0\rangle \equiv v_1$ and $\langle 0|h_u^0|0\rangle \equiv v_2$ are both real and non-zero, leading to spontaneous electroweak symmetry breaking. We can hence parameterise the two Higgs doublets in terms of excitations with respect to this ground state;

$$\mathcal{H}_1 = \begin{pmatrix} v_1 + \frac{1}{\sqrt{2}}(\phi_1 - i\chi_1) \\ -\phi_1^- \end{pmatrix}, \tag{2.3}$$

$$\mathcal{H}_2 = e^{i\xi} \begin{pmatrix} \phi_2^+ \\ v_2 + \frac{1}{\sqrt{2}}(\phi_2 + i\chi_2) \end{pmatrix}, \tag{2.4}$$

where ξ is a possible relative phase between the two doublets. Expanding the Higgs kinetic terms in terms of this parameterisation, one finds the mass terms for the $W^\pm$ and Z bosons;

$$M_W^2 = \frac{1}{2} g^2 (v_1^2 + v_2^2), \qquad M_Z^2 = \frac{1}{2}(g^2 + g'^2)(v_1^2 + v_2^2). \tag{2.5}$$

The photon remains massless. Three of the eight degrees of freedom from the two complex Higgs doublets have been used to give longitudinal components to the gauge bosons via the Higgs mechanism. One can expand the Higgs potential in this parameterisation, and write the result in terms of powers of the fields;

$$\begin{aligned} V_H &= ... - T_{\phi_1}\phi_1 - T_{\phi_2}\phi_2 - T_{\chi_1}\chi_1 - T_{\chi_2}\chi_2 \\ &\quad + \frac{1}{2}(\phi_1\ \phi_2\ \chi_1\ \chi_2)\,\mathbf{M}_{\phi\phi\chi\chi}\begin{pmatrix}\phi_1\\ \phi_2\\ \chi_1\\ \chi_2\end{pmatrix} + \frac{1}{2}(\phi_1^-\ \phi_2^-)\,\mathbf{M}_{\phi^\pm\phi^\pm}\begin{pmatrix}\phi_1^+\\ \phi_2^+\end{pmatrix} + ... \end{aligned} \quad (2.6)$$

We see that there are linear (tadpole) and bilinear (mass) Higgs terms. There are also 3- and 4- point interactions between Higgs and gauge bosons, which we do not list here. The values for the tadpole coefficients are given by

$$T_{\phi_1} = -\sqrt{2}(m_1^2 v_1 - \cos\xi |m_{12}^2| v_2 + \frac{1}{4}(g^2+g'^2)(v_1^2 - v_2^2)v_1), \quad (2.7)$$

$$T_{\phi_2} = -\sqrt{2}(m_2^2 v_2 - \cos\xi |m_{12}^2| v_1 - \frac{1}{4}(g^2+g'^2)(v_1^2 - v_2^2)v_2), \quad (2.8)$$

$$T_{\chi_1} = -T_{\chi_2}\frac{v_2}{v_1} = \sqrt{2}\sin\xi |m_{12}^2| v_2. \quad (2.9)$$

$\mathbf{M}_{\phi\phi\chi\chi}$ is a real, symmetric 4×4 mass matrix with elements given by

$$M_{\phi_1\phi_1} = m_1^2 + \frac{1}{4}(g^2+g'^2)(3v_1^2 - v_2^2), \quad (2.10)$$

$$M_{\phi_1\phi_2} = M_{\phi_2\phi_1} = -\cos\xi\, m_{12}^2 - \frac{1}{2}(g^2+g'^2)v_1 v_2, \quad (2.11)$$

$$M_{\phi_2\phi_2} = m_2^2 + \frac{1}{4}(g^2+g'^2)(3v_2^2 - v_1^2), \quad (2.12)$$

$$M_{\phi_1\chi_1} = M_{\phi_2\chi_2} = M_{\chi_1\phi_1} = M_{\chi_2\phi_2} = 0, \quad (2.13)$$

$$M_{\phi_1\chi_2} = M_{\chi_2\phi_1} = \sin\xi\, m_{12}^2, \quad (2.14)$$

$$M_{\phi_2\chi_1} = M_{\chi_1\phi_2} = -\sin\xi\, m_{12}^2, \quad (2.15)$$

$$M_{\chi_1\chi_1} = m_1^2 + \frac{1}{4}(g^2+g'^2)(v_1^2 - v_2^2), \quad (2.16)$$

$$M_{\chi_1\chi_2} = M_{\chi_2\chi_1} = -\cos\xi\, m_{12}^2, \quad (2.17)$$

$$M_{\chi_2\chi_2} = m_2^2 + \frac{1}{4}(g^2+g'^2)(v_2^2 - v_1^2), \quad (2.18)$$

and $\mathbf{M}_{\phi^\pm\phi^\pm}$ is a Hermitian 2×2 mass matrix with elements given by

$$M_{\phi_1^\pm\phi_1^\pm} = m_1^2 + \frac{1}{4}g^2(v_1^2 - v_2^2) + \frac{1}{4}g'^2(v_1^2 + v_2^2), \tag{2.19}$$

$$M_{\phi_1^\pm\phi_2^\pm} = -e^{i\xi}m_{12}^2 - \frac{1}{2}g'^2 v_1 v_2, \tag{2.20}$$

$$M_{\phi_2^\pm\phi_1^\pm} = -e^{-i\xi}m_{12}^2 - \frac{1}{2}g'^2 v_1 v_2, \tag{2.21}$$

$$M_{\phi_2^\pm\phi_2^\pm} = m_2^2 + \frac{1}{4}g^2(v_2^2 - v_1^2) + \frac{1}{4}g'^2(v_1^2 + v_2^2). \tag{2.22}$$

The conditions for minimising the Higgs potential require that the tadpole coefficients, $T_{\phi_1,\phi_2,\chi_1,\chi_2}$, and the phase between the Higgs doublets, ξ, are all equal to zero. Diagonalising $\mathbf{M}_{\phi\phi\chi\chi}$ and $\mathbf{M}_{\phi^\pm\phi^\pm}$ under these conditions leads to the physical mass eigenstates, which are a rotation from the above parameterisation as follows;

$$\begin{pmatrix} h \\ H \\ A \\ G \end{pmatrix} = \begin{pmatrix} -\sin\alpha & \cos\alpha & 0 & 0 \\ \cos\alpha & \sin\alpha & 0 & 0 \\ 0 & 0 & -\sin\beta_n & \cos\beta_n \\ 0 & 0 & \cos\beta_n & \sin\beta_n \end{pmatrix} \begin{pmatrix} \phi_1 \\ \phi_2 \\ \chi_1 \\ \chi_2 \end{pmatrix}, \tag{2.23}$$

$$\begin{pmatrix} H^\pm \\ G^\pm \end{pmatrix} = \begin{pmatrix} -\sin\beta_c & \cos\beta_c \\ \cos\beta_c & \sin\beta_c \end{pmatrix} \begin{pmatrix} \phi_1^\pm \\ \phi_2^\pm \end{pmatrix}, \tag{2.24}$$

where α, β_n and β_c are mixing angles. The $\mathcal{CP}$-even Higgs bosons are the lighter h and the heavier H, while A is the $\mathcal{CP}$-odd Higgs boson, and G and $G^\pm$ are the would-be Goldstone bosons. The null entries in the 4×4 mixing matrix above come about because the Higgs sector at lowest order contains no complex parameters. Hence at tree level there is no $\mathcal{CP}$-violating mixing between the neutral Higgs bosons – the mass eigenstates coincide with the $\mathcal{CP}$-eigenstates. It turns out that the Higgs sector can be described at tree level by two parameters; these can be chosen to be the mass of the $\mathcal{CP}$-odd Higgs boson, M_A, and the ratio of the Higgs vacuum expectation values, $\tan\beta$, where

$$\tan\beta \equiv v_2/v_1. \tag{2.25}$$

The remaining neutral Higgs masses can be expressed at tree level[1] as,

$$\{m_h^2, m_H^2\} = \frac{1}{2}\left(m_A^2 + M_Z^2 \mp \sqrt{(m_A^2 + M_Z^2)^2 - 4m_A^2 M_Z^2 \cos^2 2\beta}\right) \tag{2.26}$$

and the tree-level charged Higgs mass can be written,

$$m_{H^\pm}^2 = m_A^2 + M_W^2. \tag{2.27}$$

It turns out that the mixing angles β_n and β_c coincide with β, due to minimisation of the Higgs potential.[2] The remaining mixing angle, α, is given by

$$\alpha = \arctan\left[\frac{-(m_A^2 + M_Z^2)\sin\beta\cos\beta}{M_Z^2\cos^2\beta + m_A^2\sin^2\beta - m_h^2}\right],\ -\frac{\pi}{2} < \alpha < 0. \tag{2.28}$$

If one uses the above equation for the neutral Higgs masses, one obtains the prediction that the lightest Higgs boson mass is less than the Z boson mass, $m_h^2 \leq M_Z^2$. This value is obviously excluded by Higgs searches at LEP, but it is only a tree-level prediction. Loop corrections turn out to be very important in the Higgs sector. For instance, the contribution from loops involving the Yukawa coupling of the top quark can be of order 100%. Including these corrections up to two-loop order in the Feynman-diagrammatic approach gives an upper bound on the lightest Higgs mass of around 130 GeV [42–46].

Also in the context of loop corrections, note that, while the Higgs sector is $\mathcal{CP}$-conserving at tree level, since it contains no complex parameters, complex parameters from the sfermion and gaugino sectors can enter the Higgs sector at the loop level. Then the $\mathcal{CP}$-eigenstates, h, H and A, are no longer mass eigenstates. They can mix via loop diagrams which contain complex parameters. In the real MSSM, where there is no $\mathcal{CP}$-violation, the $\mathcal{CP}$-odd Higgs boson, A, does not mix with the other neutral Higgs states and its mass is therefore a convenient input parameter. However, in this thesis, we will consider the complex MSSM. Thus, following Ref. [41], we do not use M_A as an input parameter for $\mathcal{CP}$-violating scenarios; rather, we use the mass of the charged Higgs boson $M_{H^\pm}$ as input, along with $\tan\beta$.

[1] Note that throughout this thesis, we will always use a lower-case m to denote a tree-level mass and an upper-case M to denote a loop-corrected or physical mass.

[2] However, in our renormalisation scheme, discussed in Chapter 3, $\tan\beta$ receives a counterterm, while β_n and β_c are just mixing angles and are not renormalised. Thus in expressions depending on $\tan\beta_n$ and $\tan\beta_c$ we keep this dependence until the renormalisation has been carried out, after which $\tan\beta_n$ and $\tan\beta_c$ may be set to $\tan\beta$.

2.3 The chargino–neutralino sector at tree-level

At tree level, the physical chargino states, $\tilde{\chi}_i^{\pm}$, $(i = 1, 2)$, are Dirac spinors constructed from the mass eigenstates of the 2×2 complex mass matrix, X, which reads, in the wino-higgsino basis,

$$X = \begin{pmatrix} M_2 & \sqrt{2} M_W \sin\beta \\ \sqrt{2} M_W \cos\beta & \mu \end{pmatrix} \tag{2.29}$$

where M_2 and μ are the wino and higgsino mass parameters, respectively. The mass matrix is diagonalised by two 2×2 complex unitary matrices, U and V, where $U^* X V^\dagger = \mathrm{diag}(m_{\tilde{\chi}_1^+}, m_{\tilde{\chi}_2^+})$. Hence the Born Lagrangian for charginos reads:

$$\mathcal{L}_{\tilde{\chi}^\pm} = \overline{\tilde{\chi}_i^-}(\not{p}\delta_{ij} - \omega_L (U^* X V^\dagger)_{ij} - \omega_R (V X^\dagger U^T)_{ij}) \tilde{\chi}_j^-, \tag{2.30}$$

where $\omega_{R/L} = \frac{1}{2}(1 \pm \gamma_5)$, $\not{p} = \gamma^\mu p_\mu$, $\tilde{\chi}_j^-$ is the chargino spinor, with $\overline{\tilde{\chi}_j^-} = (\tilde{\chi}_j^-)^\dagger \gamma^0$. Similarly, the neutralinos $\tilde{\chi}_i^0$, $(i = 1, 2, 3, 4)$ are Majorana spinors constructed from mass eigenstates of the 4×4 complex mass matrix, Y, which reads, in the $(\widetilde{B}, \widetilde{W}^3, \tilde{h}_d^0, \tilde{h}_u^0)$ basis:

$$Y = \begin{pmatrix} M_1 & 0 & -M_Z c_\beta s_W & M_Z s_\beta s_W \\ 0 & M_2 & M_Z c_\beta c_W & -M_Z s_\beta c_W \\ -M_Z c_\beta s_W & M_Z c_\beta c_W & 0 & -\mu \\ M_Z s_\beta s_W & -M_Z s_\beta c_W & -\mu & 0 \end{pmatrix} \tag{2.31}$$

where M_1 is the bino mass parameter and we adopt the abbreviations $c_\beta \equiv \cos\beta$ and $s_\beta \equiv \sin\beta$. Due to the Majorana nature of neutralinos, only one 4×4 complex unitary matrix, N, is required to diagonalise Y, where $N^* Y N^\dagger = \mathrm{diag}(m_{\tilde{\chi}_1^0}, m_{\tilde{\chi}_2^0}, m_{\tilde{\chi}_3^0}, m_{\tilde{\chi}_4^0})$. Hence the Born Lagrangian for neutralinos reads:

$$\mathcal{L}_{\tilde{\chi}^0} = \frac{1}{2}\overline{\tilde{\chi}_i^0}(\not{p}\delta_{ij} - \omega_L (N^* Y N^\dagger)_{ij} - \omega_R (N Y^\dagger N^T)_{ij}) \tilde{\chi}_j^0. \tag{2.32}$$

Besides parameters from other sectors, the masses and mixings of neutralinos and charginos can thus be described by three independent input parameters, M_1, M_2 and μ. If all three parameters are real, then U and V can also be chosen to be real, while each of the rows of N can be chosen to be purely real or purely imaginary such that all

neutralino masses are positive. In the complex MSSM, however, the input parameters M_1, M_2 and μ of the chargino–neutralino sector can be chosen to be complex. In this case the elements of U, V and N will have both real and imaginary parts. We write

$$M_1 = |M_1|e^{i\phi_{M_1}}, \quad M_2 = |M_2|e^{i\phi_{M_2}}, \quad \mu = |\mu|e^{i\phi_\mu}. \tag{2.33}$$

However, we will show in Section 2.6 that only two of the three phases, ϕ_{M_1}, ϕ_{M_2} and ϕ_μ, are physical, while the other can be rotated away.

2.4 The sfermion sector at tree level

At tree level, the physical squark and charged slepton states, $\tilde{f}_1$, $\tilde{f}_2$, are the mass eigenstates of a 2×2 complex mass matrix, which reads in the $(\tilde{f}_L, \tilde{f}_R)$ basis for each flavour,

$$M_{\tilde{f}} = \begin{pmatrix} M_L^2 + m_f^2 + M_Z^2 \cos 2\beta (I_3^f - Q_f s_W^2) & m_f X_f^* \\ m_f X_f & M_{\tilde{f}_R}^2 + m_f^2 + M_Z^2 \cos 2\beta \, Q_f s_W^2 \end{pmatrix} \tag{2.34}$$

with

$$X_f = A_f - \mu^* \{\cot\beta, \tan\beta\} \tag{2.35}$$

where $\cot\beta$ applies for the up-type massive fermions, $f = u, c, t$, and $\tan\beta$ applies for the down-type fermions, $f = d, s, b, e, \mu, \tau$. The soft supersymmetry breaking parameters introduced in the sfermion sector are M_L^2 and $M_{\tilde{f}_R}^2$, which are real, and the trilinear coupling A_f, which can be complex. We write the latter as

$$A_f = |A_f|e^{i\phi_{A_f}}. \tag{2.36}$$

We will not consider processes involving sfermions as external particles. However, the sfermion sector will be important for higher order corrections. The phase ϕ_{A_f} plays a large role in the Higgs sector, particularly for loops involving the supersymmetric partners of the heavy third-generation SM fermions, t, b, τ, where the term $m_f X_f$ appears in couplings of sfermions to Higgs bosons. It also plays a role in the neutralino sector at one-loop level.

The mass matrix $M_{\tilde{f}}$ is diagonalised by a 2×2 complex, unitary matrix, $U_{\tilde{f}}$, where

$U_{\tilde{f}} M_{\tilde{f}} U_{\tilde{f}}^{\dagger} = \mathrm{diag}(m_{\tilde{f}_1}, m_{\tilde{f}_2})$, where $m_{\tilde{f}_1} < m_{\tilde{f}_2}$. The bilinear part of the Born Lagrangian for squarks and charged leptons then reads,

$$\mathcal{L}_{\tilde{f}} = -(\tilde{f}_1^{\dagger}, \tilde{f}_2^{\dagger})\, U_{\tilde{f}}\, M_{\tilde{f}}\, U_{\tilde{f}}^{\dagger} \begin{pmatrix} \tilde{f}_1 \\ \tilde{f}_2 \end{pmatrix}. \tag{2.37}$$

Since there are no right-handed neutrinos in the SM, the three sneutrinos in the MSSM have masses dependent only on M_L^2, $\tan\beta$ and SM parameters;

$$M_{\tilde{\nu}}^2 = M_L^2 + \frac{1}{2} M_Z^2 \cos 2\beta. \tag{2.38}$$

The Born Lagrangian for sneutrinos is

$$\mathcal{L}_{\tilde{\nu}} = -\tilde{\nu}^{\dagger} M_{\tilde{\nu}}^2 \tilde{\nu}. \tag{2.39}$$

2.5 The gluino sector at tree level

The bilinear part of the Born Lagrangian for the gluino is given by

$$\mathcal{L}_{\tilde{g}} = -\frac{1}{2} \bar{\tilde{g}}\, M_3\, \tilde{g} \tag{2.40}$$

where M_3 is the gluino mass parameter, which can be complex and is written;

$$M_3 = |M_3| e^{i\phi_{M_3}}. \tag{2.41}$$

The gluino mass, $m_{\tilde{g}}$, is given by $|M_3|$. We will not consider any processes involving gluinos as external particles. Gluinos only couple to coloured particles, so only enter higher order corrections in the Higgs and neutralino sectors at the two-loop level. These parameters, M_3 and ϕ_{M_3}, can play a large role in Higgs sector phenomenology.

2.6 $\mathcal{CP}$-violating phases

From the previous sections, there are fourteen parameters in the MSSM that can, in principle, take complex values; M_1, M_2, M_3, μ, m_{12}^2 and A_f for $f = u, d, c, s, t, b, e, \mu, \tau$. However, not all of the corresponding $\mathcal{CP}$-violating phases are physical; two of them

can be rotated away by a redefinition of fields. To show how this works we extend the procedure of Ref. [47] to allow independent phases for each of the gaugino masses and trilinear couplings.

We perform two $U(1)$ transformations; a Peccei-Quinn transformation (PQ) and an R_2 transformation. Under a general $U(1)$ transformation, quantities are multiplied by a factor $e^{iq\theta}$, where θ is the rotation angle and q is the $U(1)$ charge. We define the transformations of the parameters, M_i, A_f, m_{12}^2 and μ, such that the Lagrangian remains invariant. The $U(1)$ charges of the MSSM parameters and fields under PQ and R_2 are given in Table 2.2.

	M_i	A_f	m_{12}^2	μ	$\mathcal{H}_i$	F	θ
q_{PQ}	0	0	-1	-1	1/2	-1/2	0
q_{R_2}	-1	-1	0	1	0	1	-1/2

Table 2.2: The charges of the parameters, $M_{1,2,3}$, A_f, m_{13}^2 and μ, the Higgs supermultiplets, $\mathcal{H}_{1,2}$, the (s)quark and (s)lepton supermultiplet combinations, $F = Q\bar{U}, Q\bar{D}, L\bar{E}$, and the Grassman superspace coordinate, θ, under PQ and R_2 transformations.

We choose to make an R_2 transformation with angle ϕ_{M_2} on each of the parameters and fields, followed by a PQ transformation with angle $\phi_{m_{12}^2}$. This has the following effect on the phases of the parameters.

$$\begin{gathered}
\{\phi_\mu, \phi_{M_1}, \phi_{M_2}, \phi_{M_3}, \phi_{m_{12}^2}, \phi_{A_f}\} \\
\downarrow \quad R_2(\phi_{M_2}) \\
\{\phi_\mu + \phi_{M_2}, \phi_{M_1} - \phi_{M_2}, 0, \phi_{M_3} - \phi_{M_2}, \phi_{m_{12}^2}, \phi_{A_f} - \phi_{M_2}\} \\
\downarrow \quad PQ(\phi_{m_{12}^2}) \\
\{\phi_\mu + \phi_{M_2} - \phi_{m_{12}^2}, \phi_{M_1} - \phi_{M_2}, 0, \phi_{M_3} - \phi_{M_2}, 0, \phi_{A_f} - \phi_{M_2}\}
\end{gathered} \tag{2.42}$$

The phases of M_2 and m_{12}^2 have thus been rotated away. The remaining phases and fields are redefined to absorb ϕ_{M_2} and $\phi_{m_{12}^2}$. If we attempt further $U(1)$ transformations by angles ϕ_{M_1}, ϕ_{M_2}, ϕ_μ or ϕ_{A_f}, we find that no more of the phases can be absorbed. However, we could have equally chosen ϕ_{M_1} or ϕ_{M_3} instead of ϕ_{M_2} for the angle of the R_2 transformation. This is just a matter of convention. Thus, in total, there are 12 independent $\mathcal{CP}$-violating phases in the MSSM, which we choose to be ϕ_{M_1}, ϕ_{M_3}, ϕ_μ and

ϕ_{A_f} for $f = u, d, c, s, t, b, e, \mu, \tau$.

Theoretically, these 12 phases may be arbitrarily large, providing new sources of $\mathcal{CP}$-violation which could help to satisfy the Sakharov conditions required to explain the observed baryon asymmetry of the Universe. However, experimental limits on electric dipole moments (EDMs) of atoms and neutrons already place rather stringent constraints on new sources of $\mathcal{CP}$-violation beyond the single phase of the CKM matrix in the SM [48–60]. Large phases in the trilinear couplings for the first two generations of sfermions are only allowed experimentally if these generations are very heavy or if large cancellations occur. The constraints on the third generation trilinear couplings are much weaker. The higgsino phase, ϕ_μ, is quite tightly constrained in the convention where ϕ_{M_2} is zero. Ref. [59] not only provides a review of all of these constraints, but also gives a detailed study of how large cancellations can occur among various combinations of the $\mathcal{CP}$-violating phases, such that the predicted EDMs still satisfy the experimental constraints. This leaves open the possibility of large phases for both the gaugino mass parameters and the trilinear couplings of the third generation of sfermions, which we will allow in some of the scenarios we study in this thesis. We will always set the phases of the trilinear couplings for the first and second generations of sfermions to zero.

2.7 Parameters and benchmark scenarios

In order to specify a scenario in the complex MSSM, we require input values for the following 41 real parameters;

$$|M_1|,\ |M_2|,\ |M_3|,\ |\mu|,\ M_{qiL},\ M_{lL},\ M_{fR},\ |A_f|,\ \tan\beta,\ \phi_{M_1},\ \phi_{M_3},\ \phi_\mu,\ \phi_{A_f} \qquad (2.43)$$

where $i = 1, 2, 3$ labels the quark generation, $l = e, \mu, \tau$ and $f = e, \mu, \tau, u, d, c, s, t, b$. As in the SM, we must also specify a Higgs mass value; $M_{H^\pm}$ being the most convenient.[3]

The large number of parameters above is mostly due to our ignorance of the mechanism of soft supersymmetry breaking. In practice, some universality assumptions are often made at the GUT scale in order to reduce the number of parameters to a more manageable size, sometimes inspired by models which attempt to describe supersym-

[3] We do not include $M_{H^\pm}$ in the list of Equation (2.43) since it belongs in the parameter count of the SM, in which a Higgs mass value must also be specified.

metry breaking. The corresponding low-energy MSSM parameters listed in Equation (2.43) are then determined from the renormalisation group running of the GUT scale parameters down to the weak scale. In this thesis, we will instead use benchmark points and scenarios defined directly in terms of the low-energy MSSM parameters listed in Equation (2.43). Often these scenarios will have features which are inspired by the supersymmetry breaking models. For example, in many of our scenarios we assume a common gaugino mass at the GUT scale, resulting in the relation,

$$M_1 = \frac{5}{3}\left(\frac{s_W}{c_W}\right)^2 M_2, \tag{2.44}$$

at the weak scale. We will also usually assume that the first and second generations of sfermions have common mass parameters and trilinear couplings. When we assume that that the first, second and third generation of sfermions all have common mass parameters, we will denote these as $M_L = M_{\tilde{f}_R} \equiv M_{\rm SUSY}$.

The specific scenarios studied in this thesis are given in Table 2.3. We will consider in particular the standard Higgs phenomenology scenarios, including the CPX scenario [29][4], the small $\alpha_{\rm eff}$ scenario [61] and the $M_h^{\rm max}$ scenario [61, 62]. As already discussed, the CPX scenario is particularly interesting because $\mathcal{CP}$-violating effects give rise to an unexcluded parameter region with a light Higgs boson. The $\mathcal{CP}$-conserving small $\alpha_{\rm eff}$ scenario makes for an interesting comparison to the CPX scenario since it also has very large values for $|A_f|$ and μ. The $M_h^{\rm max}$ scenario is a $\mathcal{CP}$-conserving scenario often used in the literature for reporting on experimental bounds for Tevatron and LEP and the discovery potential at the LHC. In addition to the standard Higgs phenomenology scenarios, we also consider the standard set of SPS points [63], using as input the agreed low-energy values taken from Ref. [64], as shown in Table 2.3 for SPS1a.

We furthermore investigate a specific case of a $\mathcal{CP}$-conserving scenario giving rise to a very light $\tilde{\chi}_1^0$, inspired by a recent study [65] which showed that very light neutralinos are not ruled out by experimental data. Here the GUT relation in Equation (2.44) is relaxed, allowing M_1 to be chosen such that the lightest neutralino is approximately massless using,

$$M_1 = \frac{M_2 M_Z^2 \sin 2\beta s_W^2}{\mu M_2 - M_Z^2 \sin 2\beta c_W^2}. \tag{2.45}$$

[4]The value for $|A_f|$ given in Table 2.3 is an on-shell value that is slightly shifted from the $\overline{\rm DR}$ value specified in Ref. [29] (see also Ref. [30]).

For our study of decays of Higgs bosons into neutralinos in Chapters 8 and 10, we use a scenario found in the literature to have a large number of $H, A \to \tilde{\chi}_2^0 \tilde{\chi}_2^0$ events at the LHC [35]. We denote this scenario, "4L1", which corresponds to "Point 1" in Ref. [35]. We will also consider a slightly modified scenario, "4L1b", with lighter squarks and a large trilinear coupling. In Chapter 4 we will consider the scenario, "CPV1", as an example where both decays, $h_{2,3} \to \tilde{\chi}_3^0 \tilde{\chi}_1^0$ and $\tilde{\chi}_3^0 \to t\tilde{t}_1$ are kinematically open.

We always use a top quark mass of $m_t = 172.4\,\text{GeV}$. We use a running bottom quark mass, $m_b(m_t) = 2.734\,\text{GeV}$, (see Ref. [66]), except where indicated otherwise.

Scenario:	CPX	small $\alpha_{\rm eff}$	$M_h^{\rm max}$	light $\tilde{\chi}_1^0$	SPS1a	4L1	4L1b	CPV1
$\lvert M_1\rvert$	Eq.2.44	Eq.2.44	Eq.2.44	Eq.2.45	99.1	90	90	100
$\lvert M_2\rvert$	200	500	200	400	192.7	200	200	200
$\lvert M_3\rvert$	1000	500	800	1000	595.2	1000	1000	1000
$\lvert\mu\rvert$	2000	2000	200	600	352.4	500	500	500
$M_{\rm SUSY}$	500	800	1000	500	-	-	-	-
M_{q3L}	-	-	-	-	495.9	1000	500	500
M_{q12L}	-	-	-	-	539.9	1000	500	500
$M_{\tau L}$	-	-	-	-	195.8	250	250	300
$M_{e\mu L}$	-	-	-	-	196.6	250	250	200
M_{tR}	-	-	-	-	428.8	1000	500	500
M_{bR}	-	-	-	-	516.9	1000	500	500
$M_{\tau R}$	-	-	-	-	133.6	250	250	300
M_{ucR}	-	-	-	-	521.7	1000	500	500
M_{dsR}	-	-	-	-	519.5	1000	500	500
$M_{e\mu R}$	-	-	-	-	136.2	250	250	200
$\lvert A_{t,c,u}\rvert$	900	-	-	1000	510.0	0	1000	1200
$\lvert A_{b,s,d}\rvert$	900	$\lvert A_t\rvert$	$\lvert A_t\rvert$	1000	772.7	0	1000	1200
$\lvert A_{\tau,\mu,e}\rvert$	900	$\lvert A_t\rvert$	$\lvert A_t\rvert$	1000	254.2	0	1000	1000
X_t	-	-1100	2000	-	-	-	-	-
ϕ_{M_1}	0	0	0	0	0	0	0	0
ϕ_{M_3}	$\pi/2$	0	0	0	0	0	0	0
ϕ_μ	0	0	0	0	0	π	π	0
$\phi_{A_{t,b,\tau}}$	$\pi/2$	π	0	0	π	0	0	$\pi/2$
$\phi_{A_{f1,2}}$	π	0	0	0	π	0	0	0
$\tan\beta$	var	var	var	20	10	20	20	20
$M_{H^\pm}$	var	var	var	-	-	-	-	850
M_A	-	-	-	500	393.6	500	500	-

Table 2.3: Definition of scenarios in terms of the low-energy MSSM parameters. All parameters with mass dimension are given in GeV. "var" denotes a parameter which we will specify as required. We give nominal values for the phases, but will vary these when we study $\mathcal{CP}$-violating effects. Where X_t is given instead of $|A_f|$, then $|A_t|$ is evaluated from $|X_t + \mu^* \cot\beta|$. For some $\mathcal{CP}$-conserving scenarios, we choose $M_{H^\pm}$ such that M_A agrees with the values in the literature. $\phi_{A_{f1,2}}$ denotes the phase of the first and second generation sfermion trilinear couplings, which we always set to $\mathcal{CP}$-conserving values.

Chapter 3

Renormalisation of the MSSM

3.1 Regularisation and renormalisation

Much of this thesis will be concerned with higher order corrections in the MSSM.[1] Observables are evaluated using the Feynman-diagrammatic approach, in which higher order corrections to a tree-level process are obtained by computing Feynman diagrams involving one or more loops. These loop calculations involve tensor integrals over the loop momentum.[2] At the one-loop level, each tensor integral can be reduced down to a finite set of scalar integrals, via a procedure known as Passarino-Veltman Reduction [69]. Such integrals are often ultra-violet (UV) divergent; i.e. they diverge as the loop momentum gets arbitrarily large. In order to deal with these UV divergences, we employ a two step process, comprising regularisation and renormalisation.

Regularisation is the procedure by which we express divergences in such a way that they are well-defined and can be isolated from the rest of an expression. One method often used in the SM is dimensional regularisation, in which the computation is extended to $D = 4 - \epsilon$ dimensions, where ϵ is small and set to zero after the renormalisation procedure. Divergences then take the form of poles in $(D - 4)$. Dimensional regularisation is convenient in the SM because it preserves Lorentz and gauge invariance. However, since it does not preserve supersymmetry, dimensional reduction is often used instead in the MSSM. Here, while the loop integrals are evaluated in D dimensions, the fields are evaluated in four dimensions, allowing supersymmetry to be preserved up to at least two loop order [70, 71].

[1] For excellent reviews of higher order corrections in the SM, see Refs. [67, 68].
[2] See Appendix A.1 for the definitions of the loop integrals used in this thesis.

Renormalisation is the procedure by which the divergences, after having been isolated by regularisation, are systematically absorbed by a consistent re-identification of the free parameters and fields. The UV divergent bare parameters and fields which appear in the Lagrangian are interpreted as unphysical. A counterterm is required for each quantity in order to obtain a UV finite, physical result. The renormalised parameter or field, $\hat{a}$ or $\hat{\phi}$, is obtained from the bare parameter or field, a or ϕ, and its counterterm, δa or δZ_ϕ, as follows;

$$\begin{aligned} a &= \hat{a} + \delta a, \\ \phi &= \hat{\phi}(1 + \frac{1}{2}\delta Z_\phi). \end{aligned} \tag{3.1}$$

Therefore, to obtain the counterterm for a vertex involving this field or parameter at tree level, one should replace the bare parameter or field in the Lagrangian with the physical (renormalised) parameter and the counterterm;

$$\begin{aligned} a &\rightarrow a + \delta a, \\ \phi &\rightarrow \phi + \frac{1}{2}\delta Z_\phi \phi. \end{aligned} \tag{3.2}$$

Note that once this replacement has been made, it is customary to drop the hat from the renormalised quantity on the right. The value of the counterterm depends on the choice of renormalisation scheme. There are a number of schemes used in the literature. In the minimal subtraction (MS) scheme, used in conjunction with dimensional regularisation, only the divergent parts of the integrals, poles in $(D-4)$, are included in the counterterm. The $\overline{\text{MS}}$ scheme is a slightly modified scheme in which the constant, $(\log 4\pi - \gamma_E)$, which arises alongside poles in $(D-4)$ in these integrals (see Appendix A.1), is also absorbed into the counterterm. The $\overline{\text{DR}}$ scheme is similar to the $\overline{\text{MS}}$ scheme except it is used in conjunction with dimensional reduction, and is hence suitable for the MSSM. Another popular scheme for both the SM and MSSM is the on-shell scheme, in which physical masses are identified with the poles of the loop-corrected propagators.

In practice, for our calculations we have made use of the program `FeynArts`, allowing automated generation of the Feynman diagrams and amplitudes [72–74]. In conjunction, we have utilised the packages `FormCalc` and `LoopTools` for the calculation of matrix elements and the reduction and numerical evaluation of loop integrals [75]. For regularisation we use constrained differential renormalisation [76], a scheme available

in `FormCalc` which has been shown to be equivalent to dimensional reduction at the one-loop level [75].

While the MSSM model file which comes with `FeynArts` contains all the fields and vertices of the MSSM, it does not contain any counterterms, leaving it up to the user to choose and implement a renormalisation scheme. We have therefore supplemented the model files available in `FeynArts` with our own counterterms for the parameters and vertices. Arriving at a consistent renormalisation prescription for the complex MSSM was one of the major tasks of this thesis, so the rest of this and the next chapter will be devoted to describing our scheme in detail. In this chapter we describe the one-loop renormalisation of the gauge sector, the electric charge and the Higgs sector. In the following chapter we describe our renormalisation prescription for the chargino–neutralino sector, which was worked out for the first time in this thesis for the general case of complex parameters.

3.2 One-loop renormalisation of the gauge sector

For the gauge boson sector, we follow Ref. [67], since this scheme was already implemented into `FeynArts` for the SM in a way that is easily generalised to the MSSM. The main difference to be noted between the SM and MSSM is the sign convention for the covariant derivative, which is given by $D_\mu = \partial_\mu + ig\widetilde{W}_\mu + ig' y_\phi B_\mu$ in the MSSM. This results in the replacement $s_W \to -s_W$ in the corresponding Feynman rules. In Ref. [67], the parameters are renormalised with the following transformations;

$$M_Z^2 \;\to\; M_Z^2 + \delta M_Z^2, \tag{3.3}$$

$$M_W^2 \;\to\; M_W^2 + \delta M_W^2, \tag{3.4}$$

$$s_W \;\to\; s_W + \delta s_W, \tag{3.5}$$

$$c_W \;\to\; c_W + \delta c_W. \tag{3.6}$$

Using

$$s_W^2 = 1 - \frac{M_W^2}{M_Z^2}, \tag{3.7}$$

we see that δs_W and δc_W can be derived from δM_Z^2 and δM_W^2;

$$\delta s_W = \frac{c_W^2}{2 s_W}\left(\frac{\delta M_Z^2}{M_Z^2} - \frac{\delta M_W^2}{M_W^2}\right) \quad \text{and} \quad \delta c_W = -\frac{s_W}{c_W}\delta s_W. \tag{3.8}$$

The gauge fields are renormalised as

$$W^\pm \to (1 + \frac{1}{2}\delta Z_{WW})W^\pm \tag{3.9}$$

and

$$\begin{pmatrix} Z \\ \gamma \end{pmatrix} \to \begin{pmatrix} 1 + \frac{1}{2}\delta Z_{ZZ} & \frac{1}{2}\delta Z_{Z\gamma} \\ \frac{1}{2}\delta Z_{\gamma Z} & 1 + \frac{1}{2}\delta Z_{\gamma\gamma} \end{pmatrix} \begin{pmatrix} Z \\ \gamma \end{pmatrix}. \tag{3.10}$$

In the Feynman gauge, the renormalised one-particle irreducible (1PI) two-point vertex functions for gauge fields, $V, V' = W, Z, \gamma$, are given by

$$\hat{\Gamma}_{\mu\nu}^{VV'}(p) = -i g_{\mu\nu}(p^2 - M_V^2)\delta^{VV'} + i\hat{\Sigma}_{\mu\nu}^{VV'}(p) \tag{3.11}$$

where p is the incoming momentum and $\hat{\Sigma}_{\mu\nu}^{VV'}(p)$ is the self-energy evaluated at p. The hat notation is used to denote renormalised quantities. Each gauge-boson self-energy can be expressed in terms of its transverse part, Σ^T, and its longitudinal part, Σ^L;

$$\Sigma_{\mu\nu}(p) = -\left(g_{\mu\nu} - \frac{p_\mu p_\nu}{p^2}\right)\hat{\Sigma}_T(p^2) - \frac{p_\mu p_\nu}{p^2}\hat{\Sigma}_L(p^2). \tag{3.12}$$

The renormalised self-energy is related to the unrenormalised self-energy by

$$\hat{\Sigma}_{\mu\nu}^{VV'}(p) = \Sigma_{\mu\nu}^{VV'}(p) - g_{\mu\nu}\big[\frac{1}{2}(p^2 - M_V^2)\delta Z_{VV'} + \frac{1}{2}(p^2 - M_{V'}^2)\delta Z_{V'V} - \delta M_V^2 \delta^{VV'}\big]. \tag{3.13}$$

To obtain the renormalisation constants at one-loop order we apply on-shell conditions. Firstly, the propagators should have unity residues;

$$\lim_{p^2 \to M_V^2} \frac{1}{p^2 - M_V^2}\widetilde{\mathrm{Re}}\,\hat{\Gamma}_{\mu\nu}^{VV}(p)\epsilon^\nu(p) = -i\epsilon_\mu(p), \tag{3.14}$$

where $\epsilon(p)$ is the polarisation vector. Secondly, the γ and Z should not mix for on-shell external particle momenta;

$$\widetilde{\mathrm{Re}}\,\hat{\Gamma}_{\mu\nu}^{\gamma Z}(p)\epsilon^\nu(p)|_{p^2=M_Z^2} = 0 = \widetilde{\mathrm{Re}}\,\hat{\Gamma}_{\mu\nu}^{\gamma Z}(p)\epsilon^\nu(p)|_{p^2=0}. \tag{3.15}$$

Finally, the physical mass, M_V, should correspond to the real part of the pole of the propagator, or, equivalently, the zero of the corresponding 1PI two-point vertex function;

$$\widetilde{\mathrm{Re}}\,\hat{\Gamma}^{VV}_{\mu\nu}(p)\epsilon^{\nu}(p)|_{p^2=M_V^2} = 0. \tag{3.16}$$

In the above expressions, $\widetilde{\mathrm{Re}}$ takes the real part of the loop integrals appearing in a self-energy but not of the mixing matrix elements or parameters appearing as coefficients of the loop integral. (See Appendix A.2 for a discussion of the relationship between $\widetilde{\mathrm{Re}}$, $\widetilde{\mathrm{Im}}$, Re and Im.) As shown in Appendix A.2, $\widetilde{\mathrm{Re}}$ will coincide with the usual "Re" if all parameters are real. Otherwise, imaginary parts of loop integrals resulting from absorptive effects can appear with imaginary coefficients and thus contribute to the real part of the self-energy. For the SM and the MSSM with real parameters, since the only potential source of imaginary coefficients is the quark mixing matrix, which we set to unity, $\widetilde{\mathrm{Re}}$ may be replaced by Re everywhere. In the complex MSSM, there may be parameters from other sectors with non-zero phases which can enter the gauge boson self-energies as coefficients to loop integrals. However, in general, we will not consider scenarios where the SUSY particle masses are lighter than the gauge boson masses, so their loop integral contributions to the self-energies will not have absorptive parts.[3] The contributions from SM particles will contain absorptive loop integrals, but, without imaginary coefficients, these will not contribute to the real parts of self-energies. Thus, $\widetilde{\mathrm{Re}}$ may be replaced by Re in the expressions above even for the complex MSSM. We leave the notation as it is above in order to agree with the `FeynArts` SM file, which is based on Ref. [67]. The renormalisation conditions lead to the following values for the renormalisation constants;

$$\delta Z_{VV} = -\widetilde{\mathrm{Re}}\,(\Sigma_T^{VV})'(M_V^2), \tag{3.17}$$

$$\delta Z_{\gamma Z} = -\frac{2\widetilde{\mathrm{Re}}\,\Sigma_T^{\gamma Z}(M_Z^2)}{M_Z^2}, \quad \delta Z_{Z\gamma} = \frac{2\widetilde{\mathrm{Re}}\,\Sigma_T^{Z\gamma}(0)}{M_Z^2}, \tag{3.18}$$

$$\delta M_W^2 = \widetilde{\mathrm{Re}}\,\Sigma_T^{WW}(M_W^2) \quad \text{and} \quad \delta M_Z^2 = \widetilde{\mathrm{Re}}\,\Sigma_T^{ZZ}(M_Z^2), \tag{3.19}$$

where we have introduced the notation $\Sigma'(k^2) \equiv \frac{\partial\Sigma(p^2)}{\partial p^2}|_{p^2=k^2}$.

[3] The light neutralino scenario, given in Table 2.3, has a $\tilde{\chi}_1^0$ mass well below the W and Z masses, so will give an absorptive contribution to their self-energies. However, the coefficient appearing in front of this particular loop integral happens to be real even in the complex MSSM.

3.3 Charge renormalisation

The electric charge, e, is related to the electromagnetic coupling constant, $\alpha = \alpha_{\rm em}$, via $e^2(0) = 4\pi\alpha(0)$, where $\alpha(0) = 1/137.0359895$ is taken from experiment [28]. It is renormalised with the transformation

$$e(0) \to e(0)(1 + \delta Z_e), \tag{3.20}$$

where δZ_e is fixed by the renormalisation condition that the electric charge coincides with the full $ee\gamma$ coupling for on-shell external particles, $u(p)$, in the limit of zero photon momentum;

$$\bar{u}(p)\,\hat{\Gamma}^{ee\gamma}_{\mu}(p,p)\,u(p)|_{p^2=m_e^2} = \bar{u}(p)\big(\,i\,e(0)\,\gamma_\mu\big)\,u(p). \tag{3.21}$$

The full $ee\gamma$ coupling, $\hat{\Gamma}^{ee\gamma}_{\mu}$, consists of the corresponding loop-corrected vertex function together with the wavefunction renormalisation constants. Applying Equation (3.21) as in Ref. [67], one finds that

$$\begin{aligned} \delta Z_e &= -\frac{1}{2}(\delta Z_{\gamma\gamma} - \frac{s_W}{c_W}\delta Z_{Z\gamma}) \\ &= \frac{1}{2}\Pi_\gamma(0) + \frac{s_W}{c_W}\frac{\mathrm{Re}\,\Sigma^T_{\gamma Z}(0)}{M_Z^2} \end{aligned} \tag{3.22}$$

where $\Pi_\gamma(0) \equiv \frac{\partial\Sigma_{\gamma\gamma}(k^2)}{\partial k^2}|_{k^2=0}$ is the photon vacuum polarisation. One needs to be careful about how one computes $\Pi_\gamma(0)$, as it contains a logarithmic dependence on the fermion masses. The leptonic contribution can be evaluated from the known lepton masses, while for the hadronic contribution the quark masses are not well-defined input parameters since non-perturbative strong interaction effects dominate in this low energy regime. One option, used in the default settings of `FormCalc`, is to deliberately choose the quark masses as effective parameters to produce the "correct" value of $\Pi_\gamma(0)$.

Instead of using this effective approach, we use $\Delta\alpha$ as an input parameter, where

$$\alpha(M_Z^2) = \frac{\alpha(0)}{1 - \Delta\alpha} \tag{3.23}$$

includes the running of the electromagnetic coupling induced by the light fermions, resummed to all orders, with

$$\Delta\alpha \equiv \Delta\alpha_{lept} + \Delta\alpha^{(5)}_{had} \equiv -\mathrm{Re}\,\hat{\Pi}^{lept}_{\gamma}(M_Z^2) - \mathrm{Re}\,\hat{\Pi}^{had}_{\gamma}(M_Z^2). \tag{3.24}$$

The hatted quantity $\hat{\Pi}_\gamma$ is UV-convergent and is given by

$$\mathrm{Re}\,\hat{\Pi}_\gamma(M_Z^2) \equiv \frac{\mathrm{Re}\,\Sigma_{\gamma\gamma}(M_Z^2)}{M_Z^2} - \Pi_\gamma(0). \tag{3.25}$$

The abbreviations *lept* and *had* refer to the contributions from the leptons, e, μ, τ, and from the five light quarks u, d, c, s, b, respectively. We use the three-loop value of $\Delta\alpha_{lept} = 0.031498$, calculated in Ref. [77]. We use the recent literature value of $\Delta\alpha^{(5)}_{had} = 0.02758$, which was derived from experimental data in Ref. [78].

One can then rearrange the expression for δZ_e such that it depends on $\Delta\alpha$ instead of the light fermion masses;

$$\delta Z_e \;=\; \frac{1}{2}\Pi_\gamma(0)^{heavy} + \frac{s_W}{c_W}\frac{\Sigma^T_{\gamma Z}(0)}{M_Z^2} + \frac{1}{2}\mathrm{Re}\,\Pi_\gamma(M_Z^2)^{light} + \frac{1}{2}\Delta\alpha \tag{3.26}$$

where $\Pi_\gamma(0)^{heavy}$ is the photon vacuum polarisation, including only heavy particles (i.e. not the light fermions $e, \mu, \tau, u, d, c, s, b$).

In our calculations, it is appropriate to use the electric charge, $e(M_Z^2) = \sqrt{4\pi\alpha(M_Z^2)}$, defined at the electroweak scale, where

$$e(0) = e(M_Z^2)\sqrt{1-\Delta\alpha} = e(M_Z^2)(1 - \frac{\Delta\alpha}{2} + ...). \tag{3.27}$$

By using $e(M_Z^2)$ as input instead of $e(0)$, we effectively shift the large-logarithmic part of the one-loop correction to the electromagnetic coupling, $\alpha(M_Z^2)$, into the tree-level result. At the one-loop level, these parameterisations are equivalent. The bare coupling should be independent of the parameterisation chosen;

$$e(M_Z^2)\big(1 + \delta Z_e^{(M_Z^2)}\big) = e(0)(1 + \delta Z_e). \tag{3.28}$$

Hence, the $\Delta\alpha$ included in the tree-level coupling should be compensated with a $\Delta\alpha$ in the counterterm for $e(M_Z)$;

$$\begin{aligned} e(M_Z^2)(1+\delta Z_e^{(M_Z^2)}) &= e(M_Z^2)(1-\frac{\Delta\alpha}{2}+...)(1+\delta Z_e) \\ \Rightarrow\ \delta Z_e^{(M_Z^2)} &= \delta Z_e - \frac{\Delta\alpha}{2} \\ &= \frac{1}{2}\Pi_\gamma(0)^{heavy} + \frac{s_W}{c_W}\frac{\Sigma_{\gamma Z}^T(0)}{M_Z^2} + \frac{1}{2}\mathrm{Re}\,\Pi_\gamma(M_Z^2)^{light}. \end{aligned} \tag{3.29}$$

The resulting expression for $\delta Z_e^{(M_Z^2)}$ contains no explicit dependence on $\Delta\alpha$. All dependence of the electromagnetic coupling on large logarithms involving light fermions has been factored into $\alpha(M_Z^2)$, which takes $\Delta\alpha$ as input.

3.4 Renormalisation of the Higgs sector

Higher order corrections in the MSSM Higgs sector are known to be very important, especially when $\mathcal{CP}$-violation is considered. In the Feynman-diagrammatic approach, the full one-loop and the leading two-loop corrections to all Higgs self-energies, masses and mixings, as well as higher-order corrections to further relevant observables are available in the public code `FeynHiggs` [41, 79–81]. So that we can use this code to supplement our one-loop corrections with those leading two-loop corrections, we follow the same renormalisation scheme, given in Ref. [41], almost exclusively. The scheme is already valid for complex parameters in the MSSM, taking into account possible $\mathcal{CP}$-violating phases. Since the implementation of this scheme into `FeynArts` and the consistent inclusion of Higgs propagator corrections into our calculations both required numerous checks and derivations to be carried out, we present the renormalisation scheme used in this work in some detail below.

3.4.1 Tadpoles

Each of the Higgs tadpole terms is given a counterterm as follows;

$$T_{h,H,A} \to T_{h,H,A} + \delta T_{h,H,A}. \tag{3.30}$$

Note that the tadpole coefficients in terms of the physical fields, h,H and A, are related to those in Equation (2.6) via the mixing matrices of Equation (2.23). The tree level values for the tadpole coefficients vanish due to the minimisation of the Higgs potential. The renormalisation condition imposed is that the tadpole diagrams should also vanish at the one-loop order. This results in the following counterterms;

$$\delta T_{h,H,A} = -T_{h,H,A}. \tag{3.31}$$

3.4.2 Field renormalisation

One field renormalisation constant is introduced for each Higgs doublet;

$$\mathcal{H}_{1,2} \to (1 + \frac{1}{2}\delta Z_{\mathcal{H}_{1,2}})\mathcal{H}_{1,2}. \tag{3.32}$$

These are related to the counterterms for the physical fields by

$$\begin{aligned}
\delta Z_{hh} &= s_\alpha^2 \delta Z_{\mathcal{H}_1} + c_\alpha^2 \delta Z_{\mathcal{H}_2}, && (3.33)\\
\delta Z_{AA} &= s_\beta^2 \delta Z_{\mathcal{H}_1} + c_\beta^2 \delta Z_{\mathcal{H}_2}, && (3.34)\\
\delta Z_{hH} &= s_\alpha c_\alpha (\delta Z_{\mathcal{H}_2} - \delta Z_{\mathcal{H}_1}), && (3.35)\\
\delta Z_{AG} &= s_\beta c_\beta (\delta Z_{\mathcal{H}_2} - \delta Z_{\mathcal{H}_1}), && (3.36)\\
\delta Z_{HH} &= c_\alpha^2 \delta Z_{\mathcal{H}_1} + s_\alpha^2 \delta Z_{\mathcal{H}_2}, && (3.37)\\
\delta Z_{GG} &= c_\beta^2 \delta Z_{\mathcal{H}_1} + s_\beta^2 \delta Z_{\mathcal{H}_2}, && (3.38)\\
\delta Z_{H^-H^+} &= s_\beta^2 \delta Z_{\mathcal{H}_1} + c_\beta^2 \delta Z_{\mathcal{H}_2}, && (3.39)\\
\delta Z_{G^-H^+} &= \delta Z_{H^-G^+} = s_\beta c_\beta (\delta Z_{\mathcal{H}_2} - \delta Z_{\mathcal{H}_1}), && (3.40)\\
\delta Z_{G^-G^+} &= c_\beta^2 \delta Z_{\mathcal{H}_1} + s_\beta^2 \delta Z_{\mathcal{H}_2}. && (3.41)
\end{aligned}$$

The $\mathcal{CP}$-violating mixing counterterms are all zero;

$$\delta Z_{hA} = \delta Z_{HA} = \delta Z_{hG} = \delta Z_{HG} = 0. \tag{3.42}$$

As in Ref. [41], we adopt $\overline{\text{DR}}$ renormalisation for the fields, which leads to,

$$\delta Z_{\mathcal{H}_1}^{\overline{\text{DR}}} = -\text{Re}\ \Sigma'^{\,\text{div}}_{HH,\alpha=0} \tag{3.43}$$

$$\delta Z_{\mathcal{H}_2}^{\overline{\text{DR}}} = -\text{Re}\ \Sigma'^{\,\text{div}}_{hh,\alpha=0} \tag{3.44}$$

where $\Sigma'(p^2) = \frac{\partial\Sigma(p^2)}{\partial p^2}$ and "div" indicates that only the parts of the self-energy that are proportional to $\Delta \equiv 2/(4-D) - \gamma_E + \log 4\pi$ should be included (see Appendix A.1). We code this into `FeynArts` using the built-in `FormCalc` function `UVDivergentPart`.

3.4.3 Renormalisation of $\tan\beta$

The convention used in Ref. [41] for the counterterm of $\tan\beta$ is the transformation

$$\tan\beta \to \tan\beta(1 + \delta\tan\beta). \tag{3.45}$$

We will also need counterterms for other trigonometric expressions involving the angle β. For example, we can derive

$$\begin{aligned}
s_\beta &\to s_\beta + s_\beta\, c_\beta^2\, \delta t_\beta, && (3.46)\\
c_\beta &\to c_\beta - c_\beta\, s_\beta^2\, \delta t_\beta, && (3.47)\\
c_{\alpha\beta}^2 &\to c_{\alpha\beta}^2 - c_\beta s_\beta s_{2\alpha\beta}\, \delta t_\beta, && (3.48)\\
s_{\alpha\beta}^2 &\to s_{\alpha\beta}^2 + c_\beta s_\beta s_{2\alpha\beta}\, \delta t_\beta, && (3.49)\\
c_{\beta\alpha}^2 &\to c_{\beta\alpha}^2 - c_\beta s_\beta s_{2\beta\alpha}\, \delta t_\beta, && (3.50)
\end{aligned}$$

where we use the abbreviation $\delta\tan\beta \equiv \delta t_\beta$, $c_\beta \equiv \cos\beta$, $s_\beta \equiv \sin\beta$, $c_{\alpha\beta} \equiv \cos(\alpha+\beta)$, $s_{\alpha\beta} \equiv \sin(\alpha+\beta)$, $c_{\beta\alpha} \equiv \cos(\beta-\alpha)$, $s_{2\alpha\beta} \equiv \sin 2(\alpha+\beta)$ and $s_{2\beta\alpha} \equiv \sin 2(\beta-\alpha)$. As already mentioned, the mixing angles, α, β_n and β_c are not renormalised. Thus, one needs to be careful that the β appearing in a vertex being renormalised really arises from the ratio of the vacuum expectation values of the two Higgs doublets and not from the mixing angles β_c or β_n, which are equal to β at the tree level, but are not renormalised.

Following Ref. [41], we adopt $\overline{\text{DR}}$ renormalisation for $\tan\beta$. The reason this scheme has been adopted for `FeynHiggs` is that there is no obvious physical observable to which $\tan\beta$ could be related for an on-shell definition. Furthermore, the scheme has been shown to yield numerically stable and gauge invariant results at one-loop order [41]. The counterterm for $\tan\beta$ in the $\overline{\text{DR}}$ scheme is given by

$$\delta\tan\beta^{\overline{\text{DR}}} = \frac{1}{2}(\delta Z_{\mathcal{H}_2}^{\overline{\text{DR}}} - \delta Z_{\mathcal{H}_1}^{\overline{\text{DR}}}). \tag{3.51}$$

3.4.4 Mass parameter renormalisation

The mass matrices $\mathbf{M}_{\phi\phi\chi\chi}$ and $\mathbf{M}_{\phi^\pm\chi^\pm}$ from Equation (2.6) are each given a counterterm as follows;

$$\mathbf{M}_{\phi\phi\chi\chi} \rightarrow \mathbf{M}_{\phi\phi\chi\chi} + \delta\mathbf{M}_{\phi\phi\chi\chi}, \tag{3.52}$$

$$\mathbf{M}_{\phi^\pm\phi^\pm} \rightarrow M_{\phi^\pm\phi^\pm} + \delta\mathbf{M}_{\phi^\pm\phi^\pm}. \tag{3.53}$$

The resulting transformations on the elements of these matrices lead to mass counterterms for the physical fields which can be written entirely in terms of $\delta T_{h,H,A}$, δt_β and $\delta m^2_{H^\pm}$, as follows;

$$\begin{aligned}
\delta m_h^2 &= \delta m_A^2 c_{\beta\alpha}^2 + \delta M_Z^2 s_{\alpha\beta}^2 + \frac{e}{2M_Z s_W c_W}(\delta T_H c_{\beta\alpha} s_{\beta\alpha}^2 - \delta T_h s_{\beta\alpha}(1+c_{\beta\alpha}^2)) \\
&\quad +\delta t_\beta s_\beta c_\beta(-M_A^2 s_{2\beta\alpha} + M_Z^2 s_{2\alpha\beta}), && (3.54)\\
\delta m_{hH}^2 &= \frac{1}{2}(-\delta m_A^2 s_{2\beta\alpha} - \delta M_Z^2 s_{2\alpha\beta}) + \frac{e}{2M_Z s_W c_W}(-\delta T_H s_{\beta\alpha}^3 - \delta T_h c_{\beta\alpha}^3) \\
&\quad -\delta t_\beta s_\beta c_\beta(M_A^2 c_{2\beta\alpha} + M_Z^2 c_{2\alpha\beta}), && (3.55)\\
\delta m_H^2 &= \delta m_A^2 s_{\beta\alpha}^2 + \delta M_Z^2 c_{\alpha\beta}^2 - \frac{e}{2M_Z s_W c_W}(\delta T_H c_{\beta\alpha}(1+s_{\beta\alpha}^2) - \delta T_h s_{\beta\alpha} c_{\beta\alpha}^2) \\
&\quad -\delta t_\beta s_\beta c_\beta(-M_A^2 s_{2\beta\alpha} + M_Z^2 s_{2\alpha\beta}), && (3.56)\\
\delta m_{AG}^2 &= \frac{e}{2M_Z s_W c_W}(\delta T_H s_{\beta\alpha} - \delta T_h c_{\beta\alpha}) - \delta t_\beta M_A^2 s_\beta c_\beta && (3.57)\\
\delta m_G^2 &= \frac{e}{2M_Z s_W c_W}(-\delta T_H c_{\beta\alpha} - \delta T_h s_{\beta\alpha}), && (3.58)\\
\delta m_{hA}^2 &= \frac{e}{2M_Z s_W c_W}(-\delta T_A s_{\beta\alpha}), && (3.59)\\
\delta m_{hG}^2 &= \frac{e}{2M_Z s_W c_W}(\delta T_A c_{\beta\alpha}), && (3.60)\\
\delta m_{HA}^2 &= -\delta m_{hG}^2, && (3.61)\\
\delta m_{HG}^2 &= \delta m_{hA}^2, && (3.62)\\
\delta m_{H^-G^+}^2 &= \frac{e}{2M_Z s_W c_W}(\delta T_H s_{\beta\alpha} - \delta T_h c_{\beta\alpha} - i\delta T_A) - \delta t_\beta M_{H^\pm}^2 s_\beta c_\beta, && (3.63)\\
\delta m_{G^-H^+}^2 &= (\delta m_{H^-G^+}^2)^*, && (3.64)\\
\delta m_{G^\pm}^2 &= \frac{e}{2M_Z s_W c_W}(-\delta T_H c_{\beta\alpha} - \delta T_h s_{\beta\alpha}). && (3.65)
\end{aligned}$$

To fix $\delta m^2_{H^\pm}$, we use the mass of the charged Higgs boson, $M_{H^\pm}$, as input, applying the on-shell renormalisation condition that its value should agree with the real part of the

pole of the loop-corrected propagator. This leads to

$$\delta M^2_{H^\pm} = \text{Re}\,\Sigma_{H^+H^-}(M^2_{H^\pm}). \tag{3.66}$$

Note that here Re could equally be replaced with $\widetilde{\text{Re}}$, since the coefficients of the absorptive parts of the loop integrals which enter the charged Higgs boson self-energy turn out to be real, even in the MSSM with complex parameters.

3.4.5 Higgs self-energies

The renormalised Higgs self-energies can be expressed in terms of the unrenormalised self-energies and the renormalisation constants as follows;

$$\begin{aligned}
\hat{\Sigma}_{hh}(p^2) &= \Sigma_{hh}(p^2) + \delta Z_{hh}(p^2 - m_h^2) - \delta m_h^2,\\
\hat{\Sigma}_{hH}(p^2) &= \Sigma_{hH}(p^2) + \delta Z_{hH}\big(p^2 - \frac{1}{2}(m_h^2 + m_H^2)\big) - \delta m_{hH}^2,\\
\hat{\Sigma}_{HH}(p^2) &= \Sigma_{HH}(p^2) + \delta Z_{HH}(p^2 - m_H^2) - \delta m_H^2,\\
\hat{\Sigma}_{AA}(p^2) &= \Sigma_{AA}(p^2) + \delta Z_{AA}(p^2 - m_A^2) - \delta m_A^2,\\
\hat{\Sigma}_{AG}(p^2) &= \Sigma_{AG}(p^2) + \delta Z_{AG}\big(p^2 - \frac{1}{2}m_A^2\big) - \delta m_{AG}^2,\\
\hat{\Sigma}_{GG}(p^2) &= \Sigma_{GG}(p^2) + \delta Z_{GG}\, p^2 - \delta m_G^2,\\
\hat{\Sigma}_{hA}(p^2) &= \Sigma_{hA}(p^2) - \delta m_{hA}^2,\\
\hat{\Sigma}_{hG}(p^2) &= \Sigma_{hG}(p^2) - \delta m_{hG}^2,\\
\hat{\Sigma}_{HA}(p^2) &= \Sigma_{HA}(p^2) - \delta m_{HA}^2,\\
\hat{\Sigma}_{HG}(p^2) &= \Sigma_{HG}(p^2) - \delta m_{HG}^2,\\
\hat{\Sigma}_{H^-H^+}(p^2) &= \Sigma_{H^-H^+}(p^2) + \delta Z_{H^-H^+}(p^2 - m_{H^\pm}^2) - \delta m_{H^\pm}^2,\\
\hat{\Sigma}_{H^-G^+}(p^2) &= \Sigma_{H^-G^+}(p^2) + \delta Z_{H^-G^+}\big(p^2 - \frac{1}{2}m_{H^\pm}^2\big) - \delta m_{H^-G^+}^2,\\
\hat{\Sigma}_{G^-H^+}(p^2) &= \hat{\Sigma}^*_{H^-G^+}(p^2),\\
\hat{\Sigma}_{G^-G^+}(p^2) &= \Sigma_{G^-G^+}(p^2) + \delta Z_{G^-G^+}\, p^2 - \delta m_{G_\pm}^2.
\end{aligned} \tag{3.67}$$

We have performed numerous checks on the renormalised Higgs self-energies for UV convergence. We have also checked that the numerical values of the renormalised self-energies obtained using the expressions above, in conjunction with `FormCalc` and `LoopTools`, are in agreement with those obtained as output from `FeynHiggs` at the one-loop level. This is important since `FeynHiggs` can also output the two-loop renormalised

self-energies, which we use later in some parts of our calculations to supplement our one-loop results. This can only be done when we are certain that the one-loop results and conventions are in agreement.

3.4.6 Higgs masses

The loop-corrected neutral masses M_{h_a} are defined as the real parts of the poles of the diagonal elements of the 3×3 Higgs propagator matrix.[4] The latter, $\Delta_{hHA}(p^2)$, is given by the inverse of the 3×3 matrix of irreducible vertex functions, $\hat{\Gamma}_{hHA}(p^2)$;

$$\Delta_{hHA}(p^2) = -(\hat{\Gamma}_{hHA}(p^2))^{-1}, \tag{3.68}$$

where

$$\hat{\Gamma}_{hHA}(p^2) = i(p^2 \mathbb{1} - \mathbf{M}_n(p^2)), \tag{3.69}$$

with the Higgs 3×3 mass matrix in the $\{h, H, A\}$ basis defined as

$$\mathbf{M}_n(p^2) = \begin{pmatrix} m_h^2 - \hat{\Sigma}_{hh}(p^2) & -\hat{\Sigma}_{hH}(p^2) & -\hat{\Sigma}_{hA}(p^2) \\ -\hat{\Sigma}_{hH}(p^2) & m_H^2 - \hat{\Sigma}_{HH}(p^2) & -\hat{\Sigma}_{HA}(p^2) \\ -\hat{\Sigma}_{hA}(p^2) & -\hat{\Sigma}_{HA}(p^2) & m_A^2 - \hat{\Sigma}_{AA}(p^2) \end{pmatrix}. \tag{3.70}$$

The 3×3 Higgs propagator matrix can be written in terms of its elements as follows;

$$\begin{pmatrix} \Delta_{hh} & \Delta_{hH} & \Delta_{hA} \\ \Delta_{hH} & \Delta_{HH} & \Delta_{HA} \\ \Delta_{hA} & \Delta_{HA} & \Delta_{AA} \end{pmatrix} = i \begin{pmatrix} p^2 - m_h^2 + \hat{\Sigma}_{hh}(p^2) & \hat{\Sigma}_{hH}(p^2) & \hat{\Sigma}_{hA}(p^2) \\ \hat{\Sigma}_{hH}(p^2) & p^2 - m_H^2 + \hat{\Sigma}_{HH}(p^2) & \hat{\Sigma}_{HA}(p^2) \\ \hat{\Sigma}_{hA}(p^2) & \hat{\Sigma}_{HA}(p^2) & p^2 - m_A^2 + \hat{\Sigma}_{AA}(p^2) \end{pmatrix}^{-1}. \tag{3.71}$$

[4] In fact, the 3×3 propagator matrix is an approximation to the 6×6 propagator matrix which also includes mixing with the neutral would-be Goldstone boson, G, the Z boson and the photon. For the Higgs mass calculation, this has an effect of sub-leading two-loop order less than some other two-loop effects which are also not taken into account in `FeynHiggs`. Thus, a 3×3 propagator matrix is used in `FeynHiggs`. See Ref. [41] for details. In this thesis, we will include the mixing effects with the G and Z bosons when we perform one-loop vertex calculations involving external Higgs and/or Z bosons. Here they are a true one-loop effect, although numerically small, so must be included in a full one-loop calculation. See Section 5.4.

Evaluating the inverse of $\hat{\Gamma}_{hHA}$ gives, for the diagonal Higgs propagators (i=h,H,A);

$$\Delta_{ii}(p^2) = \frac{i}{p^2 - m_i^2 + \hat{\Sigma}_{ii}^{\text{eff}}(p^2)} \tag{3.72}$$

with the effective self-energy, $\hat{\Sigma}_{ii}^{\text{eff}}(p^2)$, defined to include the usual self-energy plus the mixing contributions with the remaining two Higgs bosons (labelled j and k, where i, j and k are simply some permutation of h, H and A and are therefore not summed over);

$$\hat{\Sigma}_{ii}^{\text{eff}}(p^2) = \hat{\Sigma}_{ii}(p^2) - i\frac{2\hat{\Gamma}_{ij}(p^2)\hat{\Gamma}_{jk}(p^2)\hat{\Gamma}_{ki}(p^2) - \hat{\Gamma}_{ki}^2(p^2)\hat{\Gamma}_{jj}(p^2) - \hat{\Gamma}_{ij}^2(p^2)\hat{\Gamma}_{kk}(p^2)}{\hat{\Gamma}_{jj}(p^2)\hat{\Gamma}_{kk}(p^2) - \hat{\Gamma}_{jk}^2(p^2)}. \tag{3.73}$$

We identify the poles of the diagonal Higgs propagators of Equation (3.72) with the physical Higgs masses. The complex pole $\mathcal{M}_i^2$ of the propagator Δ_{ii} is the solution of

$$\mathcal{M}_i^2 - m_i^2 + \hat{\Sigma}_{ii}^{\text{eff}}(\mathcal{M}_i^2) = 0. \tag{3.74}$$

We write the complex pole as

$$\mathcal{M}_i^2 = M_i^2 - iM_i\Gamma_i \tag{3.75}$$

where M_i is the loop-corrected Higgs mass, and Γ_i its width. One can solve Equation (3.74) iteratively to find the loop-corrected mass, M_i, in terms of the lowest order mass, m_i, where $i = h, H, A$. We implemented this iterative method of solving Equation (3.74) in `Mathematica`. We evaluated the self-energies at complex squared momentum, $p^2 \equiv p_r^2 + ip_i^2$, by using the truncated expansion

$$\hat{\Sigma}_{ij}(p^2) = \hat{\Sigma}_{ij}(p_r^2) + i\,p_i^2\hat{\Sigma}'_{ij}(p_r^2). \tag{3.76}$$

We have checked that the higher order terms in this expansion are numerically small. These expansions for the individual self-energies are then inserted into the expression for the effective self-energy in Equation (3.73). We do not expand $\hat{\Sigma}_{ii}^{\text{eff}}(p^2)$ about p_r^2 directly; instead we expand the individual terms on the right hand side of Equation (3.73) which gives more numerically reliable results. In contrast to our iterative method of solving Equation (3.74) directly to find the physical masses, note that `FeynHiggs` actually uses a diagonalisation procedure, iteratively finding the eigenvalues of the 3×3 mass matrix $\mathbf{M}_n$, and then verifying that each eigenvalue is indeed the appropriate solution of Equation

(3.74). As discussed in the next section, we find agreement between the two methods. The loop-corrected mass eigenvalues are defined with $M_{h_1} \leq M_{h_2} \leq M_{h_3}$.

3.4.7 Numerical results for Higgs masses in the CPX scenario

As an example, we show numerical results for the Higgs masses evaluated from `FeynHiggs 2.6.5` for the CPX scenario defined in Table 2.3. Figure 3.1(a) shows the three neutral Higgs masses, M_{h_i}, as a function of the on-shell charged Higgs mass, $M_{H^\pm}$, with $\tan\beta$ fixed at 5.5. We see that arbitrarily small values for the lightest Higgs mass, M_{h_1} are theoretically accessible for low $M_{H^\pm}$. For large $M_{H^\pm}$, M_{h_1} reaches an upper limit of around 111 GeV in this example. M_{h_2} and M_{h_3} increase with $M_{H^\pm}$ for large $M_{H^\pm}$. These masses are evaluated at the two-loop level, i.e. they include the complete one-loop contributions from the full MSSM, along with the leading two-loop corrections available within `FeynHiggs`.

Figure 3.1(b) shows the various contributions to the lightest Higgs mass, as a function of $M_{H^\pm}$, with $\tan\beta = 5.5$. We see that the one-loop mass exhibits a very different behaviour to the tree-level Higgs mass, emphasising the importance of loop corrections in the Higgs sector. The most important contribution to the one-loop correction comes from loops involving (s)top quarks, due to the large top Yukawa coupling.

We have also computed the one-loop Higgs masses using the iterative method described in the previous section. Our results are in perfect numerical agreement with those obtained from `FeynHiggs`. This is true whether we use as input our own one-loop renormalised self-energies computed using `FormCalc` and `LoopTools` or the one- or two-loop self-energies obtained from `FeynHiggs`. Therefore we can incorporate the higher order corrections available within `FeynHiggs` with confidence that our schemes and conventions are compatible.

Figure 3.1(b) shows the importance of including the leading two-loop corrections, which are of $\mathcal{O}(\alpha_t\alpha_s)$.[5] These can lead to corrections to the one-loop mass of some $10-30$ GeV.

[5] We do not include further two-loop corrections available within `FeynHiggs` for the MSSM with real parameters only. For the MSSM with complex parameters, `FeynHiggs` can provide an interpolated result for those corrections based on the results for real parameters. However, since this method does not always give numerically stable results for scenarios with maximal $\mathcal{CP}$-violating phases, like the CPX scenario, we do not include these further two-loop corrections; we only include the $\mathcal{O}(\alpha_t\alpha_s)$ corrections.

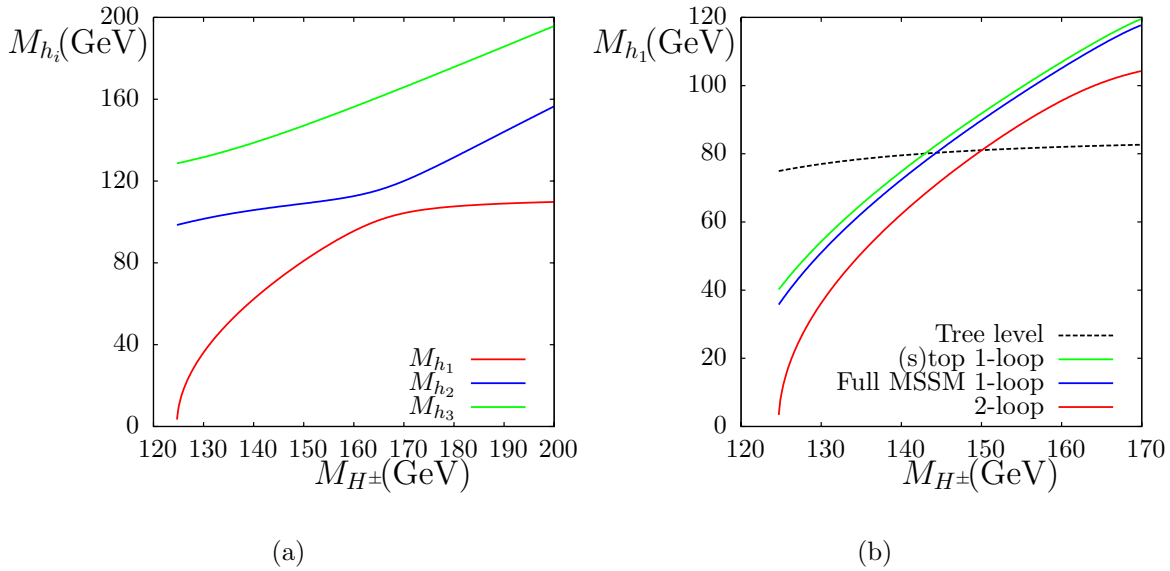

(a) (b)

Figure 3.1: (a) Neutral Higgs masses in the CPX scenario with $\tan\beta = 5.5$, evaluated at the two-loop level using `FeynHiggs 2.6.5`, shown as a function of $M_{H^\pm}$. (b) Lightest Higgs mass in CPX scenario with $\tan\beta = 5.5$ evaluated using `FeynHiggs-2.6.5`, shown as a function of $M_{H^\pm}$. The plot shows the tree-level mass, the one-loop mass evaluated including only top quarks and squarks in the loops, the one-loop mass evaluated including all MSSM particles in the loops and the "two-loop" mass which also includes the $\mathcal{O}(\alpha_t\alpha_s)$ corrections.

In practice hereafter, we obtain our Higgs masses directly from `FeynHiggs`, so as to allow these important two-loop effects to be included.

3.4.8 Higgs propagator corrections

In the previous section we found the diagonal Higgs propagators to be given by Equation (3.72). We can also obtain the off-diagonal Higgs propagators from the inverse of $\hat{\Gamma}_{hHA}$ ($i \neq j$). These are also momentum dependent, but we have dropped the p^2 below for simplicity;

$$\Delta_{ij} = \frac{\hat{\Gamma}_{ij}\hat{\Gamma}_{kk} - \hat{\Gamma}^2_{jk}\hat{\Gamma}_{ki}}{\hat{\Gamma}_{ii}\hat{\Gamma}_{jj}\hat{\Gamma}_{kk} + 2\hat{\Gamma}_{ij}\hat{\Gamma}_{jk}\hat{\Gamma}_{ki} - \hat{\Gamma}_{ii}\hat{\Gamma}^2_{jk} - \hat{\Gamma}_{jj}\hat{\Gamma}^2_{ki} - \hat{\Gamma}_{kk}\hat{\Gamma}^2_{ij}}. \tag{3.77}$$

We then find that the effective self-energy from Equation (3.73) can be written in terms of Higgs self-energies weighted by ratios of the off-diagonal and diagonal propagators as

follows;

$$\hat{\Sigma}^{\text{eff}}_{ii}(p^2) = \hat{\Sigma}_{ii}(p^2) + \frac{\Delta_{ij}(p^2)}{\Delta_{ii}(p^2)}\hat{\Sigma}_{ij}(p^2) + \frac{\Delta_{ik}(p^2)}{\Delta_{ii}(p^2)}\hat{\Sigma}_{ik}(p^2). \tag{3.78}$$

In order to understand which Feynman diagrams these loop-corrected propagators and their ratios represent, we expand the expressions in terms of the Higgs self-energies (which are momentum-dependent but again we drop the p^2 for simplicity) and the tree-level propagators in a simplified 2×2 mixing scenario, where mixing with the third Higgs boson, k, can be ignored. Then

$$\begin{aligned}
\Delta_{ii}(p^2)_{2\times2} &= \frac{i\,(p^2 - m_j^2 + \hat{\Sigma}_{jj})}{(p^2 - m_i^2 + \hat{\Sigma}_{ii})(p^2 - m_j^2 + \hat{\Sigma}_{jj}) - \hat{\Sigma}_{ij}^2} && (3.79)\\
&= \frac{i(D_j + \hat{\Sigma}_{jj})}{D_iD_j[(1 + \hat{\Sigma}_{ii}/D_i)(1 + \hat{\Sigma}_{jj}/D_j) - \hat{\Sigma}_{ij}^2/(D_iD_j)]}\\
&= i(\frac{1}{D_i} - \frac{\hat{\Sigma}_{ii}}{D_i^2} + \frac{\hat{\Sigma}_{ii}^2}{D_i^3} + \frac{\hat{\Sigma}_{ij}^2}{D_i^2D_j} + \mathcal{O}(3-\text{loop})) && (3.80)
\end{aligned}$$

where $D_i \equiv p^2 - m_i^2$. We show this diagrammatically for Δ_{HH} in Figure 3.2(a). We see that $\Delta_{ii}(p^2)$ consists of the tree level propagator, i/D_i, at the lowest order. Then at one loop it includes the diagonal self-energy, $\hat{\Sigma}_{ii}$, with tree-level propagators, i/D_i, either side. Then at two loop there are two diagrams; one with two diagonal self-energies, $\hat{\Sigma}_{ii}$, and three tree-level propagators, i/D_i, in between and either side, and one with two mixing self-energies, $\hat{\Sigma}_{ij}$, one propagator i/D_j in between and two propagators, i/D_i, either side.

Similarly in the 2×2 mixing case, the off-diagonal propagator can be written as

$$\begin{aligned}
\Delta_{ij}(p^2)_{2\times2} &= \frac{-i\,\hat{\Sigma}_{ij}}{(p^2 - m_i^2 + \hat{\Sigma}_{ii})(p^2 - m_j^2 + \hat{\Sigma}_{jj}) - \hat{\Sigma}_{ij}^2} && (3.81)\\
&= \frac{-i\hat{\Sigma}_{ij}}{D_iD_j[(1 + \hat{\Sigma}_{ii}/D_i)(1 + \hat{\Sigma}_{jj}/D_j) - \hat{\Sigma}_{ij}^2/(D_iD_j)]}\\
&= i(-\frac{\hat{\Sigma}_{ij}}{D_iD_j} + \frac{\hat{\Sigma}_{ij}\hat{\Sigma}_{ii}}{D_i^2D_j} + \frac{\hat{\Sigma}_{ij}\hat{\Sigma}_{jj}}{D_iD_j^2} + \mathcal{O}(3-\text{loop})) && (3.82)
\end{aligned}$$

where the lowest order diagram consists of one mixing self-energy, $\hat{\Sigma}_{ij}$, with two propagators, i/D_i and i/D_j either side, and so on. We show this diagrammatically for Δ_{HA} in Figure 3.2(b).

It is also useful to have an expansion of the ratio of propagators in the 2×2 mixing case;

$$\begin{aligned}
\frac{\Delta_{ij}(p^2)}{\Delta_{ii}(p^2)}_{2\times 2} &= \frac{\hat{\Sigma}_{ij}}{p^2 - m_j^2 + \hat{\Sigma}_{jj}} \\
&= -\frac{\hat{\Sigma}_{ij}}{D_j}(1 - \frac{\hat{\Sigma}_{jj}}{D_j} + \frac{\hat{\Sigma}_{jj}^2}{D_j^2} - \frac{\hat{\Sigma}_{jj}^3}{D_j^3} + ...) \\
&= -\frac{\hat{\Sigma}_{ij}}{D_j} + \frac{\hat{\Sigma}_{ij}\hat{\Sigma}_{jj}}{D_j^2} + \mathcal{O}(3-\text{loop}).
\end{aligned} \tag{3.83}$$

One can think of the diagrams for this ratio as being obtained from the diagrams for $\Delta_{ij}(p^2)$ by "dividing out" the parts of diagrams which start and end on the i^{th} propagator, i/D_i, as shown diagrammatically in Figure 3.2(c).

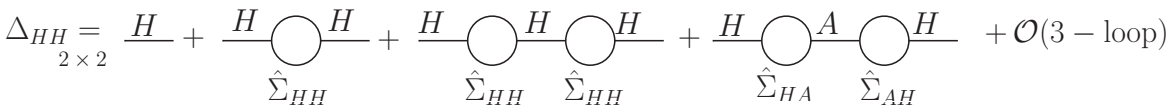

(a)

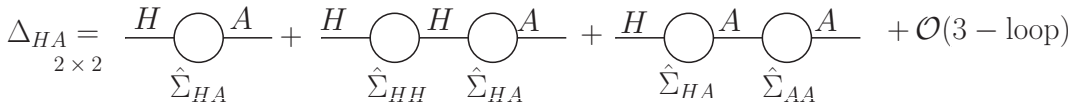

(b)

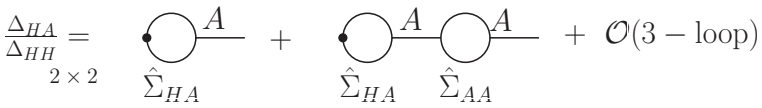

(c)

Figure 3.2: Diagrams for propagator corrections in the simplified 2×2 H-A mixing case; (a) the diagonal propagator, Δ_{HH}, (b) the off-diagonal propagator, Δ_{HA}, and (c) the ratio of propagators, Δ_{HA}/Δ_{HH}.

3.4.9 $\hat{\mathbf{Z}}$ matrices for external Higgs bosons

Where possible in the SM, physical fields, ϕ_i, with the same quantum numbers are usually renormalised using an on-shell condition, $\hat{\Gamma}_{ij}\phi_i(p)|_{p^2=m_j^2} = 0$ for $i \neq j$, to ensure that the fields do not mix on the mass shell of the physical particles at the loop-level. However, in our choice of renormalisation scheme for the Higgs fields in Equations (3.43) and (3.44), the lowest order Higgs bosons, h, H, A, are not forced to obey such a condition. Instead the $\overline{\text{DR}}$ renormalisation scheme for Higgs fields was chosen for convenience and agreement with Ref. [41]. An artefect of this choice is that the loop-corrected states, h_1, h_2, h_3, are actually mixtures of h, H, A. Therefore, in order to ensure the correct on-shell properties of Higgs bosons appearing as external particles in physical processes, and thus a properly normalised S-matrix, one has to use finite normalisation factors, $\hat{Z}_{ij}$, to account for the mixing between the Higgs bosons. A vertex with an external Higgs boson i, $(i = h, H, A)$ has the correctly normalised form;

$$\sqrt{\hat{Z}_i}(\hat{\Gamma}_i + \hat{Z}_{ij}\hat{\Gamma}_j + \hat{Z}_{ik}\hat{\Gamma}_k + ...). \tag{3.84}$$

Here $\hat{\Gamma}_i$ are the renormalised one-particle irreducible vertices, j, k are the remaining two of h, H, A and are not summed over, and the ellipsis refers to the mixing contributions with the Goldstone and Z bosons. Ignoring the latter for now (see Section 5.4), the normalisation of the wavefunctions can be expressed in terms of a 3×3 non-unitary matrix $\hat{\mathbf{Z}}_{ij} = \sqrt{\hat{Z}_i}\hat{Z}_{ij}$, with $\hat{Z}_{ii} = 1$. Rather than using the definition for the $\hat{\mathbf{Z}}$ matrix given in Ref. [41], where the self-energies are evaluated at the real part of the complex poles, $M^2_{h_{a,b,c}}$, we use the method of Ref. [30], which has also been implemented in more recent versions of `FeynHiggs`. Here all self-energies in the $\hat{\mathbf{Z}}$ matrix are evaluated at the complex poles $\mathcal{M}^2_{h_{a,b,c}}$. The $\hat{\mathbf{Z}}$ matrix elements are chosen such that

$$\lim_{p^2\to\mathcal{M}^2_{h_a}} \; -\tfrac{i}{p^2-\mathcal{M}^2_{h_a}}(\hat{\mathbf{Z}}\cdot\hat{\mathbf{\Gamma}}_{\mathbf{hHA}}\cdot\hat{\mathbf{Z}}^T)_{hh} = 1, \tag{3.85}$$

$$\lim_{p^2\to\mathcal{M}^2_{h_b}} \; -\tfrac{i}{p^2-\mathcal{M}^2_{h_b}}(\hat{\mathbf{Z}}\cdot\hat{\mathbf{\Gamma}}_{\mathbf{hHA}}\cdot\hat{\mathbf{Z}}^T)_{HH} = 1, \tag{3.86}$$

$$\lim_{p^2\to\mathcal{M}^2_{h_c}} \; -\tfrac{i}{p^2-\mathcal{M}^2_{h_a}}(\hat{\mathbf{Z}}\cdot\hat{\mathbf{\Gamma}}_{\mathbf{hHA}}\cdot\hat{\mathbf{Z}}^T)_{AA} = 1, \tag{3.87}$$

with

$$\begin{pmatrix} \hat{\Gamma}_{h_a} \\ \hat{\Gamma}_{h_b} \\ \hat{\Gamma}_{h_c} \end{pmatrix} = \begin{pmatrix} \sqrt{\hat{Z}_h} & \sqrt{\hat{Z}_h}\hat{Z}_{hH} & \sqrt{\hat{Z}_h}\hat{Z}_{hA} \\ \sqrt{\hat{Z}_H}\hat{Z}_{Hh} & \sqrt{\hat{Z}_H} & \sqrt{\hat{Z}_H}\hat{Z}_{HA} \\ \sqrt{\hat{Z}_A}\hat{Z}_{Ah} & \sqrt{\hat{Z}_A}\hat{Z}_{AH} & \sqrt{\hat{Z}_A} \end{pmatrix} \cdot \begin{pmatrix} \hat{\Gamma}_h \\ \hat{\Gamma}_H \\ \hat{\Gamma}_A \end{pmatrix}. \tag{3.88}$$

The resulting expressions, which we use in our implementation in `FeynArts`, are

$$\hat{Z}_h = \left.\frac{1}{\frac{\partial}{\partial p^2}\frac{i}{\Delta_{hh}(p^2)}}\right|_{p^2=\mathcal{M}^2_{h_a}}, \; \hat{Z}_H = \left.\frac{1}{\frac{\partial}{\partial p^2}\frac{i}{\Delta_{HH}(p^2)}}\right|_{p^2=\mathcal{M}^2_{h_b}}, \; \hat{Z}_A = \left.\frac{1}{\frac{\partial}{\partial p^2}\frac{i}{\Delta_{AA}(p^2)}}\right|_{p^2=\mathcal{M}^2_{h_c}} \tag{3.89}$$

and

$$\begin{aligned}
\hat{Z}_{hH} &= \left.\frac{\Delta_{hH}(p^2)}{\Delta_{hh}(p^2)}\right|_{p^2=\mathcal{M}^2_{h_a}}, \; \hat{Z}_{Hh} = \left.\frac{\Delta_{Hh}(p^2)}{\Delta_{HH}(p^2)}\right|_{p^2=\mathcal{M}^2_{h_b}}, \; \hat{Z}_{Ah} = \left.\frac{\Delta_{Ah}(p^2)}{\Delta_{AA}(p^2)}\right|_{p^2=\mathcal{M}^2_{h_c}}, \\
\hat{Z}_{hA} &= \left.\frac{\Delta_{hA}(p^2)}{\Delta_{hh}(p^2)}\right|_{p^2=\mathcal{M}^2_{h_a}}, \; \hat{Z}_{HA} = \left.\frac{\Delta_{HA}(p^2)}{\Delta_{HH}(p^2)}\right|_{p^2=\mathcal{M}^2_{h_b}}, \; \hat{Z}_{AH} = \left.\frac{\Delta_{AH}(p^2)}{\Delta_{AA}(p^2)}\right|_{p^2=\mathcal{M}^2_{h_c}}.
\end{aligned} \tag{3.90}$$

We choose $a = 1$, $b = 2$ and $c = 3$, but in principle other combinations are possible. Notice that $\hat{Z}_{ij}$ corresponds to the ratio of propagators described by the diagrams in Figure 3.2(c), i.e. it describes the transition of the i^{th} Higgs boson into the j^{th} Higgs boson. Also notice that $\hat{Z}_i$ can be written as

$$\hat{Z}_i = \left.\frac{1}{1 + \hat{\Sigma}^{\text{eff}\,\prime}_{ii}(p^2)}\right|_{p^2=\mathcal{M}^2_{h_a}}. \tag{3.91}$$

where $\hat{\Sigma}^{\text{eff}\,\prime}_{ii}(p^2) \equiv \frac{\partial}{\partial p^2}\hat{\Sigma}^{\text{eff}}_{ii}(p^2)$. To see what this represents, we expand the diagonal Higgs propagator, $\Delta_{ii}(p^2)$ about the complex mass solution, $p^2 = \mathcal{M}^2_i = \mathcal{M}^2_{h_a}$, where $\mathcal{M}^2_i - m^2_i + \hat{\Sigma}^{\text{eff}}_{ii}(\mathcal{M}^2_i) = 0$;

$$\begin{aligned}
\Delta_{ii}(p^2) &= \frac{i}{p^2 - m^2_i + \hat{\Sigma}^{\text{eff}}_{ii}(p^2)} \\
&= \frac{i}{p^2 - \mathcal{M}^2_i}\left(\frac{1}{1 + (\hat{\Sigma}^{\text{eff}}_{ii})'(\mathcal{M}^2_i) + \mathcal{O}(p^2 - \mathcal{M}^2_i)}\right) \\
&\approx \frac{i}{p^2 - \mathcal{M}^2_i}\hat{Z}_i \\
&= \frac{i}{p^2 - M^2_i + iM_i\Gamma_i}\hat{Z}_i \\
&= \Delta^{\text{BW}}_i(p^2)\hat{Z}_i
\end{aligned} \tag{3.92}$$

where the approximation is true if $p^2 \approx \mathcal{M}^2_i$. Thus, near its pole, $\Delta_{ii}(p^2)$ can be represented by a Breit-Wigner propagator, $\Delta^{\text{BW}}_i(p^2)$, with mass M_i and width Γ_i, weighted by a normalisation factor, $\hat{Z}_i$, evaluated at the complex pole.

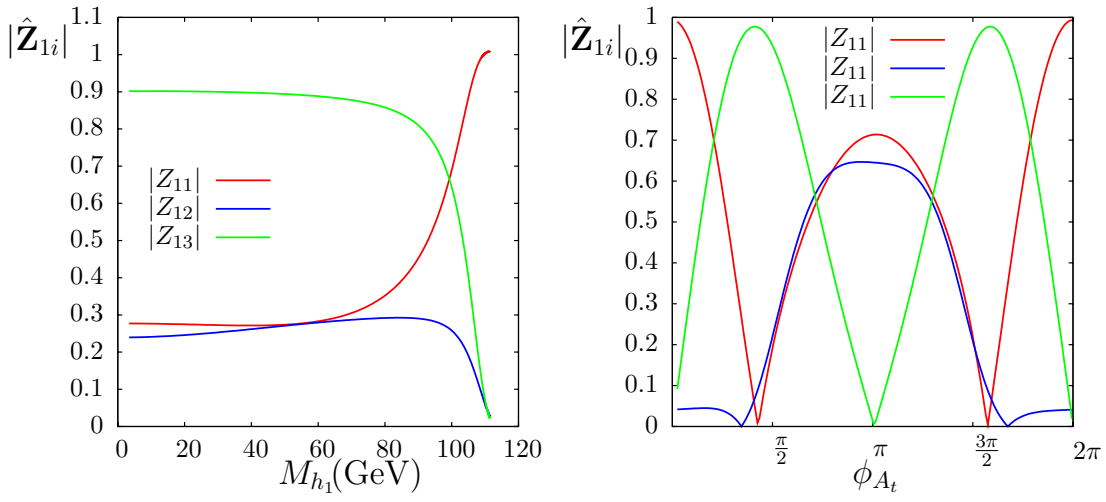

(a) (b)

Figure 3.3: $\hat{\mathbf{Z}}$ matrix elements for the lightest Higgs boson in the CPX scenario evaluated at two-loop level using `FeynHiggs 2.6.5` (a) shown as a function of M_{h_1}, with $\tan\beta = 5.5$, and (b) shown as a function of ϕ_{A_t}, with $\tan\beta = 7$ and $M_{h_1} = 45\,\text{GeV}$. (In both cases, $M_{H^\pm}$ was varied as input to produce the displayed variation in M_{h_1}.)

3.4.10 Numerical results for $\hat{\mathbf{Z}}$ matrices in the CPX scenario

As an example, we show numerical results for the $\hat{\mathbf{Z}}$ matrices evaluated from `FeynHiggs 2.6.5` for the CPX scenario defined in Table 2.3. Figure 3.3(a) shows the variation in the $\hat{\mathbf{Z}}_{1i}$ matrix elements for the lightest Higgs boson as a function of its mass for $\tan\beta = 5.5$. We see that when M_{h_1} is less than around 80 GeV, its on-shell composition is a mixture of the tree-level $\mathcal{CP}$ eigenstates, h, H, A, with a particularly large $\mathcal{CP}$-odd component, $|\hat{\mathbf{Z}}_{13}| \approx 0.9$. For larger masses near 111 GeV, the lightest Higgs boson is more SM-like, with $|\hat{\mathbf{Z}}_{11}| \approx 1$.

Figure 3.3(b) shows the variation in the $\hat{\mathbf{Z}}$ matrix elements for the lightest Higgs boson as a function of the phase of the third generation sfermion trilinear coupling, ϕ_{A_t}. As already discussed, the largest contribution to the Higgs masses and self-energies comes from the (s)top loops, so this phase plays a very important role both at one- and two-loop level.[6] When this phase is zero or a multiple of π, the scenario is close to being $\mathcal{CP}$-conserving (although the non-zero phase of M_3 still induces some $\mathcal{CP}$-violation in the Higgs mass predictions at the two-loop level). Consequently, the $\mathcal{CP}$-odd content of the

[6] In fact it is the phase of the product μA_t which plays a large role since the $\mathcal{CP}$-violating effects in the Higgs sector are most significant for large $\text{Im}(\mu A_t)/M^2_{\text{SUSY}}$ [29].

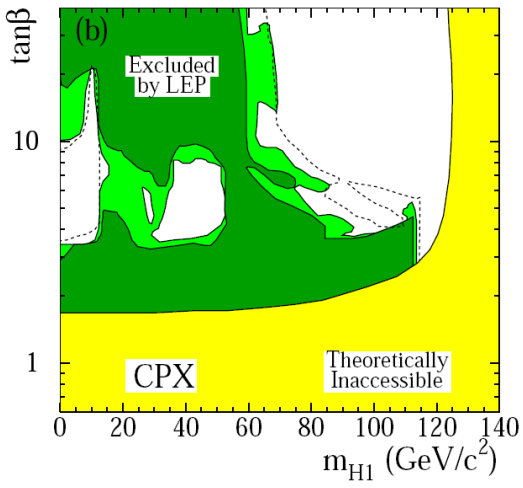

Figure 3.4: The "CPX hole" in the M_{h_1}-tan β plane (reproduced from Ref. [27]). The light green (dark green) shows the region excluded by LEP at 95% (99.7%) confidence level in the CPX scenario with $m_t = 174.3\,\text{GeV}$.

lightest Higgs boson is small; it will mostly be made up of h and H. However, when ϕ_{A_t} is $\pi/2$, as it is in the CPX scenario, $|\hat{\mathbf{Z}}_{13}|$ is close to one. This means that the lightest Higgs boson is mostly made up of the $\mathcal{CP}$-odd neutral Higgs boson, A, which will drastically change its couplings to other particles. For example, its coupling to vector bosons is highly suppressed. This reduced coupling to the Z boson is part of the reason for the "CPX hole", the parameter region in the M_{h_1}-tan β plane where a very light Higgs boson cannot be excluded by LEP (see Figure 3.4, where we show this unexcluded parameter region, as determined by the LEP collaborations, reproduced from Ref. [27]). The "CPX hole" refers to the white region with $M_{h_1} \sim 40\,\text{GeV}$ and $\tan\beta \sim 4-8$. In this region, the main production process of $e^+e \to Z^* \to Zh_1, h_1h_j$ would have been suppressed due to the small $\mathcal{CP}$-even content of the light Higgs boson. For a more detailed discussion of the bounds from Higgs boson searches in this scenario and improved theoretical predictions for the exact size and shape of the hole, see Ref. [30].

We have checked that our values for the $\hat{\mathbf{Z}}$ matrix elements obtained using Equations (3.89) and (3.90) agree numerically with those obtained as output of `FeynHiggs`. In practice, we use the $\hat{\mathbf{Z}}$ matrix values from `FeynHiggs` in our code as this allows us to easily incorporate leading two-loop corrections.

3.4.11 Comparison of full propagator matrix calculation with factorisation into production and decay processes

As well as calculations involving Higgs bosons on external legs, where $\hat{\mathbf{Z}}$ matrix elements must be used, we will also carry out calculations involving Higgs bosons on internal parts of diagrams. Here, for a complete result, including all $\mathcal{CP}$-violating effects, the full momentum dependent, loop-corrected Higgs propagators, $\Delta_{ij}(p^2)$, from Equations (3.72) and (3.77), should be included into the amplitude as follows;

$$\sum_{i,j} \hat{\Gamma}_i \Delta_{ij}(p^2) \hat{\Gamma}_j \tag{3.93}$$

where $\hat{\Gamma}_i$ are the one-particle irreducible vertices and $i, j = h, H, A$ are summed over. We have coded this full method into `FeynArts` and `FormCalc` for the calculations of the $2 \to 2$ processes studied in Chapters 9-10, using Equations (3.72) and (3.77) to evaluate Δ_{ij}, with the momentum-dependent two-loop self-energies from `FeynHiggs` as input.

However, in some situations, a good approximation can be found without requiring the full momentum dependence of the self-energies. If $p^2 \approx \mathcal{M}^2_{h_i}$, then, using Equation (3.92), we can show that the amplitude in Equation (3.93) can be approximated using

$$\sum_i (\hat{\mathbf{Z}}_{ii}\hat{\Gamma}_i + \hat{\mathbf{Z}}_{ij}\hat{\Gamma}_j + \hat{\mathbf{Z}}_{ik}\hat{\Gamma}_k)\, \Delta_i^{\mathrm{BW}}(p^2)\, (\hat{\mathbf{Z}}_{ii}\hat{\Gamma}_i + \hat{\mathbf{Z}}_{ij}\hat{\Gamma}_j + \hat{\mathbf{Z}}_{ik}\hat{\Gamma}_k). \tag{3.94}$$

The Breit-Wigner propagator captures the main part of the p^2 dependence of the propagator near the pole. The self-energies contained in the $\hat{\mathbf{Z}}$ matrix elements, the mass, M_{h_i}, and the width, Γ_{h_i}, are all evaluated for on-shell values of the momenta. If the internal Higgs boson can be on-shell and the assumptions of the narrow width approximation, described in Appendix C, apply, we can then factorise the cross-section for the full process into the separate production and decay of the Higgs boson. We will discuss this further in Chapter 9.

Another approximation that can be made is to evaluate all self-energies at $p^2 = 0$. In this case, the $\hat{\mathbf{Z}}$ matrix reduces to a unitary matrix, $\mathbf{U}$, which diagonalises the Higgs mass matrix, $\mathbf{M}_n(0)$, of Equation (3.70), evaluated at $p^2 = 0$. The $\mathbf{U}$ matrix elements are available as part of the standard output of `FeynHiggs`, and can be used to obtain effective couplings to internal Higgs bosons.

Chapter 4

Renormalisation in the chargino–neutralino sector

In this chapter we describe our scheme for the one-loop renormalisation of the fields and parameters in the chargino–neutralino sector of the MSSM with $\mathcal{CP}$-violating phases. A significant number of one-loop calculations have been carried out in the chargino–neutralino sector of the $\mathcal{CP}$-conserving MSSM with real parameters, see e.g. Ref. [82–89], with the renormalisation schemes of Refs. [88,90] also applicable for complex parameters. More recently, $\mathcal{CP}$-odd observables have been calculated at one-loop level in the MSSM with $\mathcal{CP}$-violating phases, see e.g. Refs. [90–92], but these calculations did not always require a dedicated renormalisation scheme as the specific observables calculated were UV-finite.

In order to renormalise the fields and parameters in this sector we introduce counterterms and renormalisation constants of a similar form to Ref. [86]. However, we apply different on-shell conditions for the mass parameters and we extend the formalism to the general case including $\mathcal{CP}$-violation, properly taking into account imaginary parts arising both from the complex MSSM parameters and from absorptive parts of loop integrals. Unlike Ref. [86], we will allow non-zero phases for M_1 and μ, which appear in the chargino–neutralino sector at the tree level, as well as A_f and M_3, which play a role in the chargino–neutralino sector at the one-loop level and two-loop level respectively. To supplement the existing `FeynArts` MSSM model file, which contains tree level vertices but does not contain any counterterms, we have written an additional model file which implements the scheme we develop below, along with the renormalisation for other sectors described in the previous chapter. This implementation will have many applications for loop calculations in the general MSSM with $\mathcal{CP}$-violating phases.

4.1 Renormalisation transformations

The chargino and neutralino mass matrices, of Equations (2.29) and (2.31) respectively, each receive a counterterm as follows,

$$X \;\to X + \delta X, \qquad Y \;\to Y + \delta Y, \tag{4.1}$$

where δX and δY are 2×2 and 4×4 matrices respectively. Their elements contain three new renormalisation constants, δM_1, δM_2 and $\delta\mu$, defined by the transformations;

$$\begin{aligned} M_1 &\to M_1 + \delta M_1, \\ M_2 &\to M_2 + \delta M_2, \\ \mu &\to \mu + \delta\mu, \end{aligned} \tag{4.2}$$

as well as renormalisation constants from other sectors. Writing out the matrix elements explicitly, we have

$$\begin{aligned} \delta Y_{11} &= \delta M_1, \\ \delta X_{11} &= \delta Y_{22} = \delta M_2, \\ \delta X_{22} &= \delta Y_{34} = \delta Y_{43} = \delta\mu, \\ \delta X_{12} = \sqrt{2}\delta(M_W \sin\beta) &= \frac{\delta M_W^2 s_\beta}{\sqrt{2}M_W} + M_W s_\beta c_\beta^2 \delta t_\beta, \\ \delta X_{21} = \sqrt{2}\delta(M_W \cos\beta) &= \frac{\delta M_W^2 c_\beta}{\sqrt{2}M_W} - M_W c_\beta s_\beta^2 \delta t_\beta, \\ \delta Y_{14} = \delta Y_{41} = \delta(M_Z s_\beta s_W) &= \delta s_W M_Z s_\beta + \frac{\delta M_Z^2}{2M_Z} s_W s_\beta + s_\beta c_\beta^2 \delta t_\beta s_W M_Z, \\ \delta Y_{23} = \delta Y_{32} = \delta(M_Z c_\beta c_W) &= \delta c_W M_Z c_\beta + \frac{\delta M_Z^2}{2M_Z} c_W c_\beta - c_\beta s_\beta^2 \delta t_\beta c_W M_Z, \\ \delta Y_{24} = \delta Y_{42} = -\delta(M_Z s_\beta c_W) &= -\delta c_W M_Z s_\beta - \frac{\delta M_Z^2}{2M_Z} c_W s_\beta - s_\beta c_\beta^2 \delta t_\beta c_W M_Z, \\ \delta Y_{13} = \delta Y_{31} = -\delta(M_Z c_\beta s_W) &= -\delta s_W M_Z c_\beta - \frac{\delta M_Z^2}{2M_Z} s_W c_\beta + c_\beta s_\beta^2 \delta t_\beta s_W M_Z. \end{aligned} \tag{4.3}$$

In order to be completely general for the case of $\mathcal{CP}$-violation, we introduce renormalisation constants separately for the left and right-handed components of the incoming

and outgoing fermion fields, as follows,

$$\begin{aligned}
\omega_L\tilde{\chi}_i^- &\to (1+\tfrac{1}{2}\delta Z_-^L)_{ij}\omega_L\tilde{\chi}_j^-, & \overline{\tilde{\chi}_i^-}\omega_R &\to \overline{\tilde{\chi}_i^-}(1+\tfrac{1}{2}\delta\bar{Z}_-^L)_{ij}\omega_R,\\
\omega_R\tilde{\chi}_i^- &\to (1+\tfrac{1}{2}\delta Z_-^R)_{ij}\omega_R\tilde{\chi}_j^-, & \overline{\tilde{\chi}_i^-}\omega_L &\to \overline{\tilde{\chi}_i^-}(1+\tfrac{1}{2}\delta\bar{Z}_-^R)_{ij}\omega_L,\\
\omega_L\tilde{\chi}_i^0 &\to (1+\tfrac{1}{2}\delta Z_0^L)_{ij}\omega_L\tilde{\chi}_j^0, & \overline{\tilde{\chi}_i^0}\omega_R &\to \overline{\tilde{\chi}_i^0}(1+\tfrac{1}{2}\delta\bar{Z}_0^L)_{ij}\omega_R,\\
\omega_R\tilde{\chi}_i^0 &\to (1+\tfrac{1}{2}\delta Z_0^R)_{ij}\omega_R\tilde{\chi}_j^0, & \overline{\tilde{\chi}_i^0}\omega_L &\to \overline{\tilde{\chi}_i^0}(1+\tfrac{1}{2}\delta\bar{Z}_0^R)_{ij}\omega_L,
\end{aligned} \tag{4.4}$$

where j is summed over 1,2 (1,2,3,4) for the charginos (neutralinos).[1] Note that we have introduced barred renormalisation constants for outgoing fermions and incoming antifermions. In the $\mathcal{CP}$-conserving MSSM, one can write down an equivalent renormalisation scheme where these are related to the non-barred renormalisation constants for incoming fermions and outgoing antifermions by a Hermitian conjugate, i.e. one can make the replacement $\delta\bar{Z}_{ij} \to \delta Z_{ij}^\dagger$. For the MSSM with $\mathcal{CP}$-violating phases, we choose to treat these quantities as independent at this stage, with more discussion to follow.

Inserting the above transformations into the Born Lagrangian of Equation (2.30), and decomposing fermionic self-energies as

$$\Sigma_{ij}(p^2) = \not{p}\omega_L\Sigma_{ij}^L(p^2) + \not{p}\omega_R\Sigma_{ij}^R(p^2) + \omega_L\Sigma_{ij}^{SL}(p^2) + \omega_R\Sigma_{ij}^{SR}(p^2), \tag{4.5}$$

we obtain the renormalised self-energies for the charginos;

$$\begin{aligned}
\hat{\Sigma}_{ij,-}^R(p^2) &= \Sigma_{ij,-}^R(p^2) + \frac{1}{2}(\delta Z_-^R + \delta\bar{Z}_-^R)_{ij},\\
\hat{\Sigma}_{ij,-}^L(p^2) &= \Sigma_{ij,-}^L(p^2) + \frac{1}{2}(\delta Z_-^L + \delta\bar{Z}_-^L)_{ij},\\
\hat{\Sigma}_{ij,-}^{SR}(p^2) &= \Sigma_{ij,-}^{SR}(p^2) - [V\delta X^\dagger U^T + \frac{1}{2}VX^\dagger U^T\delta Z_-^R + \frac{1}{2}\delta\bar{Z}_-^L VX^\dagger U^T]_{ij},\\
\hat{\Sigma}_{ij,-}^{SL}(p^2) &= \Sigma_{ij,-}^{SL}(p^2) - [U^*\delta XV^\dagger + \frac{1}{2}U^*XV^\dagger\delta Z_-^L + \frac{1}{2}\delta\bar{Z}_-^R U^*XV^\dagger]_{ij}.
\end{aligned} \tag{4.6}$$

[1] The renormalisation constants for incoming and outgoing $\tilde{\chi}_i^+$ fields can be obtained from the outgoing and incoming field renormalisation constants for $\tilde{\chi}_i^-$. We define the field renormalisation in terms of $\tilde{\chi}_i^-$ in order to agree with the MSSM model file in `FeynArts`.

Similarly, using Equation (2.32), we obtain the renormalised self-energies for the neutralinos;

$$\begin{aligned}
\hat{\Sigma}^R_{ij,0}(p^2) &= \Sigma^R_{ij,0}(p^2) + \frac{1}{2}(\delta Z^R_0 + \delta \bar{Z}^R_0)_{ij}, \\
\hat{\Sigma}^L_{ij,0}(p^2) &= \Sigma^L_{ij,0}(p^2) + \frac{1}{2}(\delta Z^L_0 + \delta \bar{Z}^L_0)_{ij}, \\
\hat{\Sigma}^{SR}_{ij,0}(p^2) &= \Sigma^{SR}_{ij,0}(p^2) - [N\delta Y^\dagger N^T + \frac{1}{2}NY^\dagger N^T \delta Z^R_0 + \frac{1}{2}\delta \bar{Z}^L_0 NY^\dagger N^T]_{ij}, \\
\hat{\Sigma}^{SL}_{ij,0}(p^2) &= \Sigma^{SL}_{ij,0}(p^2) - [N^*\delta Y N^\dagger + \frac{1}{2}N^* Y N^\dagger \delta Z^L_0 + \frac{1}{2}\delta \bar{Z}^R_0 N^* Y N^\dagger]_{ij}. \qquad (4.7)
\end{aligned}$$

The renormalised two-point vertex functions for neutralinos and charginos are given by

$$\hat{\Gamma}^{(2)}_{ij}(p^2) = i(\not{p} - m_i)\delta_{ij} + i\hat{\Sigma}_{ij}(p^2) \qquad (4.8)$$

and the propagators by

$$\hat{S}^{(2)}_{ij}(p^2) = (\hat{\Gamma}^{(2)}_{ij}(p^2))^{-1}. \qquad (4.9)$$

4.2 Field renormalisation

4.2.1 Field renormalisation in a general scheme

The field renormalisation constants are fixed by requiring that the renormalised two-point vertex functions, $\hat{\Gamma}^{(2)}_{ij}$, are diagonal for on-shell external particle momenta;

$$\begin{aligned}
\hat{\Gamma}^{(2)}_{ij}\tilde{\chi}_i(p)|_{p^2=m^2_{\tilde{\chi}_j}} &= 0, \qquad (4.10) \\
\overline{\tilde{\chi}}_i(p)\hat{\Gamma}^{(2)}_{ij}|_{p^2=m^2_{\tilde{\chi}_i}} &= 0, \qquad (4.11)
\end{aligned}$$

and that the propagators have unity residues;

$$\begin{aligned}
\lim_{p^2\to m^2_{\tilde{\chi}_i}} \frac{1}{\not{p} - m_{\tilde{\chi}_i}} \hat{\Gamma}^{(2)}_{ii}\tilde{\chi}_i(p) &= i\tilde{\chi}_i, \qquad (4.12) \\
\lim_{p^2\to m^2_{\tilde{\chi}_i}} \overline{\tilde{\chi}}_i(p)\hat{\Gamma}^{(2)}_{ii} \frac{1}{\not{p} - m_{\tilde{\chi}_i}} &= i\overline{\tilde{\chi}}_i, \qquad (4.13)
\end{aligned}$$

where $\tilde{\chi}_i = \tilde{\chi}^-_i$ $(i,j = 1,2)$ or $\tilde{\chi}^0_i$ $(i,j = 1,2,3,4)$ and $i \neq j$. Note that we have written these on-shell conditions in terms of the tree-level masses, $m_{\tilde{\chi}_i}$. In Sections 4.3

and 4.4, when we discuss the parameter renormalisation, we will see that, in general, there will be a distinction between the tree-level and loop-corrected masses for at least three of the six neutralinos and charginos. We denote the loop-corrected masses as $M_{\tilde{\chi}_i}$. For the one-loop field renormalisation conditions given above, the effect of using $M_{\tilde{\chi}_i}$ instead of $m_{\tilde{\chi}_i}$ is of higher order. In the MSSM with real parameters, the above conditions, together with the mass renormalisation conditions, are enough to ensure the correct on-shell conditions at one-loop. For the complex MSSM, we must also ensure that the loop-corrected propagator has the same Lorentz structure in the on-shell limit as it does at tree level. In the on-shell limit, where $p^2 \to M_{\tilde{\chi}_i^2}$, we can use the on-shell field renormalisation conditions to write the propagator in terms of the diagonal two point vertex function only, to obtain

$$i\hat{S}_{ii}^{(2)}(p^2) = \frac{\not{p}[(1+\hat{\Sigma}_{ii}^{L})\omega_L + (1+\hat{\Sigma}_{ii}^{R})\omega_R] + (m_i - \hat{\Sigma}_{ii}^{SR})\omega_L + (m_i - \hat{\Sigma}_{ii}^{SL})\omega_R}{p^2(1+\hat{\Sigma}_{ii}^{L})(1+\hat{\Sigma}_{ii}^{R}) - (m_i - \hat{\Sigma}_{ii}^{SL})(m_i - \hat{\Sigma}_{ii}^{SR})}. \tag{4.14}$$

In order to ensure that the on-shell $\hat{S}_{ii}^{(2)}$ has only a scalar and vector part (and no dependence on γ_5), we require two additional renormalisation conditions to make the ω_L and ω_R coefficients equal;

$$\hat{\Sigma}_{ii}^{L}(m_{\tilde{\chi}_i}^2) = \hat{\Sigma}_{ii}^{R}(m_{\tilde{\chi}_i}^2), \tag{4.15}$$

$$\hat{\Sigma}_{ii}^{SL}(m_{\tilde{\chi}_i}^2) = \hat{\Sigma}_{ii}^{SR}(m_{\tilde{\chi}_i}^2). \tag{4.16}$$

Equation (4.15) will turn out to be automatically satisfied even in the complex MSSM. Equation (4.16) is automatically fulfilled in the MSSM with real parameters, due to the $\mathcal{CP}$ invariance relations between the self-energies given in Equation (A.11), but it will give a non-trivial condition in the $\mathcal{CP}$-violating case. We start by applying the diagonality condition. Using Equation (4.5), we insert Equation (4.8) into Equation (4.10) for $i \neq j$ and apply $\not{p}\tilde{\chi}_i(p)|_{p^2=m_{\tilde{\chi}_j}^2} = m_{\tilde{\chi}_j}\tilde{\chi}_i$. This gives

$$\omega_R m_{\tilde{\chi}_j}\hat{\Sigma}_{ij}^{L}(m_{\tilde{\chi}_j}^2) + \omega_L m_{\tilde{\chi}_j}\hat{\Sigma}_{ij}^{R}(m_{\tilde{\chi}_j}^2) + \omega_R\hat{\Sigma}_{ij}^{SR}(m_{\tilde{\chi}_j}^2) + \omega_L\hat{\Sigma}_{ij}^{SL}(m_{\tilde{\chi}_j}^2) = 0. \tag{4.17}$$

Similarly, Equation (4.11) leads to

$$\omega_L m_{\tilde{\chi}_i}\hat{\Sigma}_{ij}^{L}(m_{\tilde{\chi}_i}^2) + \omega_R m_{\tilde{\chi}_i}\hat{\Sigma}_{ij}^{R}(m_{\tilde{\chi}_i}^2) + \omega_R\hat{\Sigma}_{ij}^{SR}(m_{\tilde{\chi}_i}^2) + \omega_L\hat{\Sigma}_{ij}^{SL}(m_{\tilde{\chi}_i}^2) = 0. \tag{4.18}$$

Next, we insert the renormalised chargino self-energies of Equation (4.6) into Equation (4.17), and use $(VX^\dagger U^T)_{ij} = (U^* X V^\dagger)_{ij} = \delta_{ij} m_{\tilde{\chi}_j}$. The ω_R coefficient of the resulting

equation gives

$$m_{\tilde{\chi}_j}\Sigma^L_{ij}(m^2_{\tilde{\chi}_j}) + \Sigma^{SR}_{ij}(m^2_{\tilde{\chi}_j}) - V\delta X^\dagger U^T + \frac{1}{2}m_{\tilde{\chi}_j}\delta Z^L_{ij} - \frac{1}{2}m_{\tilde{\chi}_i}\delta Z^R_{ij} = 0, \tag{4.19}$$

while the ω_L coefficient gives

$$m_{\tilde{\chi}_j}\Sigma^R_{ij}(m^2_{\tilde{\chi}_j}) + \Sigma^{SL}_{ij}(m^2_{\tilde{\chi}_j}) - U^*\delta X V^\dagger + \frac{1}{2}m_{\tilde{\chi}_j}\delta Z^R_{ij} - \frac{1}{2}m_{\tilde{\chi}_i}\delta Z^L_{ij} = 0. \tag{4.20}$$

Multiplying Equations (4.19) and (4.20) by $m_{\tilde{\chi}_j}$ and $m_{\tilde{\chi}_i}$ respectively and adding the two equations, we obtain

$$\begin{aligned}\delta Z^L_{-,ij} &= \frac{2}{m^2_{\tilde{\chi}^\pm_i} - m^2_{\tilde{\chi}^\pm_j}}\big[m^2_{\tilde{\chi}^\pm_j}\Sigma^L_{-,ij}(m^2_{\tilde{\chi}^\pm_j}) + m_{\tilde{\chi}^\pm_i}m_{\tilde{\chi}^\pm_j}\Sigma^R_{-,ij}(m^2_{\tilde{\chi}^\pm_j}) + m_{\tilde{\chi}^\pm_i}\Sigma^{SL}_{-,ij}(m^2_{\tilde{\chi}^\pm_j}) \\ &\quad + m_{\tilde{\chi}^\pm_j}\Sigma^{SR}_{-,ij}(m^2_{\tilde{\chi}^\pm_j}) - m_{\tilde{\chi}^\pm_i}\big(U^*\delta X V^\dagger\big)_{ij} - m_{\tilde{\chi}^\pm_j}\big(V\delta X^\dagger U^T\big)_{ij}\big],\end{aligned} \tag{4.21}$$

while multiplying Equations (4.19) and (4.20) by $m_{\tilde{\chi}_i}$ and $m_{\tilde{\chi}_j}$ respectively and adding the two equations, we obtain

$$\begin{aligned}\delta Z^R_{-,ij} &= \frac{2}{m^2_{\tilde{\chi}^\pm_i} - m^2_{\tilde{\chi}^\pm_j}}\big[m^2_{\tilde{\chi}^\pm_j}\Sigma^R_{-,ij}(m^2_{\tilde{\chi}^\pm_j}) + m_{\tilde{\chi}^\pm_i}m_{\tilde{\chi}^\pm_j}\Sigma^L_{-,ij}(m^2_{\tilde{\chi}^\pm_j}) + m_{\tilde{\chi}^\pm_i}\Sigma^{SR}_{-,ij}(m^2_{\tilde{\chi}^\pm_j}) \\ &\quad + m_{\tilde{\chi}^\pm_j}\Sigma^{SL}_{-,ij}(m^2_{\tilde{\chi}^\pm_j}) - m_{\tilde{\chi}^\pm_i}\big(U^*\delta X V^\dagger\big)_{ij} - m_{\tilde{\chi}^\pm_j}\big(V\delta X^\dagger U^T\big)_{ij}\big].\end{aligned} \tag{4.22}$$

Inserting the renormalised chargino self-energies into Equation (4.18) and following the same procedure gives the barred off-diagonal constants for charginos;

$$\begin{aligned}\delta \bar{Z}^{L/R}_{-,ij} &= \frac{2}{m^2_{\tilde{\chi}^\pm_j} - m^2_{\tilde{\chi}^\pm_i}}\big[m^2_{\tilde{\chi}^\pm_i}\Sigma^{L/R}_{-,ij}(m^2_{\tilde{\chi}^\pm_i}) + m_{\tilde{\chi}^\pm_i}m_{\tilde{\chi}^\pm_j}\Sigma^{R/L}_{-,ij}(m^2_{\tilde{\chi}^\pm_i}) + m_{\tilde{\chi}^\pm_i}\Sigma^{SL/SR}_{-,ij}(m^2_{\tilde{\chi}^\pm_i}) \\ &\quad + m_{\tilde{\chi}^\pm_j}\Sigma^{SR/SL}_{-,ij}(m^2_{\tilde{\chi}^\pm_i}) - m_{\tilde{\chi}^\pm_{i/j}}\big(U^*\delta X V^\dagger\big)_{ij} - m_{\tilde{\chi}^\pm_{j/i}}\big(V\delta X^\dagger U^T\big)_{ij}\big].\end{aligned} \tag{4.23}$$

In order to find the diagonal field renormalisation constants, we insert Equation (4.8) into Equation (4.12) for $i = j$, which gives

$$0 = \lim_{p^2\to m^2_{\tilde{\chi}_i}} \frac{1}{\not{p} - m_{\tilde{\chi}_i}}\big[\not{p}\omega_L\hat{\Sigma}^L_{ii}(p^2) + \not{p}\omega_R\hat{\Sigma}^R_{ii}(p^2) + \omega_L\hat{\Sigma}^{SL}_{ii}(p^2) + \omega_R\hat{\Sigma}^{SR}_{ii}(p^2)\big]\tilde{\chi}_i(p). \tag{4.24}$$

Subtracting and adding the term $m_{\tilde{\chi}_i}[\omega_L\hat{\Sigma}^L_{ii}(p^2)+\omega_R\hat{\Sigma}^R_{ii}(p^2)]$ allows us to write

$$\begin{aligned} 0 &= \big(\omega_L\hat{\Sigma}^L_{ii}(m^2_{\tilde{\chi}_i})+\omega_R\hat{\Sigma}^R_{ii}(m^2_{\tilde{\chi}_i})\big)\tilde{\chi}_i+\lim_{p^2\to m^2_{\tilde{\chi}_i}}\frac{\not{p}+m_{\tilde{\chi}_i}}{p^2-m_{\tilde{\chi}_i^2}}\Big[m_{\tilde{\chi}_i}\omega_L\hat{\Sigma}^L_{ii}(p^2) \\ &\quad +m_{\tilde{\chi}_i}\omega_R\hat{\Sigma}^R_{ii}(p^2)+\omega_L\hat{\Sigma}^{SL}_{ii}(p^2)+\omega_R\hat{\Sigma}^{SR}_{ii}(p^2)\Big]\tilde{\chi}_i(p). \end{aligned} \tag{4.25}$$

The term in the square brackets can be expanded about the pole mass, leaving us, at one-loop order, with terms proportional to the derivatives of the self-energies with respect to p^2, evaluated at the tree-level mass; $\Sigma'_{ii}(m^2_{\tilde{\chi}_i})\equiv\frac{\partial\Sigma_{ii}}{\partial p^2}|_{p^2=m^2_{\tilde{\chi}_i}}$. Evaluating the limit in Equation (4.25) then leads to

$$\begin{aligned} 0 &= \omega_L\hat{\Sigma}^L_{ii}(m^2_{\tilde{\chi}_i})+\omega_R\hat{\Sigma}^R_{ii}(m^2_{\tilde{\chi}_i})+m^2_{\tilde{\chi}_i}\hat{\Sigma}^{L'}_{ii}(m^2_{\tilde{\chi}_i})+m^2_{\tilde{\chi}_i}\hat{\Sigma}^{R'}_{ii}(m^2_{\tilde{\chi}_i}) \\ &\quad +m_{\tilde{\chi}_i}\hat{\Sigma}^{SL'}_{ii}(m^2_{\tilde{\chi}_i})+m_{\tilde{\chi}_i}\hat{\Sigma}^{SR'}_{ii}(m^2_{\tilde{\chi}_i}). \end{aligned} \tag{4.26}$$

Taking the ω_L and ω_R coefficients, we obtain two equations;

$$0=\hat{\Sigma}^L_{ij}(m^2_{\tilde{\chi}_i})+m^2_{\tilde{\chi}_i}[\hat{\Sigma}^{L'}_{ii}(m^2_{\tilde{\chi}_i})+\hat{\Sigma}^{R'}_{ii}(m^2_{\tilde{\chi}_i})]+m_{\tilde{\chi}_i}[\hat{\Sigma}^{SL'}_{ii}(m^2_{\tilde{\chi}_i})+\hat{\Sigma}^{SR'}_{ii}(m^2_{\tilde{\chi}_i})], \tag{4.27}$$

$$0=\hat{\Sigma}^R_{ij}(m^2_{\tilde{\chi}_i})+m^2_{\tilde{\chi}_i}[\hat{\Sigma}^{L'}_{ii}(m^2_{\tilde{\chi}_i})+\hat{\Sigma}^{R'}_{ii}(m^2_{\tilde{\chi}_i})]+m_{\tilde{\chi}_i}[\hat{\Sigma}^{SL'}_{ii}(m^2_{\tilde{\chi}_i})+\hat{\Sigma}^{SR'}_{ii}(m^2_{\tilde{\chi}_i})]. \tag{4.28}$$

Equation (4.13) also leads to Equations (4.27) and (4.28) when the ω_L and ω_R coefficients are taken. Inserting the renormalised chargino self-energies of Equation (4.6) into Equations (4.27) and (4.28) we obtain

$$\begin{aligned} \frac{1}{2}(\delta Z^R_{-,ii}+\delta\bar{Z}^R_{-,ii}) &= -\Sigma^R_{-,ii}(m^2_{\tilde{\chi}^\pm_i})-m^2_{\tilde{\chi}^\pm_i}\big[\Sigma^{L'}_{-,ii}(m^2_{\tilde{\chi}^\pm_i})+\Sigma^{R'}_{-,ii}(m^2_{\tilde{\chi}^\pm_i})\big] \\ &\quad -m_{\tilde{\chi}^\pm_i}\big[\Sigma^{SL'}_{-,ii}(m^2_{\tilde{\chi}^\pm_i})+\Sigma^{SR'}_{-,ii}(m^2_{\tilde{\chi}^\pm_i})\big], \end{aligned} \tag{4.29}$$

$$\begin{aligned} \frac{1}{2}(\delta Z^L_{-,ii}+\delta\bar{Z}^L_{-,ii}) &= -\Sigma^L_{-,ii}(m^2_{\tilde{\chi}^\pm_i})-m^2_{\tilde{\chi}^\pm_i}\big[\Sigma^{L'}_{-,ii}(m^2_{\tilde{\chi}^\pm_i})+\Sigma^{R'}_{-,ii}(m^2_{\tilde{\chi}^\pm_i})\big] \\ &\quad -m_{\tilde{\chi}^\pm_i}\big[\Sigma^{SL'}_{-,ii}(m^2_{\tilde{\chi}^\pm_i})+\Sigma^{SR'}_{-,ii}(m^2_{\tilde{\chi}^\pm_i})\big]. \end{aligned} \tag{4.30}$$

The renormalisation condition in Equation (4.15) is now automatically satisfied, so we now apply the last remaining condition in Equation (4.16) to give, for the charginos,

$$\begin{aligned} \frac{1}{2}m_{\tilde{\chi}^\pm_i}\big[(\delta Z^L_{-,ii}-\delta\bar{Z}^L_{-,ii})-(\delta Z^R_{-,ii}-\delta\bar{Z}^R_{-,ii})\big] &= \big[\Sigma^{SL}_{-,ii}(m^2_{\tilde{\chi}^\pm_i})-\Sigma^{SR}_{-,ii}(m^2_{\tilde{\chi}^\pm_i})+(V\delta X^\dagger U^T)_{ii} \\ &\quad -(U^*\delta XV^\dagger)_{ii}\big]. \end{aligned} \tag{4.31}$$

There is still some freedom in the choice of renormalisation constants since there are only three equations (Equations (4.29), (4.30) and (4.31)) and four unknowns, δZ^L_{ii}, δZ^R_{ii}, $\delta \bar{Z}^L_{ii}$ and $\delta \bar{Z}^R_{ii}$. In order to achieve symmetry in our expressions, we choose as a fourth condition;

$$\delta Z^R_{ii} - \delta \bar{Z}^R_{ii} = \delta \bar{Z}^L_{ii} - \delta Z^L_{ii}. \tag{4.32}$$

This leads to the following diagonal chargino field renormalisation constants;

$$\begin{aligned}
\delta Z^{L/R}_{-,ii} =& -\Sigma^{L/R}_{-,ii}(m^2_{\tilde{\chi}^\pm_i}) - m^2_{\tilde{\chi}^\pm_i}\left[\Sigma^{L'}_{-,ii}(m^2_{\tilde{\chi}^\pm_i}) + \Sigma^{R'}_{-,ii}(m^2_{\tilde{\chi}^\pm_i})\right] - m_{\tilde{\chi}^\pm_i}\left[\Sigma^{SL'}_{-,ii}(m^2_{\tilde{\chi}^\pm_i}) + \Sigma^{SR'}_{-,ii}(m^2_{\tilde{\chi}^\pm_i})\right] \\
& \pm \frac{1}{2m_{\tilde{\chi}^\pm_i}}\left[\Sigma^{SL}_{-,ii}(m^2_{\tilde{\chi}^\pm_i}) - \Sigma^{SR}_{-,ii}(m^2_{\tilde{\chi}^\pm_i}) + (V\delta X^\dagger U^T)_{ii} - (U^*\delta X V^\dagger)_{ii}\right], \qquad (4.33) \\
\delta \bar{Z}^{L/R}_{-,ii} =& -\Sigma^{L/R}_{-,ii}(m^2_{\tilde{\chi}^\pm_i}) - m^2_{\tilde{\chi}^\pm_i}\left[\Sigma^{L'}_{-,ii}(m^2_{\tilde{\chi}^\pm_i}) + \Sigma^{R'}_{-,ii}(m^2_{\tilde{\chi}^\pm_i})\right] - m_{\tilde{\chi}^\pm_i}\left[\Sigma^{SL'}_{-,ii}(m^2_{\tilde{\chi}^\pm_i}) + \Sigma^{SR'}_{-,ii}(m^2_{\tilde{\chi}^\pm_i})\right] \\
& \mp \frac{1}{2m_{\tilde{\chi}^\pm_i}}\left[\Sigma^{SL}_{-,ii}(m^2_{\tilde{\chi}^\pm_i}) - \Sigma^{SR}_{-,ii}(m^2_{\tilde{\chi}^\pm_i}) + (V\delta X^\dagger U^T)_{ii} - (U^*\delta X V^\dagger)_{ii}\right]. \qquad (4.34)
\end{aligned}$$

Inserting the neutralino self-energies of Equation (4.7) into Equations (4.17) and (4.18), and following the same procedure as for the charginos, leads to the following off-diagonal field renormalisation constants for the neutralinos;

$$\begin{aligned}
\delta Z^{L/R}_{0,ij} =& \frac{2}{m^2_{\tilde{\chi}^0_i} - m^2_{\tilde{\chi}^0_j}}\left[m^2_{\tilde{\chi}^0_j}\Sigma^{L/R}_{0,ij}(m^2_{\tilde{\chi}^0_j}) + m_{\tilde{\chi}^0_i}m_{\tilde{\chi}^0_j}\Sigma^{R/L}_{0,ij}(m^2_{\tilde{\chi}^0_j}) + m_{\tilde{\chi}^0_i}\Sigma^{SL/SR}_{0,ij}(m^2_{\tilde{\chi}^0_j})\right. \\
& \left. + m_{\tilde{\chi}^0_j}\Sigma^{SR/SL}_{0,ij}(m^2_{\tilde{\chi}^0_j}) - m_{\tilde{\chi}^0_{i/j}}\left(N^*\delta Y N^\dagger\right)_{ij} - m_{\tilde{\chi}^0_{j/i}}\left(N\delta Y^\dagger N^T\right)_{ij}\right], \qquad (4.35) \\
\delta \bar{Z}^{R/L}_{0,ij} =& \frac{2}{m^2_{\tilde{\chi}^0_j} - m^2_{\tilde{\chi}^0_i}}\left[m^2_{\tilde{\chi}^0_i}\Sigma^{L/R}_{0,ji}(m^2_{\tilde{\chi}^0_i}) + m_{\tilde{\chi}^0_j}m_{\tilde{\chi}^0_i}\Sigma^{R/L}_{0,ji}(m^2_{\tilde{\chi}^0_i}) + m_{\tilde{\chi}^0_j}\Sigma^{SL/SR}_{0,ji}(m^2_{\tilde{\chi}^0_i})\right. \\
& \left. + m_{\tilde{\chi}^0_i}\Sigma^{SR/SL}_{0,ji}(m^2_{\tilde{\chi}^0_i}) - m_{\tilde{\chi}^0_{j/i}}\left(N^*\delta Y N^\dagger\right)_{ji} - m_{\tilde{\chi}^0_{i/j}}\left(N\delta Y^\dagger N^T\right)_{ji}\right]. \qquad (4.36)
\end{aligned}$$

Inserting the neutralino self-energies into Equations (4.27) and (4.28) and applying the conditions of Equations (4.16) and (4.32), leads to the following diagonal field renormalisation constants for the neutralinos;

$$\begin{aligned}
\delta Z^{L/R}_{0,ii} =& -\Sigma^{L/R}_{0,ii}(m^2_{\tilde{\chi}^0_i}) - m^2_{\tilde{\chi}^0_i}\left[\Sigma^{L'}_{0,ii}(m^2_{\tilde{\chi}^0_i}) + \Sigma^{R'}_{0,ii}(m^2_{\tilde{\chi}^0_i})\right] - m_{\tilde{\chi}^0_i}\left[\Sigma^{SL'}_{0,ii}(m^2_{\tilde{\chi}^0_i}) + \Sigma^{SR'}_{0,ii}(m^2_{\tilde{\chi}^0_i})\right] \\
& \pm \frac{1}{2m_{\tilde{\chi}^0_i}}\left[\Sigma^{SL}_{0,ii}(m^2_{\tilde{\chi}^0_i}) - \Sigma^{SR}_{0,ii}(m^2_{\tilde{\chi}^0_i}) + (N\delta Y^\dagger N^T)_{ii} - (N^*\delta Y N^\dagger)_{ii}\right], \\
\delta \bar{Z}^{L/R}_{0,ii} =& -\Sigma^{R/L}_{0,ii}(m^2_{\tilde{\chi}^0_i}) - m^2_{\tilde{\chi}^0_i}\left[\Sigma^{L'}_{0,ii}(m^2_{\tilde{\chi}^0_i}) + \Sigma^{R'}_{0,ii}(m^2_{\tilde{\chi}^0_i})\right] - m_{\tilde{\chi}^0_i}\left[\Sigma^{SL'}_{0,ii}(m^2_{\tilde{\chi}^0_i}) + \Sigma^{SR'}_{0,ii}(m^2_{\tilde{\chi}^0_i})\right] \\
& \mp \frac{1}{2m_{\tilde{\chi}^0_i}}\left[\Sigma^{SL}_{0,ii}(m^2_{\tilde{\chi}^0_i}) - \Sigma^{SR}_{0,ii}(m^2_{\tilde{\chi}^0_i}) + (N\delta Y^\dagger N^T)_{ii} - (N^*\delta Y N^\dagger)_{ii}\right]. \qquad (4.37)
\end{aligned}$$

Because neutralinos are Majorana particles, their self-energies obey the $\mathcal{C}$-invariance relations given in Equation (A.12) in Appendix A. Using these relations, it can be shown that

$$\delta Z_{0,ij}^{L/R} = \delta \bar{Z}_{0,ji}^{R/L} \tag{4.38}$$

for any $i, j = 1, 2, 3, 4$. That is, the left-handed (right-handed) field renormalisation constant for incoming particles and outgoing antiparticles is the same as the right-handed (left-handed) field renormalisation constant for outgoing particles and incoming antiparticles. Thus, the barred renormalisation constants for neutralinos are fixed once the non-barred renormalisation constants are specified. However, since this does not apply to charginos, which are Dirac fermions, we will keep the formulae general and continue to refer to the barred renormalisation constants for outgoing fermions and incoming antifermions. This will help to ensure that the appropriate renormalisation constants are used in each vertex counterterm.

4.2.2 Field renormalisation in a scheme without absorptive loop integrals

Suppose we discard any absorptive parts of loop integrals occurring in the field renormalisation constants, by inserting the symbol $\widetilde{\mathrm{Re}}$ in front of any self-energies (see Appendix A.2 for a discussion of the relationship between $\widetilde{\mathrm{Re}}$, $\widetilde{\mathrm{Im}}$ and the usual Re and Im). With this procedure, our treatment would become the same as eg. Refs. [67, 93]. Recall that $\widetilde{\mathrm{Re}}$ takes the real part of any loop integrals occurring in the self-energies, but not of any mixing matrix elements or parameters appearing as coefficients to those loop integrals. This means that it removes any absorptive loop integrals, but retains all dispersive loop integrals, even if they are multiplied by an imaginary coefficient. Then we have

$$\begin{aligned}\widetilde{\mathrm{Re}}\,\delta Z_{-,ij}^{L/R} =& \frac{2}{m^2_{\tilde{\chi}_i^\pm} - m^2_{\tilde{\chi}_j^\pm}} \widetilde{\mathrm{Re}}\,\Big[m^2_{\tilde{\chi}_j^\pm}\Sigma^{L/R}_{-,ij}(m^2_{\tilde{\chi}_j^\pm}) + m_{\tilde{\chi}_i^\pm} m_{\tilde{\chi}_j^\pm}\Sigma^{R/L}_{-,ij}(m^2_{\tilde{\chi}_j^\pm}) + m_{\tilde{\chi}_i^\pm}\Sigma^{SL/SR}_{-,ij}(m^2_{\tilde{\chi}_j^\pm}) \\ &+ m_{\tilde{\chi}_j^\pm}\Sigma^{SR/SL}_{-,ij}(m^2_{\tilde{\chi}_j^\pm}) - m_{\tilde{\chi}^\pm_{i/j}}\big(U^*\delta X V^\dagger\big)_{ij} - m_{\tilde{\chi}^\pm_{j/i}}\big(V\delta X^\dagger U^T\big)_{ij}\Big], \end{aligned} \tag{4.39}$$

$$\begin{aligned}\widetilde{\mathrm{Re}}\,\delta \bar{Z}_{-,ij}^{L/R} =& \frac{2}{m^2_{\tilde{\chi}_j^\pm} - m^2_{\tilde{\chi}_i^\pm}} \widetilde{\mathrm{Re}}\,\Big[m^2_{\tilde{\chi}_i^\pm}\Sigma^{L/R}_{-,ij}(m^2_{\tilde{\chi}_i^\pm}) + m_{\tilde{\chi}_i^\pm} m_{\tilde{\chi}_j^\pm}\Sigma^{R/L}_{-,ij}(m^2_{\tilde{\chi}_i^\pm}) + m_{\tilde{\chi}_i^\pm}\Sigma^{SL/SR}_{-,ij}(m^2_{\tilde{\chi}_i^\pm}) \\ &+ m_{\tilde{\chi}_j^\pm}\Sigma^{SR/SL}_{-,ij}(m^2_{\tilde{\chi}_i^\pm}) - m_{\tilde{\chi}^\pm_{i/j}}(U^*\delta X V^\dagger)_{ij} - m_{\tilde{\chi}^\pm_{j/i}}(V\delta X^\dagger U^T)_{ij}\Big], \end{aligned} \tag{4.40}$$

$$\begin{aligned}\widetilde{\mathrm{Re}}\,\delta Z^{L/R}_{-,ii} =& -\widetilde{\mathrm{Re}}\,\Sigma^{L/R}_{-,ii}(m^2_{\tilde\chi^\pm_i}) - m^2_{\tilde\chi^\pm_i}\widetilde{\mathrm{Re}}\big[\Sigma^{L'}_{-,ii}(m^2_{\tilde\chi^\pm_i}) + \Sigma^{R'}_{-,ii}(m^2_{\tilde\chi^\pm_i})\big] - m_{\tilde\chi^\pm_i}\widetilde{\mathrm{Re}}\big[\Sigma^{SL'}_{-,ii}(m^2_{\tilde\chi^\pm_i}) \\ &+ \Sigma^{SR'}_{-,ii}(m^2_{\tilde\chi^\pm_i})\big] \pm \frac{1}{2m_{\tilde\chi^\pm_i}}\widetilde{\mathrm{Re}}\big[\Sigma^{SL}_{-,ii}(m^2_{\tilde\chi^\pm_i}) - \Sigma^{SR}_{-,ii}(m^2_{\tilde\chi^\pm_i}) + (V\delta X^\dagger U^T - U^*\delta X V^\dagger)_{ii}\big],\end{aligned} \tag{4.41}$$

$$\begin{aligned}\widetilde{\mathrm{Re}}\,\delta \bar Z^{L/R}_{-,ii} =& -\widetilde{\mathrm{Re}}\,\Sigma^{L/R}_{-,ii}(m^2_{\tilde\chi^\pm_i}) - m^2_{\tilde\chi^\pm_i}\widetilde{\mathrm{Re}}\big[\Sigma^{L'}_{-,ii}(m^2_{\tilde\chi^\pm_i}) + \Sigma^{R'}_{-,ii}(m^2_{\tilde\chi^\pm_i})\big] - m_{\tilde\chi^\pm_i}\widetilde{\mathrm{Re}}\big[\Sigma^{SL'}_{-,ii}(m^2_{\tilde\chi^\pm_i}) \\ &+ \Sigma^{SR'}_{-,ii}(m^2_{\tilde\chi^\pm_i})\big] \mp \frac{1}{2m_{\tilde\chi^\pm_i}}\widetilde{\mathrm{Re}}\big[\Sigma^{SL}_{-,ii}(m^2_{\tilde\chi^\pm_i}) - \Sigma^{SR}_{-,ii}(m^2_{\tilde\chi^\pm_i}) + (V\delta X^\dagger U^T - U^*\delta X V^\dagger)_{ii}\big].\end{aligned} \tag{4.42}$$

We evaluate the Hermitian conjugate, $(\widetilde{\mathrm{Re}}\,\delta\bar Z^{L/R})^\dagger_{-,ij} = (\widetilde{\mathrm{Re}}\,\delta\bar Z^{L/R})^*_{-,ji}$, and apply the relations between fermion self-energies due to $\mathcal{CPT}$-invariance given in Equation (A.9), to obtain

$$\begin{aligned}(\widetilde{\mathrm{Re}}\,\delta\bar Z^{L/R}_{-,ij})^\dagger =& \frac{2}{m^2_{\tilde\chi^\pm_i} - m^2_{\tilde\chi^\pm_j}}\widetilde{\mathrm{Re}}\,\big[m^2_{\tilde\chi^\pm_j}\Sigma^{L/R\,*}_{-,ji}(m^2_{\tilde\chi^\pm_j}) + m_{\tilde\chi^\pm_j}m_{\tilde\chi^\pm_i}\Sigma^{R/L\,*}_{-,ji}(m^2_{\tilde\chi^\pm_j}) + m_{\tilde\chi^\pm_j}\Sigma^{SL/SR\,*}_{-,ji}(m^2_{\tilde\chi^\pm_j}) \\ &+ m_{\tilde\chi^\pm_i}\Sigma^{SR/SL\,*}_{-,ji}(m^2_{\tilde\chi^\pm_j}) - m_{\tilde\chi^\pm_{j/i}}(U\delta X^* V^T)_{ij} - m_{\tilde\chi^\pm_{i/j}}(V^*\delta X^T U^\dagger)_{ji}\big] \\ =& \frac{2}{m^2_{\tilde\chi^\pm_i} - m^2_{\tilde\chi^\pm_j}}\widetilde{\mathrm{Re}}\,\big[m^2_{\tilde\chi^\pm_j}\Sigma^{L/R}_{-,ij}(m^2_{\tilde\chi^\pm_j}) + m_{\tilde\chi^\pm_j}m_{\tilde\chi^\pm_i}\Sigma^{R/L}_{-,ij}(m^2_{\tilde\chi^\pm_j}) + m_{\tilde\chi^\pm_j}\Sigma^{SR/SL}_{-,ij}(m^2_{\tilde\chi^\pm_j}) \\ &+ m_{\tilde\chi^\pm_i}\Sigma^{SL/SR}_{-,ij}(m^2_{\tilde\chi^\pm_j}) - m_{\tilde\chi^\pm_{j/i}}(U\delta X^* V^T)_{ij} - m_{\tilde\chi^\pm_{i/j}}(V^\dagger\delta X U^*)_{ij}\big] \\ =& \widetilde{\mathrm{Re}}\,\delta Z^{L/R}_{-,ij}.\end{aligned} \tag{4.43}$$

Similarly, again using Equation (A.9);

$$\begin{aligned}(\widetilde{\mathrm{Re}}\,\delta\bar Z^{L/R}_{-,ii})^\dagger =& -\widetilde{\mathrm{Re}}\,\Sigma^{L/R\,*}_{-,ii}(m^2_{\tilde\chi^\pm_i}) - m^2_{\tilde\chi^\pm_i}\widetilde{\mathrm{Re}}\big[\Sigma^{L\,*\prime}_{-,ii}(m^2_{\tilde\chi^\pm_i}) + \Sigma^{R\,*\prime}_{-,ii}(m^2_{\tilde\chi^\pm_i})\big] - m_{\tilde\chi^\pm_i}\widetilde{\mathrm{Re}}\big[\Sigma^{SL\,*\prime}_{-,ii}(m^2_{\tilde\chi^\pm_i}) \\ &+ \Sigma^{SR\,*\prime}_{-,ii}(m^2_{\tilde\chi^\pm_i})\big] \mp \frac{1}{2m_{\tilde\chi^\pm_i}}\widetilde{\mathrm{Re}}\big[\Sigma^{SL\,*}_{-,ii}(m^2_{\tilde\chi^\pm_i}) - \Sigma^{SR\,*}_{-,ii}(m^2_{\tilde\chi^\pm_i}) + (V^*\delta X^T U^\dagger - U\delta X^* V^T)_{ii}\big] \\ =& -\widetilde{\mathrm{Re}}\,\Sigma^{L/R}_{-,ii}(m^2_{\tilde\chi^\pm_i}) - m^2_{\tilde\chi^\pm_i}\widetilde{\mathrm{Re}}\big[\Sigma^{L'}_{-,ii}(m^2_{\tilde\chi^\pm_i}) + \Sigma^{R'}_{-,ii}(m^2_{\tilde\chi^\pm_i})\big] - m_{\tilde\chi^\pm_i}\widetilde{\mathrm{Re}}\big[\Sigma^{SR'}_{-,ii}(m^2_{\tilde\chi^\pm_i}) \\ &+ \Sigma^{SL'}_{-,ii}(m^2_{\tilde\chi^\pm_i})\big] \mp \frac{1}{2m_{\tilde\chi^\pm_i}}\widetilde{\mathrm{Re}}\big[\Sigma^{SR}_{-,ii}(m^2_{\tilde\chi^\pm_i}) - \Sigma^{SL}_{-,ii}(m^2_{\tilde\chi^\pm_i}) + (V^*\delta X^T U^\dagger - U\delta X^* V^T)_{ii}\big] \\ =& -\widetilde{\mathrm{Re}}\,\Sigma^{L/R}_{-,ii}(m^2_{\tilde\chi^\pm_i}) - m^2_{\tilde\chi^\pm_i}\widetilde{\mathrm{Re}}\big[\Sigma^{L'}_{-,ii}(m^2_{\tilde\chi^\pm_i}) + \Sigma^{R'}_{-,ii}(m^2_{\tilde\chi^\pm_i})\big] - m_{\tilde\chi^\pm_i}\widetilde{\mathrm{Re}}\big[\Sigma^{SL'}_{-,ii}(m^2_{\tilde\chi^\pm_i}) \\ &+ \Sigma^{SR'}_{-,ii}(m^2_{\tilde\chi^\pm_i})\big] \pm \frac{1}{2m_{\tilde\chi^\pm_i}}\widetilde{\mathrm{Re}}\big[\Sigma^{SL}_{-,ii}(m^2_{\tilde\chi^\pm_i}) - \Sigma^{SR}_{-,ii}(m^2_{\tilde\chi^\pm_i}) + (V\delta X^\dagger U^T - U^*\delta X V^\dagger)_{ii}\big] \\ =& \widetilde{\mathrm{Re}}\,\delta Z^{L/R}_{-,ii}.\end{aligned} \tag{4.44}$$

Hence the chargino field renormalisation constants obey $\widetilde{\mathrm{Re}}\,\delta\bar{Z}^{L/R}_{-,ij} = (\widetilde{\mathrm{Re}}\,\delta Z^{L/R})^{\dagger}_{-,ij}$ for any $i,j = 1,2$. The same procedure can be followed for neutralinos to show that $\widetilde{\mathrm{Re}}\,\delta\bar{Z}^{L/R}_{0,ij} = (\widetilde{\mathrm{Re}}\,\delta Z^{L/R})^{\dagger}_{0,ij}$ for any $i,j = 1,2,3,4$. This is in addition to the relation for neutralinos in Equation (4.38). Thus, the hermiticity relation between the field renormalisation constants for incoming and outgoing particles is restored when only dispersive parts of loop integrals are considered. The barred constants, $\delta\bar{Z}_{ij}$, are different from the hermitian conjugates, $\delta Z^{\dagger}_{ij}$, in their absorptive ($\widetilde{\mathrm{Im}}$) parts only.

Also note that the $\pm\frac{1}{2m_{\tilde{\chi}^{\pm}_i}}$ term in Equation (4.44) is purely imaginary when only dispersive parts are included (see Equation (A.10)) and can be written

$$\pm\frac{i}{m_{\tilde{\chi}^{\pm}_i}}\big[\mathrm{Im}(\widetilde{\mathrm{Re}}\,\Sigma^{SL}_{-,ii}(m^2_{\tilde{\chi}^{\pm}_i})) + \mathrm{Im}(V\delta X^{\dagger}U^{T})_{ii}\big]. \tag{4.45}$$

A similar simplification is possible for neutralinos.

For the above scheme where absorptive parts are discarded, the following definitions for the renormalisation transformations for the chargino and neutralino fields will suffice;

$$\begin{aligned}
\omega_L\tilde{\chi}^{-}_i &\to (1+\tfrac{1}{2}\delta\tilde{Z}^{L})_{ij}\omega_L\tilde{\chi}^{-}_j, & \overline{\tilde{\chi}^{-}_i}\omega_R &\to \overline{\tilde{\chi}^{-}_i}(1+\tfrac{1}{2}\delta\tilde{Z}^{L\,\dagger})_{ij}\omega_R,\\
\omega_R\tilde{\chi}^{-}_i &\to (1+\tfrac{1}{2}\delta\tilde{Z}^{R})_{ij}\omega_R\tilde{\chi}^{-}_j, & \overline{\tilde{\chi}^{-}_i}\omega_L &\to \overline{\tilde{\chi}^{-}_i}(1+\tfrac{1}{2}\delta\tilde{Z}^{R\,\dagger})_{ij}\omega_L,\\
\omega_L\tilde{\chi}^{0}_i &\to (1+\tfrac{1}{2}\delta\tilde{Z}_{0})_{ij}\omega_L\tilde{\chi}^{0}_j, & \overline{\tilde{\chi}^{0}_i}\omega_R &\to \overline{\tilde{\chi}^{0}_i}(1+\tfrac{1}{2}\delta\tilde{Z}^{0\,\dagger})_{ij}\omega_R,\\
\omega_R\tilde{\chi}^{0}_i &\to (1+\tfrac{1}{2}\delta\tilde{Z}^{0\,*})_{ij}\omega_R\tilde{\chi}^{0}_j, & \overline{\tilde{\chi}^{0}_i}\omega_L &\to \overline{\tilde{\chi}^{0}_i}(1+\tfrac{1}{2}\delta\tilde{Z}^{0\,T})_{ij}\omega_L,
\end{aligned} \tag{4.46}$$

where j is summed over 1,2,(3,4) for the charginos (neutralinos). Dirac fermions receive independent renormalisation constants for the left and right fields, $\delta\tilde{Z}^{L/R}_{ij} \equiv \widetilde{\mathrm{Re}}\,\delta Z^{L/R}_{-,ij}$, while the Majorana neutralino fields require only one renormalisation constant, $\delta\tilde{Z}^{0}_{ij} \equiv \widetilde{\mathrm{Re}}\,\delta Z^{L}_{0,ij}$, due to Equation (4.38). The field renormalisation constants for incoming antifermions are simply given by the Hermitian conjugate of the field renormalisation constants for outgoing fermions.

The same formulae for $\delta\tilde{Z}^{L/R}_{ij}$ and $\delta\tilde{Z}^{0}_{ij}$ can be arrived at by the following simplified renormalisation conditions;

$$\widetilde{\mathrm{Re}}\,\hat{\Gamma}^{(2)}_{ij}\tilde{\chi}_j(p)|_{p^2=m_j^2} = 0, \tag{4.47}$$

$$\lim_{p^2\to m_i^2}\frac{1}{\not{p}-m_i}\widetilde{\mathrm{Re}}\,\hat{\Gamma}^{(2)}_{ii}\tilde{\chi}_i(p) = \tilde{\chi}_i,$$

$$\widetilde{\mathrm{Re}}\,\hat{\Sigma}^{SL}_{ii}(m_i^2) = \widetilde{\mathrm{Re}}\,\hat{\Sigma}^{SR}_{ii}(m_i^2). \tag{4.48}$$

The corresponding renormalisation constants are in agreement with the formulae that appear in the thesis of Ref. [94], where absorptive parts of loop integrals were not included in the field renormalisation constants.

4.2.3 Discussion of absorptive parts

As shown in the previous section, the requirement of separate renormalisation constants for outgoing fermions and incoming antifermions arises from the non-zero absorptive parts of loop integrals. The issue of the treatment of absorptive parts of loop integrals is not a straightforward one. Indeed, strictly speaking, only stable particles should appear on external legs of Feynman diagrams in a quantum field theory, so that the formalism of in and out states at $t \to \pm\infty$ can be applied. However, in practice, most of the particles in the SM, and beyond, are unstable, so one must find some way to treat the imaginary parts of the loop integrals that arise in the self-energies of the unstable particles, that are related to their non-zero decay widths. At one-loop, these absorptive parts are only an issue in $\mathcal{CP}$-violating theories (such as the complex MSSM or the SM when the full CKM quark mixing matrix is used), since the squared matrix element of a process at one-loop is evaluated, up to contributions of two-loop order, as

$$|\mathcal{M}|^2 = |\mathcal{M}_{\text{born}}|^2 + 2\,\text{Re}\,(\mathcal{M}^*_{\text{born}}\mathcal{M}_{1-\text{loop}}) \tag{4.49}$$

where $\mathcal{M}_{\text{born}}$ and $\mathcal{M}_{1-\text{loop}}$ are the tree-level and one-loop matrix elements of the process respectively. In a $\mathcal{CP}$-conserving theory, an imaginary quantity can only occur in this expression if an unstable particle above threshold gives rise to a loop integral with absorptive parts in $\mathcal{M}_{1-\text{loop}}$. However, since there are no complex parameters in the couplings or mixing parameters, there will be no imaginary quantity in $\mathcal{M}_{\text{born}}$ or $\mathcal{M}_{1-\text{loop}}$ which can then multiply the imaginary loop integral to give a real contribution to $|\mathcal{M}|^2$. Even if imaginary loop integrals arise, they will not contribute to the squared matrix element at one-loop. Of course, if one includes two-loop contributions to $|\mathcal{M}|^2$, then absorptive parts may contribute. Conversely, in a $\mathcal{CP}$-violating theory, the absorptive parts of loop integrals for unstable particles may enter the squared matrix element at the one-loop level since they can be multiplied by imaginary coefficients in $\mathcal{M}_{\text{born}}$ or $\mathcal{M}_{1-\text{loop}}$ arising from the complex parameters.

In the literature, the issue of the treatment of absorptive parts of loop integrals in field renormalisation constants has found considerable attention, mostly in the context

of the renormalisation of the SM, see e.g. Refs. [67, 93, 95–98]. A possibility that has been advocated for instance in Refs. [67, 93], is to discard the absorptive parts of loop integrals in the field renormalisation constants, as we have illustrated in Section 4.2.2, while keeping any complex parameters in the coefficients, indicated by inserting the symbol $\widetilde{\text{Re}}$ into the renormalisation conditions. We have shown that, with this choice, the hermiticity relation between the field renormalisation constants for incoming and outgong particles, $\delta\bar{Z}_{ij}^{L/R} = (\delta Z_{ij}^{L/R})^\dagger$, is restored. However, the on-shell conditions of Equations (4.10), (4.11), (4.12) and (4.13) are no longer satisfied since non-zero absorptive parts of loop integrals can cause mixing between on-shell states and give contributions to the propagator residues. Instead, the weaker conditions of Equations (4.47) and (4.48) are satisfied. Therefore, for a full one-loop calculation, one must include all reducible, mixing self-energy diagrams and one will have to introduce additional finite normalisation constants to ensure the external particles have the correct on-shell properties, similar to the $\hat{\mathbf{Z}}$ factors we have introduced in the Higgs sector in Section 3.4.9.[2]

General renormalisation conditions without the $\widetilde{\text{Re}}$, as we have used in Section 4.2.1, were suggested in Ref. [96] for the SM, as a way of ensuring the correct on-shell conditions and gauge-independent matrix elements. In this scheme, the renormalisation constants are chosen to exactly eliminate all (dispersive and absorptive) contributions to the off-diagonal parts of the on-shell self-energies. There is consequently no mixing between on-shell states and the on-shell propagators remain diagonal even if absorptive parts of loop integrals arise. Thus, additional reducible self-energy diagrams and normalisation factors for external particles need not be considered. The trade-off is that one needs a field renormalisation constant, δZ, for outgoing particles and incoming antiparticles, and a separate field renormalisation constant, $\delta\bar{Z}$, for incoming particles and outgoing antiparticles, no longer given by the hermitian conjugate of the former. Although the hermiticity relation between renormalisation constants is not valid in this case, the authors of Ref. [96] showed that the $\mathcal{CPT}$ theorem still holds. In particular, the total widths of particles and antiparticles coincide, although not derived from the same renormalisation constant.

Nevertheless, the issue of an appropriate field renormalisation of unstable particles on external legs remains under debate in the literature. For the class of processes, $\tilde{\chi}_i^0 \to \tilde{\chi}_j^0 h_a$,

[2] To the author's knowledge, to date, no such Z factors have been derived for fermions in the literature. The derivation, beyond the scope of this work, is less straightforward than the derivation for scalar fields due to the Lorentz structure of the fermion propagators.

that we studied in Ref. [99], it turns out that all absorptive parts of external neutralino self-energy diagrams cancel when the squared matrix element for the full process is summed over left- and right-handed spins. This is due to the relation between the left- and right-handed components of the (Majorana) neutralinos. Hence, for the numerical results presented in Ref. [99] and in Chapters 6-7 of this thesis, absorptive parts of loop integrals do not contribute and the schemes with and without the insertion of $\widetilde{\mathrm{Re}}$ are equivalent.

However this argument does not apply for (Dirac) charginos nor for spin-dependent calculations. Our main focus in this thesis will be processes with external neutralinos; we have only considered processes involving charginos when carrying out checks of UV-finiteness, which will not be affected by these absorptive parts. In Chapter 8, we calculate partial decay widths involving Majorana neutralinos with left-handed and right-handed polarisations, and thus, absorptive parts will contribute. In Section 4.5, we will show examples where the absorptive contributions to the field renormalisation constants are numerically relevant and the general scheme of Section 4.2.1 should be used in order to ensure the correct on-shell properties are satisfied. For the rest of this thesis we will use the general scheme, including absorptive parts of loop integrals, unless otherwise stated.

4.2.4 Field renormalisation in the $\mathcal{CP}$-conserving case

In the MSSM with real parameters, we can use the $\mathcal{CP}$ invariance relations between the self-energies given in Equation (A.11) to simplify our expressions for the diagonal field renormalisation constants from Equations (4.33) and (4.37). Also, in this case, the $\pm\frac{1}{2m_{\tilde{\chi}_i}}$ terms in the diagonal constants (see Equation (4.45)) vanish. For the charginos, Equation (4.33) simplifies to

$$\begin{aligned}\delta Z^{L/R}_{-,ii,\mathrm{CPC}} =& -\Sigma^{L/R}_{-,ii}(m^2_{\tilde{\chi}^\pm_i}) - m^2_{\tilde{\chi}^\pm_i}\left[\Sigma^{L'}_{-,ii}(m^2_{\tilde{\chi}^\pm_i}) + \Sigma^{R'}_{-,ii}(m^2_{\tilde{\chi}^\pm_i})\right] - 2m_{\tilde{\chi}^\pm_i}\Sigma^{SL'}_{-,ii}(m^2_{\tilde{\chi}^\pm_i}) \\ =& \,\delta\bar{Z}^{L/R}_{-,ii,\mathrm{CPC}}\end{aligned} \tag{4.50}$$

where CPC denotes the $\mathcal{CP}$-conserving MSSM. For the neutralinos we can use Equations (A.11) and (A.12) to simplify Equation (4.37) to

$$\delta Z^{L/R}_{0,ii,\mathrm{CPC}} = \delta\bar{Z}^{L/R}_{0,ii,\mathrm{CPC}} = -\Sigma^{L/R}_{0,ii}(m^2_{\tilde{\chi}^0_i}) - 2m^2_{\tilde{\chi}^0_i}\Sigma^{L'}_{0,ii}(m^2_{\tilde{\chi}^0_i}) - 2m_{\tilde{\chi}^0_i}\Sigma^{SL'}_{-,ii}(m^2_{\tilde{\chi}^0_i}). \tag{4.51}$$

The off-diagonal field renormalisation constants can also be simplified in the $\mathcal{CP}$-conserving case to

$$\begin{aligned}\delta Z^{L/R}_{-,ij,\mathrm{CPC}} &= \frac{2}{m^2_{\tilde{\chi}^\pm_i} - m^2_{\tilde{\chi}^\pm_j}}\big[m^2_{\tilde{\chi}^\pm_j}\Sigma^{L/R}_{-,ij}(m^2_{\tilde{\chi}^\pm_j}) + m_{\tilde{\chi}^\pm_i} m_{\tilde{\chi}^\pm_j}\Sigma^{R/L}_{-,ij}(m^2_{\tilde{\chi}^\pm_j}) + m_{\tilde{\chi}^\pm_i}\Sigma^{SL/SR}_{-,ij}(m^2_{\tilde{\chi}^\pm_j}) \\ &\quad + m_{\tilde{\chi}^\pm_j}\Sigma^{SR/SL}_{-,ij}(m^2_{\tilde{\chi}^\pm_j}) - m_{\tilde{\chi}^\pm_{i/j}}\big(U\delta X V^T\big)_{ij} - m_{\tilde{\chi}^\pm_{j/i}}\big(V\delta X^T U^T\big)_{ij}\big] \\ &= \delta\bar{Z}^{L/R}_{-,ji,\mathrm{CPC}}. \end{aligned} \tag{4.52}$$

A similar simplification is possible for the neutralinos. Up to absorptive parts, the above formulae are in agreement with Ref. [86], where $\mathcal{CP}$-conservation is assumed. As already discussed, in the $\mathcal{CP}$-conserving MSSM, absorptive parts of loop integrals will not contribute to the squared matrix element of a process at one-loop order, and so will not affect results for physical quantities. Therefore, if one equivalently discards the absorptive contributions to the field renormalisation constants, then the field renormalisation constants become real and the hermiticity relation, $\delta\bar{Z}_{ij} = \delta Z^\dagger_{ij}$, is trivially satisfied.

4.3 Determining the loop-corrected masses

In order to find the loop-corrected neutralino and chargino masses, we consider the diagonal fermion propagators. We need not consider mixing between the fields, because we have applied on-shell conditions which ensure that such contributions to the masses vanish. We identify the poles of the fermion propagator in Equation (4.14) with the physical fermion masses. The complex pole, $\mathcal{M}_{\tilde{\chi}^2_i}$, of the propagator, $\hat{S}^{(2)}_{ii}$, is found by solving

$$\mathcal{M}^2_{\tilde{\chi}_i}\big(1 + \hat{\Sigma}^L_{ii}(\mathcal{M}^2_{\tilde{\chi}_i})\big)\big(1 + \hat{\Sigma}^R_{ii}(p^2)\big) - \big(m_{\tilde{\chi}_i} - \hat{\Sigma}^{SL}_{ii}(\mathcal{M}^2_{\tilde{\chi}_i})\big)\big(m_i - \hat{\Sigma}^{SR}_{ii}(\mathcal{M}^2_{\tilde{\chi}_i})\big) = 0 \tag{4.53}$$

where $\tilde{\chi}_i = \tilde{\chi}^-_i$ $(i,j = 1,2)$ or $\tilde{\chi}^0_i$ $(i,j = 1,2,3,4)$. We write the complex pole as $\mathcal{M}^2_{\tilde{\chi}_i} = M^2_{\tilde{\chi}_i} - iM_{\tilde{\chi}_i}\Gamma_{\tilde{\chi}_i}$, where $M_{\tilde{\chi}_i}$ is the loop-corrected mass and $\Gamma_{\tilde{\chi}_i}$ is the width. To obtain the complex pole up to terms of two-loop order, the self-energies can be evaluated at the tree-level masses, $m^2_{\tilde{\chi}_i}$. We thus find that at one-loop level, the physical masses may be written in terms of the renormalised self-energies as follows;

$$\begin{aligned} M_{\tilde{\chi}_i} &= m_{\tilde{\chi}_i}(1 - \frac{1}{2}\mathrm{Re}[\hat{\Sigma}^L_{ii}(m^2_{\tilde{\chi}_i}) + \hat{\Sigma}^R_{ii}(m^2_{\tilde{\chi}_i})]) - \frac{1}{2}\mathrm{Re}[\hat{\Sigma}^{SL}_{ii}(m^2_{\tilde{\chi}_i}) + \hat{\Sigma}^{SR}_{ii}(m^2_{\tilde{\chi}_i})] \\ &= m_{\tilde{\chi}_i} + \Delta m_{\tilde{\chi}_i} \end{aligned} \tag{4.54}$$

where

$$\Delta m_{\tilde{\chi}_i} \equiv -\frac{m_{\tilde{\chi}_i}}{2}\mathrm{Re}[\hat{\Sigma}^L_{ii}(m^2_{\tilde{\chi}_i}) + \hat{\Sigma}^R_{ii}(m^2_{\tilde{\chi}_i})] - \frac{1}{2}\mathrm{Re}[\hat{\Sigma}^{SL}_{ii}(m^2_{\tilde{\chi}_i}) + \hat{\Sigma}^{SR}_{ii}(m^2_{\tilde{\chi}_i})]. \tag{4.55}$$

Note that, due to the conditions in Equations (4.15) and (4.16), we have identical renormalised diagonal left and right self-energies in the on-shell limit, so we may further simplify the masses to

$$\begin{aligned} M_{\tilde{\chi}_i} &= m_{\tilde{\chi}_i}[1 - \mathrm{Re}\,\hat{\Sigma}^L_{ii}(m^2_{\tilde{\chi}_i})] - \mathrm{Re}\,\hat{\Sigma}^{SL}_{ii}(m^2_{\tilde{\chi}_i}) \\ &= m_{\tilde{\chi}_i}[1 - \mathrm{Re}\,\hat{\Sigma}^R_{ii}(m^2_{\tilde{\chi}_i})] - \mathrm{Re}\,\hat{\Sigma}^{SR}_{ii}(m^2_{\tilde{\chi}_i}) \\ &= m_{\tilde{\chi}_i}[1 - \mathrm{Re}\,\hat{\Sigma}^L_{ii}(m^2_{\tilde{\chi}_i})] - \mathrm{Re}\,\hat{\Sigma}^{SR}_{ii}(m^2_{\tilde{\chi}_i}) \\ &= m_{\tilde{\chi}_i}[1 - \mathrm{Re}\,\hat{\Sigma}^R_{ii}(m^2_{\tilde{\chi}_i})] - \mathrm{Re}\,\hat{\Sigma}^{SL}_{ii}(m^2_{\tilde{\chi}_i}) \end{aligned} \tag{4.56}$$

for both charginos and neutralinos.

4.4 Parameter renormalisation

For the parameter renormalisation of M_1, M_2, μ, we use an on-shell approach, because this is convenient in processes with external charginos and neutralinos. In the chargino–neutralino sector, we have five independent input parameters, three with mass dimension, $|M_1|$, $|M_2|$ and $|\mu|$, and two $\mathcal{CP}$-violating phases, ϕ_{M_1} and ϕ_μ (as discussed in Section 2.6, we use a convention where the phase of M_2 is set to zero). These five parameters determine the tree-level masses of the six fields, $\tilde{\chi}^+_{1,2}$, $\tilde{\chi}^0_{1,2,3,4}$. We fix three of the six masses on-shell by requiring that the pole masses, $M_{\tilde{\chi}_i}$, coincide with their tree level values, $m_{\tilde{\chi}_i}$;

$$0 = \frac{m_{\tilde{\chi}_i}}{2}\mathrm{Re}[\hat{\Sigma}^L_{ii}(m^2_{\tilde{\chi}_i}) + \hat{\Sigma}^R_{ii}(m^2_{\tilde{\chi}_i})] + \frac{1}{2}\mathrm{Re}[\hat{\Sigma}^{SL}_{ii}(m^2_{\tilde{\chi}_i}) + \hat{\Sigma}^{SR}_{ii}(m^2_{\tilde{\chi}_i})]. \tag{4.57}$$

This gives us three equations to help us fix δM_2 and the real and imaginary parts of δM_1 and $\delta\mu$. The remaining three loop-corrected masses will differ from the tree-level masses by $\Delta m_{\tilde{\chi}_i}$, given in Equation (4.55). For charginos on-shell, the condition given in Equation (4.57) becomes

$$(V\delta X^\dagger U^T + U^*\delta X V^\dagger)_{ii} = m_{\tilde{\chi}^\pm_i}\mathrm{Re}\,[\Sigma^L_{-,ii}(m^2_{\tilde{\chi}^\pm_i}) + \Sigma^R_{-,ii}(m^2_{\tilde{\chi}^\pm_i})] + \mathrm{Re}\,[\Sigma^{SL}_{-,ii}(m^2_{\tilde{\chi}^\pm_i}) + \Sigma^{SR}_{-,ii}(m^2_{\tilde{\chi}^\pm_i})]. \tag{4.58}$$

We expand the left-hand side of this equation to give

$$\begin{aligned}(U^*\delta X V^\dagger + V\delta X^\dagger U^T)_{ii} &= \mathrm{Re}\,\delta M_2(U^*_{i1}V^*_{i1} + V_{i1}U_{i1}) \\ &\quad +\mathrm{Re}\,\delta\mu(U^*_{i2}V^*_{i2} + V_{i2}U_{i2}) + i\mathrm{Im}\,\delta\mu(U^*_{i2}V^*_{i2} - V_{i2}U_{i2}) \\ &\quad +\delta X_{12}(U^*_{i1}V^*_{i2} + V_{i2}U_{i1}) + \delta X_{21}(V^*_{i1}U^*_{i2} + U_{i2}V_{i1}),\end{aligned} \tag{4.59}$$

where δX_{12} and δX_{21} are real since we do not have $\mathcal{CP}$-violation at tree-level in the gauge boson sector.

Similarly for neutralinos on-shell, the condition given in Equation (4.57) becomes

$$(Y\delta N^\dagger Y^T + Y^*\delta N Y^\dagger)_{ii} = m_{\tilde{\chi}^0_i}\mathrm{Re}\,[\Sigma^L_{0,ii}(m^2_{\tilde{\chi}^0_i}) + \Sigma^R_{0,ii}(m^2_{\tilde{\chi}^0_i})] + \mathrm{Re}\,(\Sigma^{SR}_{0,ii}(m^2_{\tilde{\chi}^0_i}) + \Sigma^{SL}_{0,ii}(m^2_{\tilde{\chi}^0_i})). \tag{4.60}$$

We expand the left-hand side of this equation to give

$$\begin{aligned}(N^*\delta Y N^\dagger + N\delta Y^\dagger N^T)_{ii} &= \mathrm{Re}\,\delta M_1\,((N^*_{i1})^2 + N^2_{i1}) + i\mathrm{Im}\,\delta M_1\,((N^*_{i1})^2 - N^2_{i1}) \\ &\quad +\mathrm{Re}\,\delta M_2\,((N^*_{i2})^2 + N^2_{i2}) + 2\delta Y_{13}(N^*_{i1}N^*_{i3} + N_{i1}N_{i3}) \\ &\quad +2\delta Y_{14}(N^*_{i1}N^*_{i4} + N_{i1}N_{i4}) + 2\delta Y_{23}(N^*_{i2}N^*_{i3} + N_{i2}N_{i3}) \\ &\quad +2\delta Y_{24}(N^*_{i2}N^*_{i4} + N_{i2}N_{i4}) - 2\mathrm{Re}\,\delta\mu\,(N^*_{i3}N^*_{i4} + N_{i3}N_{i4}) \\ &\quad -2i\mathrm{Im}\,\delta\mu\,(N^*_{i3}N^*_{i4} - N_{i3}N_{i4}).\end{aligned} \tag{4.61}$$

Introducing the following shorthand;

$$\begin{aligned}C_{(i)} &\equiv \mathrm{Re}\big[m_{\tilde{\chi}^+_i}[\Sigma^L_{-,ii}(m^2_{\tilde{\chi}^+_i}) + \Sigma^R_{-,ii}(m^2_{\tilde{\chi}^+_i})] + \Sigma^{SL}_{-,ii}(m^2_{\tilde{\chi}^+_i}) + \Sigma^{SR}_{-,ii}(m^2_{\tilde{\chi}^+_i})\big] \\ &\quad -2\delta X_{21}\,\mathrm{Re}(U_{i2}V_{i1}) - 2\delta X_{12}\,\mathrm{Re}(U_{i1}V_{i2}), \\ N_{(i)} &\equiv \mathrm{Re}\big[m_{\tilde{\chi}^0_i}[\Sigma^L_{0,ii}(m^2_{\tilde{\chi}^0_i}) + \Sigma^R_{0,ii}(m^2_{\tilde{\chi}^0_i})] + \Sigma^{SL}_{0,ii}(m^2_{\tilde{\chi}^0_i}) + \Sigma^{SR}_{0,ii}(m^2_{\tilde{\chi}^0_i})\big] - 4\delta Y_{13}\,\mathrm{Re}(N_{i1}N_{i3}) \\ &\quad -4\delta Y_{23}\,\mathrm{Re}(N_{i2}N_{i3}) - 4\delta Y_{14}\,\mathrm{Re}(N_{i1}N_{i4}) - 4\delta Y_{24}\,\mathrm{Re}(N_{i2}N_{i4}),\end{aligned} \tag{4.62}$$

we can write the condition of (4.60) for the i'th neutralino mass to be on-shell as

$$\begin{aligned}&\mathrm{Re}\,\delta M_1\,((N^*_{i'1})^2 + N^2_{i'1}) + i\mathrm{Im}\,\delta M_1\,((N^*_{i'1})^2 - N^2_{i'1}) + \mathrm{Re}\,\delta M_2\,((N^*_{i'2})^2 + N^2_{i'2}) \\ &\qquad -2\mathrm{Re}\,\delta\mu\,(N^*_{i'3}N^*_{i'4} + N_{i'3}N_{i'4}) - 2i\mathrm{Im}\,\delta\mu\,(N^*_{i'3}N^*_{i'4} - N_{i'3}N_{i'4}) = N_{(i')},\end{aligned} \tag{4.63}$$

and the condition of Equation (4.58) for the i''th chargino mass to be on-shell as

$$\mathrm{Re}\,\delta M_2(U^*_{i''1}V^*_{i''1}+V_{i''1}U_{i''1})+\mathrm{Re}\,\delta\mu(U^*_{i''2}V^*_{i''2}+V_{i''2}U_{i''2})+i\mathrm{Im}\,\delta\mu(U^*_{i''2}V^*_{i''2}-V_{i''2}U_{i''2})=C_{(i'')}. \tag{4.64}$$

4.4.1 Parameter renormalisation in the case where M_1, M_2 and μ are real

If there is no $\mathcal{CP}$-violation in the neutralino sector at tree level, i.e. M_1, M_2 and μ are real, then the rows of the mixing matrices, U, V and N, are either purely real or purely imaginary, so that the mixing matrix elements in Equations (4.63) and (4.63) always appear in combinations where the conjugate symbol can be dropped. Coefficients for the imaginary parts of δM_1 and $\delta\mu$ vanish since $N_{ij}N_{ik} = N^*_{ij}N^*_{ik}$ and $U_{ij}V_{ik} = V^*_{ij}U^*_{ik}$. Thus we only have three unknowns; $\delta M_1 = \mathrm{Re}\,\delta M_1$, $\delta M_2 = \mathrm{Re}\,\delta M_2$ and $\delta\mu = \mathrm{Re}\,\delta\mu$. These are found by solving three equations, chosen from

$$2\mathrm{Re}\,\delta M_1\, N^2_{i'1} + 2\mathrm{Re}\,\delta M_2\, N^2_{i'2} - 4\mathrm{Re}\,\delta\mu\, N_{i'3}N_{i'4} = N_{(i')}, \tag{4.65}$$

$$2\mathrm{Re}\,\delta M_2 V_{i''1}U_{i''1} + 2\mathrm{Re}\,\delta\mu V_{i''2}U_{i''2} = C_{(i'')}. \tag{4.66}$$

We implemented three options into `FeynArts`, the first with two neutralinos and one chargino mass on-shell, the second with three neutralino masses on-shell and the third with two chargino masses and one neutralino mass on-shell.

Real M_1, M_2, μ: $\tilde{\chi}^0_i$, $\tilde{\chi}^0_j$, $\tilde{\chi}^+_k$ on-shell

Assuming real M_1, M_2 and μ, we consider the case where we fix the masses of two neutralinos, $\tilde{\chi}^0_i$, $\tilde{\chi}^0_j$, and one chargino, $\tilde{\chi}^\pm_k$, on-shell, where $i \neq j = 1,2,3,4$ and $k = 1,2$. This means solving simultaneously Equation (4.65) for $i' = i, j$ and Equation (4.66) for $i'' = k$. Doing this leads to

$$\begin{aligned}\delta M_1 = [&2(N_{i3}N_{i4}N^2_{j2} - N^2_{i2}N_{j3}N_{j4})C_{(k)} + (U_{k2}V_{k2}N^2_{j2} + 2U^*_{k1}V^*_{k1}N^*_{i3}N^*_{i4})N_{(i)} + \\ &- (U_{k2}V_{k2}N^2_{i2} + 2U_{k1}V_{k1}N_{i3}N^*_{i4})N_{(j)}]/K,\end{aligned} \tag{4.67}$$

$$\delta M_2 = [-2(N_{i3}N_{i4}N^2_{j1} - N^2_{i1}N_{j3}N_{j4})C_{(k)} - U_{k2}V_{k2}N^2_{j1}N_{(i)} + U_{k2}V_{k2}N^2_{i1}N_{(j)}]/K, \tag{4.68}$$

$$\delta\mu = [-(N^2_{i2}N^2_{j1} - N^2_{i1}N^2_{j2})C_{(k)} + U_{k1}V_{k1}N^2_{j1}N_{(i)} - U_{k1}V_{k1}N^2_{i1}N_{(j)}]/K, \tag{4.69}$$

where

$$K = 2U_{k2}V_{k2}(-N_{i2}^2N_{j1}^2 + N_{i1}^2N_{j2}^2) + 4U_{k1}V_{k1}(-N_{i3}N_{i4}N_{j1}^2 + N_{i1}^2N_{j3}N_{j4}). \tag{4.70}$$

Real M_1, M_2, μ: $\tilde{\chi}_i^0$, $\tilde{\chi}_j^0$, $\tilde{\chi}_k^0$ on-shell

To fix the masses of three neutralinos, $\tilde{\chi}_i^0$, $\tilde{\chi}_j^0$, $\tilde{\chi}_k^0$, on-shell, where $i \neq j \neq k = 1, 2, 3, 4$, we must simultaneously solve Equation (4.65) for $i' = i, j, k$. Doing this leads to

$$\begin{aligned}
\delta M_1 &= [(N_{i3}N_{i4}N_{j2}^2 - N_{j3}N_{j4}N_{i2}^2)N_{(k)} + (N_{j3}N_{j4}N_{k2}^2 - N_{k3}N_{k4}N_{j2}^2)N_{(i)} \\
&\quad + (N_{k3}N_{k4}N_{i2}^2 - N_{i3}N_{i4}N_{k2}^2)N_{(j)}]/L, \qquad (4.71) \\
\delta M_2 &= [(N_{j3}N_{j4}N_{i1}^2 - N_{i3}N_{i4}N_{j1}^2)N_{(k)} + (N_{k3}N_{k4}N_{j1}^2 - N_{j3}N_{j4}N_{k1}^2)N_{(i)} \\
&\quad + (N_{i3}N_{i4}N_{k1}^2 - N_{k3}N_{k4}N_{i1}^2)N_{(j)}]/L, \qquad (4.72) \\
\delta\mu &= -[(N_{i2}^2N_{j1}^2 - N_{i1}^2N_{j2}^2)N_{(k)} + (N_{j2}^2N_{k1}^2 - N_{j1}^2N_{k2}^2)N_{(i)} \\
&\quad + (N_{i1}^2N_{k2}^2 - N_{i2}^2N_{k1}^2)N_{(j)}]/2L, \qquad (4.73)
\end{aligned}$$

where

$$\begin{aligned}
L &= 2(N_{i3}N_{i4}N_{j2}^2N_{k1}^2 - N_{i2}^2N_{j3}N_{j4}N_{k1}^2 - N_{i3}N_{i4}N_{j1}^2N_{k2}^2 \\
&\quad + N_{i1}^2N_{j3}N_{j4}N_{k2}^2 + N_{i2}^2N_{j1}^2N_{k3}N_{k4} - N_{i1}^2N_{j2}^2N_{k3}N_{k4}). \qquad (4.74)
\end{aligned}$$

Real M_1, M_2, μ: $\tilde{\chi}_i^0$, $\tilde{\chi}_j^+$, $\tilde{\chi}_k^+$ on-shell

To fix the masses of one neutralino, $\tilde{\chi}_i^0$, and two charginos, $\tilde{\chi}_j^\pm$, $\tilde{\chi}_k^\pm$, on-shell, where $i = 1, 2, 3, 4$ and $j \neq k = 1, 2$, we must simultaneously solve Equation (4.65) for $i' = i$ and Equation (4.66) for $i'' = j, k$. Doing this leads to

$$\begin{aligned}
\delta M_1 &= -[(2N_{i3}N_{i4}U_{j1}V_{j1} + N_{i2}^2U_{j2}V_{j2})C_{(k)} + (U_{j1}U_{k2}V_{j1}V_{k2} - U_{j2}U_{k1}V_{j2}V_{k1})N_{(i)} \\
&\quad - (N_{i2}^2U_{k2}V_{k2} + 2N_{i3}N_{i4}U_{k1}V_{k1})C_{(j)}]/(N_{i1}^2M), \qquad (4.75) \\
\delta M_2 &= [U_{j2}V_{j2}C_{(k)} - U_{k2}V_{k2}C_{(j)}]/M, \qquad (4.76) \\
\delta\mu &= -[U_{j1}V_{j1}C_{(k)} - U_{k1}V_{k1}C_{(j)}]/M, \qquad (4.77)
\end{aligned}$$

where

$$M = 2(U_{j2}U_{k1}V_{j2}V_{k1} - U_{j1}U_{k2}V_{j1}V_{k2}). \tag{4.78}$$

In Ref. [86], the masses of $\tilde{\chi}_1^0$, $\tilde{\chi}_1^\pm$ and $\tilde{\chi}_2^\pm$ were fixed on-shell. We find agreement between our expressions above and those that appear in Ref. [86]. This choice is advantageous for processes where charginos appear as external particles, and avoids difficulties with infra-red divergences present in QED corrections. However, it is not so convenient for processes involving more than one external neutralino.

4.4.2 Parameter renormalisation in the full complex MSSM

If there is $\mathcal{CP}$-violation in the chargino–neutralino sector at tree level, then M_1 and μ can be complex in our convention (see Section 2.6), so there are five parameter renormalisation constants to determine; Re δM_1, Re δM_2, Re $\delta\mu$, Im δM_1 and Im $\delta\mu$. Equally, one can parameterise the five renormalisation constants in terms of the absolute values and phases; $\delta|M_1|$, $\delta|M_2|$, $\delta|\mu|$, $\delta\phi_{M_1}$ and $\delta\phi_\mu$. In the latter case, the parameters are renormalised with the following transformations;

$$\begin{aligned} |M_1| &\to |M_1| + \delta|M_1|, \qquad & \phi_{M_1} &\to \phi_{M_1} + \delta\phi_{M_1}, \\ |M_2| &\to |M_2| + \delta|M_2|, & & \\ |\mu| &\to |\mu| + \delta|\mu|, & \phi_\mu &\to \phi_\mu + \delta\phi_\mu. \end{aligned} \tag{4.79}$$

while in the former case, the parameters are renormalised with

$$\begin{aligned} \mathrm{Re}\, M_1 &\to \mathrm{Re}\, M_1 + \delta(\mathrm{Re}\, M_1), & \mathrm{Im}\, M_1 &\to \mathrm{Im}\, M_1 + \delta(\mathrm{Im}\, M_1), \\ \mathrm{Re}\, M_2 &\to \mathrm{Re}\, M_2 + \delta(\mathrm{Re}\, M_2), & & \\ \mathrm{Re}\, \mu &\to \mathrm{Re}\, \mu + \delta(\mathrm{Re}\, \mu), & \mathrm{Im}\, \mu &\to \mathrm{Im}\, \mu + \delta(\mathrm{Re}\, \mu), \end{aligned} \tag{4.80}$$

where $\delta(\mathrm{Re}\ M_2) = \delta|M_2|$. We can write

$$\begin{aligned} \delta(\mathrm{Re}\ M_1) &= \delta|M_1|\cos\phi_{M_1} - |M_1|\sin\phi_{M_1}\delta\phi_{M_1}, \\ \delta(\mathrm{Im}\ M_1) &= \delta|M_1|\sin\phi_{M_1} + |M_1|\cos\phi_{M_1}\delta\phi_{M_1}, \\ \delta(\mathrm{Re}\ \mu) &= \delta|\mu|\cos\phi_\mu - |\mu|\sin\phi_\mu\delta\phi_\mu, \\ \delta(\mathrm{Im}\ \mu) &= \delta|\mu|\sin\phi_\mu + |\mu|\cos\phi_\mu\delta\phi_\mu, \end{aligned} \tag{4.81}$$

and

$$\begin{aligned}
\delta|M_1| &= \delta(\text{Re } M_1)\cos\phi_{M_1} + \delta(\text{Im } M_1)\sin\phi_{M_1}, \\
\delta\phi_{M_1} &= -(\delta(\text{Re } M_1)\sin\phi_{M_1} - \delta(\text{Im } M_1)\cos\phi_{M_1})/|M_1|, \\
\delta|\mu| &= \delta(\text{Re } \mu)\cos\phi_\mu + \delta(\text{Im } \mu)\sin\phi_\mu, \\
\delta\phi_\mu &= -(\delta(\text{Re } \mu)\sin\phi_\mu - \delta(\text{Im } \mu)\cos\phi_\mu)/|\mu|. \qquad (4.82)
\end{aligned}$$

In both parameterisations, we have five renormalisation constants to determine, and so far only three equations (chosen from Equations (4.63) and (4.64)) resulting from the condition that three of the six masses be on-shell. Two further conditions are required to fix all five renormalisation constants. This comes from having to renormalise the two $\mathcal{CP}$-violating phases, ϕ_{M_1} and ϕ_μ. Like for $\tan\beta$, there is no obvious on-shell definition of these phases. Thus a convenient scheme would be the $\overline{\text{DR}}$ scheme. The $\overline{\text{DR}}$ scheme has been advocated, in particular, in the SPA conventions for supersymmetry parameter analysis [100]. However, we will show in the following that, in fact, ϕ_{M_1} and ϕ_μ should be considered as mixing parameters, like α, β_n and β_c in the Higgs sector, and therefore need not be renormalised at all.

For demonstration purposes we investigate an "on-shell" scheme in which we require the conditions

$$\delta Z^R_{0,11} = \delta\bar{Z}^R_{0,11}, \quad \delta Z^L_{0,11} = \delta\bar{Z}^L_{0,11}, \qquad (4.83)$$

$$\delta Z^R_{-,22} = \delta\bar{Z}^R_{-,22}, \quad \delta Z^L_{-,22} = \delta\bar{Z}^L_{-,22}, \qquad (4.84)$$

in addition to the usual on-shell field renormalisation conditions of Equations (4.10), (4.11), (4.12), (4.13) and (4.16). This means that the $\pm\frac{1}{2m_{\tilde{\chi}_i}}$ terms in the diagonal field renormalisation constants for $\tilde{\chi}^0_1$ and $\tilde{\chi}^\pm_2$, in Equations 4.37 and 4.33 respectively, are zero. Equation (4.16) can now only be satisfied if

$$\begin{aligned}
0 &= \Sigma^{SL}_{-,11}(m^1_{\tilde{\chi}^\pm_1}) - \Sigma^{SR}_{-,11}(m^2_{\tilde{\chi}^\pm_1}) - (N^*\delta X Y^\dagger)_{11} + (N\delta Y^\dagger N^T)_{11} \equiv N_{(11)} \qquad (4.85) \\
0 &= \Sigma^{SL}_{-,22}(m^2_{\tilde{\chi}^\pm_2}) - \Sigma^{SR}_{-,22}(m^2_{\tilde{\chi}^\pm_2}) - (U^*\delta X V^\dagger)_{22} + (V\delta X^\dagger U^T)_{22} \equiv C_{(22)}. \qquad (4.86)
\end{aligned}$$

We use these two conditions in conjunction with the requirement that the masses of $\tilde{\chi}^0_1$, $\tilde{\chi}^\pm_1$ and $\tilde{\chi}^\pm_2$ are on-shell (Equations (4.63), with $i' = 1$, and (4.64), with $i'' = 1, 2$).

Solving simultaneously we obtain

$$\begin{aligned}
\delta(\mathrm{Re}\mu) =& \big[-2\,\mathrm{Im}(U_{12}V_{12})\,\mathrm{Re}(U_{22}V_{22})^2 + \mathrm{Im}(U_{22}V_{22})\,\mathrm{Re}(U_{21}V_{21})\,\mathrm{Re}(U_{11}V_{11}) \\
&+ C_{(2)}[\mathrm{Im}(U_{21}V_{21})\,\mathrm{Im}(U_{12}V_{12}) + \mathrm{Re}(U_{22}V_{22})\,\mathrm{Re}(U_{11}V_{11})] \\
&- C_{(1)}[\mathrm{Im}(U_{21}V_{21})\,\mathrm{Im}(U_{22}V_{22}) + \mathrm{Re}(U_{21}V_{21})\,\mathrm{Re}(U_{22}V_{22})] \\
&- C_{(22)}[\mathrm{Im}(U_{12}V_{12})\,\mathrm{Re}(U_{21}V_{21}) + \mathrm{Im}(U_{22}V_{22})\,\mathrm{Re}(U_{12}V_{12})]\big]/2X, \qquad (4.87) \\
\delta(\mathrm{Im}\mu) =& \big[-2\,\mathrm{Re}(U_{21}V_{21})\,\mathrm{Re}(U_{22}V_{22})\,\mathrm{Re}(U_{11}V_{11}) + \mathrm{Re}(U_{21}V_{21})^2\,\mathrm{Re}(U_{12}V_{12}) \\
&+ C_{(2)}[\mathrm{Im}(U_{22}V_{22})\,\mathrm{Re}(U_{11}V_{11}) - \mathrm{Im}(U_{21}V_{21})\,\mathrm{Re}(U_{12}V_{12})] \\
&- C_{(1)}[\mathrm{Im}(U_{22}V_{22})\,\mathrm{Re}(U_{21}V_{21}) - \mathrm{Im}(U_{21}V_{21})\,\mathrm{Re}(U_{22}V_{22})] \\
&+ C_{(22)}[\mathrm{Re}(U_{22}V_{22})\,\mathrm{Re}(U_{11}V_{11}) - \mathrm{Re}(U_{21}V_{21})\,\mathrm{Re}(U_{12}V_{12})]\big]/2X \qquad (4.88)
\end{aligned}$$

where X contains only U and V matrix elements. Using Equation (4.82), we can find the corresponding $\delta|\mu|$ and $\delta\phi_\mu$. The resulting expression for $\delta\phi_\mu$ turns out to be UV-convergent. The same observation is made for $\delta\phi_{M_1}$, so we have

$$\delta\phi_\mu^{\mathrm{div}} = 0, \quad \delta\phi_{M_1}^{\mathrm{div}} = 0. \qquad (4.89)$$

The phase renormalisation constants do not contain any UV divergent parts required to cancel with some other quantity to ensure the UV-finiteness of vertex functions involving neutralinos or charginos. We have confirmed that this is also true when $\tilde{\chi}_1^0$, $\tilde{\chi}_2^0$ and $\tilde{\chi}_2^\pm$ are replaced with some other choice of neutralinos and charginos in the renormalisation conditions. Accordingly, we will adopt in the following a scheme where the phases of M_1 and μ are left unrenormalised. We regard this as a more convenient choice than the "on-shell" scheme given above, which would have lead to non-zero $(\delta Z_{ii}^{L/R} - \delta \bar{Z}_{ii}^{L/R})$ for only four of the six fields. Also, even if at tree level one or all of the phases were zero, with the "on-shell" scheme this would not necessarily have been maintained at one-loop level; corrections to the phases could have been generated from another source of $\mathcal{CP}$-violation in the MSSM, such as a non-zero phase for the sfermion trilinear coupling. In the scheme where the phases are not renormalised, this will not occur and there will be no resulting confusion over what is meant by the physical phases. The phases remain at their tree-level value, whether it is zero or non-zero. It is only the renormalisation constants for the absolute values of the parameters which receive one-loop corrections.

Returning to the Born Lagrangians for charginos and neutralinos in Equations (2.30) and (2.32) respectively, it is not surprising that it is only the absolute values of M_1, M_2 and μ that need renormalising. M_1, M_2, μ appear in full along with any phases when

the Lagrangian is expressed in the gaugino-higgsino basis. However, in the mass eigenstate basis, it is only the real combinations, $U^* X V^\dagger = \mathrm{diag}(m_{\tilde{\chi}_1^+}, m_{\tilde{\chi}_2^+})$ and $N^* Y N^\dagger = \mathrm{diag}(m_{\tilde{\chi}_1^0}, m_{\tilde{\chi}_2^0}, m_{\tilde{\chi}_3^0}, m_{\tilde{\chi}_4^0})$, which appear. The elements of U, V and N contain phases which compensate the phases in M_1 and μ. However, they are mixing matrix elements and do not need to be not renormalised. It is these mixing matrix elements which appear in the couplings of neutralinos and charginos to other particles.

In the scheme where the phases are not renormalised, the conversion from the parameterisation in terms of absolute values and phases to the parameterisation in terms of real and imaginary parts simplifies to

$$\begin{aligned} \delta(\mathrm{Re}\ \mu) &= \delta|\mu| \cos\phi_\mu, & \delta(\mathrm{Im}\ \mu) &= \delta|\mu| \sin\phi_\mu, \\ \delta(\mathrm{Re}\ M_1) &= \delta|\mu| \cos\phi_{M_1}, & \delta(\mathrm{Im}\ M_1) &= \delta|\mu| \sin\phi_{M_1}. \end{aligned} \tag{4.90}$$

The condition for having the i'th neutralino mass on-shell given in Equation (4.60) can now be written as

$$\begin{aligned} N_{(i')} =& \delta|M_2| \cos\phi_{M_1} ((N^*_{i'1})^2 + N^2_{i'1}) + i\delta|M_2| \sin\phi_{M_1}, ((N^*_{i'1})^2 - N^2_{i'1}) \\ &+ \delta|M_2| ((N^*_{i'2})^2 + N^2_{i'2}) - 2\delta|\mu| \cos\phi_\mu (N^*_{i'3} N^*_{i'4} + N_{i'3} N_{i'4}) \\ &- 2i\delta|\mu| \sin\phi_\mu (N^*_{i'3} N^*_{i'4} - N_{i'3} N_{i'4}) \\ =& 2\delta|M_2| \,\mathrm{Re}(e^{-i\phi_{M_1}} N^2_{i'1}) + 2\delta|M_2| \,\mathrm{Re}(N^2_{i'2}) - 4\delta|\mu| \,\mathrm{Re}(e^{-i\phi_\mu} N_{i'3} N_{i'4}), \end{aligned} \tag{4.91}$$

while the condition for having the i''th chargino mass on-shell, given in Equation (4.58), can now be written as

$$\begin{aligned} C_{(i'')} &= \delta|M_2|(U^*_{i''1} V^*_{i''1} + V_{i''1} U_{i''1}) + \delta|\mu| \cos\phi_\mu (U^*_{i''2} V^*_{i''2} + V_{i''2} U_{i''2}) \\ &\quad + i\delta|\mu| \sin\phi_\mu (U^*_{i''2} V^*_{i''2} - V_{i''2} U_{i''2}) \qquad (4.92) \\ &= 2\delta|M_2| \,\mathrm{Re}(U_{i''1} V_{i''1}) + 2\delta|\mu| \,\mathrm{Re}(e^{-i\phi_\mu} U_{i''2} V_{i''2}). \qquad (4.93) \end{aligned}$$

$\tilde{\chi}_i^0$, $\tilde{\chi}_j^0$, $\tilde{\chi}_k^\pm$ on-shell

We first consider the case where we fix the masses of two neutralinos, $\tilde{\chi}_i^0$, $\tilde{\chi}_j^0$, and one chargino, $\tilde{\chi}_k^\pm$, on-shell. We solve Equation (4.91) with $i' = i, j$ and Equation (4.92) with

$i'' = k$ simultaneously to obtain,

$$\begin{aligned}
\delta|M_1| =&(2[\mathrm{Re}(e^{-i\phi_\mu} N_{i3}N_{i4})\,\mathrm{Re}(N_{j2}^2) - \mathrm{Re}(e^{-i\phi_{M_2}} N_{i2}^2)\,\mathrm{Re}(e^{-i\phi_\mu} N_{j3}N_{j4})]C_{(k)}\\
&+ [\mathrm{Re}(e^{-i\phi_\mu} U_{k2}V_{k2})\,\mathrm{Re}(N_{j2}^2) + 2\,\mathrm{Re}(U_{k1}V_{k1})\,\mathrm{Re}(e^{-i\phi_\mu} N_{i3}N_{i4})]N_{(i)} +\\
&- [\mathrm{Re}(e^{-i\phi_\mu} U_{k2}V_{k2})\,\mathrm{Re}(N_{i2}^2) + 2\,\mathrm{Re}(U_{k1}V_{k1})\,\mathrm{Re}(e^{-i\phi_\mu} N_{i3}N_{i4})]N_{(j)})/K,\\
\delta|M_2| =&(-2[\mathrm{Re}(e^{-i\phi_\mu} N_{i3}N_{i4})\,\mathrm{Re}(e^{-i\phi_{M_1}}\, N_{j1}^2) - \mathrm{Re}(e^{-i\phi_{M_1}}\, N_{i1}^2)\,\mathrm{Re}(e^{-i\phi_\mu} N_{j3}N_{j4})]C_{(k)}\\
&- \mathrm{Re}(e^{-i\phi_\mu} U_{k2}V_{k2})\,\mathrm{Re}(e^{-i\phi_{M_1}}\, N_{j1}^2)N_{(i)} + \mathrm{Re}(e^{-i\phi_\mu} U_{k2}V_{k2})\,\mathrm{Re}(e^{-i\phi_{M_1}} N_{i1}^2)N_{(j)})/K,\\
\delta|\mu| =&(-[\mathrm{Re}(N_{i2}^2)\,\mathrm{Re}(e^{-i\phi_{M_1}}\, N_{j1}^2) - \mathrm{Re}(e^{-i\phi_{M_1}}\, N_{i1}^2)\,\mathrm{Re}(N_{j2}^2)]C_{(k)}\\
&+ \mathrm{Re}(U_{k1}V_{k1})\,\mathrm{Re}(e^{-i\phi_{M_1}}\, N_{j1}^2)N_{(i)} - \mathrm{Re}(U_{k1}V_{k1})\,\mathrm{Re}(e^{-i\phi_{M_1}}\, N_{i1}^2)N_{(j)})/K
\end{aligned} \tag{4.94}$$

where

$$\begin{aligned}
K =&2\,\mathrm{Re}(e^{-i\phi_\mu} U_{k2}V_{k2})[-\mathrm{Re}(N_{i2}^2)\,\mathrm{Re}(e^{-i\phi_{M_1}}\, N_{j1}^2) + N_{i1}^2\,\mathrm{Re}(N_{j2}^2)]\\
&+ 4\,\mathrm{Re}(U_{k1}V_{k1})[-\mathrm{Re}(e^{-i\phi_\mu} N_{i3}N_{i4})\,\mathrm{Re}(e^{-i\phi_{M_1}} N_{j1}^2) + \mathrm{Re}(e^{-i\phi_{M_1}} N_{i1}^2)\,\mathrm{Re}(e^{-i\phi_\mu} N_{j3}N_{j4})].
\end{aligned} \tag{4.95}$$

$\tilde{\chi}_i^0$, $\tilde{\chi}_j^0$, $\tilde{\chi}_k^0$ on-shell

In order to fix the masses of three neutralinos, $\tilde{\chi}_i^0$, $\tilde{\chi}_j^0$, $\tilde{\chi}_k^0$, on-shell, we solve Equation (4.91) with $i' = i, j, k$ simultaneously to obtain,

$$\begin{aligned}
\delta|M_1| =&[(\mathrm{Re}(e^{-i\phi_\mu} N_{i3}N_{i4})\,\mathrm{Re}(N_{j2}^2) - \mathrm{Re}(e^{-i\phi_\mu} N_{j3}N_{j4})\,\mathrm{Re}(N_{i2}^2))N_{(k)}\\
&+ (\mathrm{Re}(e^{-i\phi_\mu} N_{j3}N_{j4})\,\mathrm{Re}(e^{-i\phi_{M_2}} N_{k2}^2) - \mathrm{Re}(e^{-i\phi_\mu} N_{k3}N_{k4})\,\mathrm{Re}(N_{j2}^2))N_{(i)}\\
&+ (\mathrm{Re}(e^{-i\phi_\mu} N_{k3}N_{k4})\,\mathrm{Re}(N_{i2}^2) - \mathrm{Re}(e^{-i\phi_\mu} N_{i3}N_{i4})\,\mathrm{Re}(N_{k2}^2))N_{(j)}]/L,
\end{aligned} \tag{4.96}$$

$$\begin{aligned}
\delta|M_2| =&[(\mathrm{Re}(e^{-i\phi_\mu} N_{j3}N_{j4})\,\mathrm{Re}(e^{-i\phi_{M_1}}\, N_{i1}^2) - \mathrm{Re}(e^{-i\phi_\mu} N_{i3}N_{i4})\,\mathrm{Re}(e^{-i\phi_{M_1}}\, N_{j1}^2))N_{(k)}\\
&+ (\mathrm{Re}(e^{-i\phi_\mu} N_{k3}N_{k4})\,\mathrm{Re}(e^{-i\phi_{M_1}}\, N_{j1}^2) - \mathrm{Re}(e^{-i\phi_\mu} N_{j3}N_{j4})\,\mathrm{Re}(e^{-i\phi_{M_1}}\, N_{k1}^2))N_{(i)}\\
&+ (\mathrm{Re}(e^{-i\phi_\mu} N_{i3}N_{i4})\,\mathrm{Re}(e^{-i\phi_{M_1}}\, N_{k1}^2) - \mathrm{Re}(e^{-i\phi_\mu} N_{k3}N_{k4})\,\mathrm{Re}(e^{-i\phi_{M_1}}\, N_{i1}^2))N_{(j)}]/L,
\end{aligned} \tag{4.97}$$

$$\begin{aligned}
\delta|\mu| =& -[(\mathrm{Re}(N_{i2}^2)\,\mathrm{Re}(e^{-i\phi_{M_1}}\, N_{j1}^2) - \mathrm{Re}(e^{-i\phi_{M_1}}\, N_{i1}^2)\,\mathrm{Re}(N_{j2}^2))N_{(k)}\\
&+ (\mathrm{Re}(N_{j2}^2)\,\mathrm{Re}(e^{-i\phi_{M_1}}\, N_{k1}^2) - \mathrm{Re}(e^{-i\phi_{M_1}}\, N_{k1}^2)\,\mathrm{Re}(N_{k2}^2))N_{(i)}\\
&+ (N_{i1}^2\,\mathrm{Re}(N_{k2}^2) - \mathrm{Re}(N_{i2}^2)\,\mathrm{Re}(e^{-i\phi_{M_1}}\, N_{k1}^2))N_{(j)}]/2L
\end{aligned} \tag{4.98}$$

where

$$\begin{aligned}L =&2[\mathrm{Re}(e^{-i\phi_\mu}N_{i3}N_{i4})\,\mathrm{Re}(N_{j2}^2)\,\mathrm{Re}(e^{-i\phi_{M_1}}N_{k1}^2)-\mathrm{Re}(N_{i2}^2)\,\mathrm{Re}(e^{-i\phi_\mu}N_{j3}N_{j4})\,\mathrm{Re}(e^{-i\phi_{M_1}}N_{k1}^2)\\&-\mathrm{Re}(e^{-i\phi_\mu}N_{i3}N_{i4})\,\mathrm{Re}(e^{-i\phi_{M_1}}N_{j1}^2)\,\mathrm{Re}(N_{k2}^2)+\mathrm{Re}(e^{-i\phi_{M_1}}N_{i1}^2)\,\mathrm{Re}(e^{-i\phi_\mu}N_{j3}N_{j4})\,\mathrm{Re}(N_{k2}^2)\\&+\mathrm{Re}(N_{i2}^2)\,\mathrm{Re}(e^{-i\phi_{M_1}}N_{j1}^2)\,\mathrm{Re}(e^{-i\phi_\mu}N_{k3}N_{k4})-\mathrm{Re}(e^{-i\phi_{M_1}}N_{i1}^2)\,\mathrm{Re}(N_{j2}^2)\,\mathrm{Re}(e^{-i\phi_\mu}N_{k3}N_{k4})].\end{aligned} \tag{4.99}$$

$\tilde{\chi}_i^0$, $\tilde{\chi}_j^+$, $\tilde{\chi}_k^\pm$ on-shell

In order to fix the masses of one neutralino $\tilde{\chi}_i^0$, and two chargino, $\tilde{\chi}_j^\pm$, $\tilde{\chi}_k^\pm$, on-shell, we solve Equation (4.91) with $i' = i$ and Equation (4.92) with $i'' = j, k$ simultaneously to obtain,

$$\begin{aligned}\delta|M_1| &= -[(2\,\mathrm{Re}(e^{-i\phi_\mu}N_{i3}N_{i4})\,\mathrm{Re}(U_{j1}V_{j1})+\mathrm{Re}(N_{i2}^2)\,\mathrm{Re}(e^{-i\phi_\mu}U_{j2}V_{j2}))C_{(k)}\\&\quad+(\mathrm{Re}(U_{j1}V_{j1})\,\mathrm{Re}(e^{-i\phi_\mu}U_{k2}V_{k2})-\mathrm{Re}(e^{-i\phi_\mu}U_{j2}V_{j2})\,\mathrm{Re}(U_{k1}V_{k1}))N_{(i)}\\&\quad-(\mathrm{Re}(N_{i2}^2)\,\mathrm{Re}(e^{-i\phi_\mu}U_{k2}V_{k2})+2\,\mathrm{Re}(e^{-i\phi_\mu}N_{i3}N_{i4})\,\mathrm{Re}(U_{k1}V_{k1}))C_{(j)}]\\&\quad/(\mathrm{Re}(e^{-i\phi_{M_1}}N_{i1}^2)M), \qquad (4.100)\\ \delta|M_2| &= [\mathrm{Re}(e^{-i\phi_\mu}U_{j2}V_{j2})C_{(k)}-\mathrm{Re}(e^{-i\phi_\mu}U_{k2}V_{k2})C_{(j)}]/M, \qquad (4.101)\\ \delta|\mu| &= -[\mathrm{Re}(U_{j1}V_{j1})C_{(k)}-\mathrm{Re}(U_{k1}V_{k1})C_{(j)}]/M \qquad (4.102)\end{aligned}$$

where

$$M = 2(\mathrm{Re}(U_{k1}V_{k1})\,\mathrm{Re}(e^{-i\phi_\mu}U_{j2}V_{j2})-\mathrm{Re}(U_{j1}V_{j1})\,\mathrm{Re}(e^{-i\phi_\mu}U_{k2}V_{k2})). \tag{4.103}$$

4.4.3 Comparing parameter renormalisation schemes: a toy model

In the previous sections, we derived several different schemes for on-shell parameter renormalisation in the chargino–neutralino sector for real and complex parameters. The expressions for the parameter counterterms depended on which three of the six particle masses were placed on-shell. Using the same tree-level values for the parameters, combined with the different values of the counterterms, these different schemes result in different physical (loop-corrected) values for the parameters. In order to be able to compare between different renormalisation schemes, one should consider the same phys-

ical situation; that is, the same physical masses, and in order to do this one may require different values for the tree-level parameters.

To help us understand the difference between the required input parameters to achieve the same physical situation when different combinations of neutralino and chargino masses are on-shell, we perform a comparison in a toy renormalisation scheme as follows. We consider the simplified no-mixing case, where M_W is set to zero in the neutralino and chargino mass matrices. We also assume $M_1 < M_2 < \mu$ are real and positive. Then at tree level, the masses are given by

$$m_{\tilde{\chi}_1^0} = M_1, \quad m_{\tilde{\chi}_2^0} = M_2 = m_{\tilde{\chi}_1^\pm}, \quad m_{\tilde{\chi}_2^\pm} = \mu = m_{\tilde{\chi}_3^0} = m_{\tilde{\chi}_4^0}. \tag{4.104}$$

Using Equation (4.55) under the above assumptions, the one-loop mass corrections are found to be

$$\begin{aligned}
\Delta m_{\tilde{\chi}_1^0} =& m_{\tilde{\chi}_1^0}\mathrm{Re}\Sigma^L_{0,11}(m^2_{\tilde{\chi}_1^0}) + \mathrm{Re}\Sigma^{SL}_{0,11}(m^2_{\tilde{\chi}_1^0}) - \delta M_1,\\
\Delta m_{\tilde{\chi}_2^0} =& m_{\tilde{\chi}_2^0}\mathrm{Re}\Sigma^L_{0,22}(m^2_{\tilde{\chi}_2^0}) + \mathrm{Re}\Sigma^{SL}_{0,22}(m^2_{\tilde{\chi}_2^0}) - \delta M_2,\\
\Delta m_{\tilde{\chi}_3^0} =& m_{\tilde{\chi}_3^0}\mathrm{Re}\Sigma^L_{0,33}(m^2_{\tilde{\chi}_3^0}) + \mathrm{Re}\Sigma^{SL}_{0,33}(m^2_{\tilde{\chi}_3^0}) - \delta \mu,\\
\Delta m_{\tilde{\chi}_4^0} =& m_{\tilde{\chi}_4^0}\mathrm{Re}\Sigma^L_{0,44}(m^2_{\tilde{\chi}_4^0}) + \mathrm{Re}\Sigma^{SL}_{0,44}(m^2_{\tilde{\chi}_4^0}) - \delta \mu,\\
\Delta m_{\tilde{\chi}_1^\pm} =& \frac{m_{\tilde{\chi}_1^\pm}}{2}\mathrm{Re}(\Sigma^L_{-,11} + \Sigma^R_{-,11})(m^2_{\tilde{\chi}_1^\pm}) + \mathrm{Re}\Sigma^{SL}_{-,11}(m^2_{\tilde{\chi}_1^\pm}) - \delta M_2,\\
\Delta m_{\tilde{\chi}_2^\pm} =& \frac{m_{\tilde{\chi}_2^\pm}}{2}\mathrm{Re}(\Sigma^L_{-,22} + \Sigma^R_{-,22})(m^2_{\tilde{\chi}_2^\pm}) + \mathrm{Re}\Sigma^{SL}_{-,22}(m^2_{\tilde{\chi}_2^\pm}) - \delta \mu.
\end{aligned} \tag{4.105}$$

The tree-level masses, $m_{\tilde{\chi}_i}$, still satisfy the relations in Equation (4.104), while the loop-level masses, $M_{\tilde{\chi}_i}$, in general, do not satisfy these relations.

Toy Scheme (1): $\tilde{\chi}_1^0$, $\tilde{\chi}_2^0$, $\tilde{\chi}_3^0$ on-shell

If the masses of $\tilde{\chi}_1^0$, $\tilde{\chi}_2^0$, $\tilde{\chi}_3^0$ are chosen to be on-shell, then the renormalisation constants are given by

$$\delta M_1^{(1)} = m_{\tilde{\chi}_1^0}\mathrm{Re}\Sigma^L_{11}(m^2_{\tilde{\chi}_1^0}) + \mathrm{Re}\Sigma^{SL}_{11}(m^2_{\tilde{\chi}_1^0}), \tag{4.106}$$

$$\delta M_2^{(1)} = m_{\tilde{\chi}_2^0}\mathrm{Re}\Sigma^L_{22}(m^2_{\tilde{\chi}_2^0}) + \mathrm{Re}\Sigma^{SL}_{22}(m^2_{\tilde{\chi}_2^0}), \tag{4.107}$$

$$\delta \mu^{(1)} = m_{\tilde{\chi}_3^0}\mathrm{Re}\Sigma^L_{33}(m^2_{\tilde{\chi}_3^0}) + \mathrm{Re}\Sigma^{SL}_{33}(m^2_{\tilde{\chi}_3^0}). \tag{4.108}$$

The loop-corrected masses obey the relations;

$$\begin{aligned} &M_{\tilde{\chi}_1^0} = M_1, && M_{\tilde{\chi}_2^0} = M_2, && M_{\tilde{\chi}_3^0} = \mu, \\ &M_{\tilde{\chi}_4^0} = M_{\tilde{\chi}_3^0} - \Delta m_{34}^{00}, && M_{\tilde{\chi}_1^\pm} = M_{\tilde{\chi}_2^0} + \Delta m_{12}^{+0}, && M_{\tilde{\chi}_2^\pm} = M_{\tilde{\chi}_3^0} + \Delta m_{23}^{+0} \end{aligned} \tag{4.109}$$

where the quantities, $\Delta m_{34}^{00} \equiv \Delta m_{\tilde{\chi}_3^0} - \Delta m_{\tilde{\chi}_4^0}$, $\Delta m_{12}^{+0} \equiv \Delta m_{\tilde{\chi}_1^\pm} - \Delta m_{\tilde{\chi}_2^0}$ and $\Delta m_{23}^{+0} \equiv \Delta m_{\tilde{\chi}_2^\pm} - \Delta m_{\tilde{\chi}_3^0}$, depend only on a finite combination of self-energies and tree-level masses in this case. The masses of $M_{\tilde{\chi}_4^0}$, $M_{\tilde{\chi}_1^\pm}$ and $M_{\tilde{\chi}_2^\pm}$ are determined by the input parameters, $M_{\tilde{\chi}_1^0}$, $M_{\tilde{\chi}_2^0}$ and $M_{\tilde{\chi}_3^0}$, along with these computable quantities.

Toy Scheme (2): $\tilde{\chi}_1^0$, $\tilde{\chi}_2^0$, $\tilde{\chi}_2^\pm$ on-shell

If the masses of $\tilde{\chi}_1^0$, $\tilde{\chi}_2^0$, $\tilde{\chi}_2^\pm$ are chosen to be on-shell, then the renormalisation constants are given by

$$\delta M_1^{(2)} = m_{\tilde{\chi}_1^0} \mathrm{Re}\Sigma_{0,11}^L(m_{\tilde{\chi}_1^0}^2) + \mathrm{Re}\Sigma_{0,11}^{SL}(m_{\tilde{\chi}_1^0}^2), \tag{4.110}$$

$$\delta M_2^{(2)} = m_{\tilde{\chi}_2^0} \mathrm{Re}\Sigma_{0,22}^L(m_{\tilde{\chi}_2^0}^2) + \mathrm{Re}\Sigma_{0,22}^{SL}(m_{\tilde{\chi}_2^0}^2), \tag{4.111}$$

$$\delta \mu^{(2)} = \frac{1}{2} m_{\tilde{\chi}_2^\pm} \mathrm{Re}(\Sigma_{-,22}^L + \Sigma_{-,22}^R)(m_{\tilde{\chi}_2^\pm}^2) + \mathrm{Re}\Sigma_{22}^{-,SL}(m_{\tilde{\chi}_2^\pm}^2) \tag{4.112}$$

with the loop-corrected masses satisfying the relations;

$$\begin{aligned} &M_{\tilde{\chi}_1^0} = M_1, && M_{\tilde{\chi}_2^0} = M_2, && M_{\tilde{\chi}_2^\pm} = \mu, \\ &M_{\tilde{\chi}_1^\pm} = M_{\tilde{\chi}_2^0} + \Delta m_{12}^{+0}, && M_{\tilde{\chi}_3^0} = M_{\tilde{\chi}_2^\pm} - \Delta m_{23}^{+0}, && M_{\tilde{\chi}_4^0} = M_{\tilde{\chi}_2^\pm} - \Delta m_{24}^{+0}. \end{aligned} \tag{4.113}$$

where $\Delta m_{24}^{+0} \equiv \Delta m_{\tilde{\chi}_2^\pm} - \Delta m_{\tilde{\chi}_4^0}$.

Comparing Toy Schemes (1) and (2)

The value of $\delta\mu$ in Toy Scheme (1) is different to its value in Toy Scheme (2) by a finite combination of self-energies;

$$\delta\mu^{(2)} - \delta\mu^{(1)} = \Delta m_{23}^{+0} \tag{4.114}$$

Suppose we have $M_1 = 100\,\text{GeV}$, $M_2 = 200\,\text{GeV}$ and $\mu = 400\,\text{GeV}$ and we start from Toy Scheme (1) with three neutralinos on-shell. Then;

$$\begin{aligned} &M_{\tilde{\chi}_1^0} = 100\,\text{GeV}, && M_{\tilde{\chi}_2^0} = 200\,\text{GeV}, && M_{\tilde{\chi}_3^0} = 400\,\text{GeV}, \\ &M_{\tilde{\chi}_4^0} = 400\,\text{GeV} - \Delta m_{34}^{00}, && M_{\tilde{\chi}_1^\pm} = 200\,\text{GeV} + \Delta m_{12}^{+0}, && M_{\tilde{\chi}_2^\pm} = 400\,\text{GeV} + \Delta m_{23}^{+0}. \end{aligned} \tag{4.115}$$

In order to compare the two schemes for the same physical situation, we need the same set of physical masses in scheme (2). For the three input masses, we choose

$$\begin{aligned} M_{\tilde{\chi}_1^0} &= 100\,\text{GeV} = M_1, \\ M_{\tilde{\chi}_2^0} &= 200\,\text{GeV} = M_2, \\ M_{\tilde{\chi}_2^\pm} &= 400\,\text{GeV} - \Delta m_{23}^{+0} = \mu. \end{aligned} \tag{4.116}$$

From the relations it follows that

$$\begin{aligned} M_{\tilde{\chi}_1^\pm} &= 200\,\text{GeV} + \Delta m_{12}^{+0}, \\ M_{\tilde{\chi}_3^0} &= 400\,\text{GeV} + \Delta m_{23}^{+0} - \Delta m_{23}^{+0} = 400\,\text{GeV}, \\ M_{\tilde{\chi}_4^0} &= 400\,\text{GeV} + \Delta m_{23}^{+0} - \Delta m_{24}^{+0} = 400\,\text{GeV} - \Delta m_{34}^{00}. \end{aligned} \tag{4.117}$$

So in the end, the same set of six physical masses are achieved. The tree-level values of M_1 and M_2 are still 100 GeV and 200 GeV, while the tree-level value of μ is now $\mu^{(2)} = 400\,\text{GeV} - \Delta m_{23}^{+0}$. Using Equation (4.114), it can be shown that once the corresponding counterterms are taken into account, the resulting one-loop corrected values of μ are identical. This would not be necessary in a more general situation, where μ does not directly correspond to one of the mass values. In this toy model, it is relatively simple to choose the same physical situation in each parameter renormalisation scheme. For the more general case, it is technically much more difficult to find input parameters which give the same six physical masses in different schemes since the loop corrections to those masses will have a non-trivial dependence on the input parameters.

Another issue with comparing parameter renormalisation schemes is that not all schemes work equally well for every MSSM scenario. In general, one single scheme is not expected to be suitable for the whole MSSM parameter range. In the toy schemes above with $M_1 < M_2 < \mu$, we could not have used $M_{\tilde{\chi}_1^0}$, $M_{\tilde{\chi}_2^0}$ and $M_{\tilde{\chi}_1^\pm}$ as input because there would have been no way of fixing $\delta\mu$. Similarly, if we were to choose a different parameter hierarchy with $\mu < M_1, M_2$, then the toy schemes given above would not work because only one of M_1 or M_2 could be fixed by the choice of input masses. Nevertheless, for the

more general case, when the terms depending on M_W are restored in the mass matrices, a priori it looks feasible to choose $M_{\tilde{\chi}^0_1}$, $M_{\tilde{\chi}^0_2}$ and $M_{\tilde{\chi}^\pm_1}$ as input for $M_1 < M_2 < \mu$, but one may encounter severe numerical instabilities in such a case. We will investigate this further in the next section, where we show a numerical comparison between the schemes for different scenarios and the resulting one-loop mass corrections.

4.5 Comparing renormalisation schemes: Numerical results

4.5.1 Field renormalisation

In Section 4.2, we pointed out that, in the MSSM with $\mathcal{CP}$-violating parameters, absorptive parts of loop integrals for unstable particles can enter the squared matrix element for processes at the one-loop level. In order to ensure the external particles have the correct on-shell properties in this case, we use a general scheme with separate field renormalisation constants for incoming and outgoing fermions.

In Table 4.1, we show the finite parts of the neutralino field renormalisation constants for the CPX scenario. In the first row, they are computed in the general scheme of Section 4.2.1, where absorptive parts of loop integrals are included in the field renormalisation constants, while in the second row the absorptive parts are discarded, as in Section 4.2.2. The table shows that the numerical differences between the two procedures are not significant for the constants involving only the two light neutralinos. However, the absorptive effects are large for $\delta Z^L_{0,13}$ and $\delta Z^L_{0,14}$, since, in this scenario, all two-body decays for $\tilde{\chi}^0_3$ and $\tilde{\chi}^0_4$ are kinematically open.

In Figure 4.1(a), we show the imaginary parts of the field renormalisation constants involving the third lightest neutralino, as a function of ϕ_{A_t} for the CPV1 scenario, defined in Table 2.3. In this scenario, $\tilde{\chi}^0_3$ has a mass of around 505 GeV, and can decay into the lighter third generation squarks, so phases introduced in the squark sector can be expected to play a role for the imaginary parts of the $\tilde{\chi}^0_3$ self-energies. The solid lines show the renormalisation constants in the general scheme, including absorptive effects, while for the dashed lines, these absorptive parts are discarded. We see that there is a sizeable difference between the dashed and solid curves. As discussed in Section 4.2.3, the absorptive parts in the field renormalisation constants do not contribute to

$\delta Z^L_{0,11}/10^{-2}$	$\delta Z^L_{0,12}/10^{-2}$	$\delta Z^L_{0,13}/10^{-2}$	$\delta Z^L_{0,14}/10^{-2}$
1.5346+0.9622 i	0.2550+0.1914 i	-0.1251+1.7108i	-0.0134-0.1890i
$\delta \tilde{Z}^0_{11}/10^{-2}$	$\delta \tilde{Z}^0_{12}/10^{-2}$	$\delta \tilde{Z}^0_{13}/10^{-2}$	$\delta \tilde{Z}^0_{14}/10^{-2}$
1.5346+0.9622 i	0.2550+0.1911i	-0.0425+0.0878i	-0.0887+0.0383 i

Table 4.1: Comparison of neutralino field renormalisation constants in the general scheme with absorptive parts of Section 4.2.1, and then taking $\widetilde{\text{Re}}$ of those values (indicated by a tilde), as in Section 4.2.2, for the CPX scenario with $M_{H^\pm} = 135.7\,\text{GeV}$ and $\tan\beta = 5.5$. In order to evaluate the terms involving δM_1, δM_1 and $\delta\mu$, we use the parameter renormalisation scheme where the masses of $\tilde{\chi}^0_1$, $\tilde{\chi}^0_2$ and $\tilde{\chi}^\pm_2$ are on-shell.

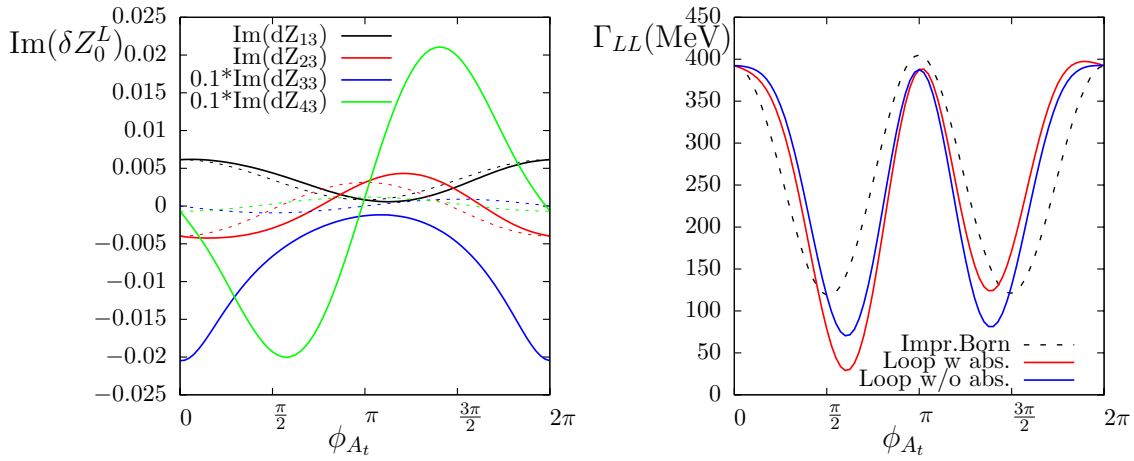

(a) (b)

Figure 4.1: (a) Imaginary parts of field renormalisation constants, δZ^L_{i3}, for $i = 1, 2, 3, 4$ (black, red, blue, green respectively) in the CPV1 scenario, defined in Table 2.3, as a function of ϕ_{A_t}. The solid curves show the full field renormalisation constants, while in the dashed curves, the absorptive parts of loop integrals are discarded. (b) Partial decay width, $\Gamma_{LL} \equiv \Gamma(h_2 \to \tilde{\chi}^{0\,L}_3 \tilde{\chi}^{0\,L}_2)$, into left-handed neutralinos in the CPV1 scenario, as a function of ϕ_{A_t}. The black dashed curve is the Improved Born result; the blue and red curves show the incorporation of one-loop vertex corrections without and with absorptive parts in the field renormalisation constants respectively. For both plots, in order to evaluate the terms involving δM_1, δM_1 and $\delta\mu$, we use the parameter renormalisation scheme where the masses of $\tilde{\chi}^0_1$, $\tilde{\chi}^0_2$ and $\tilde{\chi}^0_3$ are on-shell.

spin-summed squared matrix elements for Majorana neutralinos. They do contribute, however, to spin-dependent squared matrix elements. In Figure 4.1(b), we show their effect on the partial decay width of a heavy Higgs boson into left-handed neutralinos, $\Gamma_{LL} \equiv \Gamma(h_2 \to \tilde{\chi}^{0\,L}_3 \tilde{\chi}^{0\,L}_2)$, again in the CPV1 scenario, as a function of ϕ_{A_t}. The black

dashed curve shows the Improved Born decay width.[3] The blue curve includes the one-loop vertex corrections, discarding the effects of absorptive parts of loop integrals in the field renormalisation constants. The red curve includes the one-loop vertex corrections, using the general field renormalisation constants with absorptive parts. We see that the difference between the latter two curves can be sizeable when the $\mathcal{CP}$-violating phase is large. The absorptive parts can enhance or suppress the effect of the one-loop vertex corrections relative to the Improved Born level result. Thus, a proper treatment of absorptive parts in one-loop calculations involving neutralinos in the complex MSSM is crucial. If one were to use the field renormalisation constants containing $\widetilde{\mathrm{Re}}$, as in Section 4.2.2 or as in the blue curve of Figure 4.1(b), without separately taking into account the products of the absorptive contributions and imaginary parameters, then the calculation would be incomplete. In order to ensure the correct on-shell properties of external fermions, we adopt the general scheme given in Section 4.2.1 for the rest of this thesis.

4.5.2 Parameter renormalisation

As discussed in Section 4.4, we have implemented three schemes for the parameter renormalisation in the neutralino-chargino sector; with either three neutralinos, two neutralinos and one chargino, or two charginos and one neutralino on-shell. As seen with the toy model in the previous section, not all schemes are expected to work equally well for every given scenario in the MSSM. In Table 4.2 we show the finite parts of $\delta|M_1|$, $\delta|M_2|$ and $\delta|\mu|$ in the CPX scenario with $M_{H^\pm} = 132.1\,\mathrm{GeV}$ and $\tan\beta = 5.5$, for five different choices of parameter renormalisation; NNN with $\tilde{\chi}^0_1$, $\tilde{\chi}^0_2$ and $\tilde{\chi}^0_3$ on-shell; NNC with $\tilde{\chi}^0_1$, $\tilde{\chi}^0_2$ and $\tilde{\chi}^\pm_2$ on-shell, NNCb with $\tilde{\chi}^0_1$, $\tilde{\chi}^0_2$ and $\tilde{\chi}^\pm_1$ on-shell, NCC with $\tilde{\chi}^0_1$, $\tilde{\chi}^\pm_1$ and $\tilde{\chi}^\pm_2$ on-shell, NCCb with $\tilde{\chi}^0_2$, $\tilde{\chi}^\pm_1$ and $\tilde{\chi}^\pm_2$ on-shell, and NCCc, with $\tilde{\chi}^0_3$, $\tilde{\chi}^\pm_1$ and $\tilde{\chi}^\pm_2$ on-shell. We also show the resulting one-loop corrections to the remaining masses. We see that NNN, NNC and NCC work equally well, all giving similar values for $\delta|M_1|$, $\delta|M_2|$ and $\delta|\mu|$ and modest corrections to the masses. However, NNCb gives a very large value for $\delta|\mu|$, while NCCb and NCCc give very large values for $\delta|M_1|$ respectively. This is due to the fact that the CPX scenario has the gauge parameter hierarchy $M_1 < M_2 \ll \mu$, where the mass of $m_{\tilde{\chi}^0_1}$ is closest to $|M_1|$, $m_{\tilde{\chi}^0_2}$ and $m_{\tilde{\chi}^\pm_1}$ are close to $|M_2|$, and $m_{\tilde{\chi}^0_{3,4}}$ and $m_{\tilde{\chi}^\pm_2}$ are close to $|\mu|$. Consequently, if we do not use one of $m_{\tilde{\chi}^0_{3,4}}$ or $m_{\tilde{\chi}^\pm_2}$ as input, there is only a weak fixing of $|\mu|$. The value of its counterterm will be driven to unphysically

[3] See Chapter 5 for a full description of the method used to calculate decay widths in the Improved Born approximation and to include the one-loop vertex corrections.

large values by numerical instabilities. These instabilities also manifest themselves in the corresponding one loop corrections to the masses. Similarly, if we do not use $m_{\tilde{\chi}_1^0}$ as input, there is only a weak fixing of $|M_1|$. Thus the NNN, NNC and NCC schemes are the most numerically stable choices for the parameter hierarchy of $|M_1| < |M_2| \ll |\mu|$. This is known as a gaugino-like scenario, as the lighter neutralinos and charginos are mostly gaugino. However, for a different hierarchy, a different choice may be more favourable. In the last two columns, we show the finite parts of the parameter renormalisation constants and the one-loop mass corrections for a higgsino-like scenario, with $|\mu| < |M_1| < |M_2|$. We set $\mu = 200\,\text{GeV}$, $M_2 = 1000\,\text{GeV}$, $M_1 = (5/3)(s_W^2/c_W^2)M_2$ and all other parameters the same as for the CPX scenario. For this parameter hierarchy, the masses of $m_{\tilde{\chi}_{1,2}^0}$ and $m_{\tilde{\chi}_1^\pm}$ are closest to $|\mu|$, $m_{\tilde{\chi}_3^0}$ is closest to $|M_1|$ and $m_{\tilde{\chi}_2^\pm}$ and $m_{\tilde{\chi}_4^0}$ are close to $|M_2|$. We see that the NCCb scheme does not give numerically stable results, because $|M_1|$ is only weakly fixed. The NCCc scheme, however, where the mass of the $\tilde{\chi}_3^0$ is fixed on-shell, works well for this higgsino-like scenario.

	NNN	NNC	NNCb	NCC	NCCb	NCCc	NCCb*	NCCc*
$\delta\|M_1\|$	-1.468	-1.465	2.981	-1.468	2518.7	-3684.6	-355.6	-4.642
$\delta\|M_2\|$	-9.265	-9.265	9.704	-9.410	-9.410	-9.410	10.683	10.683
$\delta\|\mu\|$	-18.494	-18.996	-20944.2	-18.996	-18.996	-18.996	-5.136	-5.136
$\Delta m_{\tilde{\chi}_1^0}$	0	0	0	0	2518.8	-3681.1	-11.44	-0.636
$\Delta m_{\tilde{\chi}_2^0}$	0	0	0	-0.1446	0	0.356	0	-0.671
$\Delta m_{\tilde{\chi}_3^0}$	0	-0.5012	-20913.8	-0.5016	-0.8446	0	-339.5	0
$\Delta m_{\tilde{\chi}_4^0}$	0.3237	-0.1775	-20890.0	-0.1775	0.6851	-1.439	-0.0794	-0.0328
$\Delta m_{\tilde{\chi}_1^\pm}$	0.1446	0.1445	0	0	0	0	0	0
$\Delta m_{\tilde{\chi}_2^\pm}$	0.5012	0	-20888.0	0	0	0	0	0

Table 4.2: Finite parts of parameter renormalisation constants and mass corrections in GeV for the CPX scenario with $M_{H^\pm} = 132.1\,\text{GeV}$ and $\tan\beta = 5.5$ using the different parameter renormalisation schemes defined in the text. The last two columns, denoted with an asterisk, show the results for a higgsino-like scenario, with $\mu = 200\,\text{GeV}$, $M_1 = (5/3)(s_W^2/c_W^2)M_2$ and $M_2 = 1000\,\text{GeV}$, and all other parameters the same as the CPX scenario.

In Figure 4.2, we show the variation of the one-loop mass corrections in the NNC scheme, where the masses of $\tilde{\chi}_{1,2}^0$ and $\tilde{\chi}_2^\pm$ are fixed on shell. The masses of masses of $\tilde{\chi}_{3,4}^0$ and $\tilde{\chi}_1^\pm$ receive corrections. Figure 4.2(a) shows the mass corrections for the CPX scenario with $M_{H^\pm} = 132.1\,\text{GeV}$ as a function of $\tan\beta$. We see that the corrections remain modest,

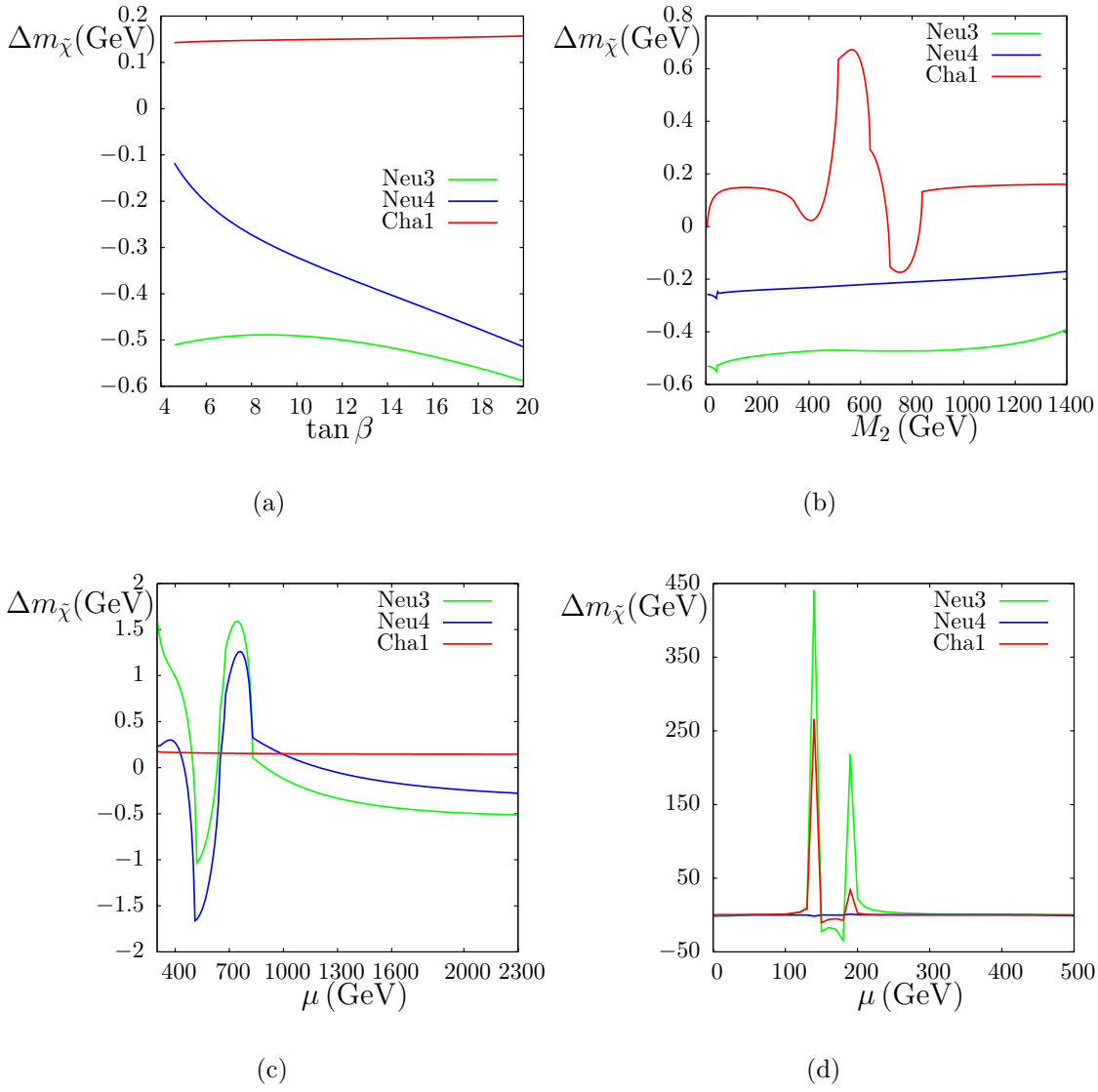

Figure 4.2: One loop corrections to the neutralino and chargino masses in the NNC scheme for the CPX scenario with $M_{H^\pm} = 132.1\,\text{GeV}$; (a) as a function of $\tan\beta$, (b) as a function of M_2 with $\tan\beta = 7$, (c,d) as a function of μ with $\tan\beta = 7$, with all other parameters as in Table 2.3.

much less than 1 GeV for the range of $\tan\beta$ shown. In Figure 4.2(b), we show the mass corrections as a function of M_2 with $\tan\beta = 7$. We see that the $\tilde{\chi}_1^\pm$ mass is affected by thresholds for quark-squark pair production between 300 and 800 GeV. Similarly, in Figure 4.2(c), where the mass corrections are shown as a function of μ with $\tan\beta = 7$, the $\tilde{\chi}_{3,4}^0$ masses are affected by thresholds below 800 GeV. In Figure 4.2(d), we lower μ further and see that near $\mu = M_2$, there is a pole in the renormalisation constants,

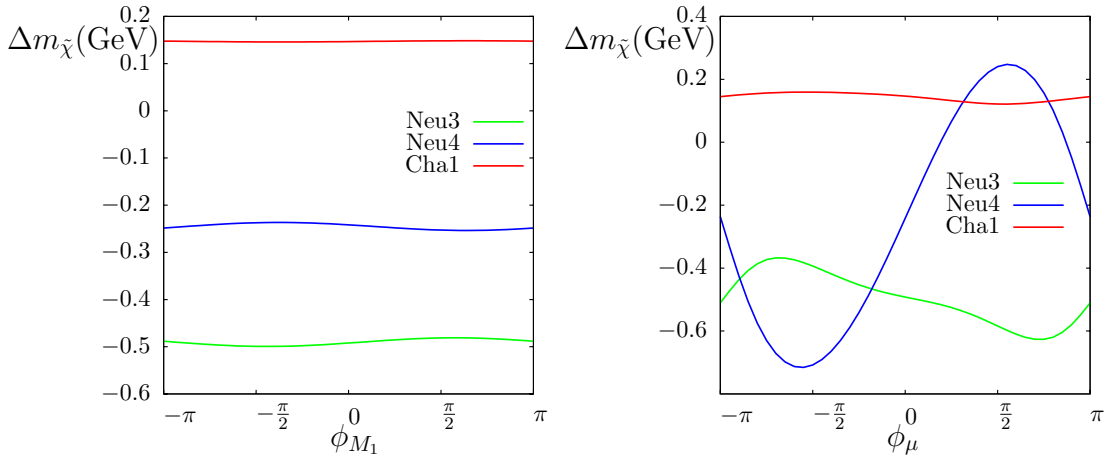

Figure 4.3: One loop corrections to the neutralino and chargino masses in the NNC scheme for the CPX scenario with $M_{H^\pm} = 132.1\,\text{GeV}$ and $\tan\beta = 7$, (a) as a function of ϕ_{M_1}, (b) as a function of ϕ_μ, with all other parameters as in Table 2.3.

where the quantity K, defined in Equation (4.70), vanishes. In this parameter region the renormalisation scheme produces unphysically large values for the mass correction.

In Figures 4.3(a) and 4.3(b) respectively, we show the dependence of the one-loop mass corrections on the phases ϕ_{M_1} and ϕ_μ, again for the CPX scenario in the NNC scheme. We see that the dependence on ϕ_{M_1} is only slight because $|M_1|$ is fixed by $m_{\tilde{\chi}_1^0}$, while the other masses do not have a strong dependence on its value. Conversely, the neutralino masses do have a strong dependence on ϕ_μ since their tree-level values lie at the scale of $|\mu|$, while the value of $|\mu|$ is fixed by the heavy chargino mass.

For most of this thesis, we examine scenarios with a gaugino-like parameter hierarchy, $|M_1| < |M_2| < |\mu|$. Therefore, we will use the NNC parameter renormalisation scheme, where the masses of $\tilde{\chi}_1^0$, $\tilde{\chi}_2^0$ and $\tilde{\chi}_2^\pm$ are fixed on-shell, unless otherwise stated.

Chapter 5

Calculation of vertex corrections

In this chapter we give a detailed description of our method for calculating higher order corrections to two-body decays involving particles from the MSSM with complex parameters. We focus in particular on the class of processes with two neutralinos and one Higgs boson, $\tilde{\chi}_i^0 \to \tilde{\chi}_j^0 h_a$ and $h_a \to \tilde{\chi}_i^0 \tilde{\chi}_j^0$, but we have also studied other processes, which we will discuss in Section 5.6. We begin in Section 5.1 by studying the $\tilde{\chi}_i^0 \tilde{\chi}_j^0 h_k^0$ vertex and its associated decay widths at tree-level. In Section 5.2, we use the renormalisation constants derived in the previous chapters to construct a counterterm for this three-point vertex. In Section 5.3, the counterterm is combined with the one-loop triangle diagrams to obtain the renormalised 1PI $\tilde{\chi}_i^0 \tilde{\chi}_j^0 h_k^0$ vertex function at one-loop, taking into account the contributions from all MSSM particles. In Section 5.4 we combine the genuine 1PI vertex contributions with the one-loop propagator-type corrections for the Higgs boson to construct the renormalised one-loop $\tilde{\chi}_i^0 \tilde{\chi}_j^0 h_a$ vertex for on-shell h_a. We also include the reducible self-energy diagrams involving mixing of the neutral Higgs bosons with the Goldstone and Z bosons. In Section 5.5 we show how we combine our full one-loop results with the state-of-the-art two-loop propagator-type corrections from the Higgs sector, obtaining the currently most precise prediction for this class of processes.

5.1 Tree-level decay width

We consider the $\tilde{\chi}_i^0 \tilde{\chi}_j^0 h_k^0$ vertex, shown in Figure 5.1(a), where $i, j = 1, 2, 3, 4$ and k labels neutral Higgs bosons, i.e. $h_k^0 = \{h, H, A, G\}$. For the interaction of neutralinos with neutral Higgs bosons, the relevant piece of the Lagrangian can be written in terms of

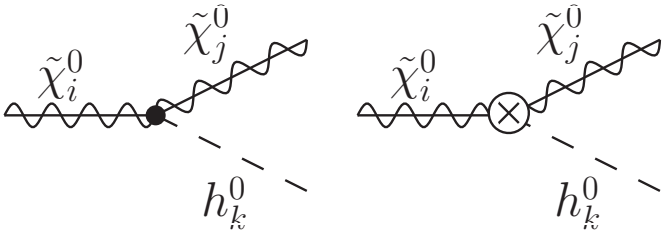

(a) (b)

Figure 5.1: (a) The tree-level neutralino-neutralino-Higgs vertex and (b) its counterterm.

tree-level mass eigenstates as

$$\mathcal{L} = \frac{i}{2}\, h_k^0\, \overline{\tilde{\chi}_i^0}\, [\omega_R C^R_{ijh_k^0} + \omega_L (-1)^{\delta_{k3}} (-1)^{\delta_{k4}} C^L_{ijh_k^0}]\, \tilde{\chi}_j^0, \tag{5.1}$$

where $\omega_{R/L} = \frac{1}{2}(1 \pm \gamma_5)$. A minus sign appears between the ω_R and ω_L terms for the $\mathcal{CP}$-odd Higgs states. The couplings, $C^{R/L}_{ijh_k^0}$, are given by

$$C^R_{ijh_k^0} = C^{L^*}_{ijh_k^0} = \frac{e}{2 c_W s_W} c_{ijh_k^0}, \tag{5.2}$$

where

$$\begin{aligned} c_{ijh_k^0} &= [(a_k N_{i3} + b_k N_{i4})(s_W N_{j1} - c_W N_{j2}) + (a_k N_{j3} + b_k N_{j4})(s_W N_{i1} - c_W N_{i2})], \\ a_k &= \{-s_\alpha, c_\alpha, i s_{\beta_n}, -i c_{\beta_n}\}, \\ b_k &= \{-c_\alpha, -s_\alpha, -i c_{\beta_n}, -i s_{\beta_n}\}. \end{aligned} \tag{5.3}$$

The quantity in the square brackets in Equation (5.1) is the three-point vertex function at tree level;

$$\Gamma^{\text{tree}}_{\tilde{\chi}_i^0 \tilde{\chi}_j^0 h_k^0} \equiv \omega_R C^R_{ijh_k^0} + \omega_L (-1)^{\delta_{k3}} (-1)^{\delta_{k4}} C^L_{ijh_k^0}. \tag{5.4}$$

where $\delta_{k3(4)} = 1$ for $k = 3(4)$ and zero otherwise. The tree-level decay width $\Gamma^{\text{tree}}_{\tilde{\chi}_i^0 \to \tilde{\chi}_j^0 h_k^0}$ for the two-body decay $\tilde{\chi}_i^0 \to \tilde{\chi}_j^0 h_k^0$, where $h_k^0 = \{h, H, A\}$, can then be written as

$$\Gamma^{\text{tree}}_{\tilde{\chi}_i^0 \to \tilde{\chi}_j^0 h_k^0} = \frac{1}{16\pi m^3_{\tilde{\chi}_i^0}} |C^R_{ijh_k^0}|^2\, \kappa(m^2_{\tilde{\chi}_i^0}, m^2_{\tilde{\chi}_j^0}, m^2_{h_k^0})\, [m^2_{\tilde{\chi}_i^0} + m^2_{\tilde{\chi}_j^0} - m^2_{h_k^0} + 2(-1)^{\delta_{k3}} m_{\tilde{\chi}_i^0} m_{\tilde{\chi}_j^0}], \tag{5.5}$$

and

$$\kappa(x,y,z) = ((x^2-y^2-z^2)^2 - 4yz)^{1/2}. \tag{5.6}$$

Similarly, the tree-level decay width $\Gamma^{\rm tree}_{h_k^0}$ for the two-body decay $h_k^0 \to \tilde{\chi}_i^0\tilde{\chi}_j^0$, where $h_k^0 = \{h, H, A\}$, can be written as

$$\Gamma^{\rm tree}_{h_k^0\to\tilde{\chi}_i^0\tilde{\chi}_j^0} = \frac{1}{8\pi m^3_{h_k^0}} |C^R_{ijh_k^0}|^2\, \kappa(m^2_{h_k^0}, m^2_{\tilde{\chi}_i^0}, m^2_{\tilde{\chi}_j^0})\, [m^2_{h_k^0} - m^2_{\tilde{\chi}_i^0} - m^2_{\tilde{\chi}_j^0} - 2(-1)^{\delta_{k3}} m_{\tilde{\chi}_i^0} m_{\tilde{\chi}_j^0}] \tag{5.7}$$

with an extra factor of 2 in the denominator if $i = j$.

In order to obtain a prediction for the decay width at one-loop level, the parameters appearing in the lowest-order result and the fields of $\tilde{\chi}_i^0, \tilde{\chi}_j^0, h_k^0$ need to be renormalised. We have described their renormalisation in the previous chapters. In the next section we describe how to put all of this together to renormalise the vertex.

5.2 $\tilde{\chi}_i^0\tilde{\chi}_j^0 h_k^0$ vertex renormalisation

The 3-point vertex for $\tilde{\chi}_i^0\tilde{\chi}_j^0 h_k^0$, where $h_k^0 = \{h, H, A, G\}$, can be renormalised by a counterterm vertex

$$\delta\Gamma_{\tilde{\chi}_i^0\tilde{\chi}_j^0 h_k^0} \equiv \omega_R \delta C^R_{ijh_k^0} + \omega_L (-1)^{\delta_{k3}} (-1)^{\delta_{k4}} \delta C^L_{ijh_k^0} \tag{5.8}$$

where the coupling counterterm is given by

$$\begin{aligned}\delta C^{R/L}_{ijh_k^0} &= \frac{e}{2c_W s_W}\delta c^{(*)}_{ijh_k^0} + C^{R/L}_{ijh_k^0}(\delta Z_e - \frac{\delta s_W}{s_W} - \frac{\delta c_W}{c_W}) + \frac{1}{2}\sum_{l=1}^{4}(\delta Z^{R/L}_{li} C^{R/L}_{ljh_k^0} + \delta \bar{Z}^{L/R}_{jl} C^{R/L}_{ilh_k^0}) \\ &\quad + \frac{1}{2}(\delta Z_{h_k^0 h} C^{R/L}_{ijh} + \delta Z_{h_k^0 H} C^{R/L}_{ijH} + \delta Z_{h_k^0 A} C^{R/L}_{ijA} + \delta Z_{h_k^0 G} C^{R/L}_{ijG})\end{aligned} \tag{5.9}$$

with

$$\delta c_{ijh_k^0} = [(a_k N_{i3} + b_k N_{i4})(\delta s_W N_{j1} - \delta c_W N_{j2}) + (a_k N_{j3} + b_k N_{j4})(\delta s_W N_{i1} - \delta c_W N_{i2})]. \tag{5.10}$$

This counterterm has been implemented into a supplementary model file for `FeynArts`. With this supplementary file, `FeynArts` can be used to generate a counterterm diagram, as shown in Figure 5.1(b), and a corresponding amplitude which can be added to the one-loop vertex contributions using `FormCalc`. There are built-in functions in FeynArts which allow the user to select which MSSM particles should be inserted into the self-energies that make up the counterterm amplitude.

5.3 One-loop $\tilde{\chi}_i^0 \tilde{\chi}_j^0 h_k^0$ vertex corrections

The one-loop diagrams which must be considered for the $\tilde{\chi}_i^0 \tilde{\chi}_j^0 h_k^0$ vertex are shown in Figure 5.2. Here we consider only triangle diagrams. Any self-energies occurring on external neutralino legs are taken care of by the neutralino field renormalisation, as described in Chapter 4. The self-energies for the external Higgs boson are included in the next section when we normalise the vertices to convert from a tree-level state, h_k^0, to a loop-corrected on-shell state, h_a.

The diagrams were generated using `FeynArts`, which applies the Feynman rules in the MSSM model file to obtain all possible particle insertions into the triangle topologies and generates the corresponding amplitudes. `FeynArts` also contains built-in functions which allow the user to insert only certain particles or groups of particles into the loops, so that smaller sets of diagrams can be considered separately. To avoid divergences, one should only consider gauge-invariant sets of diagrams.

There are, for example, 24 diagrams containing third generation quarks and squarks (t, $\tilde{t}$, b and $\tilde{b}$) in the loops (see Figure 5.2(a)). When these are combined with the vertex counterterm from Equation (5.8), also evaluated with the same restriction on which particles occur in the loops, they form a UV-finite set. One cannot separate the diagrams containing only t and $\tilde{t}$ from those containing only b and $\tilde{b}$ because there are diagrams in the counterterms in which both particles species appear. For example, δs_W depends on the W boson self-energy, Σ_{WW}, which contains contributions from a stop-sbottom loop and a top-bottom loop.

There are two further UV-finite sets of 24 diagrams, one for each of the first and second generations of quarks. For the lepton sector there are less diagrams since the neutrino does not couple to Higgs bosons and there is only one type of sneutrino in the MSSM.

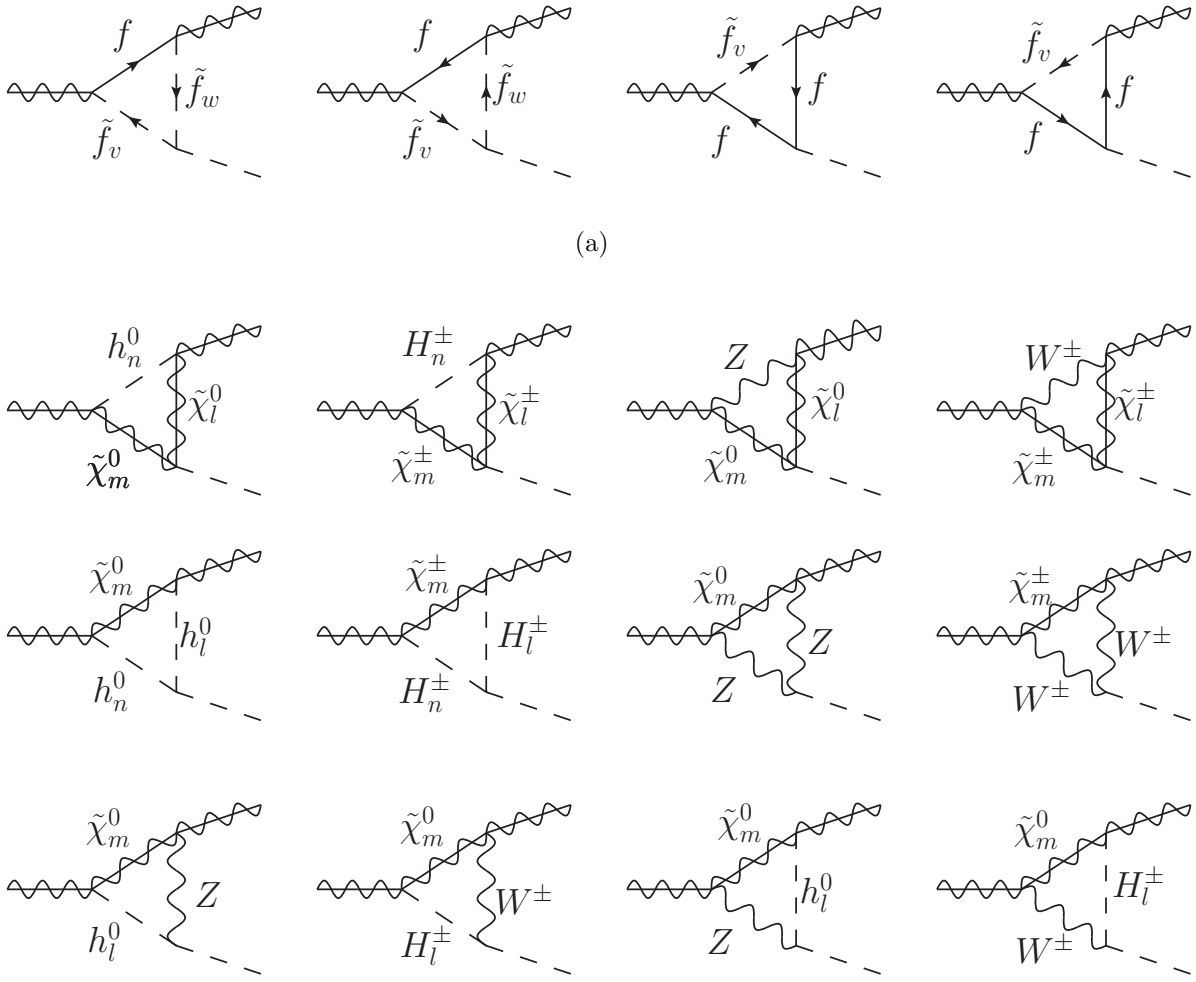

Figure 5.2: Triangle diagrams contributing to the one-loop $\tilde{\chi}_i^0\tilde{\chi}_j^0 h_k^0$ vertex. (a) Loops containing SM fermions and their scalar superpartners; for $f = u, d, c, s, t, b, e, \mu, \tau$, the subscripts v, w can take the values 1 and 2; for $f = \nu_e, \nu_\mu, \nu_\tau$, the subscripts v, w can take the value L only. The diagram with two neutrinos in the loop is always absent, the diagram with one neutrino in the loop is absent if the external Higgs boson is $\mathcal{CP}$-odd. The arrows indicating fermion flow can be reversed. (b) Loops containing Higgs bosons, vector bosons and their scalar superpartners; $h_l^0 = \{h, H, A, G\}$, $H_l^\pm = \{H^\pm, G^\pm\}$, $\tilde{\chi}_l^0 = \{\tilde{\chi}_2^0, \tilde{\chi}_2^0, \tilde{\chi}_3^0, \tilde{\chi}_4^0\}$, $\tilde{\chi}_l^0 = \{\tilde{\chi}_1^0, \tilde{\chi}_2^0\}$. Depending on the $\mathcal{CP}$-properties of the external Higgs bosons, not all combinations of Higgs boson insertions in the loops are allowed. Also, the diagrams containing two vector bosons occur only if the external Higgs boson is $\mathcal{CP}$-even.

The sneutrino does not couple to the $\mathcal{CP}$-odd Higgs boson. Each generation of leptons and sleptons hence forms a UV-finite set of 14 (12) diagrams if the external Higgs boson is $\mathcal{CP}$-even(odd).

If the external Higgs boson is $\mathcal{CP}$-even (h or H), there are then 192 remaining diagrams at the particle level (i.e. those in Figure 5.2(b)) which themselves form a UV-finite set. The loops in these diagrams contain gauge bosons, Higgs bosons and their superpartners; the charginos and neutralinos. They cannot be divided up into smaller UV-finite sets. If the external Higgs boson is $\mathcal{CP}$-even (A), the equivalent set contains only 168 diagrams.

In total we have 306 or 276 diagrams, depending on the $\mathcal{CP}$-parity of the external Higgs boson, each translated into an amplitude by the function `CreateFeynAmp` in `FeynArts`. For example; for the process $\tilde{\chi}_i^0 \to \tilde{\chi}_j^0 h_k^0$, the first diagram in Figure 5.2(a) is translated into the amplitude;

$$\begin{aligned}\mathcal{M} \;=\; & \int -\frac{d^4q_1}{16\pi^4}\bar{u}(k_1, m_{\tilde{\chi}_j^0})[\omega_L C^L_{f\tilde{\chi}_j^0\bar{\tilde{f}}_w} + \omega_R C^R_{f\tilde{\chi}_j^0\bar{\tilde{f}}_w}](\not{q}_1 + m_f)[\omega_L C^L_{\tilde{\chi}_i^0\bar{f}\tilde{f}_v} + \omega_R C^R_{\tilde{\chi}_i^0\bar{f}\tilde{f}_v}] \\ & C_{h_k^0\tilde{f}_w\bar{\tilde{f}}_v} u(p_1, m_{\tilde{\chi}_i^0})/\big((q_1^2 - m_f^2)[(q_1 - k_1)^2 - m^2_{\tilde{f}_v}][(q_1 - k_1 - k_2)^2 - m^2_{\tilde{f}_w}]\big)\end{aligned} \tag{5.11}$$

where p_1 is the incoming momentum of the $\tilde{\chi}_i^0$, k_1, k_2 are the outgoing momenta of the $\tilde{\chi}_j^0$ and h_k^0 respectively, and q_1 is the loop momentum on the internal fermion line. The couplings of neutralinos to fermion-sfermion pairs and sfermion-sfermion pairs involve masses and mixing matrices. `FormCalc` makes the task of evaluating these amplitudes relatively straightforward. The function `CalcFeynAmp` performs the contraction of indices, the calculation of traces, the reduction of tensor integrals, further simplifications and the introduction of abbreviations. In our example, Equation (5.11) is simplified to

$$\begin{aligned}\mathcal{M} \;=\; & \frac{i}{16\pi^2}[F_1(C^L_{f\tilde{\chi}_j^0\bar{\tilde{f}}_w} C^L_{\tilde{\chi}_i^0\bar{f}\tilde{f}_v} C_{h_k^0\tilde{f}_w\bar{\tilde{f}}_v} m_f \mathrm{C}_0 - C^R_{f\tilde{\chi}_j^0\bar{\tilde{f}}_w} C^L_{\tilde{\chi}_i^0\bar{f}\tilde{f}_v} C_{h_k^0\tilde{f}_w\bar{\tilde{f}}_v} m_{\tilde{\chi}_j^0} \mathrm{C}_1 \\ & - C^L_{f\tilde{\chi}_j^0\bar{\tilde{f}}_w} C^R_{\tilde{\chi}_i^0\bar{f}\tilde{f}_v} C_{h_k^0\tilde{f}_w\bar{\tilde{f}}_v} m_{\tilde{\chi}_i^0} \mathrm{C}_2) + F_2(C^R_{f\tilde{\chi}_j^0\bar{\tilde{f}}_w} C^R_{\tilde{\chi}_i^0\bar{f}\tilde{f}_v} C_{h_k^0\tilde{f}_w\bar{\tilde{f}}_v} m_f \mathrm{C}_0 \\ & - C^L_{f\tilde{\chi}_j^0\bar{\tilde{f}}_w} C^R_{\tilde{\chi}_i^0\bar{f}\tilde{f}_v} C_{h_k^0\tilde{f}_w\bar{\tilde{f}}_v} m_{\tilde{\chi}_j^0} \mathrm{C}_1 - C^R_{f\tilde{\chi}_j^0\bar{\tilde{f}}_w} C^L_{\tilde{\chi}_i^0\bar{f}\tilde{f}_v} C_{h_k^0\tilde{f}_w\bar{\tilde{f}}_v} m_{\tilde{\chi}_i^0} \mathrm{C}_2)]\end{aligned} \tag{5.12}$$

where $\mathrm{C}_i \equiv \mathrm{C}_i(m^2_{\tilde{\chi}_j^0}, m^2_{h_k^0}, m^2_{\tilde{\chi}_i^0}, m_f^2, m^2_{\tilde{f}_v}, m^2_{\tilde{f}_w})$ are scalar loop integrals (see Appendix A.1 for the definitions of the loop integrals used in this thesis) and the abbreviations

$$F_1 = \bar{u}(k_1, m_{\tilde{\chi}_j^0})\omega_L u(p_1, m_{\tilde{\chi}_i^0}), \qquad F_2 = \bar{u}(k_1, m_{\tilde{\chi}_j^0})\omega_R u(p_1, m_{\tilde{\chi}_i^0}) \tag{5.13}$$

are used. These matrix elements and abbreviations, combined with the corresponding output for the counterterms, are then converted to `Fortran` code using `WriteSquaredME`.

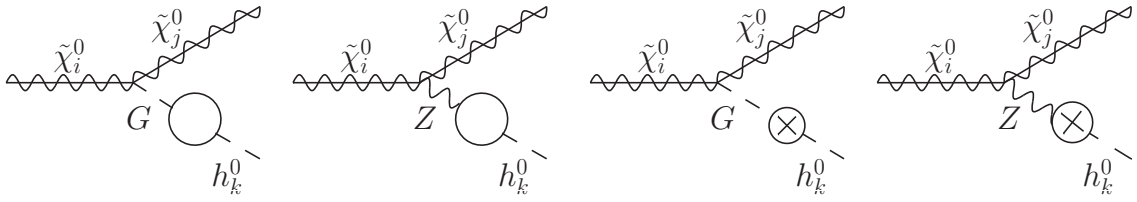

(a) (b)

Figure 5.3: Contributions to the one-loop $\tilde{\chi}_i^0\tilde{\chi}_j^0 h_k^0$ vertex involving mixing self-energies of Higgs bosons with the G and Z bosons; (a) h_k^0–G self-energy diagram, (b) h_k^0–Z self-energy diagram, (c) h_k^0–G counterterm diagram, (d) h_k^0–Z self-energy diagram.

The code contains everything required to convert these matrix elements into numerical values for decay widths and cross sections. The loop integrals are evaluated numerically using `LoopTools`. We vary the parameter $\Delta \equiv 2/(4-D) - \gamma_E + \log 4\pi$ to check the UV finiteness of the decay width and show that in the corresponding vertex function, $\hat{\Gamma}^{1PI}_{\tilde{\chi}_i^0\tilde{\chi}_j^0 h_k^0} = \Gamma^{1PI}_{\tilde{\chi}_i^0\tilde{\chi}_j^0 h_k^0} + \delta\Gamma^{1PI}_{\tilde{\chi}_i^0\tilde{\chi}_j^0 h_k^0}$, the UV divergences cancel out.

5.4 Inclusion of self-energy diagrams

In the previous section we obtained the 1PI renormalised vertex function for $\tilde{\chi}_i^0\tilde{\chi}_j^0 h_k^0$. Although it is UV-finite, this vertex function will not lead to physical amplitudes and decay widths, as the external Higgs field is not on-shell and can mix with other fields. The 3-point vertex for $\tilde{\chi}_i^0\tilde{\chi}_j^0 h_a$ is constructed from the vertices for $\tilde{\chi}_i^0\tilde{\chi}_j^0 h, H, A$ using the 3×3 $\hat{\mathbf{Z}}$ matrix for the normalisation of wavefunctions as in Equation (3.84). This automatically includes the reducible self-energy diagrams involving h, H, A.

For a complete one-loop result, reducible diagrams, of the type shown in Figure 5.3(a), involving mixing self-energies of Higgs bosons with the G and Z bosons, must also be included. In order to ensure a proper cancellation of the gauge parameter dependence, we follow the approach of Ref. [30] and evaluate these reducible contributions, $\hat{\Gamma}^{\mathrm{G,Z.se}}$, strictly at the one-loop level. The diagrams and amplitudes were generated using `FeynArts`, and added to the corresponding counterterm diagram from Figure 5.3(b). The h_k^0–G vertex counterterms from Equation (3.67) and the resulting h_k^0–Z counterterms were implemented into our `FeynArts` model file.

Our full result, $\hat{\Gamma}^{\text{Full Loop}}$, is then obtained by combining these contributions with those of genuine vertex type, $\hat{\Gamma}^{\text{1PI}}$, as follows,

$$\hat{\Gamma}^{\text{Full Loop}}_{\tilde{\chi}^0_i \tilde{\chi}^0_j h_a} = \hat{\mathbf{Z}}_{al}[\hat{\Gamma}^{\text{1PI}}_{\tilde{\chi}^0_i \tilde{\chi}^0_j h^0_l}(M^2_{h_a}) + \hat{\Gamma}^{\text{G,Z.se}}_{\tilde{\chi}^0_i \tilde{\chi}^0_j h^0_l}(m^2_{h^0_l})], \tag{5.14}$$

where $h^0_l = \{h, H, A\}$ are the tree-level states with tree-level masses, $m_{h^0_l}$, and are summed over. In contrast, M_{h_a} is the loop-corrected mass of the Higgs boson h_a in the physical process, i.e. one of h_1, h_2, h_3. Numerically, inclusion of the G–Z mixing did not have a significant effect, but we include these diagrams for a complete one-loop result. Across the CPX parameter space studied in Chapters 6 and 7, the effect of this correction on the decay widths was less than 0.1%.

5.5 Combination with higher-order results

As Higgs propagator-type corrections are known to be large, we have combined our one-loop result for the genuine vertex contribution with state-of-the-art two-loop propagator-type corrections obtained within the Feynman diagrammatic approach, as implemented in the program `FeynHiggs` [41, 79–81]. These contributions incorporate in particular the full phase dependence at $\mathcal{O}(\alpha_t \alpha_s)$, while we do not include here further two-loop corrections that are known only for the case of real MSSM parameters.[1] Using Equation (5.14), we combine the two-loop $\hat{\mathbf{Z}}$ factors and Higgs masses M_{h_a} from `FeynHiggs 2.6.5`, with our own genuine vertex ($\hat{\Gamma}^{\text{1PI}}$) and G–Z mixing ($\hat{\Gamma}^{\text{G,Z.se}}$) corrections to the processes $\tilde{\chi}^0_i \to \tilde{\chi}^0_j h_a$ and $h_a \to \tilde{\chi}^0_i \tilde{\chi}^0_j$, thereby obtaining the most precise predictions for the corresponding decay widths and branching ratios in the MSSM with complex parameters.

In order to investigate the effects of the genuine vertex contributions for the processes $\tilde{\chi}^0_i \to \tilde{\chi}^0_j h_a$ and $h_a \to \tilde{\chi}^0_i \tilde{\chi}^0_j$, we will in the following compare our full result with an Improved Born approximation. The latter is obtained by summing over the tree-level amplitudes for $\tilde{\chi}^0_i \to \tilde{\chi}^0_j h^0_k$ or $h^0_k \to \tilde{\chi}^0_i \tilde{\chi}^0_j$, weighted by the appropriate $\hat{\mathbf{Z}}$ factors and

[1] This means in `FeynHiggs` selecting the flag `t1cp1approx`= 1 instead of the default flag for complex parameters `t1cp1approx`= 3, which uses an interpolation between phases to include the further two-loop corrections evaluated at real parameters.

evaluated at the loop-corrected Higgs masses,

$$\hat{\Gamma}^{\text{Improved Born}}_{\tilde{\chi}^0_i \tilde{\chi}^0_j h_a} = \hat{\mathbf{Z}}_{al}[\hat{\Gamma}^{\text{Born}}_{\tilde{\chi}^0_i \tilde{\chi}^0_j h_l}(M_{h^2_a})]. \tag{5.15}$$

We will always compare our numerical results to this Improved Born approximation, rather than to the strict tree-level result of Equation (5.5). This allows us to separate out the effect of our new genuine (process-specific) vertex corrections from those corrections coming from mixing effects and mass shifts in the Higgs sector which are already known to be large. Thus when we speak of the relative effect of our genuine vertex loop calculations on the partial decay width, Γ, we are referring to the ratio

$$r = \frac{\Gamma_{\text{Full Loop}} - \Gamma_{\text{Improved Born}}}{\Gamma_{\text{Improved Born}}}. \tag{5.16}$$

As well as our full MSSM calculation, we will show approximations, where only some (UV-finite) sets of diagrams such as third generation quarks and squarks, i.e. $t, \tilde{t}, b, \tilde{b}$, are included in the genuine vertex corrections. In all cases, the two-loop propagator-type corrections from `FeynHiggs` are evaluated in the full MSSM. Various other approximations exist in the literature. In Ref. [101], only the one-loop 3rd generation (s)quark contributions in the real MSSM were considered. In Ref. [102], all one-loop (s)fermion contributions in the real MSSM were considered. Our full results thus go beyond these works, as we include all possible MSSM particles in the loops, we allow complex parameters, and we incorporate complete one-loop and leading two-loop contributions from the Higgs sector.

5.6 Other vertices

In addition to the $\tilde{\chi}^0_i \tilde{\chi}^0_j h^0_k$ vertex, we have renormalised all three-point vertices involving Higgs or gauge bosons with charginos and/or neutralinos. The counterterms for these vertices have been implemented into our supplementary `FeynArts` model file and checked for UV-finiteness. We give formulae for these in Appendix B for reference, but will not use all of them for the numerical results presented in this thesis.

We will present numerical results for the one-loop $\tilde{\chi}^0_i \tilde{\chi}^0_j Z$ vertex. To obtain these corrections, the procedure followed was similar to that described in the previous sections for the $\tilde{\chi}^0_i \tilde{\chi}^0_j h^0_k$ vertex. At the particle level there are 292 diagrams to compute, which

can be split into analogous UV-finite sets to the Higgs case. The three-point vertex is given at tree level by

$$\Gamma^{\text{tree}}_{\tilde{\chi}^0_{n_1}\tilde{\chi}^0_{n_2}Z} = i(C^L_{\tilde{\chi}^0_{n1},\tilde{\chi}^0_{n2},Z}\gamma^\mu\omega_L + C^R_{\tilde{\chi}^0_{n1},\tilde{\chi}^0_{n2},Z}\gamma^\mu\omega_R). \tag{5.17}$$

where

$$C^{L/R}_{\tilde{\chi}^0_{n1},\tilde{\chi}^0_{n2},Z} = \frac{e}{2c_W s_W} c^{L/R}_{\tilde{\chi}^0_{n_1}\tilde{\chi}^0_{n_2}Z} \tag{5.18}$$

with

$$\begin{aligned} c^L_{\tilde{\chi}^0_{n_1}\tilde{\chi}^0_{n_2}Z} &= -N^*_{n_2 3}N_{n_1 3} + N^*_{n_2 4}N_{n_1 4}, \\ c^R_{\tilde{\chi}^0_{n_1}\tilde{\chi}^0_{n_2}Z} &= N^*_{n_1 3}N_{n_2 3} - N^*_{n_1 4}N_{n_2 4}. \end{aligned} \tag{5.19}$$

The vertex counterterms are then given by

$$\begin{aligned} \delta C^{L/R}(\tilde{\chi}^0_{n_1},\tilde{\chi}^0_{n_2},Z) = \frac{e}{2c_W s_W}\big[&2c^{L/R}_{\tilde{\chi}^0_{n_1}\tilde{\chi}^0_{n_2}Z}(\delta Z_e - \frac{\delta c_W}{c_W} - \frac{\delta s_W}{s_W} + \frac{1}{2}\delta Z_{ZZ}) \\ &+\frac{1}{2}(\delta Z^{L/R}_{0,n_1 i}c^{L/R}_{\tilde{\chi}^0_i\tilde{\chi}^0_{n_2}Z} + c^{L/R}_{\tilde{\chi}^0_{n_1}\tilde{\chi}^0_i Z}\delta\bar{Z}^{L/R}_{0,in_2})\big]. \end{aligned} \tag{5.20}$$

Equation (5.20) is somewhat simpler than the Higgs vertex counterterm of Equation (5.9). The counterterm, $\delta c^{L/R}_{\tilde{\chi}^0_{n_1}\tilde{\chi}^0_{n_2}Z}$, is zero since it contains only mixing matrix elements. Also, the Z field renormalisation transformation (see Equation (3.10)) mixes the Z boson only with the photon, which does not couple to neutralinos, so the $\delta Z_{Z\gamma}$ term can be dropped from the vertex counterterm. Unlike the Higgs vertex, there is no need to normalise the Z vertex using finite normalisation factors, since the on-shell renormalisation conditions ensure the correct propagator residue. However, for a complete one-loop result for the process $\tilde{\chi}^0_i \to \tilde{\chi}^0_j Z$, we do include reducible diagrams involving the mixing self-energies for the Z boson with h, H, A, and G.

Chapter 6

Results for the decay width of a neutralino into a light Higgs boson

6.1 Motivation

In this chapter we present numerical results for the decay width of a neutralino into a light Higgs boson, calculating the vertex corrections using the method described in Chapter 5. Our motivation for the study of this decay is the CPX benchmark scenario [29]. As already discussed, not only does this scenario contain a parameter region in which a very light Higgs boson, of mass around 40 GeV, is unexcluded by LEP [27,30], but it is known that this unexcluded parameter region will also be difficult to cover at the LHC with the standard search channels [31–33].

While on the one hand a supersymmetric scenario such as the CPX scenario may have much worse prospects compared to the SM case for Higgs searches at the LHC in the standard channels, on the other hand additional Higgs production channels involving SUSY particles may occur in such a case. In cascade decays of heavier SUSY particles down to the lightest supersymmetric particle (LSP), Higgs bosons can in particular be produced in decays of neutralinos and charginos, via $\tilde{\chi}_i^0 \to \tilde{\chi}_j^0 h_1, h_2, h_3$ and $\tilde{\chi}_i^\pm \to \tilde{\chi}_j^0 H^\pm$, see e.g. Refs. [103, 104] for studies of these channels at the LHC in the MSSM with real parameters. These channels have also attracted recent interest for studies of scenarios with non-universal gaugino masses [105–107].

Since higher-order contributions in the MSSM Higgs sector are known to be large, a proper inclusion of Higgs-sector corrections is indispensable for a reliable prediction of this class of processes. The process-independent corrections to the mass of the outgoing

Higgs boson and to the Higgs wave function normalisation can be incorporated via an effective Born-type prediction for the neutralino decay process, see Refs. [30, 41, 108] (see Section 5.5). We show results for such an Improved Born approximation using Equation (5.15). The genuine (process-specific) vertex corrections, included in Equation (5.14), can also be very important. This has recently been demonstrated in Ref. [30] for Higgs cascade decay processes, $h_a \to h_b h_c$, in the CPX scenario, where the genuine vertex corrections were found to give rise to drastic changes in the decay widths compared to the effective Born-type predictions. In the neutralino decay processes, comprising just one instead of three external Higgs bosons, the genuine vertex corrections are not expected to be quite as large as for the Higgs cascade decays, but their effects can nevertheless be expected to be non-negligible.

Concerning existing theoretical predictions for this class of processes, partial one-loop results have been published previously for the decays $H, A \to \tilde{\chi}_i^0 \tilde{\chi}_j^0$ in both the Feynman-diagrammatic [101, 102] and effective potential [109] approaches. These predictions did not include the full MSSM, and the Feynman-diagrammatic calculations were restricted to the case of real parameters.

Here we present the full vertex corrections at the one-loop level, taking into account the contributions from all MSSM particles, and all possible complex parameters using the renormalisation scheme detailed in Chapters 4 and 5. We combine these results with state-of-the-art two-loop propagator-type corrections as implemented in the code `FeynHiggs` [41, 79–81] using Equation (5.14). In this way the currently most precise prediction for this class of processes is obtained.

In our numerical discussion we concentrate in particular on the parameter region in the CPX benchmark scenario where a light Higgs boson is unexcluded by current data (see also Refs. [110–112] and the more recent Ref. [113] for discussions of other possible LHC search channels to access this parameter region), but we also give examples for the $\mathcal{CP}$-conserving case. In addition we will also compare our results for the decay width of a neutralino into a Higgs boson to the decay width of a neutralino into a Z boson.

6.2 Numerical results for the CPX scenario

We start with numerical results for our genuine vertex corrections to the decay width for $\tilde{\chi}_2^0 \to \tilde{\chi}_1^0 h_1$ in the CPX scenario. Figure 6.1(a) shows the partial decay width

$\Gamma(\tilde{\chi}_2^0 \to \tilde{\chi}_1^0 h_1)$ as a function of M_{h_1}. The value of $\tan\beta$ is fixed at 5.5, while $M_{H^\pm}$ is varied as input. As M_{h_1} increases, the partial width decreases, becoming kinematically closed for $M_{h_1} \gtrsim 103\,\text{GeV} \sim M_{\tilde{\chi}_2^0} - M_{\tilde{\chi}_1^0}$. The dashed Improved Born curve shows the result obtained by combining the tree-level amplitudes with 2-loop $\hat{\mathbf{Z}}$ matrix elements and masses according to Eq. (5.15). The other curves incorporate our results for the genuine vertex corrections, taking into account different sets of loop contributions. Figure 6.1(b) shows the ratio r, defined in Eq. (5.16), of the genuine vertex corrections relative to the Improved Born result as a function of M_{h_1}. We see from the figure that the impact of the genuine vertex corrections on the decay width is very large. The corrections from the full MSSM contributions to the vertex amount to about 45% for Higgs mass values in the region of the "CPX hole", i.e. for $M_{h_1} \sim 40\,\text{GeV}$. As expected, the dominant effect arises from the triangle diagrams containing third generation quarks and squarks $(t, \tilde{t}, b, \tilde{b})$, due to the large top Yukawa coupling, yielding a correction of about 35% compared to the Improved Born result. The other (s)fermions also play a non-negligible role, in particular through their couplings to neutralinos, increasing the total (s)fermion contribution to just under 50%. The vertex corrections from the remainder of the particles in the MSSM, namely the vector bosons, Higgs bosons, neutralinos and charginos, are negative and contribute about a 5% correction.

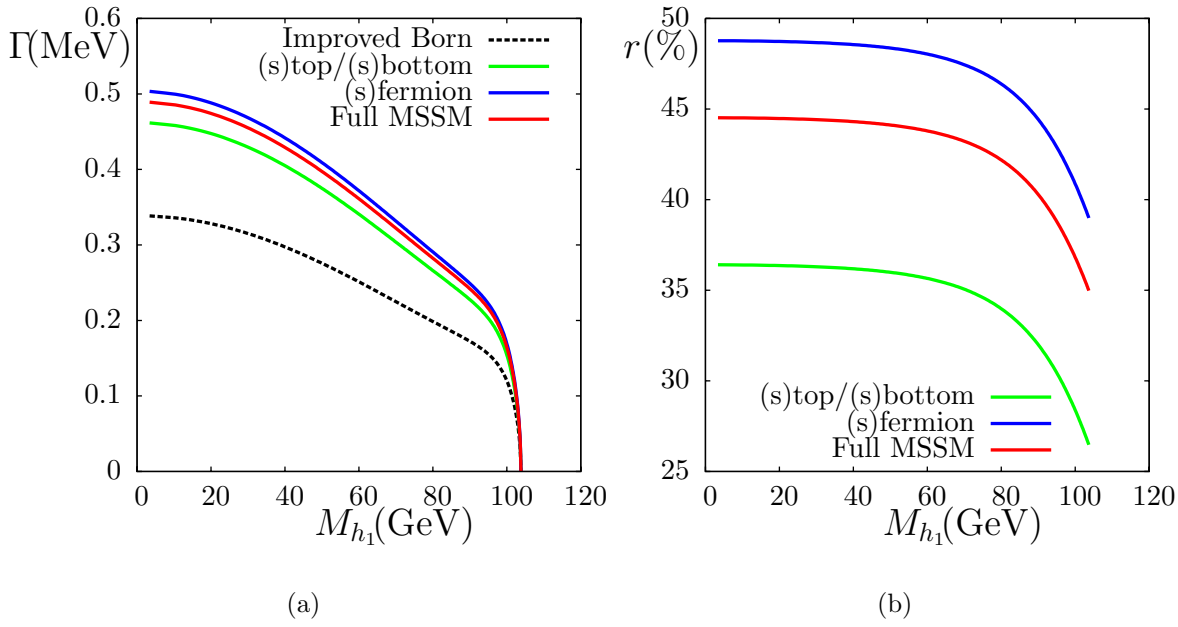

Figure 6.1: Results for (a) the decay width $\Gamma(\tilde{\chi}_2^0 \to \tilde{\chi}_1^0 h_1)$ and (b) the ratio $r = (\Gamma_{\text{Full Loop}} - \Gamma_{\text{Improved Born}})/\Gamma_{\text{Improved Born}}$ in the CPX scenario plotted against M_{h_1} for $\tan\beta = 5.5$. ($M_{H^\pm}$ was varied as input.) The different curves indicate the inclusion of various subsets of diagrams.

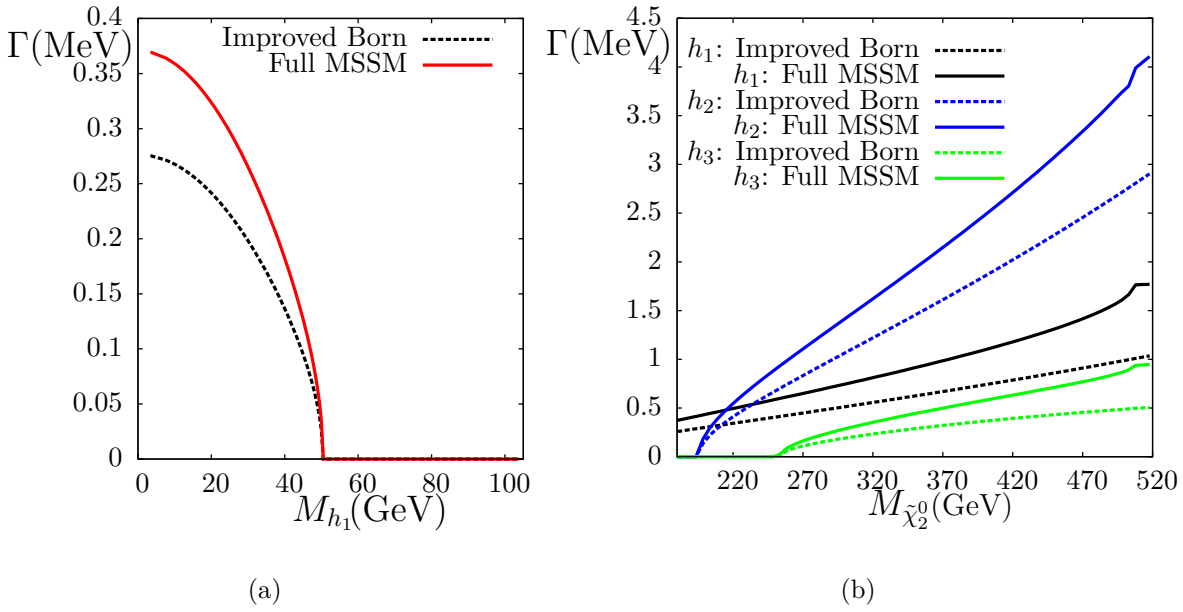

Figure 6.2: Results for (a) the decay width $\Gamma(\tilde{\chi}^0_2 \to \tilde{\chi}^0_1 h_2)$ as a function of M_{h_1} in the CPX scenario, ($M_{H^\pm}$ was varied as input, M_{h_2} and M_{h_3} will vary with $M_{H^\pm}$); and (b) the decay widths $\Gamma(\tilde{\chi}^0_2 \to \tilde{\chi}^0_1 h_{1,2,3})$ as a function of $M_{\tilde{\chi}^0_2}$ in the CPX scenario for $\tan\beta = 5.5$; (M_2 was varied as input to produce the displayed variation in $M_{\tilde{\chi}^0_2}$ (mostly wino); $M_{\tilde{\chi}^0_1}$ (mostly bino) also varies due to the GUT relation between M_1 and M_2). The different curves indicate the inclusion of various vertex corrections.

In Figure 6.2(a) we show the partial decay width $\Gamma(\tilde{\chi}^0_2 \to \tilde{\chi}^0_1 h_2)$ for the second lightest Higgs boson, as a function of M_{h_1} in the CPX scenario with $\tan\beta = 5.5$.[1] For $M_{h_1} \gtrsim 50\,\text{GeV}$, M_{h_2} drops below $M_{\tilde{\chi}^0_2} - M_{\tilde{\chi}^0_1}$, and the decay is no longer kinematically open. For the nominal CPX value of $M_2 = 200\,\text{GeV}$ and values of M_{h_1} and $\tan\beta$ chosen in the region of the "CPX hole", the decay width into h_2 is always less than the decay width into h_1, shown in Figure 6.1(a). However, for larger values of M_2 (and hence $M_{\tilde{\chi}^0_2}$), this may not always be the case, and also the decay into h_3 may become kinematically open.

In Figure 6.2(b) we show the variation in each of the partial decay widths $\Gamma(\tilde{\chi}^0_2 \to \tilde{\chi}^0_1 h_{1,2,3})$, as a function of $M_{\tilde{\chi}^0_2}$. $M_{H^\pm}$ was adjusted to keep M_{h_1} and $\tan\beta$ fixed at 40 GeV and 5.5 respectively. We see that the decay into the lightest Higgs boson, h_1, is kinematically open for the whole range of $M_{\tilde{\chi}^0_2}$ shown, while h_2 and h_3 can only be produced on-shell for $M_{\tilde{\chi}^0_2}$ greater than around 195 and 250 GeV respectively. Once $M_{\tilde{\chi}^0_2}$

[1] The variation as a function of M_{h_1} is merely for reference later in Chapter 7 when we compute the branching ratio of $\tilde{\chi}^0_2$ as a function of M_{h_1}. In fact the input parameter $M_{H^\pm}$ was varied to produce the displayed variation in M_{h_1}.

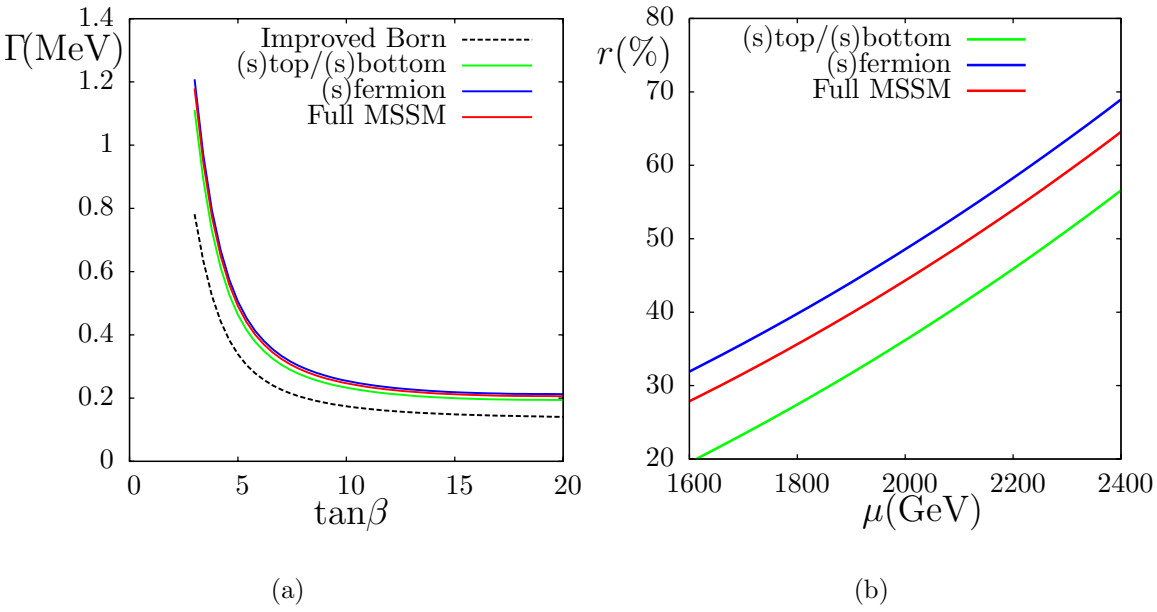

Figure 6.3: (a) The decay width $\Gamma(\tilde{\chi}_2^0 \to \tilde{\chi}_1^0 h_2)$ as a function of $\tan\beta$ in the CPX scenario, with various subsets of diagrams included. (b) The ratio $r = (\Gamma_{\text{Full Loop}} - \Gamma_{\text{Improved Born}})/\Gamma_{\text{Improved Born}}$ for $\tilde{\chi}_2^0 \to \tilde{\chi}_1^0 h_1$ plotted against μ in the CPX scenario, with $\tan\beta = 5.5$, with various subsets of diagrams included. $M_{H^\pm}$ was adjusted in order to keep $M_{h_1} = 40\,\text{GeV}$ constant for both figures.

becomes large enough, the decay into h_2 dominates over the decay into h_1, since h_2 has a larger $\mathcal{CP}$-even component. Notice that all three decay widths receive large vertex corrections of $\mathcal{O}(50\%)$. For $M_{\tilde{\chi}_2^0}$ just below 520 GeV, there is a slight enhancement in the vertex corrections, corresponding to the threshold for the decay of $\tilde{\chi}_2^0$ into squark-quark final states. We will see in Chapter 7 that, above this threshold, the squark-quark decay then begins to dominate the branching ratio of the second lightest neutralino.

In Figure 6.3(a) we show the decay width of $\Gamma(\tilde{\chi}_2^0 \to \tilde{\chi}_1^0 h_1)$ as a function of $\tan\beta$, where $M_{H^\pm}$ is adjusted to keep M_{h_1} constant at 40 GeV. We observe a similar pattern in the relative impact of the various contributions of the subsets of diagrams to the vertex corrections, the largest coming from the third generation quarks and squarks. Values of $\tan\beta$ below 5 yield a significant increase of the decay width.

Such large effects from the genuine vertex corrections are not unexpected in the CPX scenario (see also Ref. [30] for an analysis of genuine vertex corrections to Higgs cascade decays). It is well known that loop corrections in the Higgs sector can be large, especially in this rather extreme scenario with large trilinear couplings and $\mathcal{CP}$-violating phases. Such a large value of μ also enhances the effect of loop corrections in the neutralino

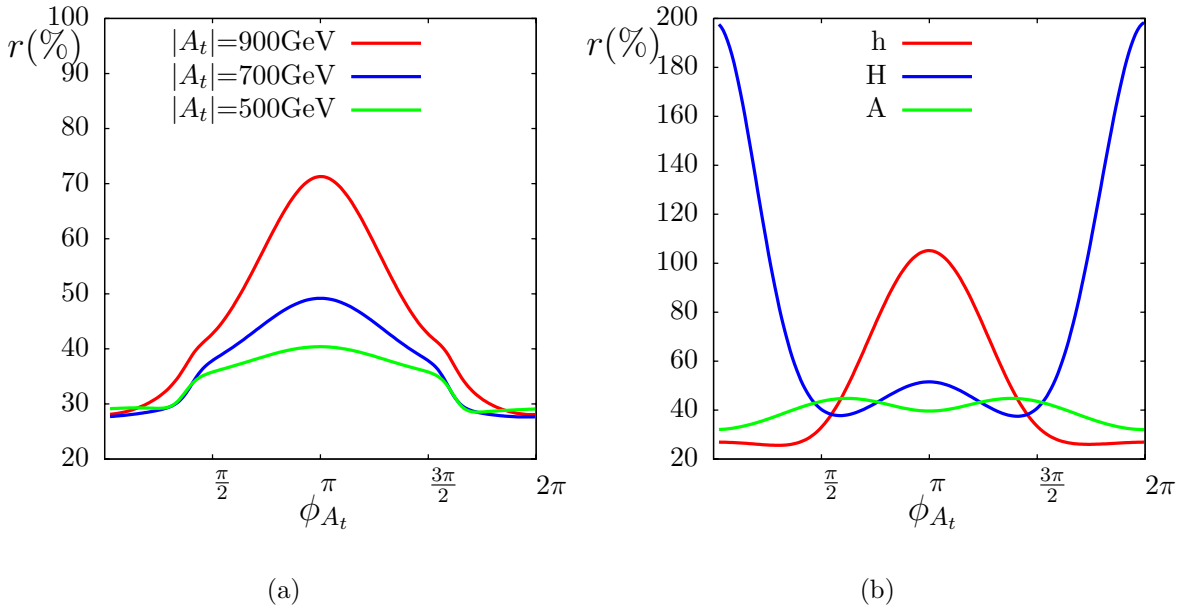

Figure 6.4: The ratio $r = (\Gamma_{\text{Full Loop}} - \Gamma_{\text{Improved Born}})/\Gamma_{\text{Improved Born}}$ in the CPX scenario: (a) r for $\tilde{\chi}_2^0 \to \tilde{\chi}_1^0 h_1$ plotted against ϕ_{A_t}. (b) r for each of $\tilde{\chi}_2^0 \to \tilde{\chi}_1^0 h, H, A$ plotted against ϕ_{A_t} for $|A_t| = 900\,\text{GeV}$, where h, H, A indicate the unnormalised Higgs $\mathcal{CP}$-eigenstates (i.e. the $\hat{\mathbf{Z}}_{1i}$ matrix elements are set to $\{1,0,0\}$, $\{0,1,0\}$ and $\{0,0,1\}$ respectively). For both figures, $M_{H^\pm}$ was adjusted in order to keep $M_{h_1} = 45\,\text{GeV}$ constant and $\tan\beta = 7$.

sector. In Figure 6.3(b) we see how the effect of the genuine vertex corrections is further enhanced to values of 60% or more if μ is increased compared to its value in the CPX scenario of $\mu = 2\,\text{TeV}$. On the other hand, if μ is decreased one obtains correspondingly smaller corrections.

We also examined the effect of varying the absolute value and $\mathcal{CP}$-violating phase of the trilinear coupling, $A_t = A_b = A_\tau$, for the third generation of sfermions. In Figure 6.4(a), we plot r for the decay $\tilde{\chi}_2^0 \to \tilde{\chi}_1^0 h_1$ as a function of ϕ_{A_t} for various values of $|A_t|$. $M_{H^\pm}$ was adjusted in order to keep $M_{h_1} = 45\,\text{GeV}$ constant and $\tan\beta = 7$. (A Higgs mass of $M_{h_1} = 40\,\text{GeV}$ was not theoretically accessible for all ϕ_{A_t} when $|A_t| = 500\,\text{GeV}$.) In Figure 6.4(b), we plot r for each of $\tilde{\chi}_2^0 \to \tilde{\chi}_1^0 h, H, A$ as a function of ϕ_{A_t} for $|A_t| = 900\,\text{GeV}$, where h, H, A are the unnormalised Higgs $\mathcal{CP}$-eigenstates. We compute the latter (unphysical) decay widths in the limit where we set the $\hat{\mathbf{Z}}_{1i}$ matrix elements for the lightest Higgs boson to $\{1,0,0\}$, $\{0,1,0\}$ and $\{0,0,1\}$ respectively. (For reasons discussed in Section 3.4.9, these will not correspond to physical mass eigenstates.) First we discuss the red curve in Figure 6.4(a), where $|A_t| = 900\,\text{GeV}$. At $\phi_{A_t} = \pi/2$, the loop corrections show a steep dependence on the phase, ϕ_{A_t}, emphasising the importance of including the effects of phases in the calculation. At this value, h_1 has its largest $\mathcal{CP}$-odd

content, i.e. $|\hat{\mathbf{Z}}_{13}|$ is largest (as shown in Figure 3.3(b)), while the $\mathcal{CP}$-even contributions are suppressed, giving rise to corrections of order $r \sim 45\%$, which is consistent with the size of the corrections to the decay width into the $\mathcal{CP}$-odd eigenstate, A, at $\phi_{A_t} = \pi/2$ shown in Figure 6.4(b). When $\phi_{A_t} = 0$, the loop corrections to $\Gamma(\tilde{\chi}_2^0 \to \tilde{\chi}_1^0 h_1)$ are found to be somewhat smaller, with $r \sim 30\%$. This is because at this value of the phase, h_1 is mostly h (see Figure 3.3(b)), and as seen in Figure 6.4(b), the decay width into the $\mathcal{CP}$-even eigenstate, h, receives corrections of around this size. On the other hand, the effect of the genuine vertex corrections to $\Gamma(\tilde{\chi}_2^0 \to \tilde{\chi}_1^0 h_1)$ is maximised for $\phi_{A_t} = \pi$, i.e. $A_t = -|A_t|$. This corresponds to maxima in $|\hat{\mathbf{Z}}_{11}|$ and $|\hat{\mathbf{Z}}_{12}|$, so that the lightest Higgs boson is mostly $\mathcal{CP}$-even (see Figure 3.3(b)). The genuine vertex corrections for a $\mathcal{CP}$-even Higgs are larger than for a $\mathcal{CP}$-odd one at $\phi_{A_t} = \pi$, so that their effect is maximised here. The corrections are particularly large for the Higgs with an h-like coupling (see Figure 6.4(b)). Hence the genuine vertex corrections in such a $\mathcal{CP}$-conserving scenario (with $\phi_{A_t} = \pi$) can even exceed the ones in the CPX scenario (where $\phi_{A_t} = \pi/2$). It should be noted in this context, however, that such a light $\mathcal{CP}$-even Higgs boson is of course experimentally excluded. Figure 6.4(b) also shows corrections of order 200% at $\phi_{A_t} = 0, 2\pi$ for the unrenormalised H state of mass 45 GeV. Note, however, that this 200% effect is not physical; it does not play a large role for the physical h_1 state since $\hat{\mathbf{Z}}_{12}$ is small at these ϕ_{A_t} values (see Figure 3.3(b)). For smaller values of $|A_t|$ (blue and green curves in Figure 6.4(a)), the corrections are in general smaller, and the variation with the phase of A_t is less pronounced. Nevertheless, even for $|A_t| = 500\,\text{GeV}$ we find $r \sim 35\%$ and $r \sim 40\%$ at $\phi_{A_t} = \pi/2$ and $\phi_{A_t} = \pi$, respectively.

6.3 Numerical results for the small α_{eff} scenario

We next consider the numerical results for the genuine vertex corrections to the decay width, $\Gamma(\tilde{\chi}_2^0 \to \tilde{\chi}_2^0 h_1)$, in the $\mathcal{CP}$-conserving small α_{eff} scenario. Like the CPX scenario, this scenario has large μ and large, negative A_t. For the small α_{eff} scenario with $M_{H^\pm} = 220\,\text{GeV}$ and $\tan\beta = 10$, we find genuine vertex corrections of size $r \sim 35\%$. The variation with μ, shown in Figure 6.5(a), results in a pattern that is very similar to the one observed for the CPX scenario in 6.3(b). The size of the correction scales approximately linearly with μ, and the inclusion of the full (s)fermion contributions yields a shift of about 10% compared to the contribution of only the third generation (s)quarks. The non-(s)fermionic corrections to the genuine vertex give rise to a downward shift of about 5%.

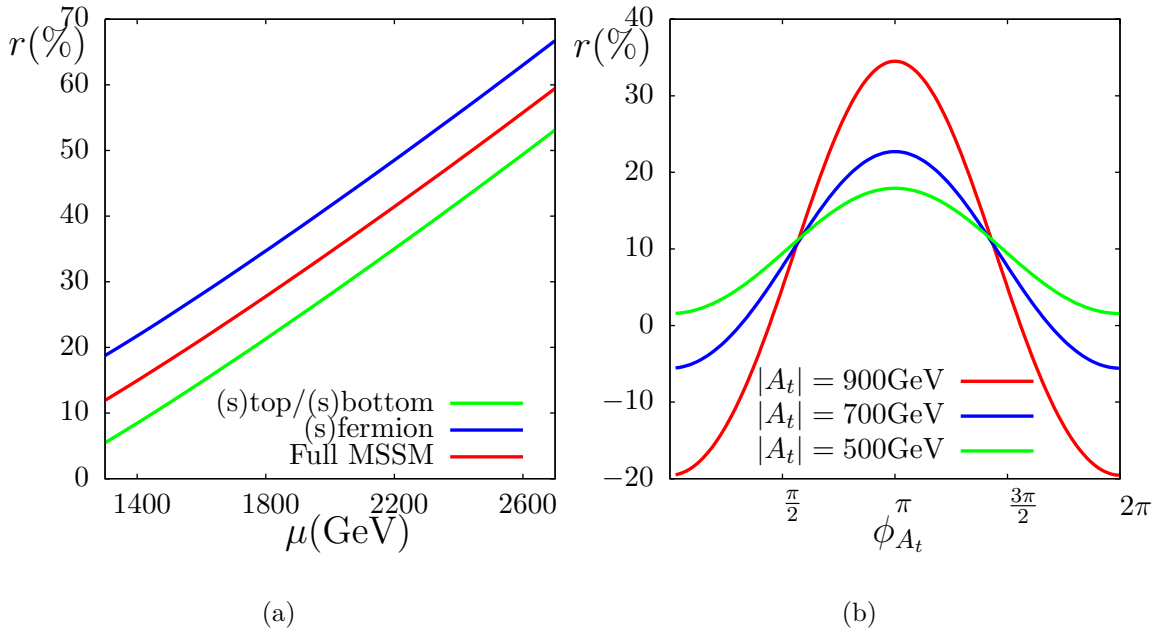

(a) (b)

Figure 6.5: The ratio $r = (\Gamma_{\text{Full Loop}} - \Gamma_{\text{Improved Born}})/\Gamma_{\text{Improved Born}}$ for $\tilde{\chi}^0_2 \to \tilde{\chi}^0_1 h_1$ in the small α_{eff} scenario. (a) r plotted against μ with various subsets of diagrams included. In this plot $M_{H^\pm} = 220\,\text{GeV}$ and $\tan\beta = 10$. b) r plotted against ϕ_{A_t} for three different values $\tan\beta = 3.3, 5, 10$ and hence $|A_t| = 500, 700, 900\,\text{GeV}$ respectively (see Eq. (2.34)), with $M_{H^\pm} = 220\,\text{GeV}$.

In Figure 6.5(b) the small α_{eff} scenario is modified by varying the phase ϕ_{A_t} while keeping $|A_t| = |X_t + \mu^* \cot\beta|$ constant. We find that, like in the CPX scenario, the genuine vertex corrections have the largest effect of order 35% at the nominal value of $\phi_{A_t} = \pi$, while the corrections are only a few percent when the phase is maximally CP-violating for $\phi_{A_t} = \pi/2$. This can again be compared with Figure 6.4(a). Unlike the CPX scenario for which the corrections to the physical decay width into h_1 are minimised at $\phi_{A_t} = 0, 2\pi$, in the small α_{eff} scenario the vertex corrections exhibit another extremum here, with $r \sim -20\%$. As for Figure 6.3(b), the dotted curves in Figure 6.5(b) show a reduced effect of the loop corrections when $|A_t|$ is decreased. Here we vary $\tan\beta$ in order to produce the desired $|A_t|$ from $X_t = -1100\,\text{GeV}$ using Eq. (2.34).

6.4 Other benchmark scenarios

In addition to the CPX and small α_{eff} scenarios, we examined all of the kinematically open decay modes of the form $\tilde{\chi}^0_i \to \tilde{\chi}^0_j h$ for the SPS benchmark points [63]. We show the

ratio r, defined in Eq. (5.16), of the genuine vertex corrections relative to the Improved Born result for the decay widths in Table 6.1. Corrections of over 10% to the partial decay widths were found to be common, indicating that significant effects are not limited to scenarios with very large values of μ.

Decay:	$\widetilde{\chi}_3^0 \to \widetilde{\chi}_2^0 h$	$\widetilde{\chi}_3^0 \to \widetilde{\chi}_1^0 h$	$\widetilde{\chi}_4^0 \to \widetilde{\chi}_1^0 h$	$\widetilde{\chi}_4^0 \to \widetilde{\chi}_2^0 h$	$\widetilde{\chi}_2^0 \to \widetilde{\chi}_1^0 h$	$\widetilde{\chi}_3^0 \to \widetilde{\chi}_1^0 h$
SPS1a	-8.8%	-0.12%	-1.6%	-10.3%	-	-
SPS1b	-11.7%	-2.5%	-2.5%	-12.1%	-	-
SPS2	-	-	-8.2%	-12.3%	-	-
SPS3	-	-	-2.5%	-12.0%	-3.0%	-
SPS4	-	-	-	-9.9%	-	-
SPS5	-	-	-	-1.5%	-	-
SPS6	-	-	-1.4%	-13.4%	-	-
SPS8	-	-	-2.9%	-9.9%	-8.7%	-
SPS9	-	-	-21.2%	-6.2%	-	-17.3%

Table 6.1: Relative effect of the genuine vertex corrections on the decay widths, shown as a percentage, $r(\%)$, for the kinematically open decay modes of the form $\tilde{\chi}_i^0 \to \tilde{\chi}_j^0 h$ for the SPS benchmark points.

Another scenario which we examined was the benchmark point LM5, studied in the CMS Technical Design Report, in the context of the decay $\tilde{\chi}_2^0 \to \tilde{\chi}_1^0 h$ [104]. For this scenario we found the corrections to the partial decay width to be around 5%. However, due to the large branching ratio of around 85% for the process, these corrections translated into an effect of less than a percent on the branching ratio. We will discuss the effect of decay width corrections on the branching ratios further in Chapter 7.

6.5 Comparison with the decay width of a neutralino into a Z boson

As detailed in Section 5.6, we have also computed the one-loop vertex corrections to the $\tilde{\chi}_i^0 \tilde{\chi}_j^0 Z$ vertex. In this section we show numerical results for the decay width, $\Gamma(\tilde{\chi}_2^0 \to \tilde{\chi}_2^0 Z)$, to serve as a comparison to $\Gamma(\tilde{\chi}_2^0 \to \tilde{\chi}_2^0 h_a)$. In Figure 6.6(a), we plot the relative size of the corrections, r, as a function of μ for $M_{h_1} = 40\,\text{GeV}$ and $\tan\beta = 5.5$ in the CPX scenario. We see that, unlike for the Higgs vertex, the vertex corrections are

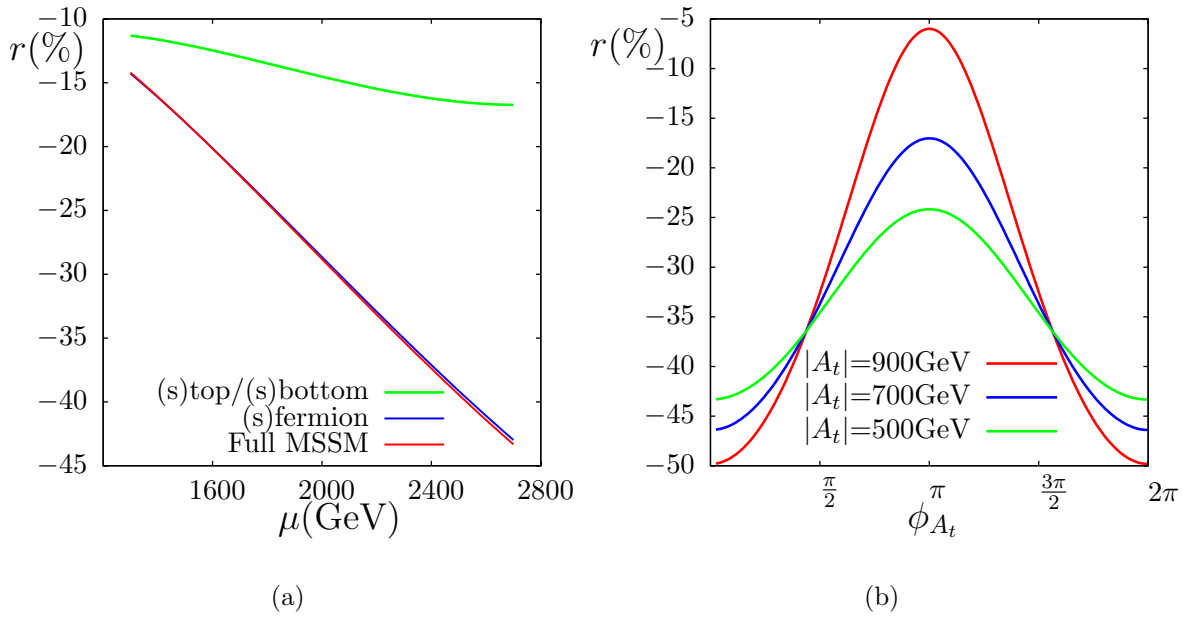

Figure 6.6: The ratio $r = (\Gamma_{\text{Full Loop}} - \Gamma_{\text{Improved Born}})/\Gamma_{\text{Improved Born}}$ for $\tilde{\chi}_2^0 \to \tilde{\chi}_1^0 Z$ in the CPX scenario. (a) r plotted against μ, with various subsets of diagrams included. $M_{H^\pm}$ was adjusted in order to keep $M_{h_1} = 40\,\text{GeV}$ constant and $\tan\beta = 5.5$. (b) r plotted against ϕ_{A_t} for several different values of $|A_t|$. $M_{H^\pm}$ was adjusted in order to keep $M_{h_1} = 45\,\text{GeV}$ constant and $\tan\beta = 7$.

negative, but, like for the Higgs vertex, they increase in relative size as μ increases. For $\mu = 2000\,\text{GeV}$, the corrections are sizeable, with $r \sim -30\%$. If μ is increased above its nominal CPX value of 2000 GeV, the corrections can reach a relative size of -40% or more. The effect from the subset of diagrams including only third generation quarks and squarks $(t, \tilde{t}, b, \tilde{b})$ is less than half of the effect of the full MSSM diagrams, yielding a correction of about -15%. This is in contrast to the Higgs vertex, for which this subset was by far the dominant contribution, enhanced by the large top Yukawa coupling. Inclusion of the other (s)fermion diagrams gives a further negative contribution of about 15% and results in a very good approximation to the full result. The remaining particles in the MSSM, namely the vector bosons, Higgs bosons, neutralinos and charginos, do not play a large role, giving a small, negative contribution.

In Figure 6.6(b), we show the relative size of the corrections to $\Gamma(\tilde{\chi}_2^0 \to \tilde{\chi}_2^0 Z)$ in the CPX scenario with $M_{h_1} = 45\,\text{GeV}$ and $\tan\beta = 7$ as a function of the phase of the trilinear coupling, $A_t = A_b = A_\tau$, for the third generation of sfermions, for various values of $|A_t|$. The red curve shows the variation when $|A_t| = 900\,\text{GeV}$. At $\phi_{A_t} = \pi/2$, the loop corrections show a steep dependence on the phase, ϕ_{A_t}, once again emphasising the

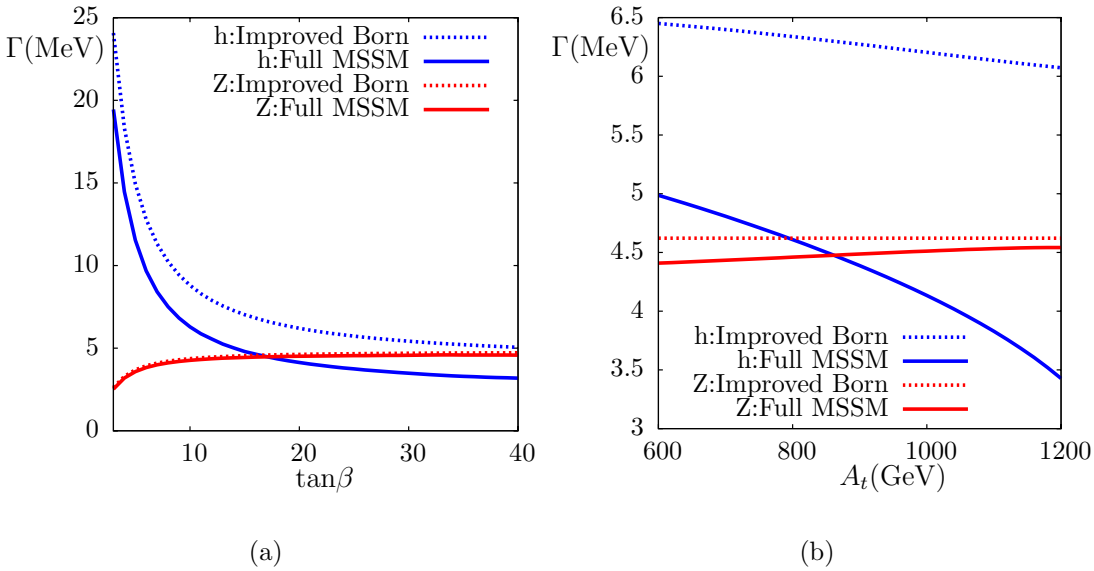

Figure 6.7: The decay widths for $\tilde{\chi}_2^0 \to \tilde{\chi}_1^0 h$ and $\tilde{\chi}_2^0 \to \tilde{\chi}_1^0 Z$ in the light $\tilde{\chi}_1^0$ scenario, (a) plotted against $\tan\beta$, and, (b) plotted against A_t.

importance of including these phases in the calculation. Unlike the Higgs vertex, the negative corrections to the Z vertex are the largest when $\phi_{A_t} = 0$, where they reach a value of $r \sim -50\%$. Here the effect of the subset of triangle diagrams including only third generations of (s)fermions is enhanced. As with the Higgs vertex, for smaller values of $|A_t|$ (blue and green curves in Figure 6.6(b)) the corrections are in general smaller, and the variation with the phase of A_t is less pronounced.

While, in the CPX scenario, the decay width for $\tilde{\chi}_2^0 \to \tilde{\chi}_1^0 Z$ receives corrections of a similar order to the $\tilde{\chi}_2^0 \to \tilde{\chi}_1^0 h_a$ processes, the decay width itself is about a factor of 100 smaller than the Higgs decay widths, and therefore it will not play such a large role in the branching ratio of $\tilde{\chi}_2^0$. We will discuss this further in Chapter 7. In contrast, a scenario in which the decay widths into the Higgs and Z bosons are of similar order is the $\mathcal{CP}$-conserving light $\tilde{\chi}_1^0$ scenario given in Table 2.3. In Figure 6.7(a) we show the variation of the decay widths of $\tilde{\chi}_2^0$ into h and Z, with and without vertex corrections, as a function of $\tan\beta$ for the light $\tilde{\chi}_1^0$ scenario. Like for the CPX scenario, we see a significant increase of the Higgs decay width for small values of $\tan\beta$, while the Z decay width gets smaller in this region. However, for values above $\tan\beta = 10$, both decays have similar widths and can contribute significantly to the $\tilde{\chi}_2^0$ branching ratio. The vertex corrections to the Z decay width are negative and of order less than 5%, while

the vertex corrections to the Higgs decay width are negative, with size increasing from 20% to 37% for the increase in $\tan\beta$ shown.

In Figure 6.7(b) we show the variation of the decay widths of $\tilde{\chi}_2^0$ into h and Z, with and without vertex corrections, as a function of the third generation sfermion trilinear coupling, A_t for the light $\tilde{\chi}_1^0$ scenario. As for their dependence on $\tan\beta$, we observe that the vertex corrections to the Z and Higgs vertices, while both negative, each display a different dependence on A_t. As A_t increases, the Z vertex corrections decrease, while the Higgs vertex corrections increase, enhanced by the diagrams containing third generation quarks and squarks.

6.6 The effect of $\mathcal{CP}$-violating phases from the neutralino sector

So far we have only shown numerical results for $\mathcal{CP}$-violating scenarios in which the phases contribute to the neutralino-chargino sector only at the loop level, such as ϕ_{A_t}. We now consider scenarios where the parameters which enter the neutralino-chargino sector at tree level can also be complex. For the $\mathcal{CP}$-violating Higgs propagator corrections, the combined phase of μA_t plays the largest role at one-loop level. For the genuine vertex corrections, which involve the neutralino sector at tree-level, ϕ_{M_1} can also be important.

In Figure 6.8(a) we show the decay width for $\tilde{\chi}_2^0 \to \tilde{\chi}_1^0 h_1$ as a function of ϕ_{M_1} in the CPX scenario with $M_{h_1} = 62\,\text{GeV}$ and $\tan\beta = 5.5$. We see in the dashed curve that ϕ_{M_1} has a significant effect on $\Gamma(\tilde{\chi}_2^0 \to \tilde{\chi}_1^0 h_1)$ even at the Improved Born level. The green, blue and red curves show the inclusion of the vertex corrections due to the third generation (s)quarks, the full set of (s)fermions and the full MSSM respectively. As seen previously, the former is the largest contribution. One can better understand the shape of the curves in Figure 6.8(a) by considering the (unphysical) "decay widths" for the unnormalised $\mathcal{CP}$-eigenstates, h, H and A, shown in Figure 6.8(b) (in this figure the $\hat{\mathbf{Z}}$ matrix elements are set to $\{1,0,0\}$, $\{0,1,0\}$ and $\{0,0,1\}$ respectively). The neutralino mixing matrix elements, N_{ij}, and hence the couplings of neutralinos to Higgs bosons, have a strong dependence on ϕ_{M_1}. We see that the $\mathcal{CP}$-odd Higgs has a different dependence on ϕ_{M_1} to the $\mathcal{CP}$-even Higgs bosons, but both are symmetric about $\phi_{M_1} = 0$, the former (latter) having a minimum (maximum) at $\phi_{M_1} = 0$. However, when $\phi_{M_1} = 0$, there is still $\mathcal{CP}$-violation in the Higgs sector due to the non-zero ϕ_{A_t} and ϕ_{M_3}. This can be seen in

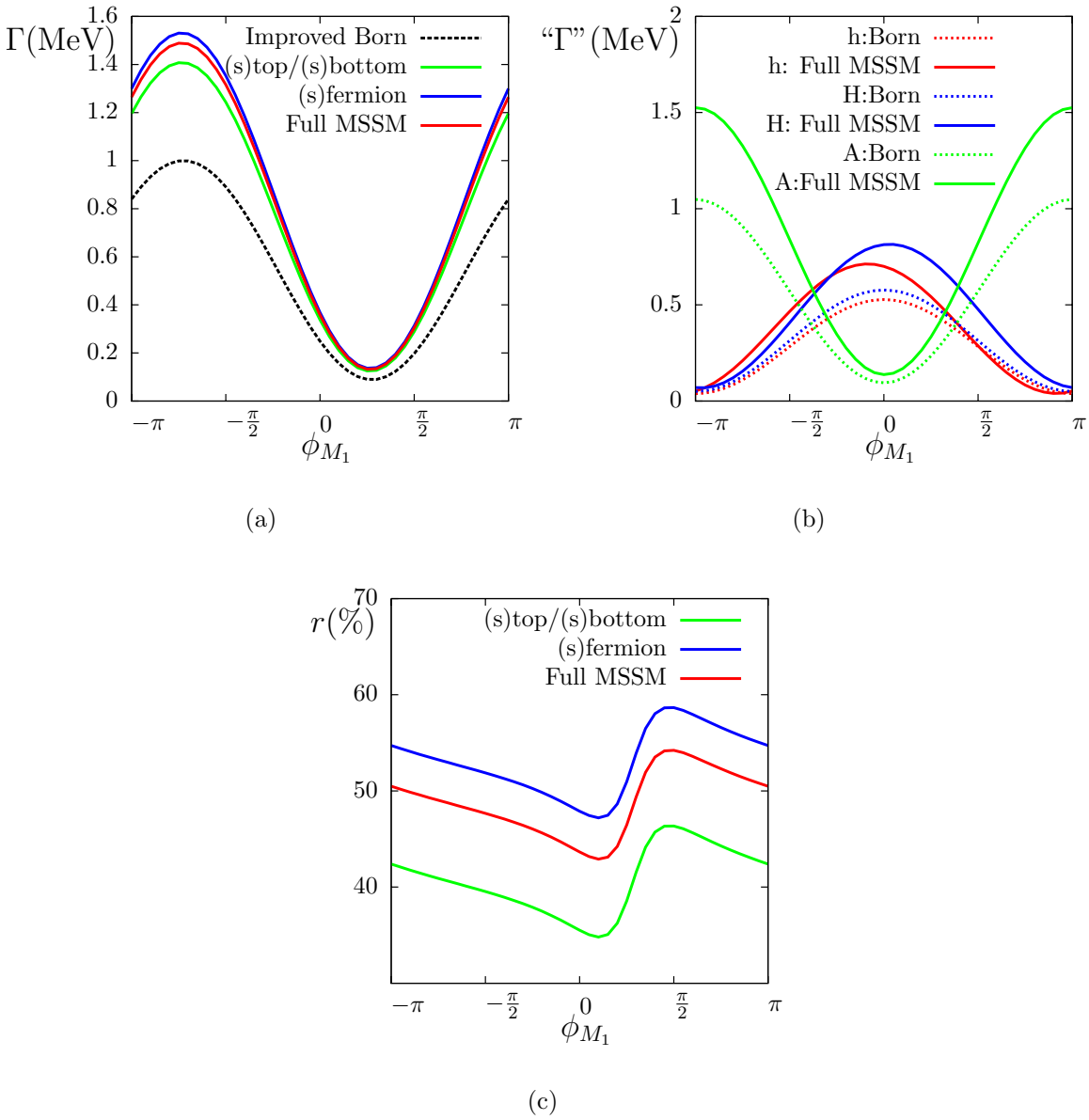

Figure 6.8: (a) Decay width for $\tilde{\chi}_2^0 \to \tilde{\chi}_1^0 h_1$ as a function of ϕ_{M_1}, with various subsets of vertex corrections included; (b) unphysical "decay widths" into unnormalised $\mathcal{CP}$-eigenstates, "Γ"$(\tilde{\chi}_2^0 \to \tilde{\chi}_1^0 h, H, A)$ as a function of ϕ_{M_1} (i.e.the $\hat{\mathbf{Z}}$ matrix elements are set to $\{1,0,0\}$, $\{0,1,0\}$ and $\{0,0,1\}$ respectively); (c) $r = (\Gamma_{\text{Full Loop}} - \Gamma_{\text{Improved Born}})/\Gamma_{\text{Improved Born}}$ for $\tilde{\chi}_2^0 \to \tilde{\chi}_1^0 h_1$, as a function of ϕ_{M_1} with various subsets of vertex corrections included. All plots are for the CPX scenario with $M_{h_1} = 60\,\text{GeV}$ and $\tan\beta = 5.5$.

the loop-corrected widths, the maxima and minima of which are shifted slightly. When the appropriate linear combination of h, H and A is made using the $\hat{\mathbf{Z}}$ factors (see Figure 3.3(b); there is almost no variation from these $\hat{\mathbf{Z}}$ factors when ϕ_{M_1} is varied), the resulting decay width for h_1 is asymmetric about $\phi_{M_1} = 0$. Although ϕ_{M_1} plays very

little role in the pure Higgs sector corrections, we see that its effect can be significant for the $\tilde{\chi}_2^0\tilde{\chi}_1^0 h_1$ vertex corrections. Moving away from the nominal CPX value of $\phi_{M_1} = 0$ where the vertex corrections amount to $r \sim 45\%$, we see in Figure 6.8(c), that the vertex corrections can increase to $r \sim 55\%$ for $\phi_{M_1} \sim \pi/2$.

6.7 Summary

In this chapter we have presented numerical results for the one-loop decay widths for $\tilde{\chi}_2^0 \to \tilde{\chi}_1^0 h_{1,2,3}$ in various $\mathcal{CP}$-violating and $\mathcal{CP}$-conserving scenarios. We compared these to results for the one-loop decay widths for $\tilde{\chi}_2^0 \to \tilde{\chi}_1^0 Z$. For the Higgs vertex, we found particularly large vertex corrections of $\mathcal{O}(45\%)$ for the unexcluded parameter region in the CPX scenario, where a light Higgs could be produced by the decay of the second lightest neutralino. These vertex corrections could be further enhanced with the variation of parameters from the neutralino sector, such as ϕ_{M_1}, which do not play a large role in the Higgs sector. In the context of utilising the decay, $\tilde{\chi}_2^0 \to \tilde{\chi}_1^0 h_1$, in the region of the "CPX hole", it was important to compute the effect of the genuine vertex corrections on the decay width, since it had been seen previously that such genuine vertex corrections for $h_2 \to h_1 h_1$ had a dramatic effect on the size and position of the hole [30]. In assessing the viability of this decay at the LHC, it will be the branching ratios rather than the decay widths that are important. In the next chapter we present results which show the effect the large corrections to the decay widths have on the branching ratios. We will then use these results to discuss the prospects for closing the "CPX hole" at the LHC using the decay $\tilde{\chi}_2^0 \to \tilde{\chi}_1^0 h_1$.

Chapter 7

Results for the branching ratio of a neutralino into a light Higgs boson

7.1 Calculation of branching ratios

In the previous chapter, we found that the genuine vertex corrections to the partial decay width $\Gamma(\tilde{\chi}_2^0 \to \tilde{\chi}_1^0 h_1)$ were of order 45% in the CPX scenario. For phenomenology at the LHC it is important to consider, in addition to the decay widths, also the branching ratios of neutralinos. In this section, we compute the branching ratios of $\tilde{\chi}_2^0$, incorporating our loop-corrected decay widths for the two-body decays, $\tilde{\chi}_2^0 \to \tilde{\chi}_1^0 h_{1,2,3}$ and $\tilde{\chi}_2^0 \to \tilde{\chi}_1^0 Z$. In the CPX scenario, depending on its mass, $\tilde{\chi}_2^0$ can decay via the following decay modes:

$$\tilde{\chi}_2^0 \;\to\; \tilde{\chi}_1^0 h_1,\ \tilde{\chi}_1^0 h_2,\ \tilde{\chi}_1^0 h_3,\ \tilde{\chi}_1^0 Z,\ \tilde{\chi}_1^0 f\bar{f},\ \tilde{f}_{1,2}\bar{f},\ \bar{\tilde{f}}_{1,2} f. \tag{7.1}$$

Where kinematically possible, we calculate the decays $\tilde{\chi}_2^0 \to \tilde{\chi}_1^0 h_a$, which produce on-shell neutral Higgs bosons, as two-body decays, including the genuine vertex corrections as detailed in the previous chapters. Where kinematically possible, we also calculate the decay $\tilde{\chi}_2^0 \to \tilde{\chi}_1^0 Z$ into an on-shell Z boson as a two-body decay, including the equivalent genuine vertex corrections as detailed in the previous chapters. Note, however, that the amplitude for this decay is suppressed by several orders of magnitude in the CPX scenario, since the Z boson only couples to the higgsino component of each of the neutralinos, while the large value of μ renders $\tilde{\chi}_1^0$ and $\tilde{\chi}_2^0$ mostly bino and wino, respectively. Finally, we calculate the 3-body decay $\tilde{\chi}_2^0 \to \tilde{\chi}_1^0 f\bar{f}$. For this, we include, firstly, the diagrams where an off-shell Higgs boson is exchanged (i.e. where some or all of h_1, h_2, h_3 are too heavy to be produced on-shell). For these diagrams we use the unitary

$\hat{\mathbf{U}}$ matrix elements and masses from `FeynHiggs` to construct effective couplings (see Section 3.4.11) which take into account the two-loop Higgs propagator-type corrections. Secondly, in the three-body decay, where the kinematics do not permit an on-shell Z boson, we include the diagram where a Z boson is exchanged, along with the diagram where the would-be Goldstone boson, G, is exchanged (in this way a proper cancellation of the gauge dependence is ensured). Thirdly, we include in the three-body decay the diagrams where a sfermion is exchanged. As the neutralino mass approaches the scale of the sfermion masses, the possibility of on-shell production of sfermions arises, which subsequently decay into $\tilde{\chi}_1^0$. To treat this threshold region, we include a finite width for each sfermion, calculated from its self-energy. All self-energies and two- and three-body partial decay widths were calculated using `FeynArts` and `FormCalc`.

7.2 Numerical results for the branching ratio in the CPX scenario

The resulting branching ratios of $\tilde{\chi}_2^0$ in the CPX scenario are plotted as a function of the neutralino mass, $M_{\tilde{\chi}_2^0}$, in Figure 7.1a, with $\tan\beta = 5.5$ and $M_{h_1} = 40\,\text{GeV}$. Both the Improved Born and full MSSM vertex-corrected results are shown. We see that for $M_{\tilde{\chi}_2^0} \lesssim 190\,\text{GeV}$, $\text{BR}(\tilde{\chi}_2^0 \to \tilde{\chi}_1^0 h_1) \approx 100\%$, and therefore the loop corrections to the $\tilde{\chi}_2^0 \to \tilde{\chi}_1^0 h_1$ partial width have negligible effect. As one increases $M_{\tilde{\chi}_2^0}$ from 190 to 470 GeV, the on-shell decays $\tilde{\chi}_2^0 \to \tilde{\chi}_1^0 h_2$ and $\tilde{\chi}_2^0 \to \tilde{\chi}_1^0 h_3$ become kinematically allowed. This causes $\text{BR}(\tilde{\chi}_2^0 \to \tilde{\chi}_1^0 h_1)$ to vary from 100% to around 25%. In this region, the three competing decay modes into Higgs bosons all receive large vertex corrections of order 50% (see Figure 6.2(b)). However, since these vertex corrections have similar structure, their effects tend to cancel each other out, producing an effect of only a few percent on the branching ratios. Thus, the Improved Born approximation works well in this region.

The effect of vertex corrections on the branching ratio will be more significant in regions of parameter space where there is another competing decay mode of $\tilde{\chi}_2^0$ which does not have loop corrections of a similar structure to $\tilde{\chi}_2^0 \to \tilde{\chi}_1^0 h_1$. In the CPX scenario, this competition will never be provided by the highly suppressed decay into a Z boson. However, for large enough $M_{\tilde{\chi}_2^0}$, decays via sfermions become important. While the Higgs bosons require both a non-zero gaugino and higgsino component to couple to neutralinos, sfermions couple only to the gaugino part. Thus, if sfermion decays can proceed on-shell, they will, in this scenario, dominate over the Higgs decay modes,

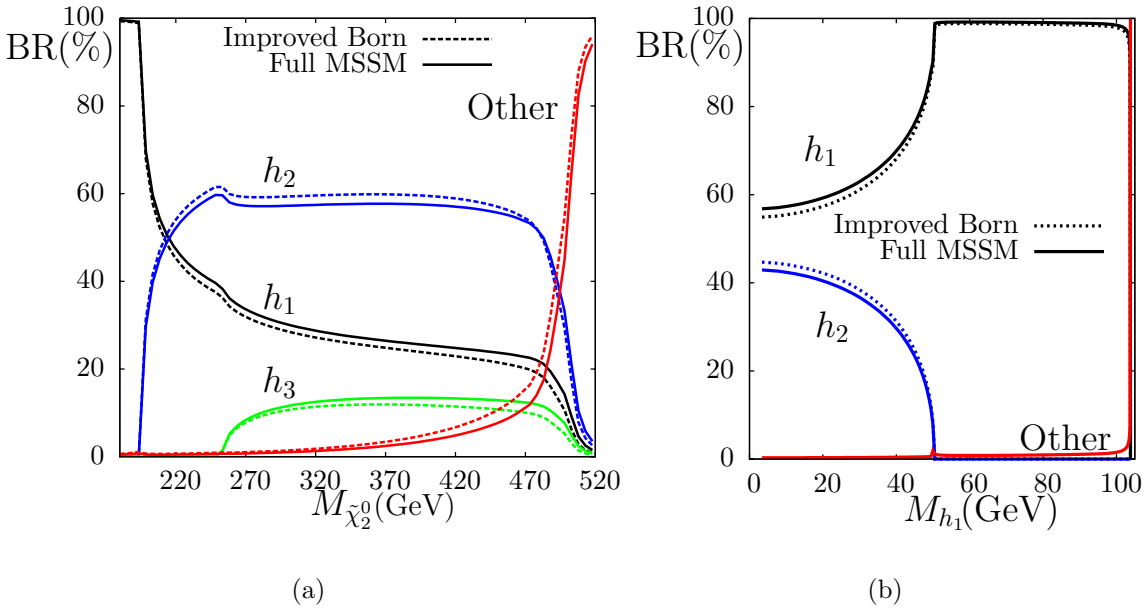

Figure 7.1: Branching ratio for each of $\tilde{\chi}_2^0 \to \tilde{\chi}_1^0 h_{1,2,3}$ and for the other decay modes, $\tilde{\chi}_2^0 \to \tilde{\chi}_1^0 Z$ and $\tilde{\chi}_2^0 \to \tilde{\chi}_1^0 f\bar{f}$ (labelled "Other") (a) shown as a function of $M_{\tilde{\chi}_2^0}$, for $M_{h_1} = 40\,\text{GeV}$ and $\tan\beta = 5.5$; (M_2 was varied as input to produce the change in $M_{\tilde{\chi}_2^0}$ (mostly wino); $M_{\tilde{\chi}_1^0}$ (mostly bino) also varies due to the GUT relation between M_2 and M_1; $M_{H^\pm}$ was varied as input to keep M_{h_1} constant; M_{h_2} and M_{h_3} will vary with $M_{H^\pm}$); and, (b) shown as a function of M_{h_1} for $\tan\beta = 5.5$ and $M_2 = 200\,\text{GeV}$ ($M_{\tilde{\chi}_2^0}$ and $M_{\tilde{\chi}_1^0}$ are 198.5 GeV and 94.7 GeV respectively; $M_{H^\pm}$ was varied as input). In both plots we show the Improved Born approximation as a dashed line and the full MSSM result as a solid line.

rendering $\text{BR}(\tilde{\chi}_2^0 \to \tilde{\chi}_1^0 h_1) \approx 0$. A threshold region for $450 \lesssim M_{\tilde{\chi}_2^0} \lesssim 520\,\text{GeV}$ can be seen in Figure 7.1(a) for the curve labelled"Other" ($\tilde{\chi}_2^0 \to \tilde{\chi}_1^0 Z$ and $\tilde{\chi}_2^0 \to \tilde{\chi}_1^0 f\bar{f}$ decays). Within this region, the existence of competing decay modes means that the genuine vertex corrections are very important. The maximum effect occurs near $M_{\tilde{\chi}_2^0} \sim 500\text{GeV}$, where the positive vertex corrections to the Higgs decay widths result in a reduction of the branching ratio $\text{BR}(\tilde{\chi}_2^0 \to \tilde{\chi}_1^0 f\bar{f})$ of more than 10% compared to its Improved Born value.

In Figure 7.1(b), we show the branching ratios of $\tilde{\chi}_2^0$ as a function of M_{h_1}, to be compared with Figures 6.1(a) and 6.2(a). Here $M_2 = 200\,\text{GeV}$ and $\tan\beta = 5.5$, so only decays into $\tilde{\chi}_1^0 h_1$, $\tilde{\chi}_1^0 h_2$, $\tilde{\chi}_1^0 Z$ and $\tilde{\chi}_1^0 f\bar{f}$ (the latter two labelled "Other") are kinematically open. For $M_{h_1} \gtrsim 50\text{GeV}$, the second lightest Higgs boson is too heavy to be produced on-shell and so $\text{BR}(\tilde{\chi}_2^0 \to \tilde{\chi}_1^0 h_1)$ is close to 100%. In the CPX hole, with $M_{h_1} \approx 40\,\text{GeV}$, we find $\text{BR}(\tilde{\chi}_2^0 \to \tilde{\chi}_1^0 h_1) \approx 79\%$, an increase of around 3% compared to the Improved Born value.

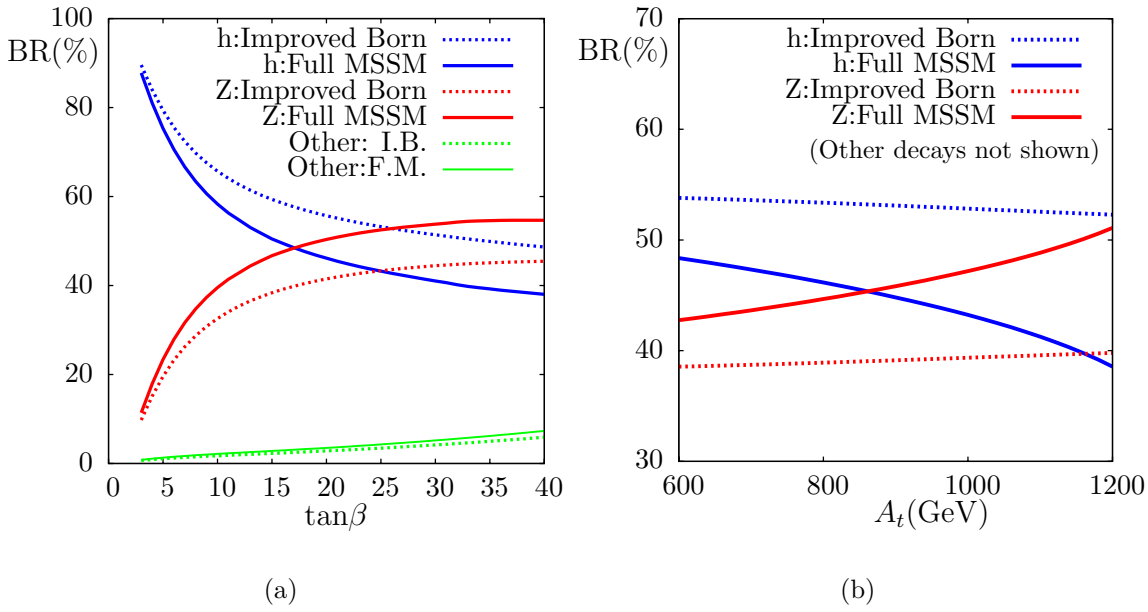

Figure 7.2: Branching ratios for each of $\tilde{\chi}_2^0 \to \tilde{\chi}_1^0 h$, $\tilde{\chi}_2^0 \to \tilde{\chi}_1^0 Z$ and $\tilde{\chi}_2^0 \to \tilde{\chi}_1^0 f\bar{f}$ (labelled "Other") in the $\mathcal{CP}$-conserving "light $\tilde{\chi}_1^0$ scenario": (a) shown as a function of $\tan\beta$, for fixed $A_f = 1\,\text{TeV}$; and, (b) shown as a function of A_t, for fixed $\tan\beta = 20$. We show the Improved Born approximation (I.B.) as the dotted line, and the full MSSM result (F.M.) as the solid line.

7.3 Numerical results for the branching ratio in other scenarios

Although we found large loop corrections to the partial decay widths of $\tilde{\chi}_2^0 \to \tilde{\chi}_1^0 h_{1,2,3}$ in the CPX scenario, the effects on the branching ratios turn out to be significantly smaller, because the Higgs decays are not competing with other modes and so the large genuine vertex corrections cancel each other out. This will also be the case for the small α_{eff} scenario, in which the Z decay mode is also suppressed and the sfermions are heavy. However, this situation is not generic, and large vertex corrections can affect the branching ratios if there are other competing decay modes with vertex corrections of a different structure. In non-gaugino-like scenarios, without a large hierarchy between M_2 and μ, the decays into Higgs bosons are more likely to compete with the decays into Z bosons and sfermions.

For example, in Figure 7.2 we show the Improved Born and full MSSM branching ratios for the "light $\tilde{\chi}_1^0$ scenario" of Table 2.3. Here we can have $\text{BR}(\tilde{\chi}_2^0 \to \tilde{\chi}_1^0 h) \sim \text{BR}(\tilde{\chi}_2^0 \to \tilde{\chi}_1^0 Z)$. In the previous chapter, we computed genuine vertex corrections to both $\Gamma(\tilde{\chi}_2^0 \to$

$\tilde{\chi}_1^0 h$) and $\Gamma(\tilde{\chi}_2^0 \to \tilde{\chi}_1^0 Z)$, and found the former (latter) to be negative and of order 20% (3%) and 35% (2%) for $A_t = 500\,\text{GeV}$ and $A_t = 1200\,\text{GeV}$, respectively (see Figures 6.7(a) and 6.7(b)). The corrections are further enhanced at large values of $\tan\beta$. In this scenario, the branching ratio for $\tilde{\chi}_2^0 \to \tilde{\chi}_1^0 h$ happens to be near 50%. Thus, the effect of the vertex corrections on the branching ratios is maximised in this case. The plots in Figure 7.2 show corrections to the branching ratio of more than 10%.

7.4 Prospects for the "CPX Hole"

In Section 7.2, we found that $\tilde{\chi}_2^0 \to \tilde{\chi}_1^0 h_1$ has a large branching ratio, $\text{BR}(\widetilde{\chi}_2^0 \to \widetilde{\chi}_1^0 h_1) \sim 79\%$, for the "CPX hole", i.e. in the region where a light Higgs is unexcluded by present data. We now investigate whether Higgs production in neutralino decays at the LHC could help to cover this parameter region. Consider the SUSY cascade decay chain starting with a gluino;

$$\widetilde{g} \to \widetilde{f}\bar{f} \to \widetilde{\chi}_2^0 f\bar{f} \to \widetilde{\chi}_1^0 f\bar{f} h_i \to \widetilde{\chi}_1^0 f\bar{f} b\bar{b}(\tau^+\tau^-). \tag{7.2}$$

Coloured sparticles like gluinos are expected to be produced in large numbers at the LHC provided they are light enough, (see eg. Ref. [114] for detailed analyses of SUSY cascade decays). These gluinos will decay into lighter coloured sparticles, namely the squarks with masses around 500 GeV (see Table 2.3). For most squarks, the only way to conserve R-parity will be to decay into $\tilde{\chi}_2^0$, $\tilde{\chi}_1^\pm$ and $\tilde{\chi}_1^0$. As shown in the previous section, 79% of the produced $\tilde{\chi}_2^0$ will decay into h_1 in this scenario for a Higgs mass of 40 GeV. The light Higgs boson then decays mostly into $b\bar{b}$ (91%), and also $\tau^+\tau^-$.

Branching ratios for all parts of the decay chain, except the decays involving Higgs bosons, were computed at tree level using `FeynArts` and `FormCalc`. For decays involving Higgs bosons, such as $\tilde{t}_2 \to \tilde{t}_1 h_a$, we use an Improved Born approximation, as in Eq. 5.15. We computed the branching ratio for $\widetilde{g} \to \tilde{q}_{1,2} q$ for each of $q = u, d, c, s, t, b$. We found that $\tilde{b}_1$, $\tilde{u}_1$, $\tilde{d}_2$, $\tilde{c}_2$, $\tilde{s}_1$, $\tilde{s}_2$ all have substantial branching ratios to decay into $\tilde{\chi}_2^0$. Summing over the various decay modes we found that 17% of all gluinos produced in this scenario decay via a squark into $\widetilde{\chi}_2^0$.

Combining $\text{BR}(\widetilde{\chi}_2^0 \to \widetilde{\chi}_1^0 h_1) \sim 79\%$ with $\text{BR}(\widetilde{g} \to \widetilde{\chi}_2^0 q\bar{q}) \sim 17\%$, we estimate that around 13% of the gluinos produced in this scenario will decay into h_1. Thus, SUSY cascade decays where a light Higgs is produced in the decay of the second-lightest neutralino

appear to be a promising possibility to cover this problematic parameter region where standard search channels may only have small sensitivities. Detailed experimental analyses would be needed to determine whether it is indeed possible in such a case to extract a Higgs signal from the SM and SUSY backgrounds.

It should be noted in this context that the CMS collaboration has performed a full detector simulation and event reconstruction for the production of a Higgs boson at the end of a cascade of supersymmetric particles starting with squarks and gluinos [104]. These results, obtained for the benchmark point LM5, cannot be directly translated to the case of the CPX scenario, since in the case of LM5 the Higgs boson is much heavier, $M_h \sim 115$ GeV, than in the region of the CPX scenario that we are considering here. The b jets resulting from the Higgs decay in the CPX scenario are therefore softer than for LM5, so that cuts on the energy of the jets will be less efficient to suppress the QCD background. Therefore, further investigation, beyond the scope of this work, would be needed to determine whether such an event reconstruction would be possible for the CPX scenario. In light of the large branching ratio we have found for this decay, and given that it remains unclear whether the "CPX hole" can be covered using other channels at the LHC, the production of the light Higgs boson in the $\widetilde{\chi}_2^0 \to \widetilde{\chi}_1^0 h_1$ decay would certainly be worth pursuing.

Chapter 8

Results for the decay width of a heavy Higgs boson into neutralinos

8.1 Motivation

In the previous chapters we saw that the one-loop corrections to the $\tilde{\chi}_i^0 \tilde{\chi}_j^0 h_a$ vertex could have a large effect on the decays of neutralinos into light Higgs bosons. A related process to the production of a Higgs boson in the decay of a neutralino is the decay of a heavy Higgs boson into two neutralinos, $h_a \to \tilde{\chi}_i^0 \tilde{\chi}_j^0$. This process, with a possible signature of four leptons plus missing energy, can also be phenomenologically important [34–37]. The CMS study in Ref. [34] focused on the decay $H, A \to \tilde{\chi}_2^0 \tilde{\chi}_2^0$, where each $\tilde{\chi}_2^0$ subsequently decays into two leptons and the $\tilde{\chi}_1^0$ LSP, i.e. $\tilde{\chi}_2^0 \to \tilde{\chi}_1^0 l^+ l^-$, where $l = e$ or μ. The authors reported a 5σ discovery potential for Higgs masses in the region of 230 to 450GeV for low to intermediate values of $\tan\beta$, and for sufficiently light neutralinos. The authors of Refs. [35, 36] extended this study to include all kinematically possible decays into neutralinos and charginos, $H, A \to \tilde{\chi}_i^0 \tilde{\chi}_j^0$, $\tilde{\chi}_k^+ \tilde{\chi}_l^-$, for $i, j = 2, 3, 4$ and $k, l = 1, 2$, finding for the scenarios studied that this extended the discovery region to even larger values of $M_A \sim 800\,\text{GeV}$, where the heavy Higgs bosons cannot be discovered using decays into SM particles (see eg. Refs. [38, 39]). The heavier neutralinos and charginos are more likely to have masses greater than those of the sleptons, $\tilde{e}_{1,2}$ and $\tilde{\mu}_{1,2}$, so that the neutralino decay into leptons and the lightest neutralino can proceed via a two-body decay into a slepton, enhancing the branching ratios to leptonic final states and hence the discovery potential. In Ref. [37], it was found that these decays can be utilised not only for the initial discovery of the Higgs bosons, but also in the determination of their masses and other MSSM parameters using invariant mass techniques.

As already mentioned, partial one-loop results have been published previously for the decays $H, A \to \tilde{\chi}_i^0 \tilde{\chi}_j^0$ in both the Feynman-diagrammatic [101, 102] and effective potential [109] approaches. The predictions in Refs. [101] and [102] were restricted to the case of real parameters, with the former including only the contributions from diagrams containing quarks and squarks in the loops, and the latter including only diagrams containing sfermions and fermions in the loops. For the effective potential approach in Ref. [109], complex parameters were allowed, but the corrections were restricted to contributions from third generation quarks and squarks, charginos, neutralinos, gauge and Higgs bosons. In this chapter we will present the full one-loop results for the decay widths, $\Gamma(h_a \to \tilde{\chi}_i^0 \tilde{\chi}_j^0)$, including all possible MSSM particles in the loops and allowing for complex parameters as described in Chapter 5.[1] As in Chapters 5-7, we use Equation (5.14) to supplement these results with the state-of-the-art two-loop Higgs propagator-type corrections as implemented in the code `FeynHiggs` [41, 79–81], thus obtaining the most precise prediction currently available for this class of processes. We will see the importance of including all particles in the loops for obtaining the correct size and magnitude of the vertex corrections in the scenarios studied. We also find that the $\mathcal{CP}$-violating phases can enhance or suppress the relative effect of the corrections. The $\mathcal{CP}$-violating phases turn out to play a particularly interesting role for the decays of Higgs bosons into polarised neutralinos. This will lead us to propose a study of $\mathcal{CP}$-asymmetries in the decays, $h_2, h_3 \to \tilde{\chi}_2^0 \tilde{\chi}_2^0$, using the polarisation of the neutralinos as way of determining the existence of $\mathcal{CP}$-violation in the Higgs sector.

8.2 Numerical results for decay widths

We begin by considering the decay widths for the parameter "Point 1" studied in Ref. [35] in the context of four-lepton events from Higgs boson decays into neutralino and chargino pairs. We give the low-energy MSSM parameters for this point in Table 2.3 under the heading, "4L1". The corresponding tree-level neutralino and chargino masses are (in GeV);

$$m_{\tilde{\chi}_1^+} = 176.3,\ m_{\tilde{\chi}_2^+} = 514.0,\ m_{\tilde{\chi}_1^0} = 89.7,\ m_{\tilde{\chi}_2^0} = 176.3,\ m_{\tilde{\chi}_3^0} = 506.9,\ m_{\tilde{\chi}_4^0} = 510.9$$

[1] Note that in this chapter we use the parameter renormalisation scheme where the masses of $\tilde{\chi}_1^0$, $\tilde{\chi}_2^0$, $\tilde{\chi}_3^0$ are fixed on-shell, as this is convenient for extending the calculations to processes where $\tilde{\chi}_3^0$ is produced in Higgs decays.

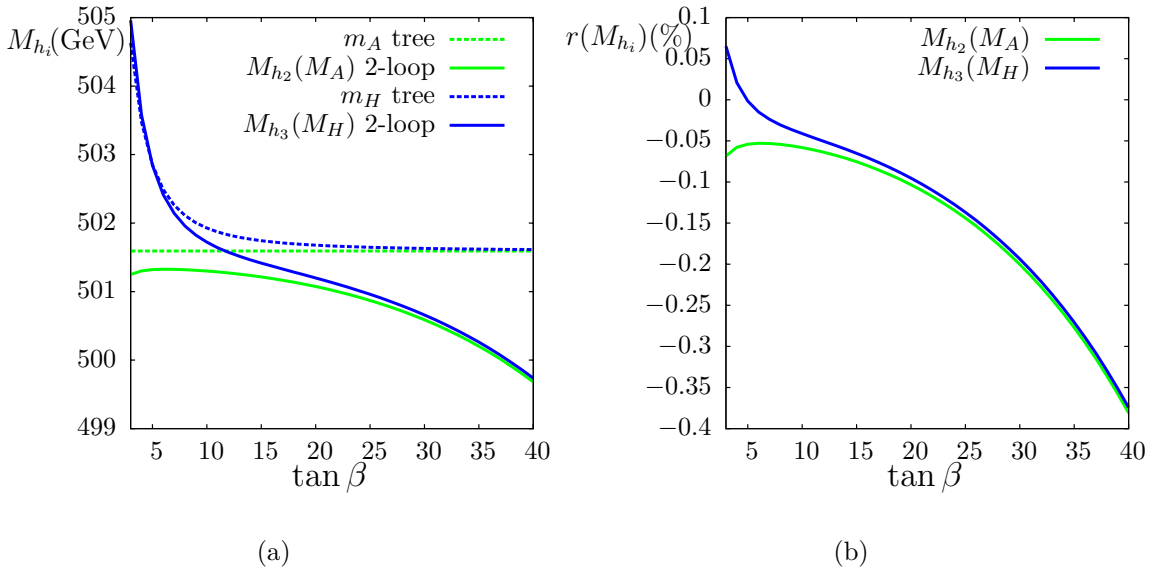

Figure 8.1: (a) Higgs masses in the 4L1 scenario, obtained from `FeynHiggs 2.7.0`, at tree-level and at loop-level, where the latter includes the full one-loop and the dominant two-loop $\mathcal{O}(\alpha_t\alpha_s)$ corrections as discussed in Section 3.4.7; (b) Size of the loop corrections to the masses relative to the corresponding tree-level Higgs masses; $r(M_{h_i}) = (M_{h_i} - m_{h_i})/m_{h_i}$.

for $\tan\beta = 20$. The authors of Ref. [35] showed that, for much of the M_A–$\tan\beta$ plane in this scenario, the percentage of $H, A \to 4l + X$ events coming from the decays into the second lightest neutralino, $H, A \to \tilde{\chi}_2^0\tilde{\chi}_2^0$, is larger than 90%. The heavier neutralinos and charginos are not kinematically accessible for $M_A \lesssim 700\,\text{GeV}$. It was shown that the highest cross section times branching ratio for four lepton events from Higgs bosons at the LHC was for the region of $\tan\beta \sim 10 - 30$ with $M_A \sim 400 - 500\,\text{GeV}$. The authors found the resulting discovery region of $\tan\beta \sim 4.5 - 40$, $M_A \sim 350 - 600\,\text{GeV}$ for $300\,\text{fb}^{-1}$ at the LHC for this particular scenario.

In Figure 8.1(a) we show how the two heavy Higgs masses, M_{h_2} and M_{h_3},[2] obtained as output from `FeynHiggs 2.70`,[3] vary with $\tan\beta$ in the 4L1 scenario with fixed $M_{H^\pm} = 508\,\text{GeV}$ as input. We see that the mass degeneracy of the heavy Higgs bosons, both at tree-level and at two-loop, becomes more pronounced for large $\tan\beta$. Figure 8.1(b) shows the size of the mass corrections relative to the tree-level Higgs masses. We see

[2]For the $\mathcal{CP}$-conserving parameters shown in this plot, h_2 is the $\mathcal{CP}$-odd A and h_3 is the $\mathcal{CP}$-even H, but we continue to denote the Higgs bosons in order of their masses so as to agree with later results where we include $\mathcal{CP}$-violation.

[3]Note that we use `FeynHiggs 2.70` for this scenario with large $\tan\beta$, since it contains improvements to the implementation of the resummation of the QCD corrections to the bottom mass for the flags chosen. Later in this chapter, when we consider SPS1a with lower $\tan\beta$ we use `FeynHiggs 2.6.5` as usual.

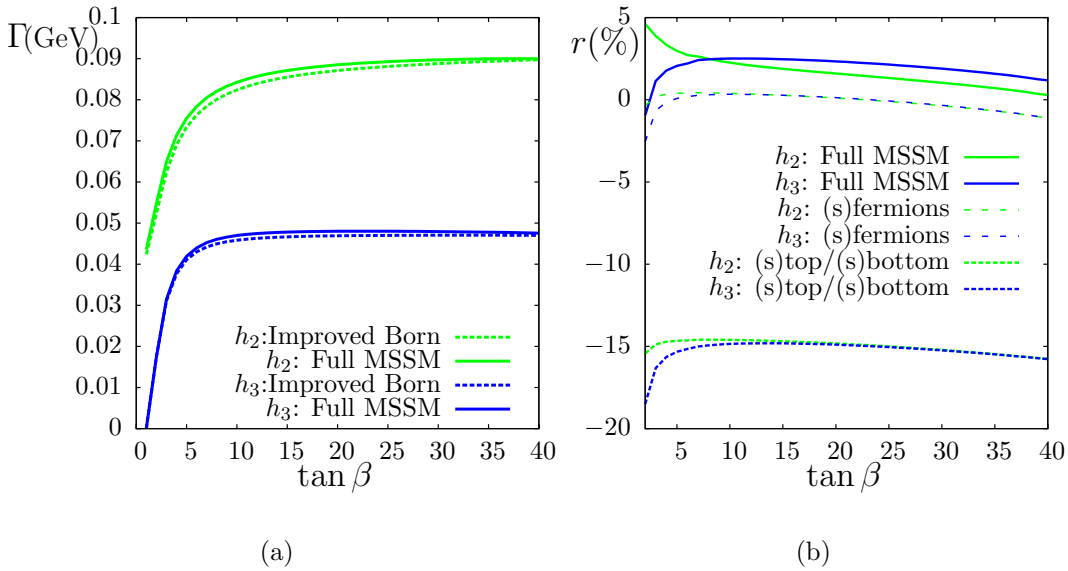

(a) (b)

Figure 8.2: (a) Decay widths $\Gamma(h_{2,3} \to \tilde{\chi}_2^0\tilde{\chi}_2^0)$ as a function of $\tan\beta$ in the 4L1 scenario, with $M_{H^\pm} = 508\,\text{GeV}$. The dashed lines show the Improved Born result, while the bold lines include the full one-loop vertex corrections; (b) Relative size of the vertex corrections compared to the Improved Born result for various UV-finite subsets of diagrams indicated by different dashing. Note that where the green dashed curves are not visible in the figure, they are directly underneath the blue dashed curves.

that, over the range of $\tan\beta$ shown, the effects are less than half a percent and generally become more negative as $\tan\beta$ increases. On the other hand, for $\tan\beta = 20$, the lightest Higgs mass at tree-level, m_h, is 90.7 GeV, while the two-loop mass, M_{h_1}, is 109.4 GeV, an increase of 20.6%. The heavier Higgs masses are significantly less sensitive to loop corrections than the lightest Higgs mass.

In Figure 8.2(a) we show the decay widths for $h_2, h_3 \to \tilde{\chi}_2^0\tilde{\chi}_2^0$, both at the Improved Born level and including the one-loop vertex corrections, as a function of $\tan\beta$ for the 4L1 scenario with $M_{H^\pm} = 508\,\text{GeV}$. We see that the decay width of h_2 (A) is nearly a factor of two larger than the decay width of h_3 (H). As $\tan\beta$ increases to large values, the decay widths become independent of $\tan\beta$, while for $\tan\beta$ below 5, both decay widths drop off due to the increase in $M_{\tilde{\chi}_2^0}$.

Figure 8.2(b) shows the relative size, r, of the genuine vertex corrections compared with the Improved Born decay widths, as a function of $\tan\beta$ for various UV-finite subsets of diagrams. We see that the vertex corrections including all the MSSM particles in the loops are only of the order of a few percent throughout the range of $\tan\beta$ shown, significantly less than the impact of the vertex corrections seen for the decay of the

second lightest neutralino into the lightest Higgs boson in the CPX scenario. This is expected since the heavier Higgs bosons are less affected by large loop corrections than the lightest Higgs boson. The 4L1 scenario furthermore has a smaller value for $|\mu|$ than the CPX scenario, so the vertex corrections are not enhanced to the same extent. Also, the squark mass parameters in the 4L1 scenario are defined to be at the TeV scale, with the trilinear coupling, A_f, is set to zero, so the contribution from self-energies and triangle diagrams containing quarks and squarks is expected to be less than for the CPX scenario. Figure 8.2(b) shows that the effect of the diagrams containing only third generation quarks and squarks is around -15% for the range of $\tan\beta$ shown. The remaining (s)fermions then have a positive effect of around $+15\%$, largely cancelling the effect of the (s)top and (s)bottom quarks. The further contributions from vector bosons, Higgs bosons and their superpartners are small and positive, giving a total effect of only a few percent. We see that including all possible MSSM particles in the loops is important for obtaining both the correct magnitude and size of the vertex corrections in this scenario. Hence our result is a significant improvement on what was previously available in the literature.

In Figure 8.3(a) we show the decay widths for $h_2, h_3 \to \tilde{\chi}^0_2\tilde{\chi}^0_2$, both at Improved Born level and including the one-loop vertex corrections, as a function of $M_{H^\pm}$ for the 4L1 scenario with $\tan\beta = 20$. As expected from phase space considerations, the decay widths increase as the Higgs masses increase. For $M_{H^\pm} \sim 688\,\text{GeV}$ there is a kink where the $\mathcal{CP}$-even Higgs boson, H, becomes lighter than the $\mathcal{CP}$-odd Higgs boson, A. Figure 8.3(b) shows the relative size of the vertex corrections for various UV-finite subsets of diagrams. The contributions from all sfermions and the third generation quarks and squarks are fairly independent of $M_{H^\pm}$. The contributions from the latter are largely cancelled to less than a few percent by the remaining (s)fermions. The vertex corrections from the full MSSM vary from $r \sim 20\%\,(5\%)$ to $r \sim -15\%$ for h_2 (h_3), changing sign from positive to negative at $M_{H^\pm} \sim 550\,\text{GeV}$.

Figure 8.4(a) shows the relative size of the vertex corrections, r, for $\Gamma(h_3 \to \tilde{\chi}^0_2\tilde{\chi}^0_2)$, as a percentage in the $M_{H^\pm}$–$\tan\beta$ plane for the 4L1 scenario. The relative size of the vertex corrections for h_2 is similar. We see that the vertex corrections have the largest effect for $M_{H^\pm} \gtrsim 600\,\text{GeV}$. For the region of particular interest in Ref. [35], near $\tan\beta \sim 10-30$ with $M_A \sim 400-500\,\text{GeV}$, where the cross section times branching ratio for $H, A \to \tilde{\chi}^0_2\tilde{\chi}^0_2$ events is largest, the effect of the vertex corrections on the decay widths is only of the order of 5%. This translates into an absolute increase in the branching ratio of a few tenths of a percent. Figure 8.4(b) shows the Improved Born level branching

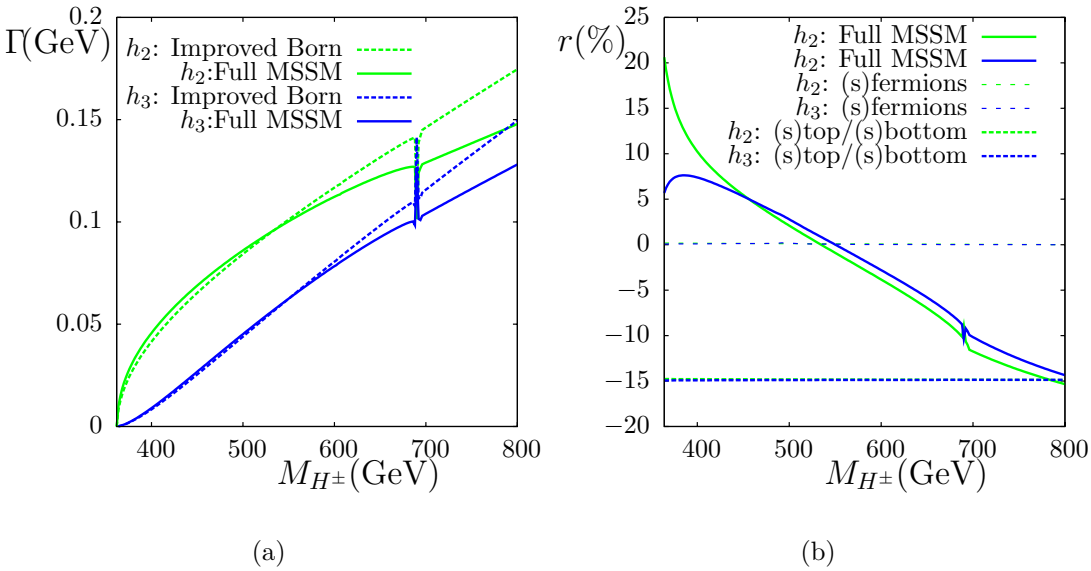

Figure 8.3: (a) Decay widths $\Gamma(h_{2,3} \to \tilde{\chi}_2^0\tilde{\chi}_2^0)$ as a function of $M_{H^\pm}$ in the 4L1 scenario, with $\tan\beta = 20$. The dashed lines show the Improved Born result, while the bold lines include the full one-loop vertex corrections; (b) Relative size of the vertex corrections compared to the Improved Born result for various UV-finite subsets of diagrams indicated by different dashing. Note that where the green dashed curves are not visible in the figure, they are directly underneath the blue dashed curves.

ratio, $\mathrm{BR}(h_3 \to \tilde{\chi}_2^0\tilde{\chi}_2^0)$, as a percentage in the $M_{H^\pm}$–$\tan\beta$ plane for the 4L1 scenario. Inclusion of the one-loop vertex corrections does not produce a noticeable change in this plot.

SPS1a is another scenario in which the dominant contribution to the four-lepton signal is $H, A \to \tilde{\chi}_2^0\tilde{\chi}_2^0$. This point was studied in some detail in Ref. [37] in the context of using four-lepton events to extract MSSM masses and Higgs masses. One important difference between the 4L1 scenario and the SPS1a scenario is that the latter has much lighter squarks and non-zero trilinear couplings. Also the sleptons are light enough to be produced in on-shell decays of $\tilde{\chi}_2^0$, which results in larger leptonic branching ratios of the neutralinos. In SPS1a, the tree-level decay width, $\Gamma(h_2 \to \tilde{\chi}_2^0\tilde{\chi}_2^0)$ is 0.103 GeV, with vertex corrections increasing this value by 6.5%, while the tree-level decay width $\Gamma(h_3 \to \tilde{\chi}_2^0\tilde{\chi}_2^0)$ is 0.0157 GeV, with vertex corrections increasing this value by 5.9%. The corresponding branching ratios of 7.9% and 1.8% increase in absolute terms by 0.5% and 0.1% respectively.

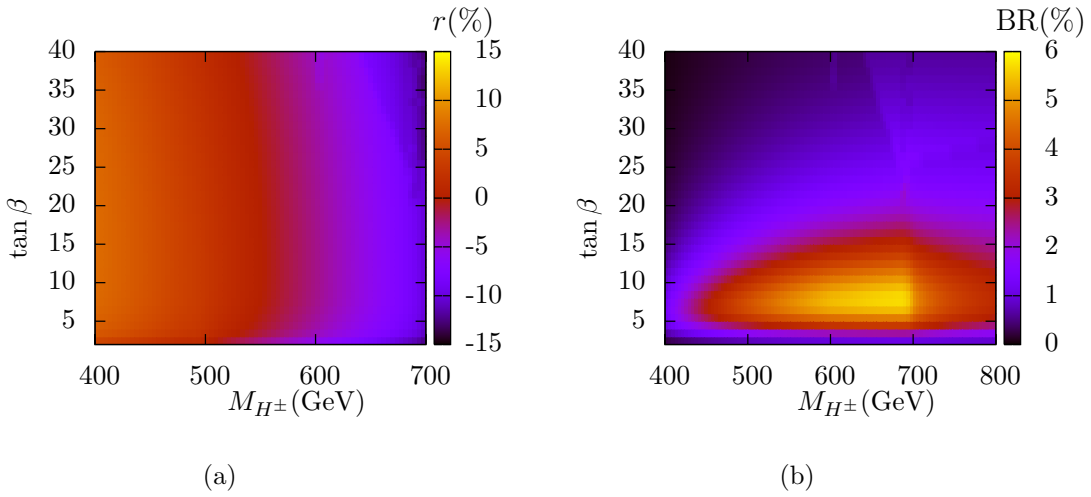

Figure 8.4: (a) The relative size of the vertex corrections, r, as a percentage in the 4L1 scenario in the $M_{H^\pm}$–$\tan\beta$ plane for $\Gamma(h_3 \to \tilde{\chi}^0_2\tilde{\chi}^0_2)$; (b) Branching ratio, $\mathrm{BR}(h_3 \to \tilde{\chi}^0_2\tilde{\chi}^0_2)$, as a percentage in the 4L1 scenario in the $M_{H^\pm}$–$\tan\beta$ plane.

8.3 Effect of $\mathcal{CP}$-violating phases

Most of the work in the literature on the decays of $h_2, h_3 \to \tilde{\chi}^0_i\tilde{\chi}^0_j$, has been for $\mathcal{CP}$-conserving scenarios, where $h_2, h_3 = H, A$ [34–37, 101, 102, 109]. We now consider the effect of $\mathcal{CP}$-violating phases on the decay widths and vertex corrections. As we have seen in Chapter 6 for the $\tilde{\chi}^0_i \to \tilde{\chi}^0_j h_a$ decays, complex parameters can be particularly important for the Higgs propagator corrections. (As usual, we absorb these into the lowest order decay widths using the Improved Born approximation of Equation (5.15)). The induced $\mathcal{CP}$-violating mixing between H and A can significantly alter the Improved Born decay widths. This can also affect the size of the genuine vertex corrections for the (physical) normalised h_2 and h_3 vertices.

The phases which usually play a large role in Higgs sector corrections are ϕ_{A_t} and/or ϕ_μ, as well as ϕ_{M_3} at the two-loop level. In order to study their effects for $h_a \to \tilde{\chi}^0_2\tilde{\chi}^0_2$, we study a modified 4L1 scenario with lighter squarks and a non-zero A_t. Our modified scenario, denoted "4L1b" in Table 2.3, has the same parameters as 4L1 except $M_{\tilde{q}R,\tilde{q}L} = 500\,\mathrm{GeV}$ and $|A_{t,b,\tau}| = 1000\,\mathrm{GeV}$. In Figure 8.5(a) we show the dependence of the decay widths for $\Gamma(h_{2,3} \to \tilde{\chi}^0_2\tilde{\chi}^0_2)$ on the phase ϕ_{A_t} in the 4L1b scenario. The dashed lines show the Improved Born result, while the solid lines include the one-loop genuine vertex corrections in the full MSSM. We see that, at the Improved Born level, the phase of A_t has a large effect on the decay widths, arising from the variation in $\mathcal{CP}$ character of the

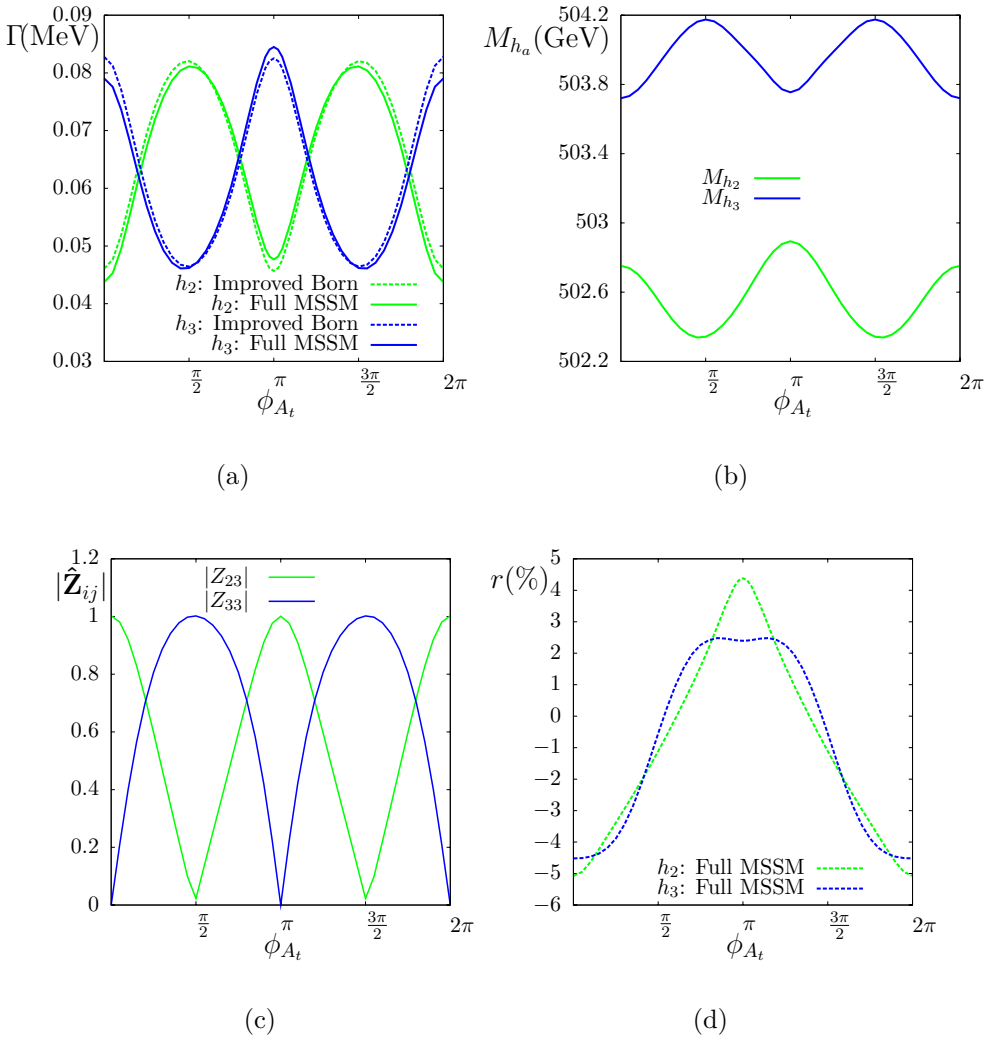

Figure 8.5: (a) Decay widths $\Gamma(h_{2,3} \to \tilde{\chi}_2^0\tilde{\chi}_2^0)$ at the Improved Born level (dashed) and including the one-loop vertex corrections in the full MSSM (solid); (b) Masses of h_2 and h_3; (c) Absolute value of $\hat{\mathbf{Z}}$ matrix elements, $|\hat{\mathbf{Z}}_{23}| \sim |\hat{\mathbf{Z}}_{32}|$ and $|\hat{\mathbf{Z}}_{33}| \sim |\hat{\mathbf{Z}}_{22}|$; (d) Relative size of vertex corrections, r; for all figures plotted as a function of ϕ_{A_t} in the 4L1b scenario.

Higgs bosons. The variation of the Higgs masses and $\hat{\mathbf{Z}}$ matrix elements are displayed in Figures 8.5(b) and 8.5(c) respectively. We see that the two masses, M_{h_2} and M_{h_3} are closest for $\phi_{A_t} = 0, \pi, 2\pi$, where h_2 (h_3) is purely $\mathcal{CP}$-odd (even) with $|\hat{\mathbf{Z}}_{23}| \sim |\hat{\mathbf{Z}}_{32}| \sim 1$ and $|\hat{\mathbf{Z}}_{22}| \sim |\hat{\mathbf{Z}}_{33}| \sim 0$. The $\hat{\mathbf{Z}}$ matrix elements vary substantially away from these $\mathcal{CP}$-conserving values for the phase; at $\phi_{A_t} = \pi/2, 3\pi/2$ we obtain $|\hat{\mathbf{Z}}_{22}| \sim |\hat{\mathbf{Z}}_{33}| \sim 1$ so that the $\mathcal{CP}$ character of the mass eigenstates is swapped relative to the $\mathcal{CP}$-conserving case. The h_2 (h_3) partial decay width varies from roughly 0.045 GeV (0.08 GeV) at $\phi_{A_t} = 0$ to 0.08 GeV (0.045 GeV) at $\phi_{A_t} = \pi/2$ back down (up) to 0.045 GeV (0.085 GeV) at $\phi_{A_t} = \pi$ respectively. The maximum and minimum decay widths correspond approximately to

the $\mathcal{CP}$-conserving decay widths shown in Figure 8.2(a), so this is consistent with the $\hat{\mathbf{Z}}$ matrix values. Figure 8.5(d) shows the relative size of the vertex corrections, r, as a function of ϕ_{A_t}. We see that for both h_2 and h_3 the corrections have the maximum negative effect of around -5% and -4.5% respectively in the $\mathcal{CP}$-conserving case where the phase is zero and A_t is positive. The maximum positive effect is around 4.5% at $\phi_{A_t} = \pi$ for h_2, while for h_3, there are two maxima of around 2.5% for ϕ_{A_t} slightly below and above zero. When the phases are maximally $\mathcal{CP}$-violating at $\phi_{A_t} = \pi/2$, the corrections are less than a percent.

We also examine the effect introducing $\mathcal{CP}$-violating phases has on the decay widths $\Gamma(h_{2,3} \to \tilde{\chi}_2^0\tilde{\chi}_2^0)$ in the SPS1a scenario. Figure 8.6(a) shows the variation of the decay widths as a function of ϕ_{A_t} for the modified SPS1a scenario. We see the dependence is not as pronounced as for the 4L1b scenario and the decay widths for h_2 and h_3 remain separated by $\sim 80\,\text{MeV}$. This is because, as seen in Figure 8.6(c) the absolute values of the $\hat{\mathbf{Z}}$ factors do not vary so far from 0 and 1 as those in the 4L1b scenario, so that the $\mathcal{CP}$ character of the mass eigenstates remains closer to, $h_2 \sim A$ and $h_3 \sim H$ for all ϕ_{A_t}, even though the masses become quite close in value, as shown in Figure 8.6(b). In Figure 8.6(d) we show the relative size of the vertex corrections, r, as a function of ϕ_{A_t}. The maximum positive effect on the decay width of h_2 is around 6.5% at $\phi_{A_t} = 0$, while the maximum negative effect is around 3.5% at $\phi_{A_t} = \pi$. The maximum positive effect on the decay width of h_3 is around 6.5% at $\phi_{A_t} \sim \pi/4, 7\pi/4$, while the maximum negative effect is around -3.7% for phases slightly above and below $\phi_{A_t} = 0$.

8.4 $\mathcal{CP}$-odd asymmetries

The results we have shown so far are for the spin-summed decay widths, $\Gamma(h_a \to \tilde{\chi}_i^0\tilde{\chi}_j^0)$, where all possible polarisations for the neutralinos are included. It is also interesting to look at spin-dependent decay widths since, in an experiment, it may be possible to study the polarisations of the neutralinos by looking at their leptonic decay products (see eg. Ref. [115]). Since the Higgs is a scalar particle, the two neutralinos will either both have left-handed polarisation or both have right-handed polarisation. In this section, we study the effect of $\mathcal{CP}$-violating phases on the partial decay widths into left- and right-handed neutralinos, $\Gamma_{LL} \equiv \Gamma(h_a \to \tilde{\chi}_i^{0\,L}\tilde{\chi}_j^{0\,L})$ and $\Gamma_{RR} \equiv \Gamma(h_a \to \tilde{\chi}_i^{0\,R}\tilde{\chi}_j^{0\,R})$ $(a = 2, 3)$ respectively. It would be particularly interesting if these quantities could tell us something about the existence and size of the $\mathcal{CP}$-violating phases.

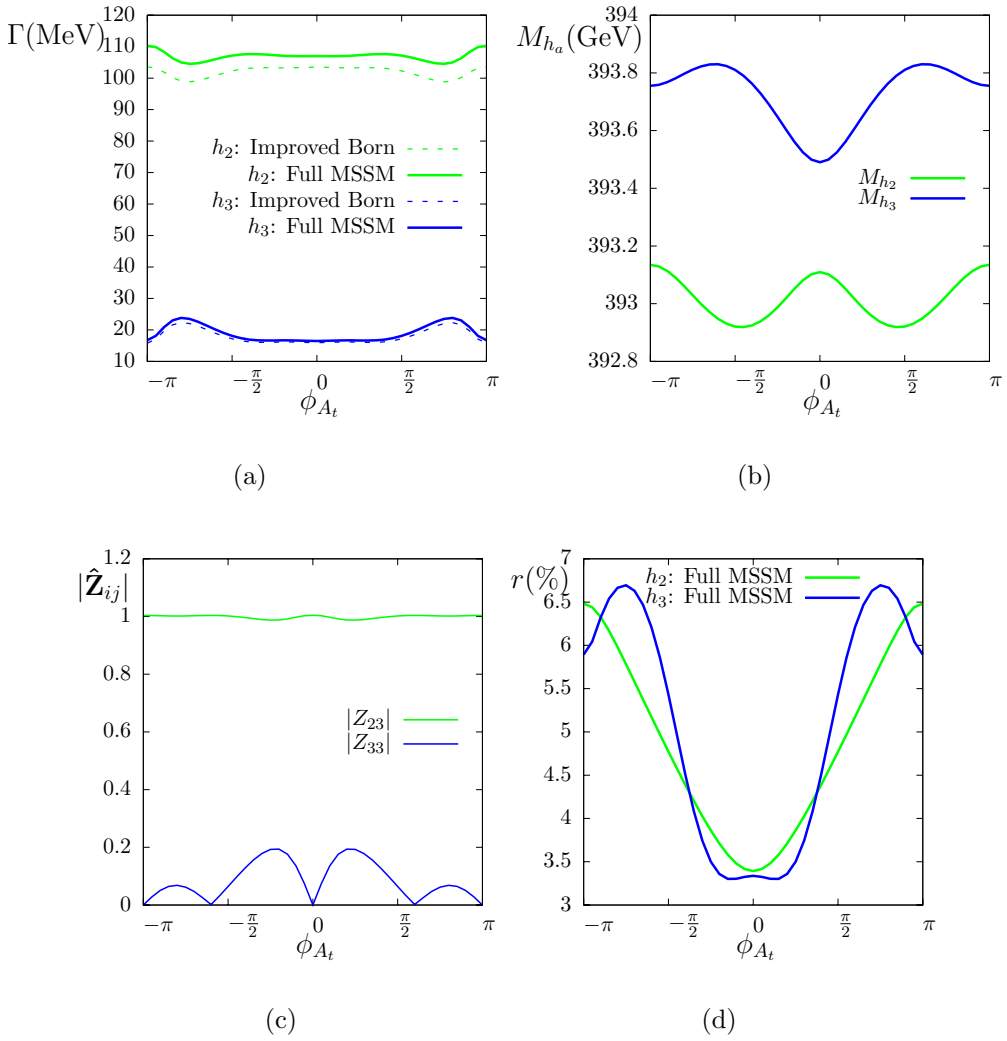

Figure 8.6: (a) Decay widths $\Gamma(h_{2,3} \to \tilde{\chi}_2^0\tilde{\chi}_2^0)$ at the Improved Born level (dashed) and including the one-loop vertex corrections in the full MSSM (solid); (b) Masses of h_2 and h_3; (c) Absolute value of $\hat{\mathbf{Z}}$ matrix elements, $|\hat{\mathbf{Z}}_{23}| \sim |\hat{\mathbf{Z}}_{32}|$ and $|\hat{\mathbf{Z}}_{33}| \sim |\hat{\mathbf{Z}}_{22}|$; (d) Relative size of vertex corrections, r; for all figures plotted as a function of ϕ_{A_t} in the modified SPS1a scenario.

Figure 8.7(a) shows the spin-dependent decay widths, Γ_{LL} and Γ_{RR}, for $h_{2,3} \to \tilde{\chi}_2^0\tilde{\chi}_2^0$ in the 4L1b scenario as a function of ϕ_{A_t}. We see that for both h_2 and h_3, Γ_{LL} and Γ_{RR} do not have their maxima and minima at multiples of $\pi/2$ like the total decay width shown in Figure 8.5(a). Rather, Γ_{LL} for h_2 (h_3) has a similar shape to to Γ_{tot} but is shifted to the left (right), while Γ_{RR} for h_2 (h_3) is obtained by a reflection of Γ_{LL} for h_2 (h_3) about $\phi_{A_t} = 0$. The polarised decay widths thus satisfy $\Gamma_{RR}(\phi_{A_t}) = \Gamma_{LL}(-\phi_{A_t})$ for each h_a.

In Figure 8.7(b) we show the spin-dependent partial decay widths, Γ_{LL} and Γ_{RR}, for $h_2 \to \tilde{\chi}_2^0\tilde{\chi}_2^0$ as a function of the trilinear coupling phase ϕ_{A_t} in the modified SPS1a

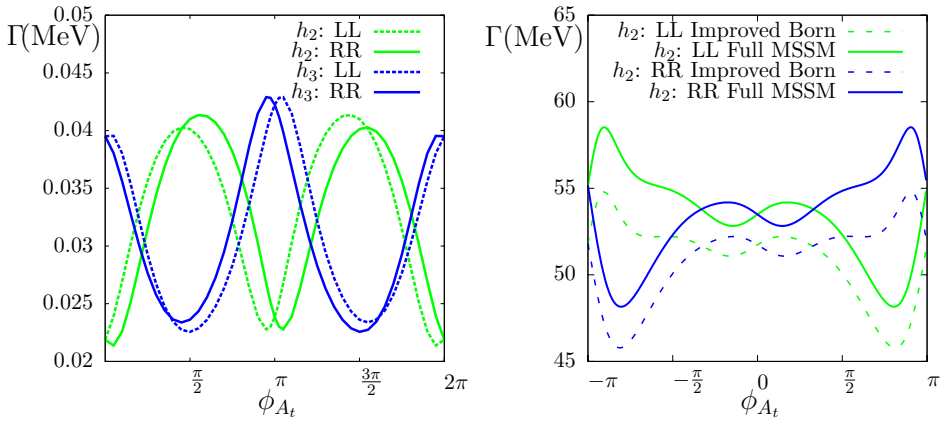

Figure 8.7: (a) Γ_{LL} and Γ_{RR} for $h_{2,3} \to \tilde{\chi}_2^0\tilde{\chi}_2^0$ for the 4L1b scenario as a function of ϕ_{A_t}, including the one-loop vertex corrections in the full MSSM (the dashed (solid) lines indicate left-handed (right-handed) polarisation); (b) Γ_{LL} and Γ_{RR} for $h_2 \to \tilde{\chi}_2^0\tilde{\chi}_2^0$ for the modified SPS1a scenario as a function of ϕ_{A_t} (the dashed lines indicate the Improved Born result, while the solid lines indicate the inclusion of the one-loop vertex corrections in the full MSSM.

scenario. Here the curves for left-handed and right-handed neutralinos are very different from the spin-summed widths shown in Figure 8.6(a). The left-handed and right-handed decay widths again satisfy $\Gamma_{LL}(\phi_{A_t}) = \Gamma_{RR}(-\phi_{A_t})$. Notice that the vertex corrections enhance both Γ_{LL} and Γ_{RR} by around $4 - 10\%$. Note also that Γ_{LL} and Γ_{RR} always coincide when the phase is a multiple of π, i.e. when the scenario is $\mathcal{CP}$-conserving.

In Figure 8.8(a) we plot the difference, $\Delta\Gamma_{LR} \equiv \Gamma_{LL} - \Gamma_{RR}$, between the left and right-handed decay widths for the modified SPS1a scenario as a function of ϕ_{A_t} and we see that it is a $\mathcal{CP}$-odd quantity, i.e. it is non-zero only in the presence of a non-zero $\mathcal{CP}$-violating phase and is antisymmetric under $\phi_{A_t} \to -\phi_{A_t}$. We also notice that the difference $\Gamma_{LL} - \Gamma_{RR}$ for h_3 can become quite large relative to the spin summed decay width, $\Gamma_{LL} + \Gamma_{RR}$, for h_3 shown in Figure 8.6(a).

In Figure 8.8(b) we plot the ratio of the difference relative to the spin summed decay width,

$$A_a \equiv \frac{\Gamma_{LL} - \Gamma_{RR}}{\Gamma_{LL} + \Gamma_{RR}}, \tag{8.1}$$

as a function of ϕ_{A_t} for $h_a \to \tilde{\chi}_2^0\tilde{\chi}_2^0$ $(a = 2, 3)$ for the modified SPS1a scenario. A_2 (A_3) has its peak values of $\sim \pm 38\%$ $(\pm 9\%)$ for $\phi_{A_t} \sim \pm 7\pi/8$, not far from the nominal $\mathcal{CP}$-

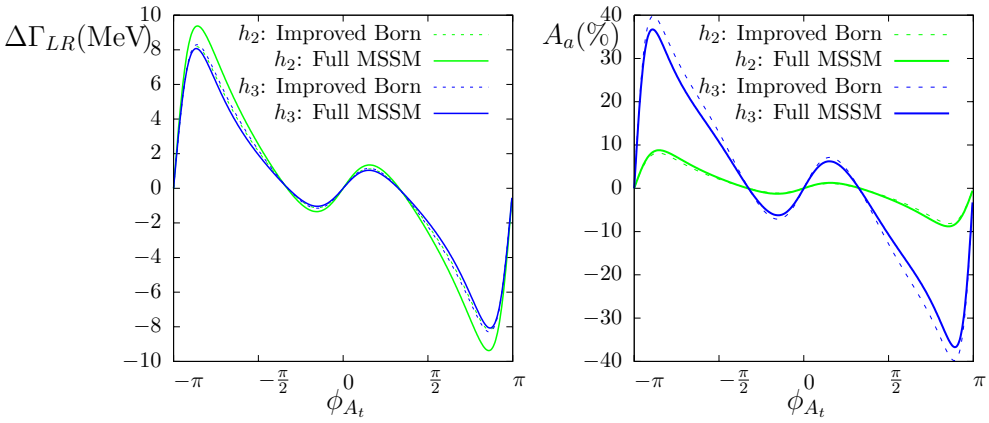

(a) (b)

Figure 8.8: (a) The difference, $\Delta_{LR} \equiv \Gamma_{LL} - \Gamma_{RR}$, as a function of ϕ_{A_t} in the modified SPS1a scenario for each of h_2 and h_3; (b) $A_a \equiv (\Gamma_{LL} - \Gamma_{RR})/(\Gamma_{LL} + \Gamma_{RR})$ as a function of ϕ_{A_t} for $h_a \to \tilde{\chi}_2^0 \tilde{\chi}_2^0$ for the modified SPS1a scenario.

conserving values of $\pm\pi$. The slopes of the curves are steepest near $\phi_{A_t} = \pm\pi$, showing that even a small phase introduced into SPS1a can make a big difference to this ratio. The genuine vertex corrections reduce (increase) A_2 (A_3) at its peak values by a few percent.

In Figure 8.9(a) we show the ratios, A_2 and A_3, as function of ϕ_μ for the SPS1a scenario. Here the peak values for A_2 and A_3 occur at different values of the phase; $|A_2|$ has a maximum value of $\sim 38\%$ at $\phi_\mu \sim \pm\pi/3$, while $|A_3|$ has a maximum value of $\sim 46\%$ at $\phi_\mu \sim \pm\pi/8$. However, both A_2 and A_3 are zero at $\phi_\mu = 0, \pm\pi$. In Figure 8.9(b) we show the ratios, A_2 and A_3, as a function of ϕ_{A_t} for the 4L1b scenario. $|A_2|$ and $|A_3|$ have peak values of around 12% and 7% respectively. The former is enhanced by a few percent by the vertex corrections, while the latter is reduced by the vertex corrections.

The key message gained from the results shown in Figures 8.8 and 8.9 is that a non-zero value of the $\mathcal{CP}$-odd ratio, A_a, would be a clear signal of $\mathcal{CP}$-violation. In each of the plots, if the phases are set to their $\mathcal{CP}$-conserving values of 0, $\pm\pi$, the ratio, A_a, is exactly zero. If the phases are not a multiple of π, then there is $\mathcal{CP}$-violation and the ratio is non-zero. This is true even when the vertex corrections to the Higgs-neutralino-neutralino vertex are taken into account. In the scenarios studied, the vertex corrections for h_2 reduce the total ratio by a few percent, while for h_3 they increase it by a few percent, but in both cases they do not alter the $\mathcal{CP}$-odd behaviour of the ratio. Furthermore, the ratios A_2 and A_3 have the same sign for a given $\mathcal{CP}$-violating phase,

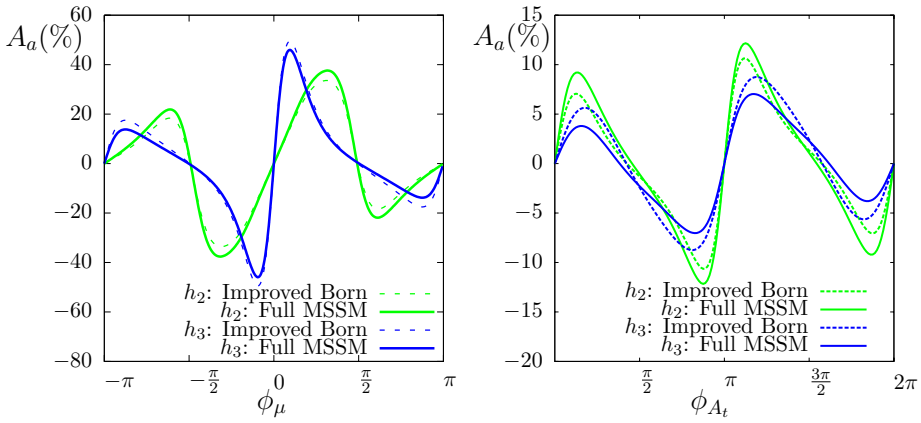

Figure 8.9: (a) $A_a \equiv (\Gamma_{LL} - \Gamma_{RR})/(\Gamma_{LL} + \Gamma_{RR})$ as a function of ϕ_μ for $h_a \to \tilde{\chi}_2^0\tilde{\chi}_2^0$ for the modified SPS1a scenario; (b) A_a as a function of ϕ_{A_t} for $h_a \to \tilde{\chi}_2^0\tilde{\chi}_2^0$ for the 4L1b scenario.

so their effects will reinforce when added together or averaged over. This is important because the two heavy Higgs bosons are nearly mass degenerate. In an experiment it will not be possible to tell them apart and measure polarisation effects in their decay products separately. Thus it would be less encouraging if the ratios for h_2 and h_3 had opposite signs and cancelled one another out.

With this mind, it is also significant that A_2 and A_3 each vanish in the case where there is no $\mathcal{CP}$-violation. Despite the $\mathcal{CP}$-even H and $\mathcal{CP}$-odd A states being nearly mass degenerate, they do not behave as one effective $\mathcal{CP}$-violating state. This is interesting in the context of experimentally distinguishing between the "true" $\mathcal{CP}$-violating case, with two mass eigenstates h_2 and h_3, and the "faked" case where the $\mathcal{CP}$-eigenstates, H and A, are experimentally indistinguishable mass eigenstates with near-degenerate masses, mimicking the effect of $\mathcal{CP}$-violation. For a true $\mathcal{CP}$-odd quantity like A_a, the two cases are indeed distinguishable. A non-zero value of A_a does not arise in the case where H and A are mass degenerate but there are no non-zero $\mathcal{CP}$-violating phases. One would not need to be able to experimentally distinguish between the mass degenerate h_2 and h_3 to confirm a nonzero value for this ratio and hence the existence of $\mathcal{CP}$-violation.

The next question is what could actually be measured at a collider experiment. If there is an asymmetry between the number of left-handed and right-handed neutralinos produced in heavy Higgs boson decays, this can show up in asymmetries constructed from the properties of the leptonic decay products of those neutralinos [115]. Suppose

that the neutralinos decay via two-body decays into a lepton and a slepton, which then decays into the lightest neutralino, i.e. $\tilde{\chi}_2^0 \to \tilde{l}_{1,2}^+ l_{\text{near}}^- \to \tilde{\chi}_1^0 l_{\text{far}}^+ l_{\text{near}}^-$. Then there exist methods for reconstructing the momenta in the decay chains on an event-by-event basis if the particle masses in the cascade are known (see eg. Refs. [116, 117]). Provided that this technique can be carried over to this example, one could use it to measure, for example, the angle, $\theta_{\tilde{\chi}_2^0 l_{\text{near}}}$, between the decaying neutralino and the near lepton. One could then construct a forward-backward asymmetry, $A_{FB} \equiv (N_f - N_b)/(N_f + N_b)$, by counting the number of events, N_f, with $\cos\theta_{\tilde{\chi}_2^0 l_{\text{near}}} > 0$ and the number of events, N_b, with $\cos\theta_{\tilde{\chi}_2^0 l_{\text{near}}} < 0$. A_{FB} is related directly to the asymmetry between left- and right-handed neutralino production. In order to obtain a prediction for A_{FB} in various scenarios, we need to calculate the number of events where a heavy Higgs boson decays into left-handed and right-handed neutralinos respectively. In order to calculate the number of events, for example at the LHC, we need the Higgs production cross sections as well as the partial and total decay widths. This is made more complicated by the fact that the Higgs masses are close to degenerate and therefore interference effects can occur in the presence of $\mathcal{CP}$-violation.

Normally we can use the narrow width approximation to separate the production and decay of a Higgs boson into two separate parts, a cross section multiplied by a branching ratio (see Appendix C for a review of the narrow width approximation). The polarisation-dependent partial decay widths calculated in this chapter belong in the decay part of the calculation. However, we are considering a scenario where the assumptions of the narrow width approximation break down because the two nearly mass degenerate Higgs bosons are not $\mathcal{CP}$-eigenstates and can interfere with one another in the squared matrix calculation. Thus, we must consider the full production and decay process of the Higgs bosons. We cannot simply weight each A_a by the h_a production cross section multiplied by the branching ratio for $h_a \to \tilde{\chi}_2^0 \tilde{\chi}_2^0$ and add them together; this would miss interference effects between the h_2 and h_3 which may enhance or suppress the asymmetry. In Chapter 9 we explore interference effects for nearly mass degenerate Higgs bosons and develop methods for calculating an effective cross section times branching ratio. In Chapter 10 we return to the calculation of the asymmetry between the number of left- and right-handed neutralinos produced in heavy Higgs boson decays at the LHC, taking into account the full production and decay processes.

Chapter 9

Interference effects for nearly mass degenerate Higgs bosons

9.1 Beyond the narrow width approximation

Until now we have used the $\hat{\mathbf{Z}}$ matrix formalism given in Section 3.4.9 to compute amplitudes, cross sections and branching ratios involving on-shell Higgs bosons. This formalism takes into account higher-order propagator-type corrections in the Higgs sector, but in essence it is based on the narrow-width approximation; i.e. it assumes that it is possible to factorise the production and decay of the Higgs boson into two separate parts, a production cross section and a decay branching ratio, each evaluated on-shell. In Appendix C we give a brief review of the narrow width approximation. One of the assumptions of the approximation is that there should be no interference of the resonant diagram with other diagrams that have the same initial and final state. For most cases where we apply the $\hat{\mathbf{Z}}$ matrix formalism, the splittings between the Higgs boson masses are large compared with their widths, and therefore this assumption holds. However, in the context presented in the last chapter – on-shell decays of Higgs bosons into neutralinos, $h_a \to \tilde{\chi}_i^0 \tilde{\chi}_j^0$ – the kinematics require us to consider scenarios that have Higgs bosons with masses larger than the neutralino masses. As is the case quite generically for scenarios with large M_A, the two heavy Higgs bosons, h_2 and h_3, are almost mass-degenerate, while the light Higgs boson has a mass very far below the others so is not usually relevant for interference effects.

In the $\mathcal{CP}$-conserving case, assuming no non-resonant exchange diagrams are important, and neglecting the contributions for h, one can express the squared matrix element for

the full production and decay process, $ab \to H, A \to de$, as

$$|\mathcal{M}|^2 \;=\; |\mathcal{M}_{ab\to H\to de}|^2 + |\mathcal{M}_{ab\to A\to de}|^2 \tag{9.1}$$

because the $\mathcal{CP}$-violating interference term,

$$2\mathrm{Re}(\mathcal{M}_{ab\to H\to de}\mathcal{M}^*_{ab\to A\to de}), \tag{9.2}$$

vanishes. This means that the narrow width approximation can be separately applied to the two processes containing H and A respectively. The total integrated cross section for the full production and decay process, $\sigma(pp \to ab \to H, A \to de)$, can then be written in terms of the sum of the individual production cross sections, each weighted by the appropriate branching ratio;

$$\sigma_{pp\to ab\to H,A\to de} = \sigma_{pp\to ab\to H}\mathrm{BR}_{H\to de} + \sigma_{pp\to ab\to A}\mathrm{BR}_{A\to de}. \tag{9.3}$$

If we consider the MSSM with $\mathcal{CP}$-violating parameters, however, things become very different. Not only do the $\mathcal{CP}$-eigenstates, H and A, mix to form the mass eigenstates h_2 and h_3, but, when the full production and decay process of the Higgs bosons is considered, there is also the possibility of diagrams containing the h_2 and h_3 to interfere; i.e. the interference term,

$$2\mathrm{Re}[\mathcal{M}_{ab\to h_2\to de}\mathcal{M}^*_{ab\to h_3\to de}], \tag{9.4}$$

is non-vanishing. Hence, the fifth assumption given for the narrow width approximation in Appendix C fails and one cannot simply add the individual cross sections for h_2 and h_3 weighted by their branching ratios because this could miss out large interference terms. The same applies for the polarisation dependent asymmetries, A_a, considered at the end of Chapter 8.

Another situation where interference effects can be important, even in the $\mathcal{CP}$-conserving MSSM, is for scenarios with low M_A and large $\tan\beta$, where it is possible to have an h and H that are nearly mass-degenerate. This could be important for the interpretation of the Higgs boson exclusion limits set by the Tevatron and for the prospects of discovering MSSM Higgs bosons with early LHC data. We will discuss this further in Section 9.6.

The idea that calculations in the MSSM and other BSM models may need to go beyond the narrow width approximation has received considerable recent attention in the liter-

ature [118–123]. Some of the effects of nearby resonances in new physics models were also studied in Ref. [124], but most of these references mainly focus on the importance of including off-shell effects near thresholds and in situations where the width can be measured. In Ref. [118], a weight factor was derived to include off-shell effects by reintroducing the momentum dependence of the Breit-Wigner distribution of the intermediate propagator. It was noted that this method was not suitable in situations where interference between intermediate particles was important, such as the interference between the intermediate Z boson and selectrons, $\tilde{e}_{L,R}$ in the three-body decay, $\tilde{\chi}_2^0 \to \tilde{\chi}_1^0 e^+ e^-$, particularly just above the Z threshold. In our case, we are far from any thresholds; the only reason the narrow width approximation fails is that there can be interference between the nearby Higgs resonances.

In this chapter we show several methods for calculating the combined production and decay process which include the interference effects between Higgs bosons. For illustration purposes, we include the Higgs propagator corrections (up to $\mathcal{O}(\alpha_t \alpha_s)$ at two-loop), but we do not consider higher order corrections for the production and decay vertices. The first method, in Section 9.2, incorporates the full 3×3 Higgs propagator matrix, which includes the full momentum dependence of the Higgs self-energies and all possible mixing and interference terms between h, H, A. The second method, in Section 9.3, is an on-shell approximation to the full Higgs propagator matrix, using the $\hat{\mathbf{Z}}$ factor formalism to include mixing effects between h, H, A, along with Breit-Wigner propagators for the resulting h_1, h_2, h_3 to include the interference and leading momentum dependence of the resonances. Both of these methods require a squared matrix element calculation of the combined production and decay process, which may not be practicable in all situations. Thus, in Section 9.5, we develop a method where the separate production and decay processes are weighted by an appropriate interference factor. We find that this gives a good approximation to the full squared matrix element calculations in the scenarios where the interference effects are important. As an application, in Section 9.6, we use this method to show that interference effects could have a noticeable effect on the interpretation of the Higgs exclusion limits in the MSSM.

9.2 Full 3×3 Higgs propagator matrix calculation

Consider the $2 \to 2$ process, $ab \to h, H, A \to cd$, mediated by intermediate Higgs bosons (for simplicity, we neglect other possible intermediate particles here). The full

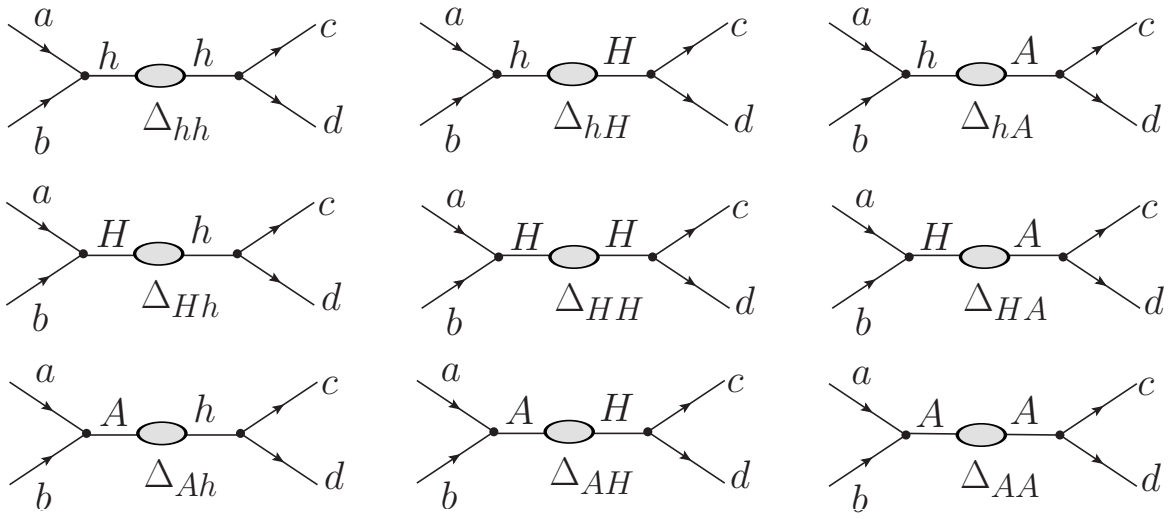

Figure 9.1: Diagrams for the process $ab \to cd$ allowing for internal Higgs bosons, h, H, A, taking into account higher-order mixing between the tree-level Higgs bosons using the full 3×3 propagator matrix elements, $\Delta_{ij}(p^2)$. Diagrams for the same process but with other intermediate particles, such as vector bosons, sfermions and fermions, are not considered here.

3×3 Higgs propagator matrix calculation,[1] illustrated diagrammatically in Figure 9.1, includes the full loop-corrected Higgs propagator matrix elements, $\Delta_{ij}(p^2)$, evaluated using Equations (3.72) and (3.77), into the matrix element as follows;

$$\begin{aligned}\mathcal{M}_{ab\to cd} \;=\; & \mathcal{M}_{ab\to h}\Delta_{hh}\mathcal{M}_{h\to cd} + \mathcal{M}_{ab\to h}\Delta_{hH}\mathcal{M}_{H\to cd} + \mathcal{M}_{ab\to h}\Delta_{hA}\mathcal{M}_{A\to cd} \\ & + \mathcal{M}_{ab\to H}\Delta_{Hh}\mathcal{M}_{h\to cd} + \mathcal{M}_{ab\to H}\Delta_{HH}\mathcal{M}_{H\to cd} + \mathcal{M}_{ab\to H}\Delta_{HA}\mathcal{M}_{A\to cd} \\ & + \mathcal{M}_{ab\to A}\Delta_{Ah}\mathcal{M}_{h\to cd} + \mathcal{M}_{ab\to A}\Delta_{AH}\mathcal{M}_{H\to cd} + \mathcal{M}_{ab\to A}\Delta_{AA}\mathcal{M}_{A\to cd},\end{aligned} \tag{9.5}$$

where, for example, the matrix elements $\mathcal{M}_{ab\to h}$ and $\mathcal{M}_{h\to cd}$ are calculated using the tree-level couplings of h to ab and cd respectively. A generalisation to loop-corrected effective couplings is possible. We have coded this full method into `FeynArts` by defining new particles with the appropriate couplings and propagators. (For example, the particle "hH" couples to ab like the tree-level h boson, couples to cd like the tree level H boson and has the propagator Δ_{hH}.) The propagators are then evaluated in `FormCalc` using the momentum dependent two-loop self-energies from `FeynHiggs` as input.

[1] We neglect here the Higgs mixing with the gauge and Goldstone bosons, which would result in a 6x6 Higgs propagator matrix (see Sections 3.4.6 and 5.4).

9.2.1 Example: H–A mixing in $b\bar{b} \to \tau^+\tau^-$

Consider for example, the matrix element for $b\bar{b} \to \tau^+\tau^-$, mediated by Higgs boson exchange. We write the general tree-level Higgs-fermion-fermion vertex as

$$\begin{aligned}
\hat{\Gamma}_{hf\bar{f}} &= -G_{hff}\omega_L - G^*_{hff}\omega_R, \\
\hat{\Gamma}_{Hf\bar{f}} &= G_{Hff}\omega_L + G^*_{Hff}\omega_R, \\
\hat{\Gamma}_{Af\bar{f}} &= -iG_{Aff}\omega_L + iG^*_{Aff}\omega_R.
\end{aligned} \tag{9.6}$$

where, for $f\bar{f} = b\bar{b}$ or $\tau^+\tau^-$, the couplings are given by

$$\begin{aligned}
G_{hb\bar{b}(\tau^+\tau^-)} &= \frac{em_{b(\tau)}}{2M_W s_W}\left(\frac{s_\alpha}{c_\beta}\right), \\
G_{Hb\bar{b}(\tau^+\tau^-)} &= \frac{em_{b(\tau)}}{2M_W s_W}\left(\frac{c_\alpha}{c_\beta}\right), \\
G_{Ab\bar{b}(\tau^+\tau^-)} &= \frac{em_{b(\tau)}}{2M_W s_W}\left(\frac{s_\beta}{c_\beta}\right).
\end{aligned} \tag{9.7}$$

In the case where $M_{H^\pm}$ is large, the dominant mixing and interference contributions will be between H and A, and the lightest Higgs boson, h, need not be considered. Ignoring the Δ_{hi} and Δ_{ih} propagators and other non-Higgs propagators, we can write the matrix element for $b\bar{b} \to \tau^+\tau^-$ as

$$\mathcal{M} = \bar{v}_b u_b \big[\hat{\Gamma}_{Hb\bar{b}}\Delta_{HH}\hat{\Gamma}_{H\tau\tau} + \hat{\Gamma}_{Hb\bar{b}}\Delta_{HA}\hat{\Gamma}_{A\tau\tau} + \hat{\Gamma}_{Ab\bar{b}}\Delta_{AH}\hat{\Gamma}_{H\tau\tau} + \hat{\Gamma}_{Ab\bar{b}}\Delta_{AA}\hat{\Gamma}_{A\tau\tau}\big]\bar{u}_\tau v_\tau \tag{9.8}$$

where $u_b \equiv u_b^{s_1}(k_1)$ and $\bar{v}_b \equiv \bar{v}_b^{s_2}(k_2)$ are the spinors for the incoming b and $\bar{b}$, with momenta k_1 and k_2 respectively, with the squared centre of mass energy, $s \equiv (k_1 + k_2)^2$. $\bar{u}_\tau \equiv \bar{u}_\tau^{s_3}(k_3)$ and $v_\tau \equiv v_\tau^{s_4}(k_4)$ are the spinors for the outgoing τ^+ and τ^-, with momenta k_3 and k_4 respectively. Squaring the matrix element, summing over τ polarisations, s_3 and s_4, and averaging over b polarisations, s_1 and s_2, and keeping the fermion masses only in the Yukawa couplings, we obtain

$$|\mathcal{M}|^2 = \frac{e^4 m_b^2 m_\tau^2 s^2}{16 c_\beta^4 M_W^4 s_W^4}\left[c_\alpha^4|\Delta_{HH}|^2 + c_\alpha^2 s_\beta^2(\Delta_{HA}\Delta^*_{HA} + \Delta_{AH}\Delta^*_{AH}) + s_\beta^4|\Delta_{AA}|^2\right]. \tag{9.9}$$

The second term in the square brackets contains the mixing propagator between H and A, which is only non-zero in the case of $\mathcal{CP}$-violation. Further interference terms, such as those proportional to $\Delta_{AA}\Delta^*_{AH}$, cancel out in this simple example because the $b\bar{b}$ and

$\tau^+\tau^-$ couplings to Higgs bosons are real and proportional to one another. Note that the propagators Δ_{ij} are evaluated at $p^2 = s$.

In Section 9.4 we will compare our numerical results for $b\bar{b} \to \tau^+\tau^-$ obtained in this way to the numerical results obtained using the on-shell ($\hat{\mathbf{Z}}$) approximation of Section 9.3.

9.3 On-shell ($\hat{\mathbf{Z}}$ matrix) approximation to Higgs propagator matrix calculation

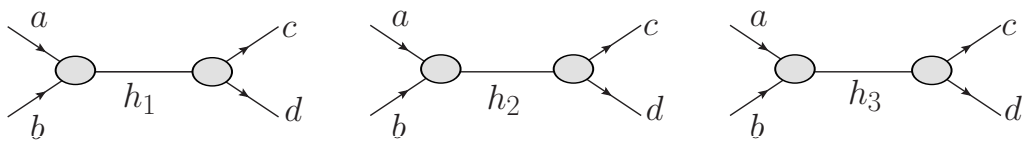

Figure 9.2: Process $ab \to cd$, with on-shell production and decay of the Higgs bosons, h_1, h_2, h_3, taking into account higher-order mixing between the Higgs bosons by using vertices weighted by $\hat{\mathbf{Z}}$ factors. Breit-Wigner propagators are used for the h_1, h_2 and h_3.

As an on-shell approximation to the full Higgs propagator matrix calculation for the process $ab \to h, H, A \to cd$, we use the $\hat{\mathbf{Z}}$ factor formalism for on-shell external Higgs bosons. As explained for the external Higgs bosons in Section 3.4.9, we replace the tree-level coupling, $g_{h_k^0 X}$, to particle X (where $h_k^0 = h, H, A$), with a loop-corrected coupling, $g_{h_a X}$ (where $h_a = h_1, h_2, h_3$), thus including the Higgs propagator-type corrections as follows;

$$g_{h_a X} = \hat{\mathbf{Z}}_{a1} g_{hX} + \hat{\mathbf{Z}}_{a2} g_{HX} + \hat{\mathbf{Z}}_{a3} g_{AX}. \tag{9.10}$$

This can be combined with the effective Breit-Wigner propagator

$$\Delta_{h_a}^{\mathrm{BW}}(p^2) = \frac{i}{p^2 - \mathcal{M}_{h_a}^2} = \frac{i}{p^2 - M_{h_a}^2 + iM_{h_a}\Gamma_{h_a}} \tag{9.11}$$

where $\mathcal{M}_{h_a}^2 = M_{h_a}^2 - iM_{h_a}\Gamma_{h_a}$, for $a = 1, 2, 3$, is the complex pole of the corresponding diagonal Higgs propagator, to produce an approximation to an amplitude involving intermediate on-shell Higgs bosons. Recall from Equation (3.92), that the expansion of the full diagonal Higgs propagator $\Delta_{ii}(p^2)$ about the complex pole results in $\hat{Z}_i \times \Delta_{h_i}^{\mathrm{BW}}(p^2)$, plus terms of higher order in $(p^2 - \mathcal{M}_{h_i}^2)$, so we expect the combination of

Equations (9.10) and (9.11) to give a good approximation to the full process for $p^2 \approx \mathcal{M}_{h_i}^2$.

For the process $ab \to cd$, shown diagrammatically in Figure 9.2, the matrix element is calculated in the on-shell approximation as

$$\mathcal{M}_{ab\to cd} = \mathcal{M}_{ab\to h_1}\Delta_{h_1}^{\mathrm{BW}}\mathcal{M}_{h_1\to cd} + \mathcal{M}_{ab\to h_2}\Delta_{h_2}^{\mathrm{BW}}\mathcal{M}_{h_2\to cd} + \mathcal{M}_{ab\to h_3}\Delta_{h_3}^{\mathrm{BW}}\mathcal{M}_{h_3\to cd}, \tag{9.12}$$

where the couplings in $\mathcal{M}_{ab\to h_a}$ and $\mathcal{M}_{h_a\to cd}$ are derived using Equation (9.10). We have coded this method into `FeynArts` and `FormCalc` using the Higgs masses, M_{h_a}, and $\hat{\mathbf{Z}}$ factors from `FeynHiggs` as input. For a direct comparison with the 3×3 propagator matrix approach from Section 9.2, the widths, Γ_{h_a}, are obtained from the imaginary part of the complex pole, $\mathcal{M}_{h_a}^2$. In practice, higher order contributions to the width can also be included. A generalisation to loop-corrected effective couplings is also possible.

9.3.1 Example: H–A mixing in $b\bar{b} \to \tau^+\tau^-$

Consider the process studied in Section 9.2.1, $b\bar{b} \to \tau^+\tau^-$, mediated by Higgs bosons. In the case where $M_{H^\pm}$ is large, the dominant mixing and interference contributions will be between H and A, and the contributions from h can be ignored. Omitting the $\Delta_{h_1}^{\mathrm{BW}}$ propagators and non-Higgs propagators, we can write the matrix element for $b\bar{b} \to \tau^+\tau^-$ as

$$\mathcal{M} = \bar{v}_b u_b [\hat{\Gamma}_{h_2 b\bar{b}}\Delta_{h_2}^{\mathrm{BW}}\hat{\Gamma}_{h_2\tau\tau} + \hat{\Gamma}_{h_3 b\bar{b}}\Delta_{h_3}^{\mathrm{BW}}\hat{\Gamma}_{h_3\tau\tau}]\bar{u}_\tau v_\tau \tag{9.13}$$

where

$$\begin{aligned} \hat{\Gamma}_{h_2 f\bar{f}} &= \hat{\mathbf{Z}}_{22}\hat{\Gamma}_{Hf\bar{f}} + \hat{\mathbf{Z}}_{23}\hat{\Gamma}_{Af\bar{f}}, \\ \hat{\Gamma}_{h_3 f\bar{f}} &= \hat{\mathbf{Z}}_{32}\hat{\Gamma}_{Hf\bar{f}} + \hat{\mathbf{Z}}_{33}\hat{\Gamma}_{Af\bar{f}}. \end{aligned} \tag{9.14}$$

We find that the spin-averaged squared matrix element, in the limit where the fermion masses are kept only in the Yukawa couplings, is given by

$$|\mathcal{M}|^2 = \frac{e^4 m_b^2 m_\tau^2 s^2}{16 c_\beta^4 M_W^4 s_W^4} \Big[(c_\alpha^2 |\hat{\mathbf{Z}}_{22}|^2 + s_\beta^2 |\hat{\mathbf{Z}}_{23}|^2)^2 |\Delta_{h_2}^{\rm BW}(s)|^2 + (c_\alpha^2 |\hat{\mathbf{Z}}_{32}|^2 + s_\beta^2 |\hat{\mathbf{Z}}_{33}|^2)^2 \times |\Delta_{h_3}^{\rm BW}(s)|^2 + 2\,{\rm Re}\left[(c_\alpha^2 \hat{\mathbf{Z}}_{22} \hat{\mathbf{Z}}_{32}^* + s_\beta^2 \hat{\mathbf{Z}}_{23} \hat{\mathbf{Z}}_{33}^*)^2 \Delta_{h_2}^{\rm BW}(s) (\Delta_{h_3}^{\rm BW}(s))^* \right] \Big]. \quad (9.15)$$

The third term in the square brackets represents the interference between h_2 and h_3. If there is no $\mathcal{CP}$-violation, then $\hat{\mathbf{Z}}_{23} = 0 = \hat{\mathbf{Z}}_{32}$ (or $\hat{\mathbf{Z}}_{22} = 0 = \hat{\mathbf{Z}}_{33}$ if $M_A < M_H$), and the interference term vanishes. The interference will only be large if there is significant overlap between the two Breit-Wigner functions, $\Delta_{h_2}^{\rm BW}$ and $\Delta_{h_3}^{\rm BW}$, which occurs when the masses are nearly degenerate, $M_{h_3} - M_{h_2} \sim \Gamma_{h_2}, \Gamma_{h_3}$.

So long as there is not much mixing with h, we can approximate the 2×2 part of the $\hat{\mathbf{Z}}$ matrix by a mixing matrix with the properties

$$\begin{pmatrix} \hat{\mathbf{Z}}_{22} & \hat{\mathbf{Z}}_{23} \\ \hat{\mathbf{Z}}_{32} & \hat{\mathbf{Z}}_{33} \end{pmatrix} \sim \begin{pmatrix} c_\theta & s_\theta \\ s_\theta & -c_\theta \end{pmatrix} \quad (9.16)$$

where $c_\theta = \cos\theta$, $s_\theta = \sin\theta$ and θ is a (complex) mixing angle. In the limit of $m_A \gg M_Z$ and large $\tan\beta \gg 1$, we can write $c_\alpha/c_\beta \approx t_\beta$, leaving the two heavy Higgs bosons with very similar couplings to the fermions and hence with very similar widths, $\Gamma_{h_2} \approx \Gamma_{h_3}$. In the limit of $c_\alpha/c_\beta \to t_\beta$, $\Gamma_{h_3} \to \Gamma_{h_2}$ and $M_{h_3} \to M_{h_2}$, our expression for the squared matrix element reduces to

$$|\mathcal{M}|^2 \;\propto\; 2t_\beta^4 \left(\frac{|c_\theta^2|^2 + 2|c_\theta s_\theta|^2 + |s_\theta^2|^2 - 4[{\rm Im}(c_\theta){\rm Re}(s_\theta) - {\rm Im}(s_\theta){\rm Re}(c_\theta)]^2}{(s - M_{h_2}^2)^2 + M_{h_2}^2 \Gamma_{h_2}^2} \right). \quad (9.17)$$

In this limit, the effect of the interference term in the square brackets is only large if the $\hat{\mathbf{Z}}$ matrix elements contain large imaginary parts, caused by large absorptive parts of loop integrals in the Higgs self-energies. Away from this limit, there can be significant interference even if the $\hat{\mathbf{Z}}$ matrix elements do not contain large imaginary parts, since the different widths, Γ_{h_2} and Γ_{h_3}, weighted by different couplings, can also contribute.

9.3.2 Example: h–H mixing for $b\bar{b} \to \tau^+\tau^-$

We again consider the process $b\bar{b} \to \tau^+\tau^-$, but this time in the case of small M_A, where h and H can be close in mass. In this case, there can be significant interference effects even when there are no $\mathcal{CP}$-violating parameters. Leaving out the contributions from A for simplicity, and keeping the fermion masses only in the Yukawa couplings, the spin-averaged squared matrix element can be written as

$$|\mathcal{M}|^2 = \frac{e^4 m_b^2 m_\tau^2 s^2}{16 c_\beta^4 M_W^4 s_W^4} \Big(|(s_\alpha \hat{\mathbf{Z}}_{11} - c_\alpha \hat{\mathbf{Z}}_{12})^2|^2 |\Delta_{h_1}^{\mathrm{BW}}(s)|^2 + |(s_\alpha \hat{\mathbf{Z}}_{21} - c_\alpha \hat{\mathbf{Z}}_{22})^2|^2 |\Delta_{h_2}^{\mathrm{BW}}(s)|^2 + 2\,\mathrm{Re}\left[(s_\alpha \hat{\mathbf{Z}}_{11} - c_\alpha \hat{\mathbf{Z}}_{12})^2 (s_\alpha \hat{\mathbf{Z}}_{21}^* - c_\alpha \hat{\mathbf{Z}}_{22}^*)^2 \Delta_{h_1}^{\mathrm{BW}}(s) (\Delta_{h_2}^{\mathrm{BW}}(s))^* \right] \Big). \tag{9.18}$$

The interference term in square brackets between $\Delta_{h_1}^{\mathrm{BW}}$ and $\Delta_{h_2}^{\mathrm{BW}}$ can be large if the masses are nearly degenerate, with $M_H - M_h \sim \Gamma_h, \Gamma_H$, and there is significant mixing between h and H, leading to large values for $\hat{\mathbf{Z}}_{12}$ and $\hat{\mathbf{Z}}_{21}$.

9.4 Numerical comparison between 3×3 propagator matrix calculation and on-shell approximation

In Figure 9.3, we show the total spin-summed cross section, $\sigma(b\bar{b} \to H, A \to \tau^+\tau^-)$, as a function of the centre of mass energy, $\sqrt{s}$, in three modified SPS1a scenarios, each with non-zero $\mathcal{CP}$-violating phases. We use the masses, $\hat{\mathbf{Z}}$ matrix elements and self-energies from `FeynHiggs 2.6.5`, obtaining the widths from the imaginary part of the complex pole. In Figure 9.3(a), the modified parameters are $\mu = 1000\,\mathrm{GeV}$ and $\phi_{A_t} = -7\pi/10$, resulting in $M_{h_2} = 392.5\,\mathrm{GeV}$, $M_{h_3} = 394.7\,\mathrm{GeV}$, $\Gamma_{h_2} = 1.6\,\mathrm{GeV}$, $\Gamma_{h_3} = 1.6\,\mathrm{GeV}$ and $\hat{\mathbf{Z}}_{22} \sim -0.6$, $\hat{\mathbf{Z}}_{23} \sim 0.8$. We see that the two resonances are separated by about $2\,\mathrm{GeV}$, which is larger than the widths involved. The full 3×3 propagator matrix result (black), the on-shell Breit-Wigner result (green), and the on-shell Breit-Wigner result without the interference term (blue) are in good numerical agreement (the curves are indistinguishable in the figure because they are on top of one another). Despite the $\hat{\mathbf{Z}}$ matrix elements showing a large amount of $\mathcal{CP}$-violating mixing between H and A, the masses are not close enough for interference to have a large effect.

In Figure 9.3(b), we use $\phi_{A_t} = -4\pi/5$, with μ returned to its usual SPS1a value of $-352.4\,\mathrm{GeV}$, resulting in $M_{h_2} = 393.0\,\mathrm{GeV}$, $M_{h_3} = 393.6\,\mathrm{GeV}$, $\Gamma_{h_2} = 2.1\,\mathrm{GeV}$, $\Gamma_{h_3} =$

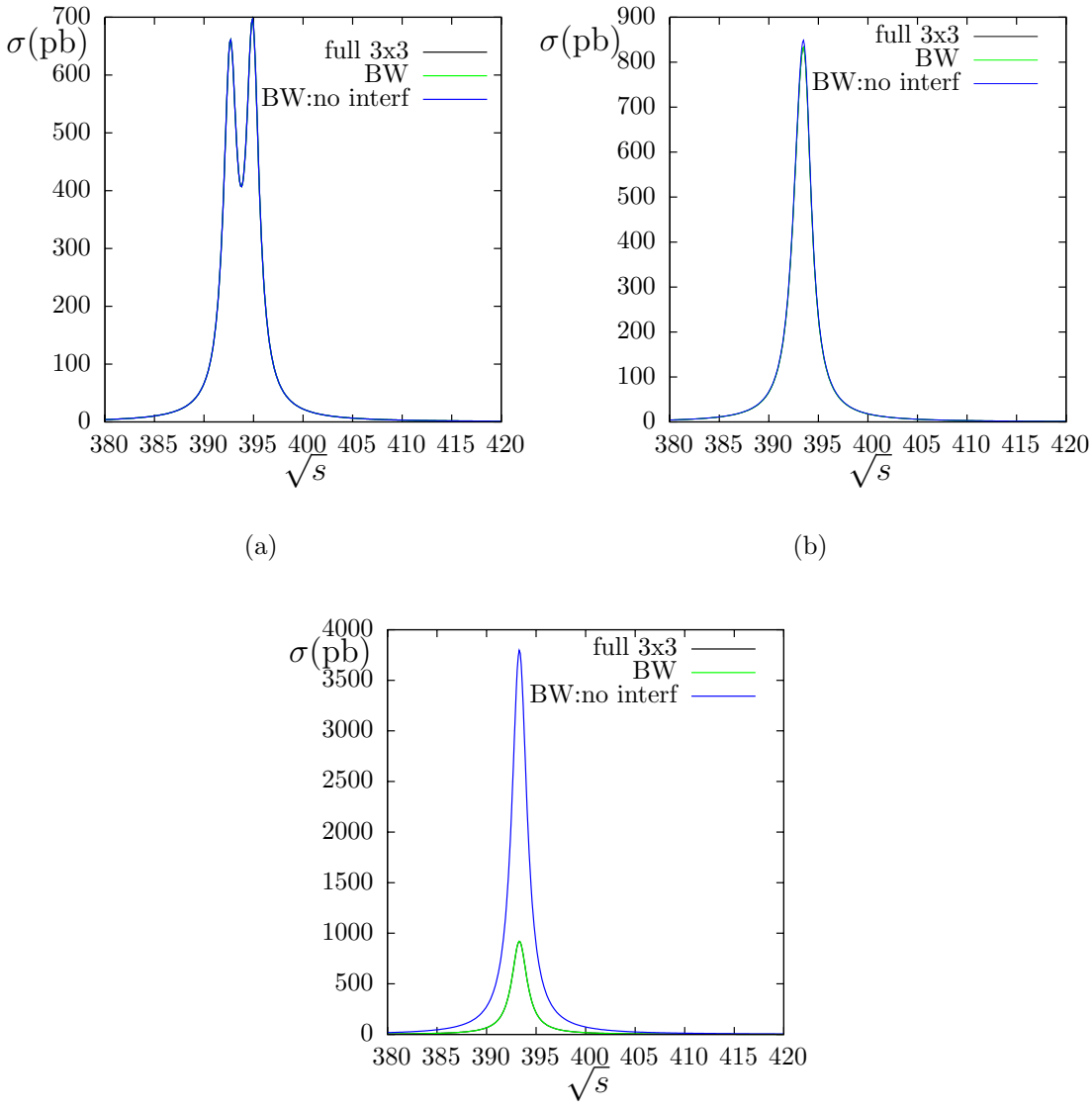

Figure 9.3: Spin summed cross section $\sigma(bb \to \tau\tau)$ in the modified SPS1a scenario as a function of $\sqrt{s}$; (a) with $\mu = 1000\,\text{GeV}$ and $\phi_{A_t} = -7\pi/10$, (b) with $\mu = -354.2\,\text{GeV}$ and $\phi_{A_t} = -4\pi/5$, (c) with $\mu = -354.2\,\text{GeV}$ and $\phi_{M_2} = -9\pi/20$. The black, green and blue curves show the full 3×3 Higgs propagator matrix calculation, the on-shell approximation using $\hat{\mathbf{Z}}$ matrix elements and Breit-Wigner propagators, and the latter without the inclusion of the Breit-Wigner interference term, respectively. Note that some curves cannot be seen in the figures because they are directly underneath other curves.

1.7 GeV and $\hat{\mathbf{Z}}_{22} \sim -0.2 + 0.07i$, $\hat{\mathbf{Z}}_{23} \sim 0.99 + 0.01i$. We see that the separation between the two resonances is too small to be resolved. The full 3×3 propagator matrix result (black) agrees well with the on-shell approximation using $\hat{\mathbf{Z}}$ matrix elements and Breit-Wigner propagators (green) (the curves are indistinguishable in the figure because they

are on top of one another). However, if the interference term is not included in the calculation (blue), the cross section is overestimated by a few percent at its peak value.

In Figure 9.3(c), we use $\phi_{M_2} = -9\pi/20$,[2] with all other parameters as in the usual SPS1a scenario, resulting in $M_{h_2} = 393.3\,\text{GeV}$, $M_{h_3} = 393.3\,\text{GeV}$, $\Gamma_{h_2} = 1.9\,\text{GeV}$, $\Gamma_{h_3} = 1.9\,\text{GeV}$ and $\hat{\mathbf{Z}}_{22} \sim -0.3 - 0.7i$, $\hat{\mathbf{Z}}_{23} \sim 1.2 - 0.2i$. We see that the separation between the two resonances is too small to be resolved. Again, the full 3×3 propagator matrix result (black) agrees well with the on-shell approximation using $\hat{\mathbf{Z}}$ matrix elements and Breit-Wigner propagators (green) (the curves are indistinguishable in the figure because they are on top of one another). However, if the interference term is not included in the on-shell approximation (blue), the cross section is overestimated by around 400%. The interference effect is enhanced for these particular parameters because the masses and widths are almost identical and there is a large amount of $\mathcal{CP}$-violating mixing between H and A, as seen by the $\hat{\mathbf{Z}}$ matrix values.

In Figure 9.4 we consider the M_h^{max} scenario. The M_h^{max} scenario is a standard $\mathcal{CP}$-conserving scenario in which Higgs boson searches are interpreted in the MSSM. An important channel at hadron colliders is $(b)bh, h \to \tau\tau$ in which a Higgs is produced in association with bottom quarks and then decays to taus. Usually the exclusion bounds or discovery sensitivity are interpreted using the individual cross sections for h, H and A, each weighted by their individual branching ratios. When the masses are approximately degenerate, then these are simply added together (see eg. Ref. [123]). For $M_A \gtrsim 150\,\text{GeV}$ and large $\tan\beta$, this method works well in the $\mathcal{CP}$-conserving case, since M_h is well below M_H. Here, however, we consider values of $M_A \sim 120 - 130\,\text{GeV}$ with large $\tan\beta$, which is an interesting part of parameter space where all three neutral Higgs bosons can be nearly mass degenerate. Here we expect interference effects between h and H to be important.

We compute the cross section for $b\bar{b} \to h, H, A \to \tau^+\tau^-$ as a function of $\sqrt{s}$ in the M_h^{max} scenario with $M_{H^\pm} = 170\,\text{GeV}$ and $\tan\beta = 40$, using the masses, $\hat{\mathbf{Z}}$ matrix elements and self-energies from `FeynHiggs 2.6.5`, and obtaining the widths from the imaginary part of the mass solution. For these parameters, the masses are $M_h = 123.0$, $M_H = 125.8$ and $M_A = 124.9\,\text{GeV}$, the widths are $\Gamma_h = 2.5\,\text{GeV}$, $\Gamma_H = 4.8\,\text{GeV}$ and $\Gamma_A = 7.3\,\text{GeV}$

[2] In our convention, we do not normally allow a phase for M_2 since only two of the three phases in the neutralino sector are physical. We only introduce one here because it provides an interesting example of degenerate masses and large $\hat{\mathbf{Z}}$ matrix elements with large imaginary parts. This should not be combined with the simultaneous introduction of phases for M_1 and μ.

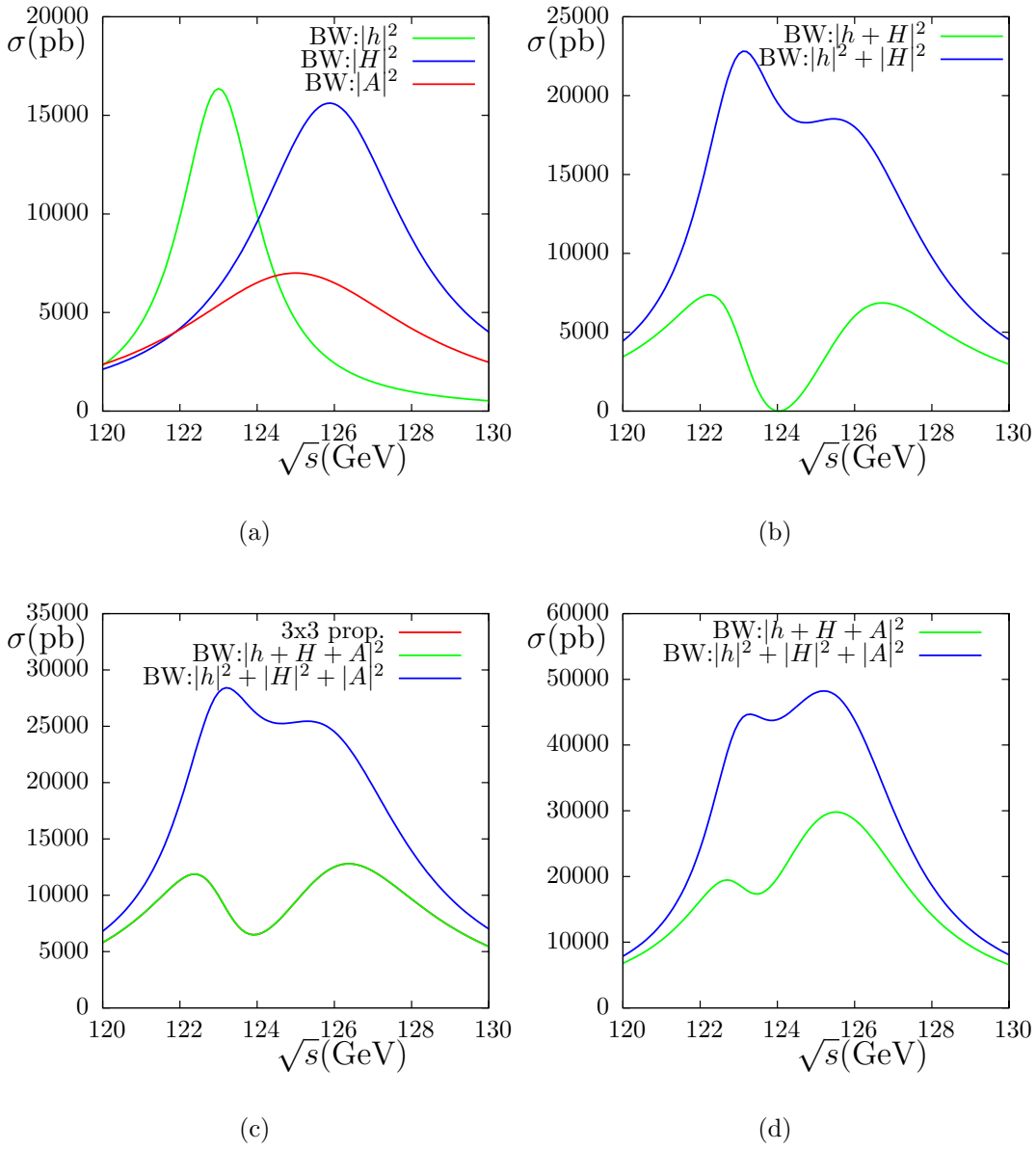

Figure 9.4: Cross section for $b\bar{b} \to h, H, A \to \tau^+\tau^-$ in the $M_h^{\max}$ scenario with $M_{H^\pm} = 170\,\text{GeV}$ and $\tan\beta = 40$ using `FeynHiggs 2.6.5`; (a) Computed using the on-shell approximation with $\hat{\mathbf{Z}}$ matrix elements and Breit-Wigner propagators for each of h, H and A separately (green, blue and red respectively); (b) Computed by adding the on-shell approximations for h and H separately without interference (blue), and with interference (green); (c) Full 3×3 Higgs propagator matrix result (red), compared with on-shell approximation with interference terms (green) and without any interference terms (blue) (note that the red curve is directly underneath the green curve); (d) Comparison between the on-shell approximation with interference (green) and without interference (blue), this time using the total decay widths, $\Gamma^{\text{tot}}_{h_a}$ as input for the Breit-Wigner widths. For (a), (b) and (c) the Breit-Wigner widths are obtained from the imaginary part of the complex mass pole.

and the $\hat{\mathbf{Z}}$ matrix elements of interest are $\hat{\mathbf{Z}}_{hh} = 0.99 - 0.24i$, $\hat{\mathbf{Z}}_{hH} = 0.53 + 0.42i$, $\hat{\mathbf{Z}}_{Hh} = -0.53 - 0.44i$ and $\hat{\mathbf{Z}}_{HH} = 0.96 - 0.26i$.

Figure 9.4(a) shows the cross sections computed from the individual squared matrix elements, each with only one of h, H and A as the intermediate particle, i.e. $b\bar{b} \to h \to \tau^+\tau^-$, $b\bar{b} \to H \to \tau^+\tau^-$ and $b\bar{b} \to A \to \tau^+\tau^-$ respectively, in the on-shell approximation using $\hat{\mathbf{Z}}$ factors and Breit-Wigner propagators. We see that while the masses are separated by a few GeV, the widths are also of the order of a few GeV, so that there is significant overlap of the three resonances. The curve in blue in Figure 9.4(b) shows the cross section obtained by simply adding together the resonances for h and H without including any interference, while we show in green the cross section computed from squaring the matrix element that includes both the h and H Breit-Wigner terms so that interference is included. We see that the effect of including interference is quite dramatic, reducing the peak value of the cross section by more than a factor of three, and shifting the corresponding peak centre of mass energies away from M_h and M_H. Destructive interference between the h and H matrix elements causes the cross section to drop dramatically to zero at $\sqrt{s} \approx 124\,\text{GeV}$.

In Figure 9.4(c) we include the effect of all three neutral Higgs bosons. We see that the on-shell approximation obtained from squaring the matrix element computed from $\hat{\mathbf{Z}}$ factors and Breit-Wigner propagators (green) agrees well with the full 3×3 propagator matrix result (red) which includes further momentum dependence coming from the self-energies (note that the red curve is not visible in the figure because it is directly underneath the green curve). The on-shell approximation using the $\hat{\mathbf{Z}}$ matrix formalism works well because the cross section is dominated by resonant contributions. Inclusion of the leading order momentum dependence using the Breit-Wigner propagators with a constant width does just as well as including the full momentum dependence of the Higgs propagator matrix. It correctly predicts the reduction of the total cross section compared to the cross sections where no interference is included. Any further momentum dependence is only expected to be important near thresholds, where the narrow width approximation breaks down anyway. In such situations it can be advantageous to use a running width, but for our purposes we see that this is not necessary.

Note that in order to find the agreement shown above between the full propagator matrix method and the on-shell approximation, the width, Γ_{h_a}, used in the Breit-Wigner propagator must be obtained from the imaginary part of the complex pole, $\mathcal{M}^2_{h_a}$. This is essentially a tree-level width, obtained from considering the one-loop effective self-energy. However, QCD corrections to the total Higgs boson decay widths can be large,

particularly in parts of parameter space where $h_a \to b\bar{b}$ is the dominant decay channel. The total Higgs decay widths, $\Gamma^{\rm tot}_{h_a}$, that can be obtained as output from `FeynHiggs`, are evaluated as the sum of the partial decay widths for all possible decay modes. Many of these partial decay widths are evaluated with higher order corrections. For example, the $h_a \to b\bar{b}$ partial decay width contains higher-order SM-type and SUSY-type QCD corrections, as well as electroweak corrections. Now that we have demonstrated that the on-shell approximation computed from $\hat{\mathbf{Z}}$ factors and Breit-Wigner propagators agrees with the full propagator matrix result when the same effective width is used, as a further improvement we use the total decay widths, $\Gamma^{\rm tot}_{h_a}$ instead of the complex pole decay widths, thereby incorporating higher order effects. For the scenario and version of `FeynHiggs` considered above, this has a big impact on the widths; resulting in $\Gamma^{\rm tot}_h = 2.0$, $\Gamma^{\rm tot}_H = 3.9$ and $\Gamma^{\rm tot}_A = 4.0\,\text{GeV}$. The results for the cross section $\sigma(b\bar{b} \to h, H, A \to \tau^+\tau^-)$ obtained using these widths for the Breit-Wigner propagators instead of the widths obtained from the complex pole, are shown in Figure 9.4(d). Because the widths are smaller, the interference between h and H has less of an effect. The large difference in the methods for obtaining the widths for this version of `FeynHiggs 2.6.5` is due to the different implementations of the running bottom mass in the calculation of the self-energies compared to the calculation of the partial decay widths. In the more recent version, `FeynHiggs 2.7.0`, there is much better agreement between the two methods. Thus, for our final results in Section 9.6, where we show the effect interference can have on the interpretation of the Higgs exclusion limits, we will use `FeynHiggs 2.7.0`.

9.5 Factorisation into cross section × branching ratio: Incorporation of interference effects

In the previous sections, we showed two different approaches for calculating the full squared matrix element for the production and decay of Higgs bosons. The on-shell approximation using $\hat{\mathbf{Z}}$ factors and Breit-Wigner propagators was found to be in numerical agreement with the full 3×3 Higgs propagator matrix calculation. We also showed that, in parts of parameter space where two or more Higgs bosons are nearly mass-degenerate, there can be significant interference between the intermediate Higgs propagators. These interference effects will not be included when one treats the production and decay processes independently, and thus the narrow width approximation is not applicable in these parts of parameter space. However, carrying out a full matrix

element calculation is not always practicable, especially if one wants to incorporate the important higher order corrections that are available in the literature for the separate production and decay processes. Our aim in the following is to find a generalised narrow width approximation which is applicable to the situation where there is more than one resonance, with $M_i - M_j \lesssim \Gamma_i, \Gamma_j$.

In order to find a generalised narrow width approximation, we consider carefully where the narrow width approximation, reviewed in Appendix C, breaks down. In its usual formulation, the narrow width approximation is expected to work well if the resonant propagator is separable from the matrix elements, one is sufficiently far away from thresholds, the width is small compared to the mass, $\Gamma \ll M$, and interference between resonances can be neglected. In the situation of the production and decay of nearly mass degenerate Higgs bosons, it is usually only the last assumption that does not apply. While the widths are small compared to the masses, $\Gamma_{h_i} \ll M_{h_i}$, they are not small compared to the mass splittings; $\Gamma_{h_i} \sim |M_{h_i} - M_{h_j}|$. Since there can therefore be significant overlap between the resonances, there can be interference between the resonant diagrams. Nevertheless, since the other assumptions still apply, we expect to be able to find a generalised narrow width approximation. In the following section, we find that we can incorporate the main interference effects by introducing an "interference weight factor", which contains the integration over the interfering Breit-Wigner propagators, while still treating the production and decay processes in factorised form, with the matrix elements evaluated on-shell.

9.5.1 Interference weight factor

As in Appendix C, we consider the process, $ab \to cef$, shown in Figure C.1, but we now allow both h_1 and h_2 to appear as resonant internal propagators. As in Equation (C.1) we can write the production matrix elements, the propagators and the decay matrix elements separately. The Lorentz invariant phase space element can be factored into its production and decay parts in the same way as Equation (C.6). The resulting cross

section can then be written as

$$\begin{aligned}\sigma_{ab\to cef} =&\frac{1}{2\pi}\frac{1}{2\lambda^{\frac{1}{2}}(s,m_a^2,m_b^2)}\int dq^2 \mathrm{dlips}(s;p_c,q)\mathrm{dlips}(q;p_e,p_f)\times\left(\frac{|\mathcal{M}_{ab\to ch_1}|^2|\mathcal{M}_{h_1\to ef}|^2}{(q^2-M_{h_1}^2)^2+M_{h_1}^2\Gamma_{h_1}^2}\right.\\ &\left.+\frac{|\mathcal{M}_{ab\to ch_2}|^2|\mathcal{M}_{h_2\to ef}|^2)}{(q^2-M_{h_2}^2)^2+M_{h_2}^2\Gamma_{h_2}^2}+2\mathrm{Re}\left[\frac{\mathcal{M}_{ab\to ch_1}\mathcal{M}^*_{ab\to ch_2}\mathcal{M}_{h_1\to ef}\mathcal{M}^*_{h_2\to ef}}{(q^2-M_{h_1}^2+iM_{h_1}\Gamma_{h_1})(q^2-M_{h_2}^2-iM_{h_2}\Gamma_{h_2})}\right]\right).\\ =&\frac{1}{\pi}\int dq^2\left(\frac{\sigma_{ab\to ch_1}(q^2)\sqrt{q^2}\Gamma_{h_1\to ef}(q^2)}{(q^2-M_{h_1}^2)^2+M_{h_1}^2\Gamma_{h_1}^2}+\frac{\sigma_{ab\to ch_2}(q^2)\sqrt{q^2}\Gamma_{h_2\to ef}(q^2)}{(q^2-M_{h_2}^2)^2+M_{h_2}^2\Gamma_{h_2}^2}\right.\\ &\left.+\int d\Omega\, 2\mathrm{Re}\left[\frac{\mathcal{M}_{ab\to ch_1}\mathcal{M}^*_{ab\to ch_2}\mathcal{M}_{h_1\to ef}\mathcal{M}^*_{h_2\to ef}}{(q^2-M_{h_1}^2+iM_{h_1}\Gamma_{h_1})(q^2-M_{h_2}^2-iM_{h_2}\Gamma_{h_2})}\right]\right)\end{aligned} \tag{9.19}$$

where $d\Omega \equiv \mathrm{dlips}(s;p_c,q)\mathrm{dlips}(q;p_e,p_f)/(4\lambda^{\frac{1}{2}}(s,m_a^2,m_b^2))$ (see Appendix C for the phase space definitions). $\sigma_{ab\to ch_a}(q^2)$ is the off-shell cross section for the production of h_a with momentum q^2, while $\Gamma_{h_a\to ef}(q^2)$ is the off-shell decay width for h_a, decaying at momentum q^2 ($a=1,2$). In the limit of narrow width, the squares of the Breit-Wigner propagators in the first two terms can each be approximated by a constant multiplied by a delta function, $\delta(q^2-M_{h_a}^2)$, as in Equation (C.8), which allows the cross sections and decay widths to be evaluated on-shell, at $q^2=M_{h_1^2}$ and $q^2=M_{h_2^2}$ respectively. Essentially, the resonant structure of the propagators singles out the most important matrix element contributions to be those which are evaluated on-shell. Although the third term does not contain the square of Breit-Wigner propagators, for $M_{h_1}\sim M_{h_2}$, it does have a resonant structure, and is only expected to be large near $q^2\sim M_{h_1}^2\sim M_{h_2}^2$. Our claim is that, so long as the other assumptions of the narrow width approximation apply, the matrix elements in the interference term can be evaluated on-shell and taken outside the dq^2 integral. We can therefore make the following on-shell approximation;

$$\begin{aligned}\sigma_{ab\to cef} \approx&\sigma_{ab\to ch_1}\mathrm{BR}_{h_1\to ef}+\sigma_{ab\to ch_2}\mathrm{BR}_{h_2\to ef}\\ &+2\Omega\mathrm{Re}\big[\big(\mathcal{M}_{ab\to ch_1}\mathcal{M}^*_{ab\to ch_2}\mathcal{M}_{h_1\to ef}\mathcal{M}^*_{h_2\to ef}\big)\int dq^2\Delta_{h_1}^{\mathrm{BW}}(q^2)(\Delta_{h_2}^{\mathrm{BW}}(q^2))^*\big],\end{aligned} \tag{9.20}$$

where the cross sections, branching ratios and matrix elements are all evaluated on-shell. The first two terms are the usual cross sections multiplied by the respective branching ratios, while the third term is the interference term written as a universal integral over the interfering Breit-Wigner propagators, multiplied by a coefficient consisting of process-specific matrix elements evaluated on-shell and a phase space factor, Ω.

To make a further approximation, we note that we can often express the on-shell matrix elements for the interference term in terms of the on-shell matrix elements for the h_1 and h_2 production and decay processes respectively;

$$\mathcal{M}_{ab\to ch_1}\mathcal{M}^*_{ab\to ch_2}\mathcal{M}_{h_1\to ef}\mathcal{M}^*_{h_2\to ef} \approx x_a\,|\mathcal{M}_{ab\to ch_a}|^2|\mathcal{M}_{h_a\to ef}|^2 \tag{9.21}$$

where x_a ($a = 1$ or 2) is a numerical scaling factor and $M_{h_1} \approx M_{h_2}$. For example, for h–H mixing in $b\bar{b} \to \tau^+\tau^-$, we use Equation (9.18) to obtain the scaling factor,

$$x_a = \frac{(s_\alpha \hat{\mathbf{Z}}_{11} - c_\alpha \hat{\mathbf{Z}}_{12})^2 (s_\alpha \hat{\mathbf{Z}}^*_{21} - c_\alpha \hat{\mathbf{Z}}^*_{22})^2}{|(s_\alpha \hat{\mathbf{Z}}_{a1} - c_\alpha \hat{\mathbf{Z}}_{a2})^2|^2}. \tag{9.22}$$

This simple scaling factor allows us to write the total cross section as

$$\sigma_{ab\to cef} \approx \sigma_{ab\to ch_1}\mathrm{BR}_{h_1\to ef}(1 + R_1) + \sigma_{ab\to ch_2}\mathrm{BR}_{h_2\to ef}(1 + R_2) \tag{9.23}$$

where

$$R_a = \frac{M_{h_a}\Gamma_{h_a}}{\pi}\frac{\sigma_{ab\to ch_a}\mathrm{BR}_{h_a\to ef}}{\sigma_{ab\to ch_1}\mathrm{BR}_{h_1\to ef} + \sigma_{ab\to ch_2}\mathrm{BR}_{h_2\to ef}}\; 2\;\mathrm{Re}\left[x_a \int_{q^2_{\min}}^{q^2_{\max}} dq^2 \Delta^{\mathrm{BW}}_{h_1}(q^2)(\Delta^{\mathrm{BW}}_{h_2}(q^2))^*\right] \tag{9.24}$$

is the interference weight factor, for $a = 1$ or 2, where $q^2_{\max}$ and $q^2_{\min}$ are chosen to be the square of M_{h_a} plus or minus a few times Γ_{h_a} respectively. The first term in R_a divides out the Breit-Wigner integral contained in the h_a cross section times branching ratio, while the second term is a weight factor which takes into the account the fact that we could equally choose to express the interference matrix elements in terms of the h_1 or h_2 matrix elements. The term inside the square brackets consists of the process-dependent scaling factor, x_a, and the universal integral over the interfering Breit-Wigner propagators. Note that this equation applies to both partonic and hadronic cross sections, as well as in the case where higher-order corrections are included in the cross sections and decay widths. Thus, in order to obtain an estimate for the cross section of the full production and decay process in the generalised narrow width approximation, all one needs is the production cross sections and decay branching ratios at the desired order, the masses and total decay widths for the universal integral contained in R_a, and a number, x_a, for the scaling factor. All but the latter are available in the literature, for example, in `FeynHiggs`, with many important higher-order corrections already included. One can easily obtain a leading order estimate for x_a in terms of tree-level couplings and $\hat{\mathbf{Z}}$ matrices by considering

the leading partonic process as we have done for $b\bar{b} \to \tau^+\tau^-$. Note that the factor we have derived for this process also applies to the often experimentally indistinguishable processes $gb \to bh_a \to b\tau^+\tau^-$, $g\bar{b} \to \bar{b}h_a \to \bar{b}\tau^+\tau^-$ and $gg \to b\bar{b}h_a \to b\bar{b}\tau^+\tau^-$. This can then be conveniently combined with the state-of-the-art hadronic cross sections and branching ratios, to obtain an improved estimate of the effective cross section times branching ratio including interference effects.

9.5.2 Numerical testing for $b\bar{b} \to h_i \to \tau^+\tau^-$

In going from the integral over q^2 in Equation (9.19) to the on-shell approximation in Equation (9.20), we made the assertion that the matrix elements could be evaluated at fixed momentum, $q^2 \approx M_{h_1}^2$ or $M_{h_2}^2$, outside the integral, leaving only the Breit-Wigner dependence inside the integral. We show the validity of this assumption for the partonic process, $b\bar{b} \to h_1, h_2 \to \tau^+\tau^-$, by considering the integrand from Equation (9.19);

$$\begin{aligned} f(q^2, q'^2, q''^2) = {} & q'\sigma_{b\bar{b}\to h_1}(q'^2)|\Delta_{h_1}^{\mathrm{BW}}(q^2)|^2\Gamma_{h_1\to\tau\tau}(q'^2) + q''\sigma_{b\bar{b}\to h_2}(q''^2)|\Delta_{h_2}^{\mathrm{BW}}(q^2)|^2\Gamma_{h_2\to\tau\tau}(q''^2) \\ & + \int d\Omega\, 2\mathrm{Re}\big[\big(\mathcal{M}_{ab\to ch_1}\mathcal{M}^*_{ab\to ch_2}\mathcal{M}_{h_1\to ef}\mathcal{M}^*_{h_2\to ef}\big)|_{q^2=q'^2}\Delta_{h_1}^{\mathrm{BW}}(q^2)(\Delta_{h_2}^{\mathrm{BW}}(q^2))^*\big] \end{aligned} \tag{9.25}$$

where $q'^{(\prime)} \equiv \sqrt{q'^{(\prime)\,2}}$. In Figure 9.5 we show the dependence of f on $\sqrt{s} = \sqrt{q^2}$ for the $M_h^{\max}$ scenario with $M_{H^\pm} = 173\,\mathrm{GeV}$ and $\tan\beta = 40$, for several values of q'^2 and q''^2. For these parameters, using `FeynHiggs 2.6.5` and the widths derived from the complex pole, we have $M_{h_1} \equiv M_h = 121.5\,\mathrm{GeV}$, $M_{h_2} \equiv M_H = 124.3\,\mathrm{GeV}$, $\Gamma_{h_1} = 2.1\,\mathrm{GeV}$ and $\Gamma_{h_2} = 6.1\,\mathrm{GeV}$. In the black curve, $q'^2 = q''^2 = q^2$; in the green curve $q'^2 = q''^2 = M_{h_1}^2$ and in the blue curve $q'^2 = q''^2 = M_{h_2}^2$. The red curve shows the dependence of f for $q'^2 = q''^2 = q^2$ when the interference term is not included. We see that the curves where q' and q''^2 are taken to be constants, $M_{h_1}^2$ or $M_{h_2}^2$, give a good approximation to full q^2 dependence of f. In particular, they give a much better approximation to the (black) curve with the full q^2 dependence than the (red) curve for which interference is ignored altogether. In the situations where interference is important, the masses are nearly degenerate, and the main q^2 dependence of f comes from the Breit-Wigner propagators and their interference. Thus the integrand, f, can be evaluated at $q^2 \approx M_{h_1}^2$ or $M_{h_2}^2$ with only small errors in reproducing the full integrand.

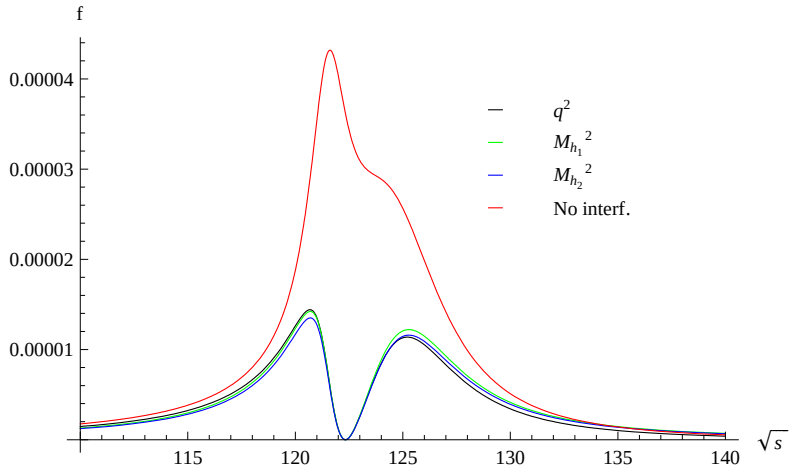

Figure 9.5: Dependence of function $f(q^2, q'^2, q''^2)$ defined in Equation (9.25) on $\sqrt{q^2}$. In the black curve, $q'^2 = q''^2 = q^2$; in the green curve $q'^2 = q''^2 = M^2_{h_1}$; in the blue curve $q'^2 = q''^2 = M^2_{h_2}$; in the red curve the interference term is not included.

9.5.3 Application to $pp \to bb \to h_i \to \tau^+\tau^-$

We have tested the generalised narrow width approximation of Equation (9.23) with interference weight factors, R_a, for the calculation of the LHC integrated cross section for $pp \to b\bar{b} \to h, H \to \tau^+\tau^-$ in the $M_h^{\max}$ scenario with $M_{H^\pm} = 170\,\text{GeV}$. We calculate the squared matrix element for the partonic process using the on-shell approximation with $\hat{\mathbf{Z}}$ matrix elements and Breit-Wigner propagators as in Section 9.3. We then use the built-in option in `FormCalc` to convert our squared matrix element calculation into an integrated cross section with protons in the initial state. For the pdf distributions, we use CTEQ5L [125] because it is the default option in `FormCalc` and sufficient for our purpose of testing the validity of the interference factor method. The Higgs masses and $\hat{\mathbf{Z}}$ matrix elements were obtained from `FeynHiggs 2.6.5`, including the $\mathcal{O}(\alpha_t\alpha_s)$ corrections, while the total widths were obtained from the imaginary part of the complex pole. In this way we obtain numerical values for $\sigma_h \equiv \sigma(pp \to b\bar{b} \to h\,\text{only} \to \tau^+\tau^-)$, $\sigma_H \equiv \sigma(pp \to b\bar{b} \to H\,\text{only} \to \tau^+\tau^-)$ and $\sigma_{hH} \equiv \sigma(pp \to b\bar{b} \to h, H \to \tau^+\tau^-)$. For simplicity we ignore the contributions from A.

The resulting cross sections are shown in Figure 9.6(a) as a function of $\tan\beta$. The black points show σ_{hH}, i.e. they include the h–H interference. The blue points show $\sigma_h + \sigma_H$, i.e. they do not include the h–H interference. The green points are obtained using $\sigma_h(1+R_1)+\sigma_H(1+R_2)$, where the interference weight factors are calculated using Equation (9.24). We see that for $35 \lesssim \tan\beta \lesssim 45$, simply adding together σ_h and

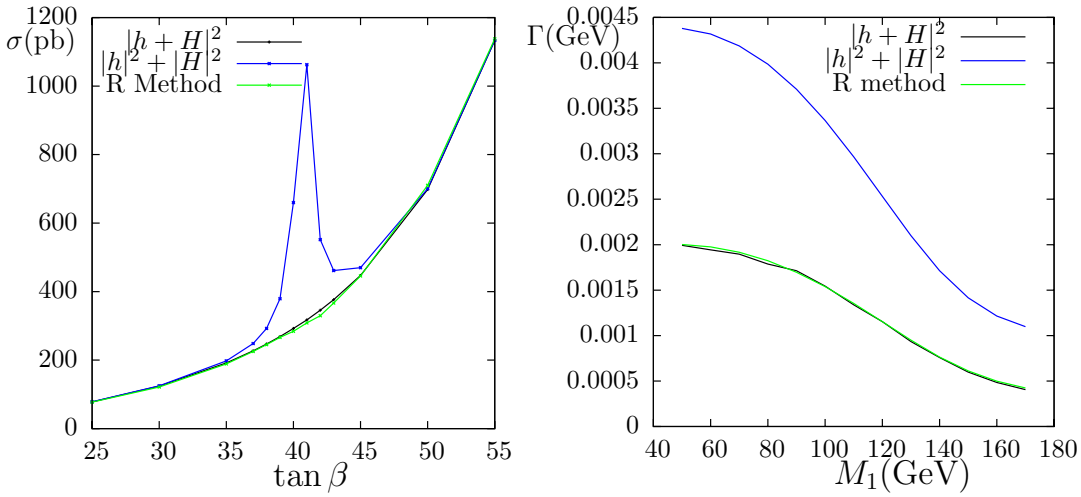

(a) (b)

Figure 9.6: (a) Integrated LHC cross section for $pp \to b\bar{b} \to h, H \to \tau^+\tau^-$ in the $M_h^{\max}$ scenario with $M_{H^\pm} = 170\,\text{GeV}$ as a function of $\tan\beta$. The black points are computed using the Breit-Wigner propagators and $\hat{\mathbf{Z}}$ matrix elements for h and H, including interference. The blue curve ignores the interference. The green points show the generalised narrow width approximation using the interference weight factor; (b) The decay width in GeV for the process $\tilde{\chi}_4^0 \to \tilde{\chi}_1^0\tau^+\tau^-$ in the $M_h^{\max}$ scenario with $\tan\beta = 40$ and $M_{H^\pm} = 170\,\text{GeV}$ as a function of M_1, ignoring contributions from intermediate $\mathcal{CP}$-odd Higgs bosons and other non-Higgs intermediate particles. The black curve shows the three-body decay width computed using the Breit-Wigner and $\hat{\mathbf{Z}}$ matrix method, including h and H and their interference. The blue curve shows the standard narrow width approximation, while green red curve includes the interference weight factor to obtain a generalised narrow width approximation.

σ_H in a "narrow width estimation" (blue) leads to an overestimation for σ_{hH} (black) by up to a factor of 8, due to the resonant enhancement of the $\hat{\mathbf{Z}}$ matrix elements in this region. The generalised narrow width approximation using the interference weight factors (green), however, gives a good estimation of the full σ_{hH} result.

9.5.4 Application to $\tilde{\chi}_4^0 \to \tilde{\chi}_1^0\tau^+\tau^-$

The generalised narrow width approximation of Equation (9.23) applies to decay widths as well as cross sections. We have applied the method to the calculation of the three body decay width of a neutralino into a lighter neutralino and two taus; $\tilde{\chi}_4^0 \to \tilde{\chi}_1^0\tau^+\tau^-$. In the $\mathcal{CP}$-conserving case with h–H mixing, one can write down a relatively compact expression for x_a, involving only $\hat{\mathbf{Z}}$ matrix elements and couplings. This can be combined with the universal integral over Breit-Wigner propagators to obtain the appropriate in-

terference factor, R_a, using Equation (9.24). The two-body and three-body decay widths were computed using `FormCalc`, the Higgs masses and $\hat{\mathbf{Z}}$ matrix elements were obtained from `FeynHiggs 2.6.5`, including the $\mathcal{O}(\alpha_t\alpha_s)$ corrections, while the total widths were obtained from the imaginary part of the complex pole. Figure 9.6(b) shows the decay width in GeV for the process, $\tilde{\chi}_4^0 \to \tilde{\chi}_1^0\tau^+\tau^-$ in the $M_h^{\max}$ scenario with $\tan\beta = 40$ and $M_{H^\pm} = 170\,\text{GeV}$ as a function of M_1, ignoring contributions from the intermediate $\mathcal{CP}$-odd Higgs boson and other non-Higgs intermediate particles. The black curve shows the three-body decay width computed using the on-shell approximation with Breit-Wigner propagators and $\hat{\mathbf{Z}}$ matrix elements, as in Section 9.3, including the interference between h and H. The blue curve shows the usual narrow width approximation, obtained by adding the two body Improved Born decay widths into h and H, each weighted by their respective branching ratios into taus. Finally the green curve includes the interference weight factors using the generalised narrow width approximation of Equation (9.23). We see that the usual narrow width approximation overestimates the full three-body decay width by more than a factor of two. Inclusion of the interference weight factor in the generalised narrow width approximation, however, predicts the full three-body decay width to within a few percent.

9.6 Interference effects on the interpretation of experimental limits for Higgs searches

As a phenomenologically relevant application of the generalised narrow width approximation with interference weight factors, as described in Equations (9.23) and (9.24), we investigate the effect that interference between h and H can have on the interpretation of the Higgs exclusion limits at the Tevatron. We focus on the di-tau channel in the $M_h^{\max}$ scenario. In their analyses of this channel so far [123, 126–130], the Tevatron collaborations have not included the effect of interference between h and H. The cross section, $\sigma(p\bar{p} \to \phi + X)$, times branching ratio, $\text{BR}(\phi \to \tau^+\tau^-)$, is computed for a given Higgs boson, ϕ, with mass M_ϕ, taking the cross sections, branching ratios and masses from `FeynHiggs`. The predicted cross section times branching ratio is then compared with the experimental limit for this quantity at this particular Higgs mass. In cases where the Higgs bosons have nearly degenerate masses, their production cross sections are added [123]. Finite width effects for large $\tan\beta$ were investigated in Ref. [123], where they were simulated by multiplying the individual Higgs cross sections by a Breit-

Wigner function. It was found that the effect of the width was small for most of the $M_h^{\max}$ parameter space. However, the effect of interfering Breit-Wigner propagators was not studied.

In the previous section, we showed examples where interference can lead to a significant decrease in the cross sections for $pp \to b\bar{b} \to h, H, A \to \tau^+\tau^-$. $b\bar{b}$ fusion is the main Higgs production channel for much of the $M_h^{\max}$ parameter space. For $\tan\beta \lesssim 30$, gluon fusion can also be important. We include gluon fusion in our total cross section, but, since we are mostly interested in larger $\tan\beta$, we do not incorporate the interference effects for gluon fusion here; these could easily be included in a future work. Note that the examples shown in the previous sections with large interference effects for $\tan\beta \sim 40$ and $M_A \sim 122\,\text{GeV}$ were computed using the Higgs masses and $\hat{\mathbf{Z}}$ matrix elements from `FeynHiggs 2.6.5`, including the $\mathcal{O}(\alpha_t\alpha_s)$ corrections, while the total widths were obtained from the imaginary part of the complex pole. In fact, when we use `FeynHiggs 2.7.0`, and furthermore include the full set of available two-loop corrections for the real MSSM (i.e. beyond $O(\alpha_t\alpha_s)$), we find that the interference between h and H is largest in the $M_h^{\max}$ scenario for $M_A \sim 132\,\text{GeV}$ and $\tan\beta \sim 70$. Such high values of $\tan\beta$ are not very relevant for the recent Tevatron exclusion limits, which are at much smaller $\tan\beta$. Thus, what follows should be treated as an example for illustration purposes only.

The Tevatron collaboration has published numerous dedicated analyses of their exclusion limits interpreted in the $M_h^{\max}$ scenario, as well as model independent upper limits at the 95% confidence level for the cross sections times branching ratio for a single Higgs boson with a certain mass. `HiggsBounds` is a computer tool designed for interpreting these limits in the MSSM and other models [131]. We use a version of `HiggsBounds` modified by the authors to take as input our modified cross sections, $\sigma_{pp\to b\bar{b}\to h_a X}(1+R_a)$, as well as the other usual cross sections, masses, branching ratios and decay widths. We obtain all of these quantities from `FeynHiggs` and compute the interference factors, R_a, from Equation (9.24). The output from `HiggsBounds` indicates whether a given parameter point is excluded or unexcluded on the basis of the Tevatron analysis with the highest sensitivity. For illustration purposes, we do not use all available analyses; we select the analysis where the exclusion limit is close to the values of $\tan\beta$ where the maximum interference between h and H occurs.

In Figure 9.7, we show results for the $M_h^{\max}$ scenario in the M_A–$\tan\beta$ plane using `FeynHiggs 2.6.5`, including the $\mathcal{O}(\alpha_t\alpha_s)$ corrections and obtaining the widths from the imaginary part of the complex pole. Figure 9.7(a) shows the difference in the $\mathcal{CP}$-even Higgs masses, $M_H - M_h$, in the M_A–$\tan\beta$ plane. We see a band for $M_A \sim 122 - 125\,\text{GeV}$

and $\tan\beta > 40$, where the mass difference is well below a GeV and interference effects can be expected to be large. Figures 9.7(b) shows the interference weight factor, R_1, for the $b\bar{b} \to \tau^+\tau^-$ in the M_A–$\tan\beta$ plane. We see that its value can deviate significantly from zero for $M_A \sim 120{-}125\,\text{GeV}$ and $30 < \tan\beta < 60$, thus leading to large interference effects. Figure 9.7(c) shows the sum of the three $b\bar{b}$ cross sections each multiplied by the $\tau^+\tau^-$ branching ratios; $\sigma_{b\bar{b}h} \times BR_{h\to\tau\tau} + \sigma_{b\bar{b}H} \times BR_{H\to\tau\tau} + \sigma_{b\bar{b}A} \times BR_{h\to\tau\tau}$. We see that the cross section generally rises with $\tan\beta$, but we also see an interesting region near $M_A \sim 122\,\text{GeV}$ and $\tan\beta \sim 40$, where the resonant enhancement of the $\hat{\mathbf{Z}}$ matrix elements leads to a very large cross section. Figure 9.7(d) shows the equivalent cross section including interference; $\sigma_{b\bar{b}h} \times BR_{h\to\tau\tau}(1+R_1) + \sigma_{b\bar{b}H} \times BR_{H\to\tau\tau}(1+R_2) + \sigma_{b\bar{b}A} \times BR_{h\to\tau\tau}$. We see that the cross section near $M_A \sim 122\,\text{GeV}$ and $\tan\beta \sim 40$ is significantly suppressed. Figure 9.7(e) shows the output from `HiggsBounds` when interference is not included. We restrict the analysis to that by the CDF collaboration in Ref. [127], where the search was performed in the $\phi \to \tau\tau$ channel using $1.8\,\text{fb}^{-1}$ of data collected with the CDF detector in Run II of the Tevatron. The red points are excluded by this analysis at the 95% confidence level for the particular cross sections, branching ratios, masses and widths we obtained from `FeynHiggs 2.6.5` as detailed above. Taking the same values for these quantities, but including the interference factors, R_1 and R_2, results in the `HiggsBounds` output shown in Figure 9.7(f). We see that a significant number of points in blue below $\tan\beta = 43$ which were excluded in Figure 9.7(e) can no longer be excluded for these particular numbers and this particular analysis.

In Figure 9.8 we show results for the M_h^{max} scenario in the M_A–$\tan\beta$ plane using `FeynHiggs 2.7.0`, now obtaining the widths from the sum of the partial decay widths. As already discussed, the on-shell approximation using these widths will not agree so well with the full propagator matrix approach, but will include further important higher-order QCD corrections that are available in `FeynHiggs` for the Higgs partial decay widths. Figure 9.8(a) shows the difference in the $\mathcal{CP}$-even Higgs masses, $M_H - M_h$, in the M_A–$\tan\beta$ plane. This time we see a band for $M_A \sim 122 - 125\,\text{GeV}$ and $\tan\beta > 55$, where the mass difference is well below a GeV. This mass degeneracy occurs at much larger $\tan\beta$ than for `FeynHiggs 2.6.5`. Figures 9.8(b) shows that the interference weight factor also has its largest deviation from zero around this region. Figures 9.8(c) and 9.8(d) again show the sum of the three $b\bar{b}$ cross sections each multiplied by their respective $\tau\tau$ branching ratios, without and with interference respectively. We see that the total cross section near $M_A \sim 124\,\text{GeV}$ and $\tan\beta \sim 55$ is significantly suppressed by the interference. Figure 9.8(e) shows the output from `HiggsBounds` when interference is not included. We restrict the analysis to that by the D0 collaboration in Ref. [123], where

the search was performed in the $\phi \to \tau\tau$ channel using $1\,\text{fb}^{-1}$ of data collected with the D0 detector at the Tevatron. The red points are excluded by this analysis at the 95% confidence level for the particular cross sections, branching ratios, masses and widths we obtained from `FeynHiggs 2.7.0` as detailed above. Taking the same values for these quantities, but including the interference factors, R_1 and R_2, results in the `HiggsBounds` output shown in Figure 9.8(f). We see that a significant number of blue points around $\tan\beta = 50$ which were excluded in Figure 9.8(f) can no longer be excluded for these particular numbers and this particular analysis.

As already explained, the shifts in the Tevatron Higgs exclusion limits described above for the M_h^{max} scenario should not be taken literally, since, first of all, we do not include all available higher-order corrections in the Higgs sector; we only include the $O(\alpha_t\alpha_s)$ corrections. Secondly, the Tevatron analyses we use are not the most recent available. The recent published analysis in Ref. [126] combines the results for searches for a neutral Higgs boson in the di-tau final state using $1.8\,\text{fb}^{-1}$ and $2.2\,\text{fb}^{-1}$ of integrated luminosity collected at the CDF and D0 experiments respectively. The resulting exclusion limits reach a much lower $\tan\beta$ of around 35. Including the interference effects as described above using `FeynHiggs 2.7.0` does not have a large effect on this boundary. Our examples are simply to illustrate that, for certain Higgs masses, mixings and widths, interference between h and H can have a significant impact on the interpretation of Higgs exclusion bounds with a certain sensitivity. There may be other $\mathcal{CP}$-conserving and $\mathcal{CP}$-violating scenarios with large interference between h_1, h_2 and/or h_3 occurring in regions of parameter space where the most recent exclusion limits are significantly affected. The $\mathcal{CP}$-violating case is also of particular interest for the Higgs discovery potential for large $\tan\beta$ in the early stages at the LHC. Unlike the interference between h and H in the M_h^{max} scenario, which only occurs for a small resonance region in the M_A–$\tan\beta$ plane, the interference between H and A can be significant quite generically since their masses are usually nearly degenerate for moderate to large values of M_A and large $\tan\beta$. It is clear that for such scenarios, one cannot simply add the cross sections for H and A production as has been done in the past. In this chapter we have developed a method for using simple interference factors in conjunction with the state-of-the-art cross sections and branching ratios to include these effects. The method is more convenient than doing a full squared matrix element calculation but produces a good estimate of the effects. The method has been implemented and tested for the particular case of h–H mixing in the $b\bar{b} \to \tau^+\tau^-$, but can easily be applied to other processes and the $\mathcal{CP}$-violating case. In the next chapter, we study $\mathcal{CP}$ asymmetries in the processes, $b\bar{b}, W^+W^-, gg \to h_a \to \tilde{\chi}_2^0\tilde{\chi}_2^0$. In Section 10.5, we will use a generalised narrow width

approximation with interference factors to produce estimates of the asymmetries at the LHC.

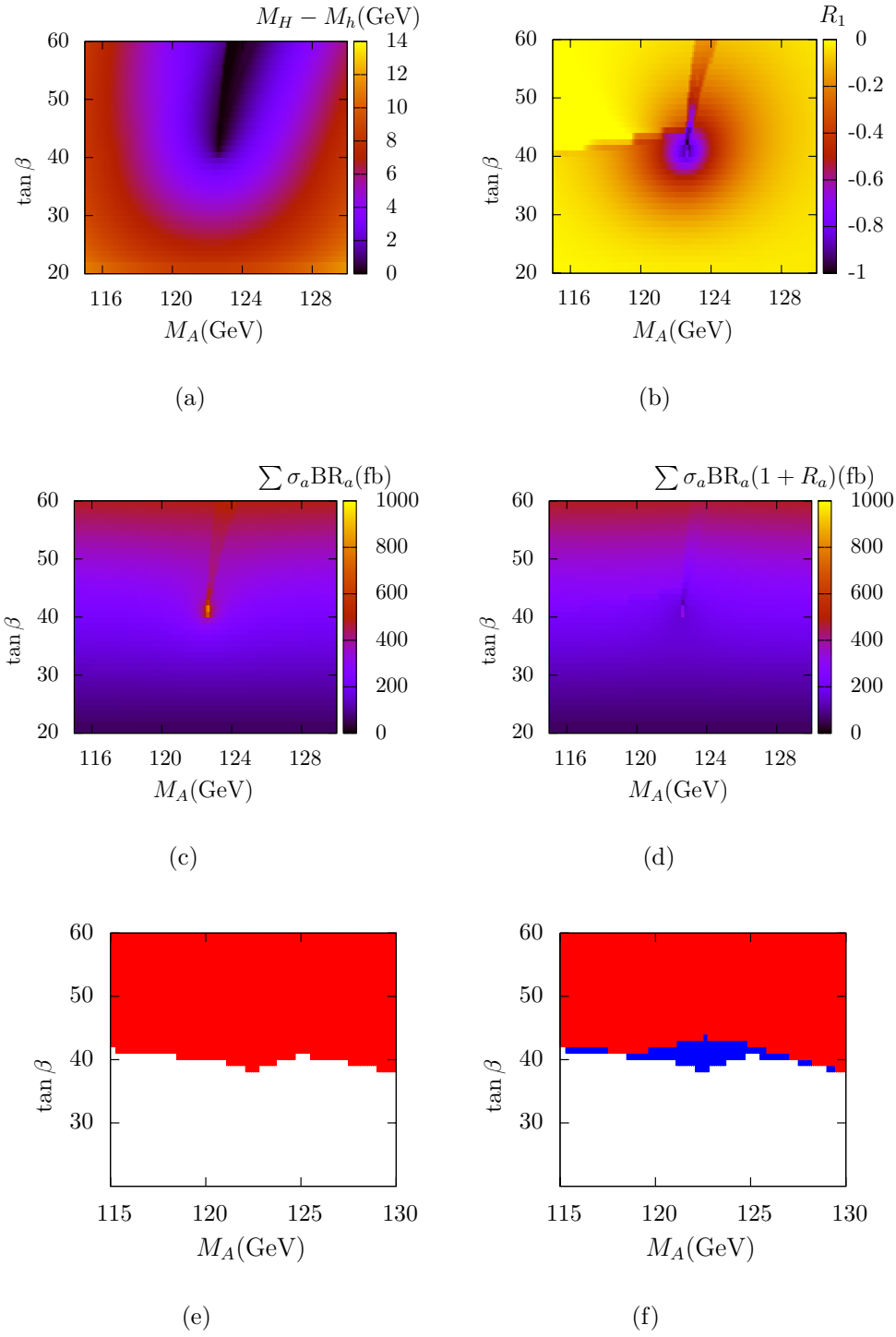

Figure 9.7: Results for the $M_h^{\max}$ scenario in the M_A–$\tan\beta$ plane using `FeynHiggs 2.6.5`, including the $\mathcal{O}(\alpha_t\alpha_s)$ corrections, and obtaining the widths from the imaginary part of the mass solution; (a) $M_H - M_h$; (b) R_1; (c) Cross section for $b\bar{b}h_a, h_a \to \tau\tau$ without interference; i.e. $\sigma_h \times \mathrm{BR}_{h\to\tau\tau} + \sigma_H \times \mathrm{BR}_{H\to\tau\tau} + \sigma_A \times \mathrm{BR}_{A\to\tau\tau}$; (d) Cross section for $b\bar{b}h_a, h_a \to \tau\tau$ with interference; i.e. $\sigma_h \times \mathrm{BR}_{h\to\tau\tau}(1+R_1) + \sigma_H \times \mathrm{BR}_{H\to\tau\tau}(1+R_2) + \sigma_A \times \mathrm{BR}_{A\to\tau\tau}$; (g) Exclusion of these parameters by CDF analysis 9071 without interference (Red=Excluded); (f) Exclusion of these parameters by CDF analysis 9071 with interference (Red=excluded, blue or white=unexcluded).

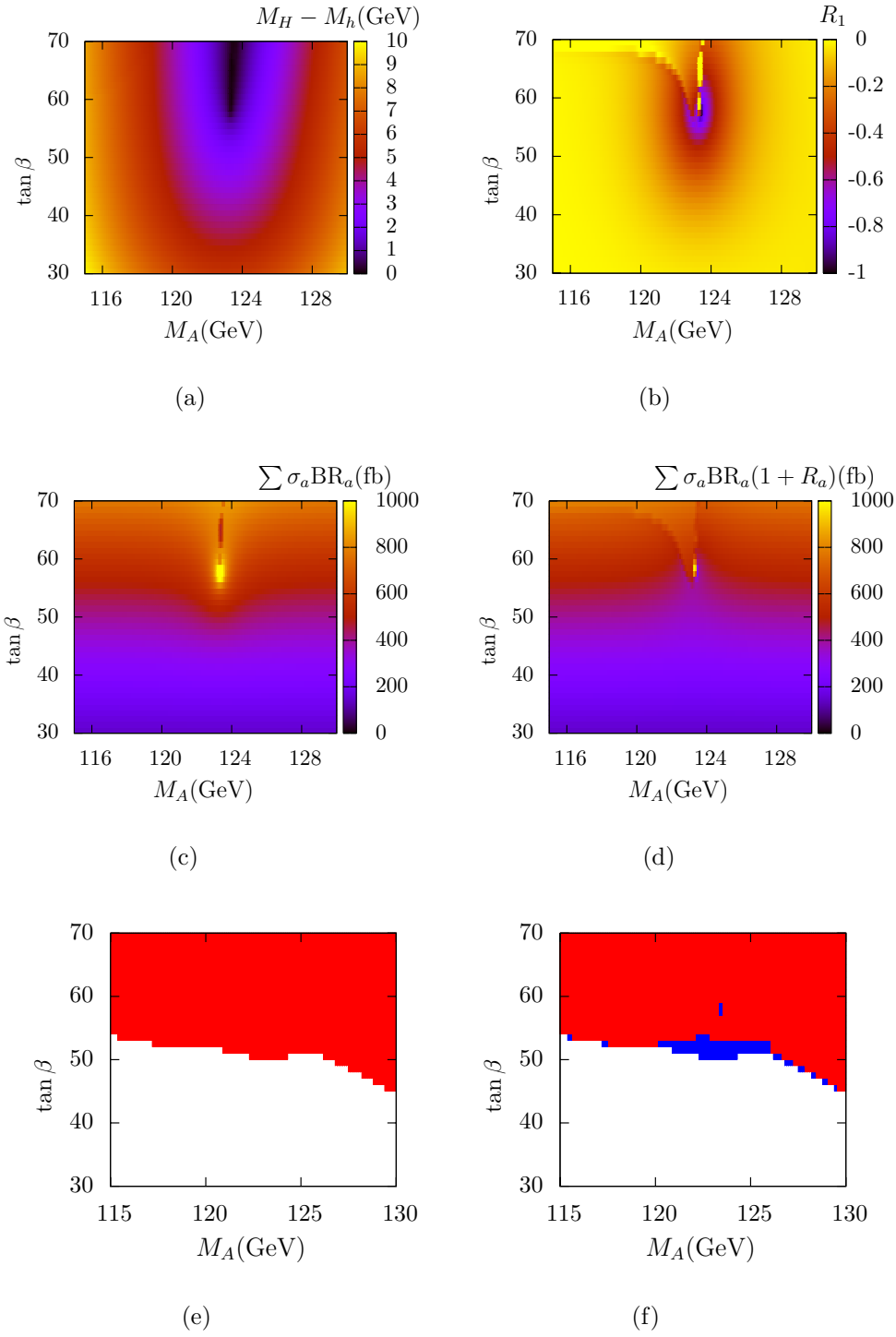

Figure 9.8: Results for the $M_h^{\max}$ scenario in the M_A–$\tan\beta$ plane using `FeynHiggs 2.7.0`, including the $\mathcal{O}(\alpha_t\alpha_s)$ corrections, and obtaining the widths from the sum of the partial decay widths; (a) $M_H - M_h$; (b) R_1; (c) Cross section for $b\bar{b}h_a, h_a \to \tau\tau$ without interference; i.e. $\sigma_h \times \mathrm{BR}_{h\to\tau\tau} + \sigma_H \times \mathrm{BR}_{H\to\tau\tau} + \sigma_A \times \mathrm{BR}_{A\to\tau\tau}$; (d) Cross section for $b\bar{b}h_a, h_a \to \tau\tau$ with interference; i.e. $\sigma_h \times \mathrm{BR}_{h\to\tau\tau}(1+R_1) + \sigma_H \times \mathrm{BR}_{H\to\tau\tau}(1+R_2) + \sigma_A \times \mathrm{BR}_{A\to\tau\tau}$; (g) Exclusion of these parameters by D0 analysis 2491 without interference (Red=Excluded); (f) Exclusion of these parameters by D0 analysis 2491 with interference (Red=excluded, blue or white=unexcluded).

Chapter 10

Asymmetry in the full production and decay process

10.1 Motivation

In Chapter 8 we showed that, in the presence of $\mathcal{CP}$-violating phases, there could be a significant difference between the partial decay widths of a heavy Higgs boson into two neutralinos with left-handed polarisation, $\Gamma^a_{LL} \equiv \Gamma(h_a \to \tilde{\chi}^{0\,L}_2 \tilde{\chi}^{0\,L}_2)$, and right-handed polarisation, $\Gamma^a_{RR} \equiv \Gamma(h_a \to \tilde{\chi}^{0\,R}_2 \tilde{\chi}^{0\,R}_2)$, respectively. The ratio $A_a \equiv (\Gamma^a_{LL} - \Gamma^a_{RR})/(\Gamma^a_{LL} + \Gamma^a_{RR})$ was found to be a $\mathcal{CP}$-odd quantity. Namely, it is antisymmetric with respect to the transformation, $\phi \to -\phi$, where ϕ is a $\mathcal{CP}$-violating phase, even when loop corrections to the Higgs-neutralino-neutralino vertex are included. Thus, a non-zero value for A_a would indicate the existence of $\mathcal{CP}$-violation in the MSSM. Furthermore, A_a was found to have the same sign for both $h_a = h_2$ and $h_a = h_3$, so that the individual ratios, once combined, would reinforce rather than cancel one another. One might naively expect to be able to construct a relevant physical observable by combining A_2 and A_3 into an average, weighted by the cross sections for h_2 and h_3 production and branching ratios for their subsequent decay into neutralinos.

However, we noted that in scenarios where this decay is important, where the Higgs bosons are heavier than the mass of the neutralinos, the Higgs masses are likely to be nearly degenerate, $M_{h_2} \sim M_{h_3}$, with the mass splitting of the same order as the widths of the Higgs bosons, $|M_{h_2} - M_{h_3}| \sim \Gamma_{h_2}, \Gamma_{h_3}$. Thus, it would not be appropriate to construct a weighted average of A_2 and A_3 using the narrow width approximation, the assumptions for which fail in this situation. In order to construct a $\mathcal{CP}$-odd asymmetry

that could be an observable at experiments like the LHC, one must include the full production and decay process for the the nearly mass degenerate Higgs bosons. As seen in Chapter 9, interference effects between the two Higgs propagators in the full squared matrix element can play a large role for the total cross section. It can thus be anticipated that the interference terms may also have the effect of decreasing or even increasing an asymmetry constructed from the polarisation dependent cross sections.

On the one hand, the fact that the asymmetry must be evaluated in situations with nearly degenerate masses is computationally more difficult, on the other hand, we will see that the mass degeneracy of the two Higgs bosons causes the resonant enhancement of $\mathcal{CP}$-violation in the Higgs sector, thus increasing the $\mathcal{CP}$-odd asymmetry.

The resonant enhancement of $\mathcal{CP}$-violating asymmetries in the Higgs sector has received much attention in the literature for the LHC and future colliders. A study of the $\mathcal{CP}$ asymmetries in the polarisations of taus produced in Higgs decays at the LHC was carried out in Ref. [132] using the method developed in Refs. [133, 134]. Scenarios were considered where all three Higgs bosons are light and the mass eigenstates are mixtures of all three $\mathcal{CP}$-eigenstates. It was found that large asymmetries were possible in the longitudinal and transverse polarisations of the tau pairs. The same authors considered similar $\mathcal{CP}$ asymmetries at photon-photon colliders [135] and e^+e^- colliders [136] (see also Ref. [137] for a study of the Higgs line-shape in such scenarios with 3x3 mixing). In our study, we wish to consider asymmetries in neutralino polarisations, and so the Higgs bosons in question, must, of course, be heavier than the masses of the neutralinos. In such cases, the lightest Higgs boson has a mass well below the masses of the h_2 and h_3, so the $\mathcal{CP}$-violating Higgs mixing is effectively 2×2 mixing between H and A. Resonant enhancement of $\mathcal{CP}$ asymmetries in the polarisation of top quarks at photon colliders was studied in the 2×2 mixing case in Ref. [138] (see also Ref. [139] for a similar analysis at the LHC). The Higgs line-shape has also been studied in the 2×2 mixing case [140]. Similar asymmetries were also studied for photon colliders in Ref. [141] and muon colliders in Refs. [142–145]. Asymmetries in Higgs decays into Z boson pairs were studied in Ref. [146] as a method of determining the spin as well as the $\mathcal{CP}$ properties of Higgs bosons (see also Refs. [147, 148]). Asymmetries in the polarisation of neutralinos produced in Higgs decays were studied in Ref. [144] in the context of a muon collider. This study turns out to be rather different to our study of neutralino production in Higgs decays for the LHC, since their technique makes use of polarised muon beams.

In this chapter we consider the asymmetry between the production of left- and right-handed neutralinos in Higgs decays at the LHC. We compute the asymmetries expected

at the parton level for the full production and decay processes, $b\bar{b} \to h_i \to \tilde{\chi}_2^0\tilde{\chi}_2^0$, $W^+W^- \to h_i \to \tilde{\chi}_2^0\tilde{\chi}_2^0$ and $gg \to h_i \to \tilde{\chi}_2^0\tilde{\chi}_2^0$, using both the full propagator matrix method and the on-shell approximation using $\hat{\mathbf{Z}}$ factors described in Chapter 9. We find that the asymmetry for the $b\bar{b}$ fusion process is suppressed by several orders of magnitude, while WW and gg fusion can each result in large asymmetries. We therefore continue by considering the parts of parameter space where Higgs bosons can be detected by their production in gluon fusion and subsequent decay via neutralinos into four leptons. We finally compute the left-right asymmetries in the hadron-level LHC production cross sections for $pp \to h_i \to \tilde{\chi}_2^0\tilde{\chi}_2^0$, comparing the full squared matrix element method to the use of a generalised narrow width approximation with an interference weight factor, as in Section 9.5.

10.2 Calculation of $\mathcal{CP}$-odd asymmetry

For each partonic Higgs production and decay process, $xx' \to h_i \to \tilde{\chi}_2^0\tilde{\chi}_2^0$, where $xx' = b\bar{b}$, W^-W^+, or gg, we define the asymmetry

$$\mathcal{A}_{xx'}(\sqrt{s}) \equiv \frac{\sigma_2}{\sigma_1} \tag{10.1}$$

with

$$\sigma_1(\sqrt{s}) \equiv \sigma_{xx'\to H_i\to\tilde{\chi}_2^{0\,L}\tilde{\chi}_2^{0\,L}} + \sigma_{xx'\to H_i\to\tilde{\chi}_2^{0\,R}\tilde{\chi}_2^{0\,R}} = \int d\Omega(|\mathcal{M}_{LL}|^2 + |\mathcal{M}_{RR}|^2), \tag{10.2}$$

$$\sigma_2(\sqrt{s}) \equiv \sigma_{xx'\to H_i\to\tilde{\chi}_2^{0\,L}\tilde{\chi}_2^{0\,L}} - \sigma_{xx'\to H_i\to\tilde{\chi}_2^{0\,R}\tilde{\chi}_2^{0\,R}} = \int d\Omega(|\mathcal{M}_{LL}|^2 - |\mathcal{M}_{RR}|^2) \tag{10.3}$$

where $d\Omega \equiv \mathrm{dlips}(s; k_3, k_4)/(2\lambda^{\frac{1}{2}}(s, m_x^2, m_{x'}^2))$, $s = (k_1 + k_2)^2 = (k_3 + k_4)^2$ is the squared centre of mass energy, k_1 and k_2 are the four-momenta of the incoming particles, k_3 and k_4 are the four-momenta of the outgoing fermions, and $|\mathcal{M}_{LL}|^2$ and $|\mathcal{M}_{RR}|^2$ are the squared matrix elements for the decay into neutralinos with both left-handed and both right-handed polarisation respectively, averaged over the xx' polarisations. Note that, if O^L and O^R are the effective couplings of xx' to left-handed and right-handed fermions respectively, i.e.

$$\mathcal{M}_{xx'\to H_i\to f\bar{f}} = \bar{u}_f(O^L\omega_L + O^R\omega_R)v_f, \tag{10.4}$$

then

$$|\mathcal{M}_{LL}|^2 - |\mathcal{M}_{RR}|^2 = (|O^L|^2 - |O^R|^2)\sqrt{s(s-4m_f^2)}, \quad (10.5)$$
$$|\mathcal{M}_{LL}|^2 + |\mathcal{M}_{RR}|^2 = (|O^L|^2 + |O^R|^2)(s-2m_f^2) - 4m_f^2 \mathrm{Re}[O^R(O^L)^*]. \quad (10.6)$$

10.2.1 Full propagator matrix approach

In Section 9.2 we showed how to evaluate σ_1 for a general process in the full Higgs propagator matrix approach, using Equation (9.5). The same method can be applied to compute σ_2. There are nine diagrams to consider, illustrated in Figure 9.1, coded into `FeynArts` as nine particles, "ij", where $i, j = h, H, A$. There are three initial state vertices to consider, $\hat{\Gamma}_{x\bar{x}i}$, and three final state vertices, $\hat{\Gamma}_{jf\bar{f}}$, connected by nine full loop-corrected Higgs propagator matrix elements Δ_{ij}, obtained from Equations (3.72) and (3.77). The general tree-level Higgs-fermion-fermion vertex is given in Equation (9.6), where the relevant neutralino-neutralino-Higgs couplings can be obtained from Equation (5.2). We will write the following in terms of general outgoing fermion-antifermion pairs, f and $\bar{f}$, so that our results can also be used to compute asymmetries for eg. $\tau^+\tau^-$ and $t\bar{t}$ production.

$b\bar{b} \to h_i \to \tilde{\chi}_2^0\tilde{\chi}_2^0$

The $b\bar{b}$-Higgs couplings are given in Equation (9.7). We have coded the full 3x3 propagator matrix result into `FeynArts`. Setting Δ_{hi} and Δ_{ih} to zero leads to the simplified 2×2 mixing case where

$$|\mathcal{M}_{LL}|^2 - |\mathcal{M}_{RR}|^2 = -2\sqrt{s(s-4m_f^2)}\mathrm{Re}(G_{ffA}G_{ffH}^*) \\ [s\, G_{bbA}^2 \mathrm{Im}(\Delta_{AA}\Delta_{AH}^*) + G_{bbH}^2(4m_b^2 - s)\mathrm{Im}(\Delta_{HH}\Delta_{HA}^*)] \quad (10.7)$$

We see that the asymmetry will vanish in the limit of $\mathcal{CP}$-conservation in the Higgs sector, where Δ_{HA} and Δ_{AH} are zero. A non-zero asymmetry also requires the loop-corrected propagator matrix elements to have imaginary parts. This will only come about if the Higgs self-energies contain absorptive loop integrals. Absorptive effects on their own, however, cannot fake an asymmetry just because there exist both $\mathcal{CP}$-even and $\mathcal{CP}$-odd Higgs bosons in the same matrix squared element. The $\mathcal{CP}$-eigenstates really have to mix due to $\mathcal{CP}$-violation, so σ_2 is a true $\mathcal{CP}$-odd observable. Also note that complex

neutralino couplings from the vertex alone are not enough to cause an asymmetry; they only appear explicitly in $\mathrm{Re}(G_{ffA}G^*_{ffH})$. Complex neutralino couplings could, however, enter the Higgs self-energies in such a way as to cause $\mathcal{CP}$-violating mixing in the Higgs sector, which would contribute to the asymmetry.

$W^+W^- \to h_i \to \tilde{\chi}^0_2\tilde{\chi}^0_2$

The tree-level Higgs-WW vertex is written as

$$\begin{aligned} \hat{\Gamma}_{hW_\mu W_\nu} &= iG_{hWW}g_{\mu\nu}, \\ \hat{\Gamma}_{HW_\mu W_\nu} &= iG_{HWW}g_{\mu\nu} \end{aligned} \tag{10.8}$$

with $\hat{\Gamma}_{AW_\mu W_\nu} = 0$ and

$$G_{hWW} = \frac{eM_W}{s_W}s_{\beta\alpha}, \qquad G_{HWW} = \frac{eM_W}{s_W}c_{\beta\alpha}. \tag{10.9}$$

In the 2×2 case we obtain

$$|\mathcal{M}_{LL}|^2 - |\mathcal{M}_{RR}|^2 = 4\sqrt{s(s-4m_f^2)}|\epsilon_1.\epsilon_2|^2 G^2_{WWH}\mathrm{Re}(G_{ffA}G^*_{ffH})\mathrm{Im}(\Delta_{HH}\Delta^*_{AH}) \tag{10.10}$$

where ϵ_1 and ϵ_2 are the W boson polarisation vectors;

$$\begin{aligned} \epsilon_1^\mu(\pm) &= \frac{1}{\sqrt{2}}(0, \mp 1, -i, 0), & \epsilon_2^\mu(\pm) &= \frac{1}{\sqrt{2}}(0, \mp 1, i, 0), \\ \epsilon_1^\mu(0) &= \frac{1}{M_W}(|\mathbf{k}_1|, 0, 0, k_1^0), & \epsilon_2^\mu(0) &= \frac{1}{M_W}(|\mathbf{k}_2|, 0, 0, -k_2^0) \end{aligned} \tag{10.11}$$

where the $\pm$ denote right-handed and left-handed W polarisations respectively, while 0 denotes the W longitudinal polarisation. A centre of mass frame is assumed, with initial state four-momentum vectors $k_{1,2} = (\sqrt{M_W^2 + |\mathbf{k}_1|^2}, 0, 0, \pm|\mathbf{k}_1|)$ (see Ref. [149]). Again note that the asymmetry vanishes in the $\mathcal{CP}$-conserving limit and in the limit where there are no absorptive parts in the propagator matrix elements.

$gg \to h_i \to \tilde{\chi}^0_2\tilde{\chi}^0_2$

Gluon-gluon fusion is an important Higgs production process at the LHC (see eg. Ref. [150]). In the SM, the largest contribution to the gluon-gluon vertex is the one-loop

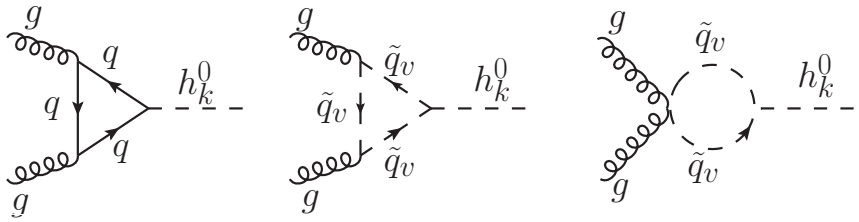

Figure 10.1: Leading order contributions to gluon fusion in the MSSM, where $h_k^0 = \{h, H, A\}$.

top quark triangle diagram. One can write down an effective scalar-type coupling of gluons to the Higgs boson using form factors. In the MSSM, the top quark loop is not always the leading contribution. There are three types of one-loop diagrams, with quarks and squarks running in the loops as shown in Figure 10.1. In the MSSM, the bottom quark loop and the sbottom quark loops can become important for large $\tan\beta$. As in the SM, one can write down effective couplings of the tree-level MSSM Higgs bosons to gluons using gluon fusion form factors, but now there is the possibility for pseudoscalar-type couplings, which have a different Lorentz structure. The effective vertices to the $\mathcal{CP}$-even eigenstates h and H can be written in terms of scalar-type form-factors, $S^g_{h,H}$, while the effective vertex to A can be written in terms of a scalar and pseudoscalar-type form-factor, S^g_A and P^g_A respectively, as follows;

$$\begin{aligned}
\hat{\Gamma}_{hg^\mu g^\nu} &= S^g_h(g^{\mu\nu}k_1.k_2 - k_1^\mu k_2^\mu), \\
\hat{\Gamma}_{Hg^\mu g^\nu} &= S^g_H(g^{\mu\nu}k_1.k_2 - k_1^\mu k_2^\mu), \\
\hat{\Gamma}_{Ag^\mu g^\nu} &= S^g_A(g^{\mu\nu}k_1.k_2 - k_1^\mu k_2^\mu) + P^g_A(i\varepsilon_{\mu\nu\rho\sigma}\epsilon_1^\mu\epsilon_2^\nu k_1^\rho k_2^\sigma),
\end{aligned} \tag{10.12}$$

where $\varepsilon_{\mu\nu\rho\sigma}$ is the antisymmetric Levi-Civita tensor with $\varepsilon^{0123} = 1$ and we use the expressions for $S^g_{h,H,A}$ and P^g_A from Ref. [151];

$$\begin{aligned}
S^g_{h(H)} &= \sum_{f=b,t} G_{h(H)ff}\frac{F_{sf}(\tau_{h(H)f})}{m_f} - \sum_{\tilde{f}_l=\tilde{b}_1,\tilde{b}_2,\tilde{t}_1,\tilde{t}_2} G_{h(H)\tilde{f}\tilde{f}}\frac{F_0(\tau_{h(H)\tilde{f}_l})}{4m^2_{\tilde{f}}}, \\
S^g_A &= -\sum_{\tilde{f}_l=-\tilde{b}_1,\tilde{b}_2,\tilde{t}_1,\tilde{t}_2} G_{A\tilde{f}\tilde{f}}\frac{F_0(\tau_{A\tilde{f}_l})}{4m^2_{\tilde{f}}}, \\
P^g_A &= \sum_{f=b,t} G_{Aff}\frac{F_{pf}(\tau_{Af})}{m_f},
\end{aligned} \tag{10.13}$$

where $\tau_{h_k^0 f} \equiv m_{h_k^0}^2/4m_f^2$, $\tau_{A\tilde{f}_l} \equiv m_{h_k^0}^2/4m_{\tilde{f}}^2$ and the functions F_0, F_{sf} and F_{pf} are defined as

$$\begin{aligned} F_{sf}(\tau) &\equiv (\tau + (\tau-1)f(\tau))/\tau^2, \\ F_{pf}(\tau) &\equiv f(\tau)/\tau, \\ F_0(\tau) &\equiv (-\tau + f(\tau))/\tau^2, \end{aligned} \tag{10.14}$$

where

$$f(\tau) \equiv \left\{ \begin{array}{ll} \arcsin^2(\sqrt{\tau}) & : \tau < 1 \\ -\frac{1}{4}[\ln \frac{\sqrt{\tau}+\sqrt{\tau-1}}{\sqrt{\tau}-\sqrt{\tau-1}} - i\pi]^2 & : \tau > 1 \end{array} \right\}. \tag{10.15}$$

We include only third generation quarks and squarks; they are the most important due to their large Yukawa coupling. The scalar type couplings to $\mathcal{CP}$-even Higgs bosons, $S_{h,H}^g$, come from contributions from all three diagrams in Figure 10.1. There is no pseudoscalar-type coupling for the $\mathcal{CP}$-even Higgs bosons. The pseudoscalar coupling for the $\mathcal{CP}$-odd Higgs boson, P_A^g, comes from the first type of diagram containing quarks only. In the $\mathcal{CP}$-conserving MSSM, these are the only contributions, and S_A^g is zero. When there is $\mathcal{CP}$-violation in the squark sector, due to a non-zero A_f or μ, the contribution to the $\hat{\Gamma}_{ggA}$ vertex is no longer pure pseudoscalar as there can be scalar sfermion loop contributions of the type arising from the second and third diagrams in Figure 10.1. The sfermion loops were found to have a large impact on the gluon fusion couplings in some $\mathcal{CP}$-violating scenarios [152]. Even in $\mathcal{CP}$-conserving scenarios, the sfermion loops can play a significant role for the scalar couplings of the $\mathcal{CP}$-even Higgs bosons [153]. Thus we include all three types of form factors in our asymmetry calculation. We have coded these expressions into `FeynArts` and `FormCalc`.

We construct the matrix element for $gg \to h, H, A \to f\bar{f}$ in the full 3x3 propagator matrix approach by considering the nine propagators, Δ_{ij} $(i, j = h, H, A)$, and the corresponding tree-level vertices, $\Gamma_{hg^\mu g^\nu}$, $\Gamma_{Hg^\mu g^\nu}$, $\Gamma_{Ag^\mu g^\nu}$, $\Gamma_{hf\bar{f}}$, $\Gamma_{Hf\bar{f}}$ and $\Gamma_{Af\bar{f}}$. In the 2×2 mixing case, ignoring, Δ_{hi} and Δ_{ih}, we obtain

$$\begin{aligned} |\mathcal{M}_{LL}|^2 - |\mathcal{M}_{RR}|^2 &= -s^2\sqrt{s(s-4m_f^2)}\mathrm{Re}(G_{ffA}G_{ffH}^*) \times \\ &\quad [|S_H^g|^2\mathrm{Im}(\Delta_{HH}\Delta_{HA}^*) + (|P_A^g|^2 - |S_A^g|^2)\mathrm{Im}(\Delta_{AA}\Delta_{AH}^*) \\ &\quad +\mathrm{Im}(S_H^g S_A^{g*}\Delta_{HA}\Delta_{AH}^* + S_H^{g*}S_A^g\Delta_{AA}\Delta_{HH}^*)] \end{aligned} \tag{10.16}$$

where ϵ_1 and ϵ_2 are the gluon polarisation vectors

$$\epsilon_1^\mu = \frac{1}{\sqrt{2}}(0, \mp 1, -i, 0), \qquad \epsilon_2^\mu = \frac{1}{\sqrt{2}}(0, \mp 1, i, 0) \tag{10.17}$$

where the $\pm$ indicates right and left gluon helicities respectively, and a centre of mass frame is assumed with the gluons moving in the $\pm z$ direction respectively (see Ref. [149]). Again note that the asymmetry vanishes in the $\mathcal{CP}$-conserving limit and is only non-zero if there are absorptive effects in the Higgs self-energies.

10.2.2 On-shell ($\hat{\mathbf{Z}}$ matrix) approximation to Higgs propagator matrix calculation

We follow the method shown in Figure 9.2 and Equation (9.12). Recall that the on-shell approximation with $\hat{\mathbf{Z}}$ matrices is an approximation which keeps only the momentum dependence of the Breit-Wigner propagator, while any other momentum dependent quantities are evaluated with the Higgs boson on-shell. Here there are three particles to consider, h_1, h_2 and h_3, each with a Breit-Wigner propagator, given by Equation (9.11), and vertices determined by the tree-level vertices given in the previous subsection, weighted by $\hat{\mathbf{Z}}$ matrix elements as in Equation (9.10).

$b\bar{b} \to h_i \to \tilde{\chi}_2^0\tilde{\chi}_2^0$

For the $b\bar{b} \to h_i \to f\bar{f}$ process in the limit of H–A mixing, with the h terms ignored, we obtain,

$$\begin{aligned}
|\mathcal{M}_{LL}|^2 - |\mathcal{M}_{RR}|^2 = &-2\sqrt{s(s-4m_f^2)}\mathrm{Re}(G_{ffA}G^*_{ffH}) \\
&\Big[|\Delta^{\mathrm{BW}}_{h_2}|^2\mathrm{Im}(\hat{\mathbf{Z}}_{22}\hat{\mathbf{Z}}^*_{23})[(4m_b^2 - s)G^2_{Hbb}|\hat{\mathbf{Z}}_{22}|^2 - sG^2_{Abb}|\hat{\mathbf{Z}}_{23}|^2] \\
&+ |\Delta^{\mathrm{BW}}_{h_3}|^2\mathrm{Im}(\hat{\mathbf{Z}}_{32}\hat{\mathbf{Z}}^*_{33})[(4m_b^2 - s)G^2_{Hbb}|\hat{\mathbf{Z}}_{32}|^2 - sG^2_{Abb}|\hat{\mathbf{Z}}_{33}|^2] \\
&+ \mathrm{Im}\big[\Delta^{\mathrm{BW}}_{h_2}(\Delta^{\mathrm{BW}}_{h_3})^*(\hat{\mathbf{Z}}_{22}\hat{\mathbf{Z}}^*_{33} - \hat{\mathbf{Z}}_{23}\hat{\mathbf{Z}}^*_{32})[(4m_b^2 - s)G^2_{Hbb}\hat{\mathbf{Z}}_{22}\hat{\mathbf{Z}}^*_{32} \\
&- sG^2_{Abb}\hat{\mathbf{Z}}_{23}\hat{\mathbf{Z}}^*_{33}]\big]\Big].
\end{aligned} \tag{10.18}$$

.

$W^+W^- \to h_i \to \tilde{\chi}_2^0\tilde{\chi}_2^0$

For the $W^+W^- \to h_i \to f\bar{f}$ process in the limit of H–A mixing, with the h terms ignored, we obtain,

$$\begin{aligned}|\mathcal{M}_{LL}|^2 - |\mathcal{M}_{RR}|^2 = &-4\sqrt{s(s-4m_f^2)}|\epsilon_1.\epsilon_2|^2 G_{WWH}^2 |\mathrm{Re}(G_{ffA}G_{ffH}^*) \\ &\Big[|\Delta_{h_2}^{\mathrm{BW}}|^2 \mathrm{Im}(\hat{\mathbf{Z}}_{22}^*\hat{\mathbf{Z}}_{23})|\hat{\mathbf{Z}}_{22}|^2 + |\Delta_{h_3}^{\mathrm{BW}}|^2 \mathrm{Im}(\hat{\mathbf{Z}}_{32}^*\hat{\mathbf{Z}}_{33})|\hat{\mathbf{Z}}_{32}|^2 \\ &+ \mathrm{Im}\big[\Delta_{h_2}^{\mathrm{BW}}(\Delta_{h_3}^{\mathrm{BW}})^*(\hat{\mathbf{Z}}_{23}\hat{\mathbf{Z}}_{32}^* - \hat{\mathbf{Z}}_{22}\hat{\mathbf{Z}}_{32}^*)\hat{\mathbf{Z}}_{22}\hat{\mathbf{Z}}_{32}^*\big]\Big]. \end{aligned} \tag{10.19}$$

.

$gg \to h_i \to \tilde{\chi}_2^0\tilde{\chi}_2^0$

For the $gg \to h_i \to f\bar{f}$ process in the limit of H–A mixing, with the h terms ignored, we obtain,

$$\begin{aligned}|\mathcal{M}_{LL}|^2 - |\mathcal{M}_{RR}|^2 \;=\; &-s^2\sqrt{s(s-4m_f^2)}\mathrm{Re}(G_{ffA}G_{ffH}^*) \\ &\Big[|\Delta_{h_2}^{\mathrm{BW}}|^2 \mathrm{Im}(\hat{\mathbf{Z}}_{22}\hat{\mathbf{Z}}_{23}^*)(|S_H^g\hat{\mathbf{Z}}_{22} + S_A^g\hat{\mathbf{Z}}_{23}|^2 + |P_A^g\hat{\mathbf{Z}}_{23}|^2) \\ &+|\Delta_{h_3}^{\mathrm{BW}}|^2 \mathrm{Im}(\hat{\mathbf{Z}}_{32}\hat{\mathbf{Z}}_{33}^*)(|S_H^g\hat{\mathbf{Z}}_{32} + S_A^g\hat{\mathbf{Z}}_{33}|^2 + |P_A^g\hat{\mathbf{Z}}_{33}|^2) \\ &+\mathrm{Im}\Big(\Delta_{h_2}^{\mathrm{BW}}(\Delta_{h_3}^{\mathrm{BW}})^*(\hat{\mathbf{Z}}_{23}\hat{\mathbf{Z}}_{32}^* - \hat{\mathbf{Z}}_{22}\hat{\mathbf{Z}}_{33}^*)[(S_H^g\hat{\mathbf{Z}}_{22} + S_A^g\hat{\mathbf{Z}}_{23}) \\ &\times(S_H^{g*}\hat{\mathbf{Z}}_{32}^* + S_A^{g*}\hat{\mathbf{Z}}_{33}^*) + |P_A^g|^2\hat{\mathbf{Z}}_{23}\hat{\mathbf{Z}}_{33}^*]\Big)\Big]. \end{aligned} \tag{10.20}$$

For reference in a later example we also write down the spin summed matrix element, $|\mathcal{M}_{LL}|^2 + |\mathcal{M}_{RR}|^2$ in the limit where the fermion masses are only kept in the Yukawa

couplings;

$$
\begin{aligned}
|\mathcal{M}_{LL}|^2+|\mathcal{M}_{RR}|^2 =& \frac{s^3}{2}\Bigg[|\Delta_{h_2}^{\mathrm{BW}}|^2\big(|S_H^g\hat{\mathbf{Z}}_{22}+S_A^g\hat{\mathbf{Z}}_{23}|^2+|P_A^g\hat{\mathbf{Z}}_{23}|^2\big)\big(|G_{Hff}\hat{\mathbf{Z}}_{22}|^2+|G_{Aff}\hat{\mathbf{Z}}_{23}|^2 \\
&+2\mathrm{Re}(\hat{\mathbf{Z}}_{22}\hat{\mathbf{Z}}_{23}^*)\mathrm{Im}(G_{Aff}G_{Hff}^*)\big)+|\Delta_{h_3}^{\mathrm{BW}}|^2\big(|S_H^g\hat{\mathbf{Z}}_{32}+S_A^g\hat{\mathbf{Z}}_{33}|^2 \\
&+|P_A^g\hat{\mathbf{Z}}_{33}|^2\big)\big(|G_{Hff}\hat{\mathbf{Z}}_{32}|^2+|G_{Aff}\hat{\mathbf{Z}}_{33}|^2+2\mathrm{Re}(\hat{\mathbf{Z}}_{32}\hat{\mathbf{Z}}_{33}^*)\mathrm{Im}(G_{Aff}G_{Hff}^*)\big) \\
&+2i\mathrm{Im}\Bigg(\Delta_{h_2}^{\mathrm{BW}}(\Delta_{h_3}^{\mathrm{BW}})^*\big[(S_H^g\hat{\mathbf{Z}}_{22}+S_A^g\hat{\mathbf{Z}}_{23})(S_H^g\hat{\mathbf{Z}}_{32}^*+S_A^g\hat{\mathbf{Z}}_{33}^*) \\
&+|P_A^g|^2\hat{\mathbf{Z}}_{23}\hat{\mathbf{Z}}_{33}^*\big]\big[|G_{Hff}|^2\hat{\mathbf{Z}}_{22}\hat{\mathbf{Z}}_{32}^*+|G_{Aff}|^2\hat{\mathbf{Z}}_{23}\hat{\mathbf{Z}}_{33}^*+(\hat{\mathbf{Z}}_{23}\hat{\mathbf{Z}}_{32}^* \\
&+\hat{\mathbf{Z}}_{22}\hat{\mathbf{Z}}_{33}^*)\mathrm{Im}(G_{Aff}G_{Hff}^*)\big]\Bigg)\Bigg]. \qquad (10.21)
\end{aligned}
$$

10.2.3 Importance of interference effects

In the $\hat{\mathbf{Z}}$ matrix approach, the interference terms can have a large effect if there is significant overlap of the two Breit-Wigner functions and significant $\mathcal{CP}$-violating mixing so that the $\hat{\mathbf{Z}}$ matrix elements are all non-zero. In order to see the importance of interference to obtain the correct value for σ_2, we consider the process $b\bar{b}\to h_2,h_3\to\tau^+\tau^-$. We assume degenerate masses, $M_{h_2}\sim M_{h_3}$, and widths, $\Gamma_{h_2}\sim\Gamma_{h_3}$, and $c_\alpha/c_\beta\approx t_\beta$. We then use Equation (9.16) to write the $\hat{\mathbf{Z}}$ matrix elements in Equation (10.18) in terms of a complex mixing angle, θ, to obtain

$$
\begin{aligned}
|\mathcal{M}_{LL}|^2-|\mathcal{M}_{LL}|^2 &\propto t_\beta^4|\Delta_{h_2}^{\mathrm{BW}}|^2\big[\big(c_\theta s_\theta c_\theta^{*2}+s_\theta^2c_\theta^*s_\theta^*-s_\theta c_\theta s_\theta^{*2}-c_\theta^2s_\theta^*c_\theta^*\big) \\
&\quad+\big(c_\theta s_\theta s_\theta^{*2}-s_\theta^2s_\theta^*c_\theta^*-s_\theta c_\theta c_\theta^{*2}+c_\theta^2c_\theta^*s_\theta^*\big)\big] \\
&= 0. \qquad (10.22)
\end{aligned}
$$

The first bracket comes from $|\Delta_{h_2}^{\mathrm{BW}}|^2$ and $|\Delta_{h_3}^{\mathrm{BW}}|^2$, while the second bracket is the interference term from $\Delta_{h_2}^{\mathrm{BW}}(\Delta_{h_3}^{\mathrm{BW}})^*$ and $\Delta_{h_3}^{\mathrm{BW}}(\Delta_{h_2}^{\mathrm{BW}})^*$. One can see that they exactly cancel in this limit. If we had not included the interference term in the second bracket we would have wrongly predicted a non-zero asymmetry between the squared matrix elements for the left and right-handed tau polarisations. Of course, this cancellation only occurs under the exact conditions given above. We shall see in the next section that asymmetries are possible with masses that are nearly but not exactly degenerate. The point made here is that interference can have a very large effect on asymmetries and must be taken into account for accurate predictions.

A similar cancellation occurs for $gg \to h_2, h_3 \to f\bar{f}$ in this limit. Assuming degenerate masses and widths, $M_{h_2} \sim M_{h_3}$ and $\Gamma_{h_2} \sim \Gamma_{h_3}$ and ignoring S_A^g, we use Equation (9.16) to write the $\hat{\mathbf{Z}}$ matrix elements in Equation (10.20) in terms of a complex mixing angle, θ, to obtain

$$\begin{aligned} |\mathcal{M}_{LL}|^2 - |\mathcal{M}_{RR}|^2 &\propto |\Delta_{h_2}^{\mathrm{BW}}|^2 \mathrm{Im}(c_\theta s_\theta^*)\big[(|c_\theta|^2 - |s_\theta|^2)(|S_H^g|^2 - |P_A^g|^2) \\ &\quad + (|s_\theta|^2 + |c_\theta|^2)(|S_H^g|^2 - |P_A^g|^2)\big] \\ &= 2|\Delta_{h_2}^{\mathrm{BW}}|^2 \mathrm{Im}(c_\theta s_\theta^* |c_\theta|^2)\big[|S_H^g|^2 - |P_A^g|^2\big] \end{aligned} \tag{10.23}$$

where the term in the second line is the interference term from $\Delta_{h_2}^{\mathrm{BW}}(\Delta_{h_3}^{\mathrm{BW}})^*$. The scalar coupling, S_H^g, is often of a similar size to the pseudoscalar coupling, P_A^g. Hence, in the limit of exactly degenerate masses and widths, we expect the asymmetry to be suppressed. On the other hand, resonant enhancement of the $\mathcal{CP}$-violating mixing self-energies, and hence $\hat{\mathbf{Z}}_{AH} \sim c_\theta$, also occurs in the limit of degenerate masses. So there are two effects in play which may enhance or suppress the asymmetry in this case.

10.3 Numerical results for asymmetry at the parton level

We report on numerical results for $\mathcal{A}_{xx'}(\sqrt{s})$ in the modified SPS1a scenario with $\mathcal{CP}$-violating phases. In Figures 10.2(a) and 10.2(b) we show $\sigma_1(\sqrt{s})$ and $\sigma_2(\sqrt{s})$ respectively for $b\bar{b} \to h_i \to \tilde{\chi}_2^0\tilde{\chi}_2^0$ in the modified SPS1a scenario with $A_t = 510\, e^{-i7\pi/10}\,\mathrm{GeV}$. In the previous chapter we showed examples where interference could have a large effect on the value of σ_1. As seen previously, the full 3x3 propagator matrix result (black curve) and the on-shell approximation using Breit-Wigner propagators and $\hat{\mathbf{Z}}$ matrices (green curve) agree very well (the latter is not visible in the plot because it is directly underneath the black curve). As discussed in the previous chapter, this is expected because the Breit-Wigner propagator captures the leading momentum dependence of the diagonal propagator matrix elements, while the remaining non-resonant momentum dependence of the self-energies is not as important. In addition, the on-shell approximation in the 2×2 case with no interference term (blue curve) also agrees quite well, only slightly overestimating the peak value of σ_1 by a few percent. Based on this result, one might be tempted to use the narrow width approximation to calculate the asymmetry, $\mathcal{A}_{b\bar{b}}$. However, as the blue curve in Figure 10.2(b) for σ_2 shows, leaving out

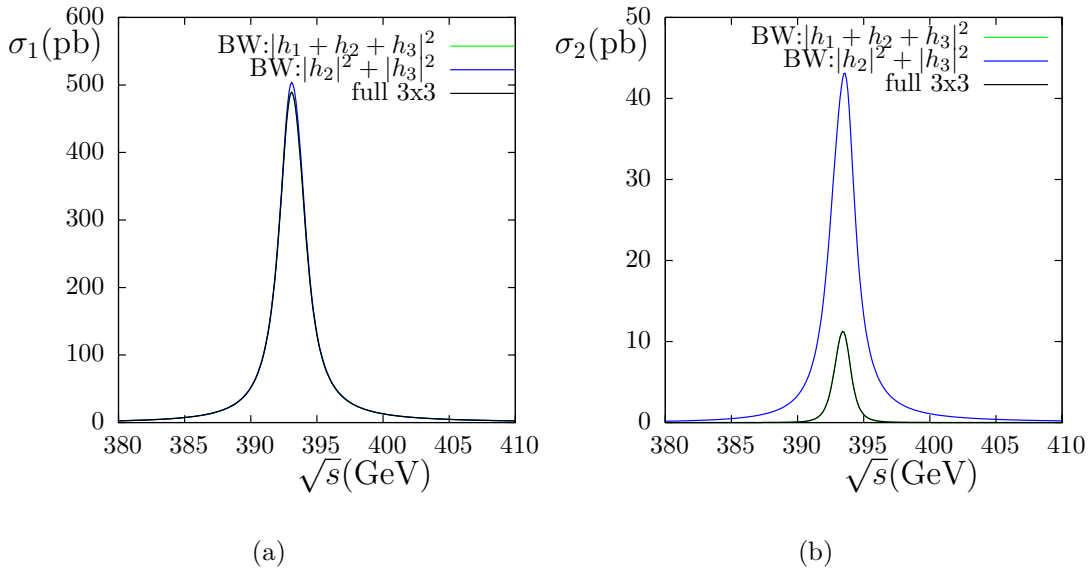

(a) (b)

Figure 10.2: Partonic cross sections for $bb \to h_i \to \tilde{\chi}_2^0\tilde{\chi}_2^0$ in the modified SPS1a scenario with $\phi_{A_t} = -7\pi/10$; (a) σ_1 as a function of $\sqrt{s}$; (b) σ_2 as a function of $\sqrt{s}$. The black curve is obtained from the full 3x3 propagator matrix calculation, while the green and blue curves are obtained using the on-shell approximation with $\hat{\mathbf{Z}}$ factors and Breit-Wigner propagators. The green curve contains 3x3 mixing with interference, while the blue curve contains only 2×2 mixing and no interference. Note that the green curve is directly underneath the black curve.

the important interference terms overestimates the size of σ_2 in the full 3x3 propagator matrix method (black curve) by around 400%. The on-shell approximation including interference between the Breit-Wigner propagators (green) does give a good estimation of σ_2 if interference is included (the green curve is directly underneath the black curve). It is interesting to note that, despite the large values for $A_2 \sim 40\%$ and $A_3 \sim 9\%$ found for the individual decays $h_2 \to \tilde{\chi}_2^0\tilde{\chi}_2^0$ in Figure 8.8(b), the asymmetry for the full production and decay process is small. σ_1 has a peak value of nearly 500 pb, while σ_2 has a peak value of only ~ 10 pb, leading to an asymmetry of only around 2%. The same observation was also made in Ref. [132] for the process $b\bar{b} \to h_1, h_2, h_3 \to \tau^+\tau^-$. It turns out to be particular to asymmetries with down-type fermions in the initial state, for scenarios where the main contribution to the absorptive parts of the Higgs self-energies also comes from down-type SM fermions. We will explain this in more detail in the next section.

In Figures 10.3(a) and 10.3(b) we show $\sigma_1(\sqrt{s})$ and $\sigma_2(\sqrt{s})$ respectively for $W^+W^- \to h_i \to \tilde{\chi}_2^0\tilde{\chi}_2^0$ in the SPS1a scenario again modified so that $A_t = 510\, e^{-i7\pi/10}$ GeV. We see that again, for this process, the full 3x3 propagator matrix method (black) and on-shell

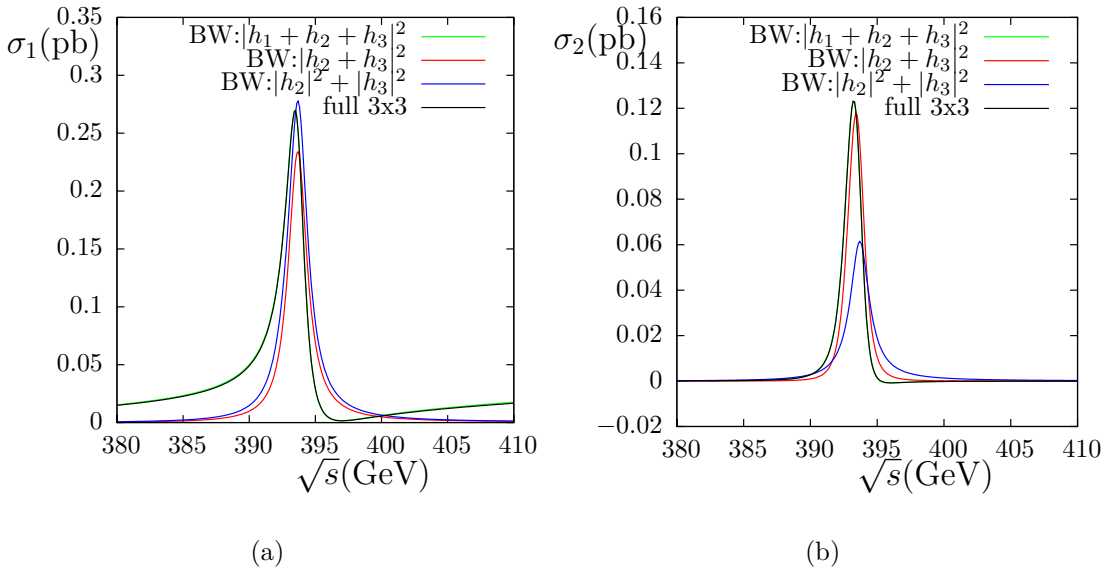

(a) (b)

Figure 10.3: Partonic cross sections for $WW \to h_i \to \tilde{\chi}_2^0\tilde{\chi}_2^0$ in the SPS1a scenario with $\phi_{A_t} = -7\pi/10$; (a) σ_1 as a function of $\sqrt{s}$; (b) σ_2 as a function of $\sqrt{s}$. The black curve is obtained from the full 3x3 propagator matrix calculation, while the green, red and blue curves are obtained using the on-shell approximation with $\hat{\mathbf{Z}}$ factors and Breit-Wigner propagators. The green curve contains 3x3 mixing with interference, while the red (blue) curve contains 2×2 mixing with (without) interference. Note that the green curve is directly underneath the black curve.

apporximation with Breit-Wigner propagators and $\hat{\mathbf{Z}}$ factors with 3x3 mixing (green) give results in almost perfect agreement for σ_1 (the green curve is directly underneath the black curve). The latter approach using only 2×2 mixing (red curve) does not do so well, resulting in a different line-shape. For WW fusion, the h_1 continuum production continues to have an effect at larger $\sqrt{s} \sim M_{h_{2,3}}$, since it has a much larger coupling to gauge bosons than the heavy Higgs bosons. This distorts the combined line-shape of the h_2 and h_3 resonances. The on-shell Breit-Wigner approximation in the 2×2 case underestimates the cross section for $\sqrt{s} \lesssim M_{h_{2,3}}$ and for $\sqrt{s} \gtrsim 400\,\text{GeV}$ where the continuum h_1 production dominates. The 2×2 method also overestimates the total cross section for $M_{h_{2,3}} \lesssim \sqrt{s} \lesssim 400\,\text{GeV}$, where h_2 and h_3 exhibit destructive interference with the h_1. Thus, for the WW initial state, it is important to include 3x3 mixing to get the correct line-shape. The effect of not including the interference between h_2 and h_3 in the 2×2 case (blue curve) is to overestimate the peak value of σ_1 compared with the 2×2 calculation with interference (red curve). For the asymmetric cross section, σ_2, shown in Figure 10.3(b), the line-shape effects from the h_1 interference are less prominent. The full 3x3 propagator matrix method and on-shell Breit-Wigner approximation in the

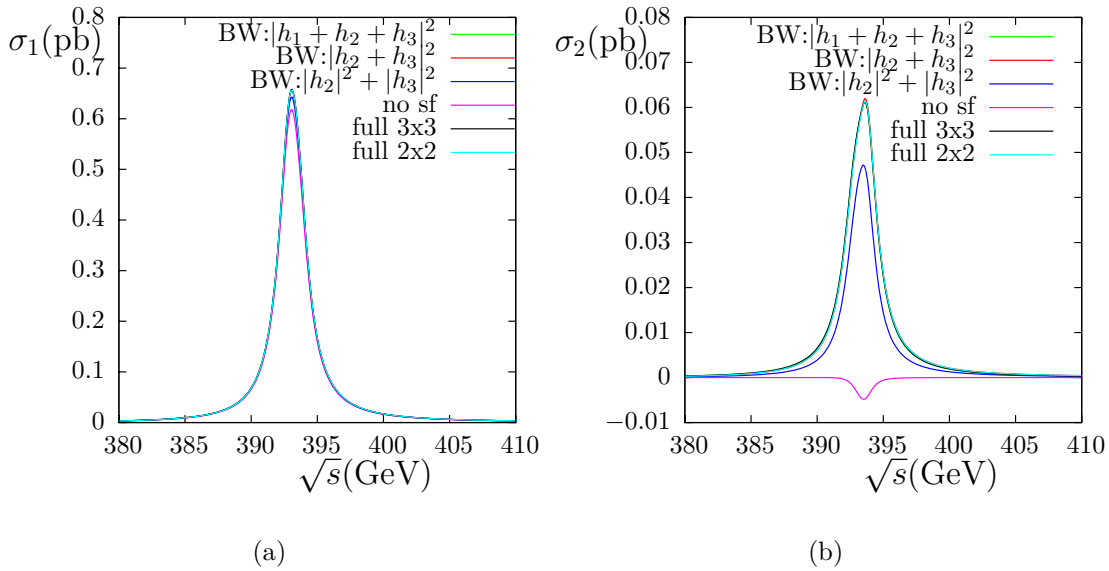

Figure 10.4: Partonic cross sections for $gg \to h_i \to \tilde{\chi}_2^0\tilde{\chi}_2^0$ in the modified SPS1a scenario with $\phi_{A_t} = -7\pi/10$; (a) σ_1 as a function of $\sqrt{\hat{s}}$; (b) σ_2 as a function of $\sqrt{\hat{s}}$. The black (cyan) curve is obtained from the full 3x3 (2×2) propagator matrix calculation, while the green, red and blue curves are obtained using the on-shell approximation with $\hat{\mathbf{Z}}$ factors and Breit-Wigner propagators. The green curve contains 3x3 mixing with interference, while the red (blue) curve contains 2×2 mixing with (without) interference. The pink curve, denoted "no sf" indicates that the sfermion couplings are set to zero in the gluon fusion form factors. Note that curves not visible in the plot are directly underneath other curves.

3x3 case give results in perfect agreement (the green curve is directly underneath the black curve). The peak value of σ_2 is around 0.12 pb, while the peak value of σ_1 is around 0.27 pb. The resulting asymmetry is $\sim 45\%$, a much more promising result than that seen for the $b\bar{b}$ initial state. The results obtained using the on-shell Breit-Wigner approximation in the 2×2 case (red) slightly underestimate the peak value of σ_2, and result in a slightly different line-shape compared to the full 3x3 result, but this is not nearly as noticeable as for σ_1. The effect of not including the interference between h_2 and h_3 (blue) is to underestimate σ_2, and hence the asymmetry, by nearly a factor of 2. The interference term can therefore enhance, as well as suppress, the asymmetry.

In Figures 10.4(a) and 10.4(b) we show $\sigma_1(\sqrt{s})$ and $\sigma_2(\sqrt{s})$ for $gg \to h_i \to \tilde{\chi}_2^0\tilde{\chi}_2^0$ in the SPS1a scenario again modified so that $A_t = 510\, e^{-i7\pi/10}$ GeV. The black and green curves, which use the full 3x3 propagator matrix method and the 3x3 on-shell approximation with Breit-Wigner propagators and $\hat{\mathbf{Z}}$ matrices respectively to calculate σ_1, are indistinguishable, with a peak value of $\sigma_1 \sim 0.6$ pb. Similarly, the cyan and red curves, which use the 2×2 propagator matrix method and the 2×2 on-shell Breit-Wigner

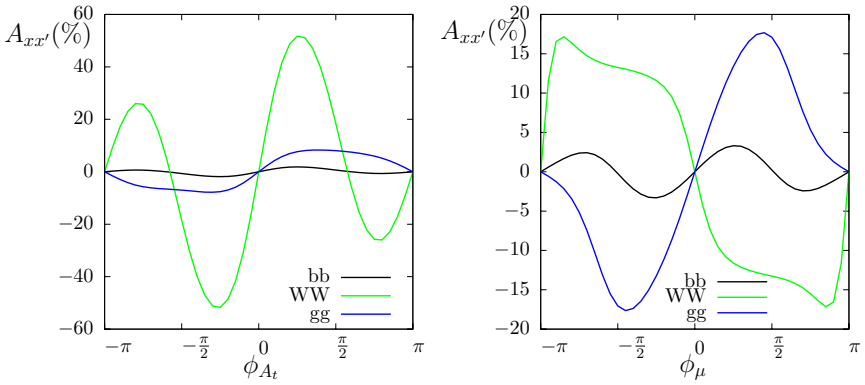

(a) (b)

Figure 10.5: Asymmetry, $\mathcal{A}_{xx'}$, for $xx' = b\bar{b}$, WW and gg (black, green and blue respectively) with $\sqrt{s} = 393\,\text{GeV}$; (a) as a function of ϕ_{A_t} in the modified SPS1a scenario (with $\phi_\mu = 0$); (b) as a function of ϕ_μ in the modified SPS1a scenario (with $\phi_{A_t} = \pi$ as in the usual SPS1a scenario).

approximation with interference respectively, are in good numerical agreement with the full 3x3 results. On the other hand, the 2×2 on-shell Breit-Wigner approximation without the interference between h_2 and h_3 (dark blue) underestimates the full result by a few percent. We also show in pink the 3x3 on-shell Breit-Wigner approximation, where we only include top and bottom quark contributions in the gluon fusion form factors. This underestimates the full result by even more than the BW without interference, emphasising the importance of including the squark contributions to the gluon fusion form factors. For the asymmetric cross section, σ_2, shown in Figure 10.4(b), again the black and green curves for the full 3x3 propagator matrix result and the 3x3 on-shell Breit-Wigner approximation respectively, are indistinguishable, with a peak value of $\sim 0.06\,\text{pb}$, resulting in an asymmetry of $\sim 9\%$. The 2×2 propagator matrix result (light blue) and the 2×2 on-shell Breit-Wigner approximation (red) are also very close to this value. The 2×2 on-shell Breit-Wigner approximation with no interference (dark blue) is well below these curves, with a peak value of $\sim 0.045\,\text{pb}$, underestimating the asymmetry by $\sim 20\%$. Finally, in pink we also show the 3x3 on-shell Breit-Wigner approximation, where we only include top and bottom quark contributions in the gluon fusion form factors, omitting the sfermion contributions. This results in the wrong sign and magnitude for σ_2, highlighting the importance of including the additional scalar contributions to the gluon fusion form factors from squarks in this scenario.

In Figure 10.5(a) we show the asymmetry, $\mathcal{A}_{xx'}$, for $xx' = b\bar{b}$, WW and gg (black, green and blue respectively), as a function of ϕ_{A_t} in the SPS1a scenario, with $\sqrt{s} = 393\,\text{GeV}$. As already discussed, the asymmetry for the $b\bar{b}$ fusion process is much less than for the other processes. We see that WW fusion has the largest asymmetry of the three processes, with a peak value of more than 50% for $\phi_{A_t} \sim \pm\pi/4$. This is much larger than the peak values of the asymmetry for gg of around 9%. We can explain the asymmetry values by looking at the values of A_2 and A_3 in Figure 8.8(b). A_3 exhibits a much larger peak asymmetry of $\sim 38\%$, compared to A_2, which has a peak value of $\sim 9\%$. The $\hat{\mathbf{Z}}$ matrix elements shown in Figure 8.6(c) for this scenario indicate that h_2 is mostly A and h_3 is mostly H. (Note also that the peaks in the asymmetry correspond roughly to the peaks for the $\hat{\mathbf{Z}}$ matrix elements in Figure 8.6(c).) Since gauge bosons do not couple to A, the effect of the larger asymmetry, A_3, will dominate for WW. For gg on the other hand, the couplings to H and A are similar so that both contribute significantly. However, as shown in Figure 8.6(a), the decay width (and, correspondingly, the branching ratio) for $h_2 \to \tilde{\chi}_2^0\tilde{\chi}_2^0$ is about 7 times larger that that of $h_3 \to \tilde{\chi}_2^0\tilde{\chi}_2^0$ for the range of ϕ_{A_t} shown. This explains why the $\mathcal{A}_{gg}$ asymmetry is much closer to $A_2 \sim 9\%$ than the larger A_3.

This suppression of $\mathcal{A}_{gg}$ relative to $\mathcal{A}_{WW}$ is not, however, universal. In Figure 10.5(b) we show the asymmetry, $\mathcal{A}_{xx'}$, for $xx' = b\bar{b}$, WW and gg (black, green and blue respectively), as a function of ϕ_μ in the SPS1a scenario, again with $\sqrt{s} = 393\,\text{GeV}$. Here we find that $\mathcal{A}_{gg}$ has peak values of $\sim \pm 18\%$, while $\mathcal{A}_{WW}$ has peak values of $\sim \pm 17\%$. Once again, we find that $\mathcal{A}_{b\bar{b}}$ is much less than $\mathcal{A}_{gg}$ and $\mathcal{A}_{WW}$. In the next section we explore the reason behind this observation.

10.4 A closer look at the asymmetry using the propagator matrix approach

In this section we take a closer look at the expressions derived for $|\mathcal{M}_{LL}|^2 - |\mathcal{M}_{RR}|^2$ in Section 10.2.1 using the 2×2 propagator matrix approach in order to show why the asymmetry between the production of left and right fermions in Higgs decays is suppressed for $b\bar{b}$ in the initial state, but not for WW and gg.

For $b\bar{b} \to H, A \to f\bar{f}$, in the limit of massless bottom quarks (retaining their mass in the Yukawa couplings), we have,

$$|\mathcal{M}_{LL}|^2 - |\mathcal{M}_{RR}|^2 = -2s^2 \mathrm{Re}(G_{ffA} G^*_{ffH})[G^2_{bbA} \mathrm{Im}(\Delta_{AA}\Delta^*_{AH}) - G^2_{bbH} \mathrm{Im}(\Delta^*_{HH}\Delta^*_{HA})] \tag{10.24}$$

In the 2×2 mixing case, the propagators Δ_{ii} and Δ_{ij} are given by Equations (3.79) and (3.81) respectively. Using these expressions we obtain

$$\mathrm{Im}(\Delta_{HH}\Delta^*_{HA}) = \frac{-\mathrm{Im}[(p^2 - m^2_A)\hat{\Sigma}^*_{HA} + \hat{\Sigma}_{AA}\hat{\Sigma}^*_{HA}]}{|(p^2 - m^2_H + \hat{\Sigma}_{HH})(p^2 - m^2_A + \hat{\Sigma}_{AA}) - \hat{\Sigma}^2_{HA}|^2} \tag{10.25}$$

and

$$\mathrm{Im}(\Delta_{AA}\Delta^*_{AH}) = \frac{-\mathrm{Im}[(p^2 - m^2_H)\hat{\Sigma}^*_{HA} + \hat{\Sigma}_{HH}\hat{\Sigma}^*_{HA}]}{|(p^2 - m^2_H + \hat{\Sigma}_{HH})(p^2 - m^2_A + \hat{\Sigma}_{AA}) - \hat{\Sigma}^2_{HA}|^2} \tag{10.26}$$

For the scenarios studied, $\mathrm{Im}(\hat{\Sigma}_{HA}) \ll \mathrm{Im}(\hat{\Sigma}_{HH}, \hat{\Sigma}_{AA})$, so we will assume that the only significant contribution to the imaginary part comes from the latter. Then

$$|\mathcal{M}_{LL}|^2 - |\mathcal{M}_{RR}|^2 \propto G^2_{bbH}(\mathrm{Im}\,\hat{\Sigma}_{AA})(\mathrm{Re}\,\hat{\Sigma}_{HA}) - G^2_{bbA}(\mathrm{Im}\,\hat{\Sigma}_{HH})(\mathrm{Re}\,\hat{\Sigma}_{HA}). \tag{10.27}$$

This so far confirms what we have already claimed; in order to have an asymmetry, there must be an absorptive part, i.e. non-zero $\mathrm{Im}\,\hat{\Sigma}_{HH}$ and/or $\mathrm{Im}\,\hat{\Sigma}_{AA}$, and there must be $\mathcal{CP}$-violation, i.e non-zero $\mathrm{Re}\,\hat{\Sigma}_{HA}$. The reason that, even with these conditions satisfied, the asymmetry for $b\bar{b}$ is suppressed, is that the main contribution to the imaginary part of the Higgs self-energies comes from the b-quark loop. In each case this contribution is given by

$$\begin{aligned}
\mathrm{Im}(\hat{\Sigma}^b_{AA}) &= -\frac{3}{\pi^2} G^2_{bbA} \mathrm{Im}[p^2\, B_1(p^2, m^2_b, m^2_b)] \equiv G^2_{bbA} Y, \\
\mathrm{Im}(\hat{\Sigma}^b_{HH}) &= -\frac{3}{\pi^2} G^2_{bbH} \mathrm{Im}[p^2\, B_1(p^2, m^2_b, m^2_b) + 2m^2_b B_0(p^2, m^2_b, m^2_b)] \approx G^2_{bbH} Y
\end{aligned} \tag{10.28}$$

where the $m^2_b \mathrm{Im}[B_0(p^2, m^2_b, m^2_b)]$ term is small. Thus, the imaginary parts of the H and A self-energies can each be written in terms of the same expression, Y, weighted by the coupling factors, G^2_{bbH} and G^2_{bbA} respectively. This leads to

$$|\mathcal{M}_{LL}|^2 - |\mathcal{M}_{RR}|^2 \propto -G^2_{bbH}(G^2_{bbA} Y) + G^2_{bbA}(G^2_{bbH} Y) = 0. \tag{10.29}$$

Thus, the main contribution to the asymmetry vanishes. Of course there are other, smaller contributions to the imaginary parts of $\Delta_{HH}\Delta^*_{HA}$ and $\Delta_{AA}\Delta^*_{AH}$ which do not cancel, so the asymmetry is not exactly zero. However, the asymmetry is significantly suppressed due to the fact that the fermions in the initial state have the same couplings as the b-quarks contributing to the absorptive parts of the Higgs self-energies. The authors of Ref. [132] made a similar observation for the tau polarisation asymmetry in $b\bar{b} \to h, H, A \to \tau\tau$ and gave an explanation using the optical theorem. We also note that the same cancellation will occur if the initial state fermions are muons or any other down-type fermions, since $m_b^2 G^2_{\mu\mu H} = m_\mu^2 G^2_{bbH}$ and $m_b^2 G^2_{\mu\mu A} = m_\mu^2 G^2_{bbA}$.

In their study of asymmetries in the polarisation of neutralinos in the process $\mu^+\mu^- \to H, A \to \tilde{\chi}^0_2\tilde{\chi}^0_2$ at a muon collider, the authors of Ref. [144] assume polarised muon beams, which enhances the effect of the asymmetry. At the LHC we do not have the option of polarised beams, so we will need to consider processes which do not involve down-type fermions in the initial state.[1]

Applying the same argument as above for $WW \to H, A \to f\bar{f}$, we obtain,

$$|\mathcal{M}_{LL}|^2 - |\mathcal{M}_{RR}|^2 \approx \frac{4\sqrt{s(s-4m_f^2)}|\epsilon_1.\epsilon_2|^2 G^2_{WWH}\mathrm{Re}(G_{ffA}G^*_{ffH})[G^2_{bbA}Y\mathrm{Re}(\Sigma_{HA})]}{|(p^2 - m_H^2 + \hat{\Sigma}_{HH})(p^2 - m_A^2 + \hat{\Sigma}_{AA}) - \hat{\Sigma}^2_{HA}|^2}. \tag{10.30}$$

Here there can be no cancellation; there is only one term since gauge bosons do not couple to the $\mathcal{CP}$-odd Higgs boson and in any case there is no down-type fermion-fermion-Higgs coupling in the initial state. For $gg \to H, A \to f\bar{f}$, we obtain,

$$\begin{aligned}|\mathcal{M}_{LL}|^2 - |\mathcal{M}_{RR}|^2 \approx\ & -s^2\sqrt{s(s-4m_f^2)}\mathrm{Re}(G_{ffA}G^*_{ffH})\, Y\, \mathrm{Re}(\Sigma_{HA}) \times \\ & \frac{(|P^g_A|^2 - |S^g_A|^2)G^2_{bbH} + |S^g_H|^2 G^2_{bbA}}{|(p^2 - m_H^2 + \hat{\Sigma}_{HH})(p^2 - m_A^2 + \hat{\Sigma}_{AA}) - \hat{\Sigma}^2_{HA}|^2}\end{aligned} \tag{10.31}$$

Again there is no cancellation. Even in the case where the gluon fusion form factors are dominated by a bottom quark loop, so that the Higgs is effectively coupling to $b\bar{b}$, with

[1] Note, however, that, while the asymmetry between left and right fermion polarisations is proportional to $|O^L|^2 - |O^R|^2$, where O^L and O^R are defined in Equation (10.4), triple product asymmetries in the momenta of the decay products arise from non-zero $\mathrm{Im}(O_R O^*_L)$. We have checked that $\mathrm{Im}(O_R O^*_L)$ for $xx' = b\bar{b}$ does not suffer from the same cancellation as $|O_L|^2 - |O_R|^2$. Thus, triple product asymmetries may offer a method complementary to the neutralino polarisation asymmetries, especially for large $\tan\beta$, where $b\bar{b}$ fusion is the dominant production process for heavy Higgs bosons [150], and neutralino decays may be one of the only decay channels in which they are visible [35]. This is, however, beyond the scope of this work.

$|P_A^g|^2 \propto G_{Abb}^2$, $|S_H^g|^2 \propto G_{Hbb}^2$ and $|S_A^g|^2 \approx 0$, there is no cancellation due to the plus sign between the two terms.

Note that in both Equations 10.30 and 10.31, the asymmetry is proportional to the absorptive loop integral, Y, and the $\mathcal{CP}$-violating self-energy, $\mathrm{Re}(\Sigma_{HA})$. Also note that the denominator becomes small when the masses are nearly degenerate; i.e. for $p^2 \sim M_{h_2}^2 \sim M_{h_3}^2 \sim m_H^2 \sim m_A^2$, causing the resonant enhancement of the asymmetry.

10.5 Factorisation of asymmetry into production and decay including interference effects

10.5.1 Asymmetry factor method

In the previous sections we have shown that studying the asymmetry between the production of left- and right-handed neutralinos in heavy Higgs decays is a promising method of determining the existence of $\mathcal{CP}$-violation in the Higgs sector. We have shown that, in order to predict the values of these asymmetries for a particular set of parameters, interference effects between the two heavy Higgs bosons must be taken into account. We have also shown that the on-shell approximation using Breit-Wigner propagators and $\hat{\mathbf{Z}}$ factors gives good numerical agreement with the full Higgs propagator matrix calculation. The only reason that the narrow width approximation breaks down is that the mass splitting between the two heavy Higgs bosons is of the order of their widths, $M_i - M_j \lesssim \Gamma_i, \Gamma_j$. All other assumptions of the narrow width approximation are satisfied. Thus our goal in the following is to find a method for calculating the asymmetry using a generalised narrow width approximation, similar to the method developed for calculating the full cross section in Section 9.5.1.

To agree with Section 9.5.1 and Appendix C, we consider the general process, $ab \to cef$, shown in Figure C.1, this time with intermediate h_2 and h_3. In order to compute the asymmetry, we are interested in σ_2, which is obtained from the difference between the squared matrix elements for left-handed e and f and for right-handed e and f in the

final state (the polarisation states of c (a and b) are summed (averaged) over);

$$\begin{aligned}|\mathcal{M}_{ab\to ce^Lf^L}|^2-|\mathcal{M}_{ab\to ce^Rf^R}|^2=&|\mathcal{M}_{ab\to ch_2}|^2|\Delta_{h_2}^{\rm BW}|^2(|\mathcal{M}_{h_2\to e^Lf^L}|^2-|\mathcal{M}_{h_2\to e^Rf^R}|^2)\\&+|\mathcal{M}_{ab\to ch_3}|^2|\Delta_{h_3}^{\rm BW}|^2(|\mathcal{M}_{h_3\to e^Lf^L}|^2-|\mathcal{M}_{h_3\to e^Rf^R}|^2)\\&+2\ {\rm Re}\left[\mathcal{M}_{ab\to ch_2}\mathcal{M}^*_{ab\to ch_3}\Delta_{h_2}^{\rm BW}(\Delta_{h_3}^{\rm BW})^*\times\right.\\&\left.(\mathcal{M}_{h_2\to e^Lf^L}\mathcal{M}^*_{h_3\to e^Lf^L}-\mathcal{M}_{h_2\to e^Rf^R}\mathcal{M}^*_{h_3\to e^Rf^R})\right].\end{aligned}\tag{10.32}$$

Inserting this expression into the integral over phase space, as in Equation (9.19), and making the same assumption that in the limit of narrow width we can evaluate all matrix elements on-shell outside the dq^2 integral, we can write down the following on-shell approximation for σ_2;

$$\begin{aligned}\sigma_2(ab\to cef)\approx&\sigma_{ab\to ch_2}\frac{\Gamma_{h_2\to e^Lf^L}-\Gamma_{h_2\to e^Rf^R}}{\Gamma_{h_2}}+\sigma_{ab\to ch_3}\frac{\Gamma_{h_3\to e^Lf^L}-\Gamma_{h_3\to e^Rf^R}}{\Gamma_{h_3}}\\&+2\,\Omega\,{\rm Re}\big[\mathcal{M}_{ab\to ch_2}\mathcal{M}^*_{ab\to ch_3}(\mathcal{M}_{h_2\to e^Lf^L}\mathcal{M}^*_{h_3\to e^Lf^L}-\mathcal{M}_{h_2\to e^Rf^R}\mathcal{M}^*_{h_3\to e^Rf^R})\\&\times\int dq^2\Delta_{h_2}^{\rm BW}(q^2)(\Delta_{h_3}^{\rm BW}(q^2))^*\big]\end{aligned}\tag{10.33}$$

where the integral in the last line is the same universal integral over interfering Breit-Wigner propagators that appears in Equation (9.20), and Ω is the phase space factor also in this equation. We can conveniently express the on-shell matrix elements for the interference term at leading order in terms of the on-shell matrix elements for the h_2 and h_3 production and decay processes respectively;

$$\begin{aligned}&\mathcal{M}_{ab\to ch_2}\mathcal{M}^*_{ab\to ch_3}(\mathcal{M}_{h_2\to e^Lf^L}\mathcal{M}^*_{h_3\to e^Lf^L}-\mathcal{M}_{h_2\to e^Rf^R}\mathcal{M}^*_{h_3\to e^Rf^R})\\&\approx\ y_a\,|\mathcal{M}_{ab\to ch_a}|^2\big(|\mathcal{M}_{h_a\to e^Lf^L}|^2-|\mathcal{M}_{h_a\to e^Rf^R}|^2\big)\end{aligned}\tag{10.34}$$

where y_a ($a=2$ or 3) is a numerical scaling factor and $M_{h_2}\approx M_{h_3}$. For example, for H–A mixing in $gg\to f\bar{f}$, we use Equation (10.20) to obtain the scaling factor,

$$y_a=-\frac{i(\hat{\mathbf{Z}}_{23}\hat{\mathbf{Z}}^*_{32}-\hat{\mathbf{Z}}_{22}\hat{\mathbf{Z}}^*_{33})[(S_H^g\hat{\mathbf{Z}}_{22}+S_A^g\hat{\mathbf{Z}}_{23})(S_H^{g*}\hat{\mathbf{Z}}^*_{32}+S_A^{g*}\hat{\mathbf{Z}}^*_{33})+|P_A^g|^2\hat{\mathbf{Z}}_{23}\hat{\mathbf{Z}}^*_{33}]}{2{\rm Im}(\hat{\mathbf{Z}}_{a2}\hat{\mathbf{Z}}^*_{a3})(|S_H^g\hat{\mathbf{Z}}_{a2}+S_A^g\hat{\mathbf{Z}}_{a3}|^2+|P_A^g\hat{\mathbf{Z}}_{a3}|^2)}\tag{10.35}$$

This simple scaling factor allows us to write the spin-dependent cross section as

$$\sigma_2(ab\to cef)\approx\sigma_{ab\to ch_2}{\rm BR}_{h_2\to ef}A_2(1+r_2^A)+\sigma_{ab\to ch_3}{\rm BR}_{h_3\to ef}A_3(1+r_3^A)\tag{10.36}$$

where

$$r_a^A = \frac{M_{h_a}\Gamma_{h_a}}{\pi}\frac{\sigma_{ab\to ch_a}\mathrm{BR}_{h_a\to ef}}{\sigma_{ab\to ch_2}\mathrm{BR}_{h_2\to ef}+\sigma_{ab\to ch_3}\mathrm{BR}_{h_3\to ef}}\ 2\ \mathrm{Re}\left[y_a\int_{q^2_{\min}}^{q^2_{\max}} dq^2\Delta^{\mathrm{BW}}_{h_2}(q^2)(\Delta^{\mathrm{BW}}_{h_3}(q^2))^*\right] \tag{10.37}$$

are the asymmetry interference weight factors and $A_a \equiv (\Gamma_{LL}-\Gamma_{RR})/(\Gamma_{LL}+\Gamma_{RR})$ is the decay asymmetry defined in Equation (8.1), with $\Gamma_{LL} \equiv \Gamma(h_a \to e^L f^L)$ and $\Gamma_{RR} \equiv \Gamma(h_a \to e^R f^R)$. Equation (10.36) is a convenient way of converting the decay width asymmetries, A_a, into an estimate of the asymmetry for the full production and decay process, using only cross sections, branching ratios, and the asymmetry interference weight factors, r_a^A. One could, in particular, use cross sections at the hadron level, incorporating higher order corrections. One could also incorporate higher-order corrections into the branching ratios and A_a, as studied in Chapter 8. This could be important when $\mathcal{CP}$-violating and absorptive effects in the loop-corrected Higgs-fermion-fermion vertex give a large enhancement to the asymmetry. In scenarios where the dominant contribution to the asymmetries comes from Higgs propagator corrections contained in the $\hat{\mathbf{Z}}$ matrix elements, it can be convenient to make a further approximation relating the on-shell matrix elements in terms of a scaling factor w_a;

$$|\mathcal{M}_{ab\to ch_a}|^2(|\mathcal{M}_{h_a\to e^Lf^L}|^2-|\mathcal{M}_{h_a\to e^Rf^R}|^2)\ \approx w_a\,|\mathcal{M}_{ab\to ch_a}|^2|\mathcal{M}_{h_a\to ef}|^2 \tag{10.38}$$

where, like y_a, w_a consists of couplings and $\hat{\mathbf{Z}}$ matrix elements. For example, for H–A mixing in $gg \to f\bar{f}$ in the limit where the fermion masses are only kept in the couplings, we can compare Equations (10.20) and (10.21) to obtain the scaling factor

$$w_a \approx \frac{-2\mathrm{Re}(G_{ffA}G^*_{ffH})\mathrm{Im}(\hat{\mathbf{Z}}_{a2}\hat{\mathbf{Z}}^*_{a3})}{\left(|G_{Hff}\hat{\mathbf{Z}}_{a2}|^2+|G_{Aff}\hat{\mathbf{Z}}_{a3}|^2+2\mathrm{Re}(\hat{\mathbf{Z}}_{a2}\hat{\mathbf{Z}}^*_{a3})\mathrm{Im}(G_{Aff}G^*_{Hff})\right)} \tag{10.39}$$

Using such a scaling factor, we can make the approximation

$$\sigma_2(ab\to cef) \approx \sigma_{ab\to ch_2}\mathrm{BR}_{h_2\to ef}w_2(1+r_2^A)+\sigma_{ab\to ch_3}\mathrm{BR}_{h_3\to ef}w_3(1+r_3^A). \tag{10.40}$$

10.5.2 Numerical testing of asymmetry factor method

In Figure 10.6(a), we show the hadronic level asymmetry for gluon fusion, $A_{gg} = \sigma_2(pp \to gg \to h_2, h_3 \to \tilde{\chi}_2^0\tilde{\chi}_2^0)/\sigma_1(pp \to gg \to h_2, h_3 \to \tilde{\chi}_2^0\tilde{\chi}_2^0)$, in the SPS1a scenario modified

to have $A_t = 510\, e^{-i7\pi/10}\,\text{GeV}$. For simplicity we do not include higher order vertex corrections to the neutralino-neutralino Higgs vertex. We calculated the squared matrix element for the partonic process using the on-shell approximation with $\hat{\mathbf{Z}}$ matrix elements and Breit-Wigner propagators for case of the 2×2 H–A mixing (for simplicity we ignore the contributions from h and other non-Higgs intermediate particles). We then use the built-in option in `FormCalc` to convert our squared matrix calculation into the integrated LHC cross sections, σ_1 and σ_2, using the default pdf set, CTEQ5L [125]. We use `FeynHiggs 2.6.5` to obtain the Higgs masses, $\hat{\mathbf{Z}}$ matrix elements and widths, the latter from the imaginary part of the complex pole. The black points include the interference between the h_2 and h_3 propagators. We see that the asymmetry becomes more resonantly enhanced as $\tan\beta$ increases, with a value of around 2% at $\tan\beta = 5$ increasing to around 23% at $\tan\beta = 20$. For larger $\tan\beta$ values the asymmetry decreases. The blue points are obtained by summing the separate contributions $\sigma_{1,2}$, $\sigma_{i,h_a} \equiv \sigma_i(pp \to gg \to h_a \,\text{only} \to \tilde{\chi}_2^0\tilde{\chi}_2^0)$ $(i = 1, 2,\, a = 2, 3)$, i.e. without the interference between h_2 and h_3. This results in an underestimation of the asymmetry by several percent for $\tan\beta \lesssim 25$. Above this value, the asymmetry obtained in this way continues to increase with $\tan\beta$, resulting in an overestimation compared to the full result. For the green curve, we compute σ_1 from the sum $\sigma_{1,h_2}(1 + R_2) + \sigma_{1,h_3}(1 + R_3)$, where the interference weight factors, R_2 and R_3, are obtained from Equation (9.24), while for σ_2 we compute the sum $\sigma_{2,h_2} w_2(1 + r_2^A) + \sigma_{2,h_3} w_3(1 + r_3^A)$ using the asymmetry interference weight factors r_2^A and r_3^A from Equation (10.37) and $w_{2,3}$ from Equation (10.38). This approximation is in good numerical agreement with the full squared matrix element result, predicting the asymmetry to within a couple of percent for the range of $\tan\beta$ shown, including the decrease for large $\tan\beta$. These results confirm that we can use Equation 10.36 to construct the asymmetry from the h_2 and h_3 asymmetries.

In order to help explain the general trends as $\tan\beta$ increases, in Figure 10.6(b) we show the mass differences, widths and $\hat{\mathbf{Z}}$ matrices as a function of $\tan\beta$ for the modified SPS1a scenario. We see an enhancement of $\text{Re}(\hat{\mathbf{Z}}_{33}) = \text{Re}(\hat{\mathbf{Z}}_{HA})$ as $\tan\beta$ increases. This causes a resonant enhancement of the asymmetry. For larger $\tan\beta$ values, however, we showed that the asymmetry decreases, despite the fact that Figure 10.6(b) shows the masses and widths becoming more degenerate and $\text{Re}(\hat{\mathbf{Z}}_{33})$ becoming large. This is due to cancellations between the interference term and the h_2 and h_3 terms for degenerate masses, widths and couplings, as discussed in Section 10.2.3 (see in particular Equation (10.23)). If one does not include interference effects then the asymmetry will continue to increase as $\text{Re}(\hat{\mathbf{Z}}_{33})$ increases with $\tan\beta$.

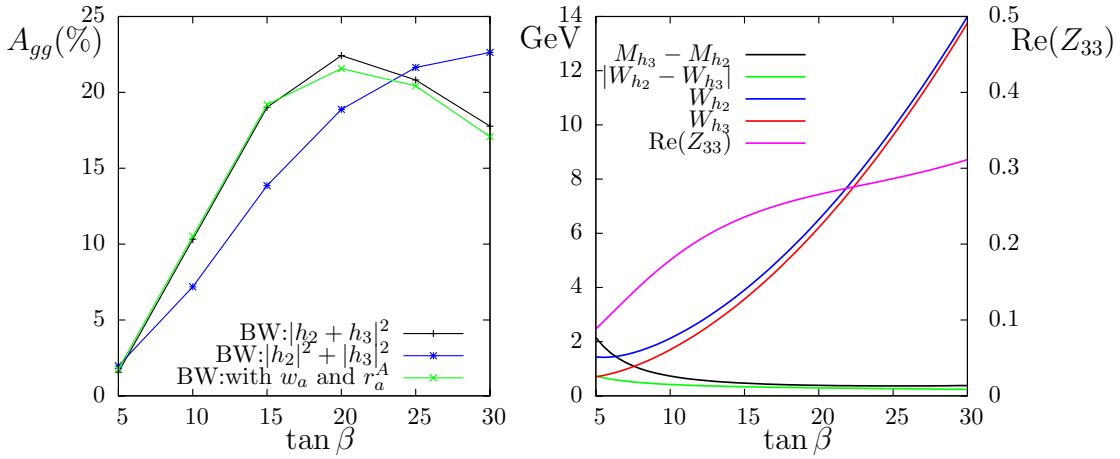

(a) (b)

Figure 10.6: (a) $A_{gg} = \sigma_2(pp \to gg \to h_2, h_3 \to \tilde{\chi}_2^0\tilde{\chi}_2^0)/\sigma_1(pp \to gg \to h_2, h_3 \to \tilde{\chi}_2^0\tilde{\chi}_2^0)$, in the modified SPS1a scenario with $A_t = 510e^{-i7\pi/10}$ GeV, computed using several different methods with Breit-Wigner propagators and $\mathbf{Z}$ matrices; in black is the 2×2 result with interference, in blue is the 2×2 result without interference, in green is result using the generalised narrow width approximation, i.e. σ_1 is calculated from $\sigma_{1,h2}(1 + R_2) + \sigma_{1,h_3}(1 + R_3)$ and σ_2 is calculated from $\sigma_{2,h_2} w_2(1 + r_2^A) + \sigma_{2,h_3} w_3(1 + r_3^A)$ where $\sigma_{i,h_{2,3}}$ are the cross sections for h_2 only and h_3 only, respectively. (b) The difference between the masses (black) and widths (green) as a function of $\tan\beta$ in the SPS1a with $A_t = 510e^{-i7\pi/10}$ GeV with fixed $M_{H^\pm}$. Also shown are the absolute widths from the imaginary part of the mass solution Γ_{h_2} (blue) and Γ_{h_3} (red). In pink is shown $\mathrm{Re}\hat{\mathbf{Z}}_{33} \approx \mathrm{Re}\hat{\mathbf{Z}}_{22}$.

10.6 Asymmetries at the LHC

We now use the on-shell generalised narrow width approximation of Equations (9.23) and (10.40) to compute the total asymmetry in terms of LHC cross sections,

$$A = \frac{\sigma(pp \to h_2, h_3 \to \tilde{\chi}_2^{0\,L}\tilde{\chi}_2^{0\,L}) - \sigma(pp \to h_2, h_3 \to \tilde{\chi}_2^{0\,R}\tilde{\chi}_2^{0\,R})}{\sigma(pp \to h_2, h_3 \to \tilde{\chi}_2^{0\,L}\tilde{\chi}_2^{0\,L}) + \sigma(pp \to h_2, h_3 \to \tilde{\chi}_2^{0\,R}\tilde{\chi}_2^{0\,R})} \tag{10.41}$$

in the $M_{H^\pm}$–$\tan\beta$ plane for the SPS1a scenario with $A_t = 510e^{-i13\pi/20}$ GeV. We use the cross sections, masses, total widths and branching ratios from `FeynHiggs 2.7.1`[2] and the interference weight factors and asymmetry interference weight factors computed from Equations (9.24) and (10.37) respectively. We include both the gg fusion and $b\bar{b}$ fusion processes, which are the main production methods for the Higgs masses considered.

[2]This recently released version of `FeynHiggs` contains improvements to the gluon fusion production cross section.

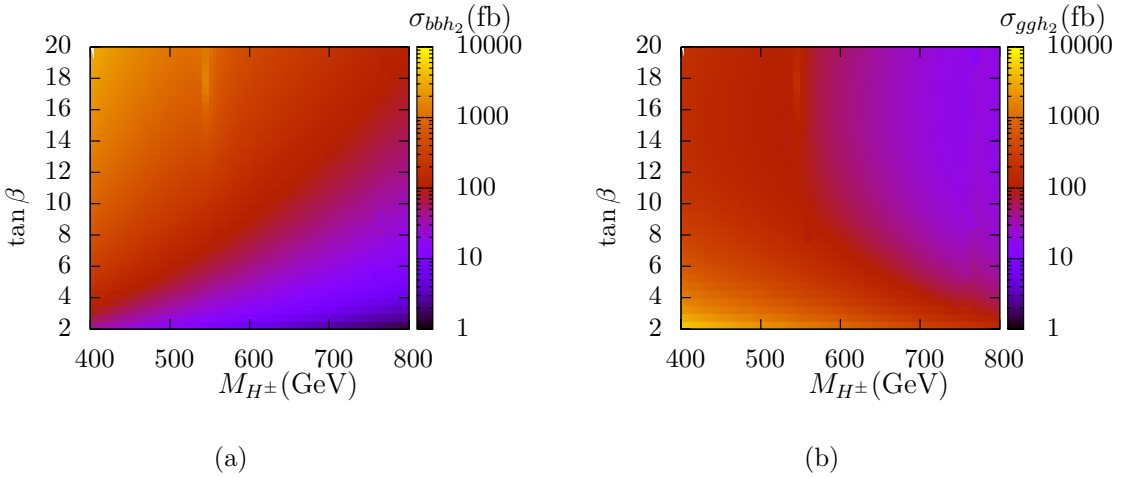

Figure 10.7: LHC cross sections in fb from `FeynHiggs 2.7.1` for the SPS1a scenario with $A_t = 510e^{-i13\pi/20}$ GeV for (a) $\sigma(pp \to b\bar{b} \to h_2X)$; (b) $\sigma(pp \to gg \to h_2X)$.

Figure 10.7(a) shows the LHC cross section, $\sigma(pp \to b\bar{b} \to h_2X)$, in the $M_{H^\pm}$–$\tan\beta$ plane for the SPS1a scenario with $A_t = 510e^{-i13\pi/20}$ GeV, obtained as output from `FeynHiggs 2.7.1`. Figure 10.7(b) shows the corresponding gluon fusion cross section, $\sigma(pp \to gg \to h_2X)$. We see that $b\bar{b}$ fusion has the largest cross section for large $\tan\beta$, while gluon fusion process can dominate for $\tan\beta \lesssim 8$.

We showed in Section 10.4 that $b\bar{b}$ fusion does not exhibit a large asymmetry between the production of neutralinos with left- and right-handed polarisation, due to a cancellation between the couplings to down-type fermions in the initial state and in the imaginary parts of Higgs self-energies. Gluon fusion is much more promising in this respect. It would therefore seem that we have the most chance of seeing this asymmetry at low $\tan\beta$. At large $\tan\beta$, the signal will be washed out by events with $b\bar{b}$ in the initial state, which are experimentally indistinguishable from gg, and have a much smaller asymmetry. For these low $\tan\beta$ values it will be difficult to detect such heavy Higgs bosons using their decays into SM particles. According to the study in Ref. [35], however, there may be a significant discovery potential for heavy Higgs bosons from utilising their decay into neutralinos, $h_a \to \tilde{\chi}_i^0\tilde{\chi}_j^0 \to 4lX$. For the 4L1 scenario, given in Table 2.3 and studied in Chapter 8, the authors claimed a 5σ discovery potential for $\tan\beta \geq 5$, while for the other parameter point analysed, where the decays into heavier neutralinos are open and can be utilised for the four lepton signal, they claim that the discovery potential extends to values of $\tan\beta$ below 5. In scenarios with low $\tan\beta$, there will also be less stau mixing, so that more neutralinos will decay via on-shell selectron and smuon decay, to produce

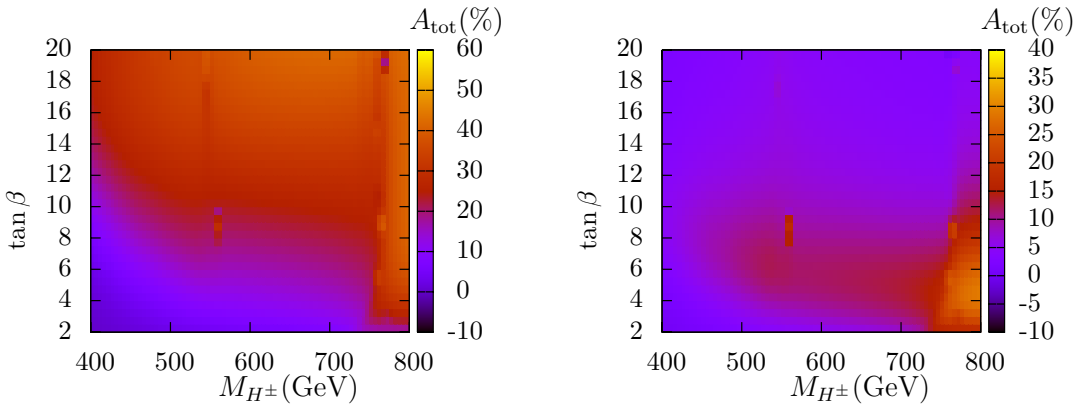

Figure 10.8: Asymmetry, $A = (\sigma(pp \to h_2, h_3 \to \tilde{\chi}_2^{0\,L}\tilde{\chi}_2^{0\,L}) - \sigma(pp \to h_2, h_3 \to \tilde{\chi}_2^{0\,R}\tilde{\chi}_2^{0\,R}))/(\sigma(pp \to h_2, h_3 \to \tilde{\chi}_2^{0\,L}\tilde{\chi}_2^{0\,L}) + \sigma(pp \to h_2, h_3 \to \tilde{\chi}_2^{0\,R}\tilde{\chi}_2^{0\,R}))$ as a percentage in the $M_{H^\pm}$–$\tan\beta$ plane for the SPS1a scenario with $A_t = 510e^{-i13\pi/20}$GeV; (a) with only the gluon fusion production process included; (b) with both gluon fusion and $b\bar{b}$ fusion included.

a clean lepton signature. It may be that we can utilise decays of Higgs bosons into the heavier neutralinos for the asymmetry signal. Low $\tan\beta$, however, does mean less resonant enhancement of the asymmetry, since the mass splitting of the Higgs bosons will be larger. The interplay between these effects should be fully considered in further studies.

In Figure 10.8(a), we show the asymmetry as a percentage in the $M_{H^\pm}$–$\tan\beta$ plane for the SPS1a scenario with $A_t = 510e^{-i13\pi/20}\,\text{GeV}$ when only the gg fusion production process is included. We see it can be particularly large for large $\tan\beta \gtrsim 8$, and also in the region of small $\tan\beta$ and $M_{H^\pm} \gtrsim 750\,\text{GeV}$. For much of the $M_{H^\pm}$–$\tan\beta$ plane, the asymmetry is sizeable, with values above 40%. However, this is not including the $b\bar{b}$ fusion process, which will be experimentally indistinguishable from the gluon fusion process. We include both processes in Figure 10.8(b). We see that the region with large $\tan\beta$ no longer has a large asymmetry, since the $b\bar{b}$ fusion process has a much higher cross section, but only a suppressed asymmetry. For these parts of the $M_{H^\pm}$–$\tan\beta$ plane, where the $b\bar{b}$ fusion process dominates, it may be interesting to study other $\mathcal{CP}$-asymmetries, such as triple product asymmetries in the momenta of the decay products, which appear to be more promising for the $b\bar{b}$ fusion process. The region with low $\tan\beta \lesssim 8$ and large $M_{H^\pm} \gtrsim 500\,\text{GeV}$ looks the most promising for measuring the asymmetry between the production of left- and right-handed neutralinos. In this region, the asymmetry can be $10-20\%$. Such asymmetries are certainly worth further investigation. A full assessment

of the capability of the LHC to measure such an asymmetry will require a realistic detector simulation, which is beyond the scope of this work.

Our study indicates that there is certainly scope for utilising the decays of Higgs bosons into neutralinos, not only for Higgs discovery at the LHC, but also for probing $\mathcal{CP}$-violation in the MSSM. The methods developed in this chapter can be used to calculate the asymmetry in various approximations that include important interference effects, and they will also have applications in studies of other $\mathcal{CP}$-asymmetries.

Chapter 11

Conclusion

We are entering an exciting era for particle physics. The LHC is expected to finally shed light on the mechanism of electroweak symmetry breaking, for which many popular models predict the existence of one or more Higgs boson(s) within the discovery reach of the LHC. There are also compelling motivations for discovering supersymmetric particles at the TeV energy scale explored by the LHC. Supersymmetry may help to explain the Hierarchy Problem, dark matter, the unification of the fundamental forces and, in supersymmetric models with $\mathcal{CP}$-violation, the baryon asymmetry of the Universe.

In this thesis we have investigated the effects of higher order corrections and $\mathcal{CP}$-violation in the Higgs and neutralino sectors of the MSSM. We have focused in particular on cases where the searches for Higgs bosons and supersymmetry can go hand-in-hand. In particular, the decays of neutralinos into Higgs bosons may offer good prospects for detecting a very light Higgs boson in the CPX scenario, where standard search channels may fail. Conversely, studies of the polarisation of neutralinos produced in Higgs decays may offer good prospects for determining the existence of $\mathcal{CP}$-violation in the MSSM.

Complete one-loop results were obtained for the processes $\tilde{\chi}_i^0 \to \tilde{\chi}_j^0 h_a$ and $h_a \to \tilde{\chi}_i^0 \tilde{\chi}_j^0$ in the MSSM with complex parameters. The renormalisation scheme used for the Higgs sector was described in some detail, paying particular attention to the incorporation of important Higgs propagator corrections. In this scheme, finite wavefunction normalisation factors ($\hat{\mathbf{Z}}$ matrix elements) are used to ensure the correct on-shell properties of Higgs bosons appearing as external particles in a process. For a complete treatment of Higgs bosons appearing in internal parts of diagrams, the full 3×3 Higgs propagator matrix should be used to include all $\mathcal{CP}$-violating and momentum dependent self-energy contributions.

An on-shell renormalisation scheme was developed for the first time in this thesis for the chargino–neutralino sector of the MSSM with $\mathcal{CP}$-violating parameters. The field renormalisation prescription takes into account the imaginary parts arising from complex parameters and absorptive parts of loop integrals. Unlike in $\mathcal{CP}$-conserving theories, the latter can enter the squared matrix element at the one-loop level in the complex MSSM and can have a large impact on decay widths and cross sections of charginos and polarised neutralinos. In order to ensure the correct on-shell conditions, we developed a scheme in which the renormalisation constants introduced for the outgoing fermions and incoming antifermions, $\delta\bar{Z}_{ij}$, are different to those introduced for the incoming fermions and outgoing antifermions, δZ_{ij}. The hermiticity relation, $\delta\bar{Z}_{ij} = \delta Z_{ij}^{\dagger}$, can be restored in the $\mathcal{CP}$-conserving case where absorptive parts of loop integrals do not contribute to physical quantities at the one-loop level.

For the renormalisation of the parameters of the chargino–neutralino sector, $|M_1|$, $|M_2|$ and $|\mu|$, we compared three different on-shell schemes, where the masses of either three neutralinos, two neutralinos and one chargino, or two charginos and one neutralino were fixed on-shell. From these options, no one single scheme was found to be suitable for the whole MSSM parameter space, with the most appropriate choice depending on the gauge parameter hierarchy of the scenario. For most of the scenarios studied in this thesis, the scheme with the masses of $\tilde{\chi}_1^0$, $\tilde{\chi}_2^0$ and $\tilde{\chi}_2^{\pm}$ on-shell was found to be the most appropriate. We found that the phases entering the chargino–neutralino sector at tree-level, ϕ_{M_1} and ϕ_μ, should be considered as mixing parameters and therefore do not need to be renormalised. The renormalisation scheme we have developed, which we have implemented into `FeynArts`, will have numerous applications for loop calculations in the MSSM with $\mathcal{CP}$-violating parameters.

For both $\tilde{\chi}_i^0 \to \tilde{\chi}_j^0 h_a$ and $h_a \to \tilde{\chi}_i^0 \tilde{\chi}_j^0$, the complete one-loop genuine vertex contributions were combined with dominant two-loop Higgs propagator-type corrections to obtain the most precise prediction currently available for this class of processes. Previous work for this process using the Feynman-diagrammatic approach included only a subset of the one-loop contributions and did not allow for $\mathcal{CP}$-violation.

The numerical impact of the genuine vertex corrections on the decay $\tilde{\chi}_i^0 \to \tilde{\chi}_j^0 h_a$ was studied for several examples of $\mathcal{CP}$-conserving and $\mathcal{CP}$-violating scenarios. We found that significant effects on the decay widths and branching ratios were possible even in the $\mathcal{CP}$-conserving MSSM. In the $\mathcal{CP}$-violating CPX benchmark scenario, the corrections to the decay width, $\tilde{\chi}_2^0 \to \tilde{\chi}_1^0 h_1$, were found to be particularly large – of order 45% for a Higgs mass of 40 GeV. This parameter region of the CPX scenario, where a very light Higgs

boson is not excluded by present data, was analysed in detail. We found that in this parameter region, which will be difficult to cover with standard Higgs search channels at the LHC, the branching ratio for the decay $\tilde{\chi}_2^0 \to \tilde{\chi}_1^0 h_1$ is large. This may offer good prospects of detecting such a light Higgs boson in cascade decays of supersymmetric particles.

The numerical impact of the genuine vertex corrections was also studied for the decay $h_a \to \tilde{\chi}_i^0 \tilde{\chi}_j^0$ in scenarios where the resulting signature of four leptons plus missing energy may be phenomenologically important at the LHC. For these scenarios, it was shown that the inclusion of the full MSSM corrections is crucial for obtaining the correct sign and magnitude of the vertex corrections, since cancellations between the various UV-finite subsets of diagrams can occur. Thus, our result is a significant improvement over previous calculations in the literature for this process. For the 4L1 and SPS1a scenarios we found modest corrections to the partial decay widths of order $5 - 10\%$, resulting in an effect on the branching ratios of less than a percent. We also showed that in these scenarios, the introduction of $\mathcal{CP}$-violating phases can have a significant effect on the decay widths and relative size of the vertex corrections. They can also have a large impact on the decay widths for Higgs bosons into polarised neutralinos. The ratio, $A_a \equiv (\Gamma_{LL} - \Gamma_{RR})/(\Gamma_{LL} + \Gamma_{RR})$, where $\Gamma_{LL} \equiv \Gamma(h_a \to \tilde{\chi}_2^{0\,L} \tilde{\chi}_2^{0\,L})$ and $\Gamma_{RR} \equiv \Gamma(h_a \to \tilde{\chi}_2^{0\,R} \tilde{\chi}_2^{0\,R})$ $(a = 2, 3)$, was found to be a $\mathcal{CP}$-odd quantity, which could help identify the existence of $\mathcal{CP}$-violation in the MSSM. It was noted, however, that in the scenarios of interest, the two heavy Higgs bosons, h_2 and h_3, are nearly mass degenerate and can interfere, so one needs to calculate the full production and decay process in order to assess the viability of such an observable.

Interference effects for nearly mass degenerate Higgs bosons were then studied in some detail, both analytically and numerically. Several methods were developed for calculating the full production and decay process in the case where the splitting between the masses of the intermediate Higgs bosons, $|M_{h_i} - M_{h_j}|$, is of the order of their widths, Γ_{h_i} and Γ_{h_j}. The full 3×3 propagator matrix calculation was employed to include the full momentum dependence of the self-energies and all possible mixing and interference terms between the three neutral Higgs bosons. An on-shell approximation, using Breit-Wigner propagators for the Higgs bosons and the $\hat{\mathbf{Z}}$ matrix formalism to describe the mixing, was found to give results in good numerical agreement with the full propagator matrix calculation. As an example, interference effects were studied in the process $b\bar{b} \to h_i \to \tau^+\tau^-$, both in the case of small M_A where h and H (and A) can be mass degenerate and in the case of large M_A where h_2 and h_3 can be mass degenerate and

interfere in the presence of $\mathcal{CP}$-violating parameters. When there was significant overlap between the propagators and the mixing self-energy contributions were large, it was found that omitting the interference term could lead to an overestimation of the cross section by up to 400%. Thus the usual narrow width approximation for factorising the process into separate parts for production and decay is not applicable in such a case.

Given that the full squared matrix calculation is not practicable in all situations, we developed a generalised narrow width approximation for the process $ab \to ch_a \to cde$ ($a = 1, 2$), to be applied in situations where the individual masses of the intermediate Higgs bosons satisfy $M_{h_a} \gg \Gamma_{h_a}$ and we are sufficiently far from thresholds, but the masses are nearly degenerate, with $|M_{h_1} - M_{h_2}| \sim \Gamma_{h_1}, \Gamma_{h_2}$. In our approximation, we add the usual cross section times branching ratio for each of the Higgs bosons to an interference term. This interference term is expressed as a universal integral over the interfering Breit-Wigner propagators with a process-dependent coefficient made up of on-shell matrix elements. These on-shell matrix elements can be estimated at leading order from the individual h_1 and h_2 cross sections and branching ratios multiplied by an appropriate scaling factor. Combining this process-specific scaling factor with the universal integral over interfering Breit-Wigner propagators, we obtained an interference weight factor, R_a. This can be conveniently combined with the state-of-the-art Higgs branching ratios and hadronic cross sections to obtain an effective cross section times branching ratio which includes interference effects; $\sigma_{ab\to ch_1}\mathrm{BR}_{h_1\to de}(1 + R_1) + \sigma_{ab\to ch_2}\mathrm{BR}_{h_2\to de}(1 + R_2)$. We have tested this method for several processes and found that it gives results in numerical agreement with the full squared matrix calculation. As an example, we used the generalised narrow width approximation to investigate the effect of interference between h and H on the interpretation of Higgs exclusion limits by Tevatron analyses in the $M_h^{\max}$ scenario. Although we found that the interference did not affect the most recent exclusion bounds in this scenario which reach to $\tan\beta \sim 35$, we showed examples where we interpreted previous exclusion limits at larger $\tan\beta$ without including the full set of available higher-order corrections to the Higgs masses. For these particular masses and widths, the interference effects resulted in a significant shift in our interpretation of the exclusion limits. Such interference effects could also be important for Higgs discovery at the LHC, in both $\mathcal{CP}$-conserving and $\mathcal{CP}$-violating scenarios.

Asymmetries between the production of left- and right-handed neutralinos were studied analytically and numerically for the production and decay processes $b\bar{b}, gg, WW \to h_i \to \tilde{\chi}_2^0\tilde{\chi}_2^0$ at the LHC. A non-zero asymmetry results from the existence of both $\mathcal{CP}$-violation and absorptive effects in the Higgs self-energies. Large asymmetries were found to be

possible for the gg and W^+W^- fusion production processes, while for the $b\bar{b}$ fusion the asymmetry was found to be suppressed due to a cancellation between the couplings of down-type fermions in the initial state and in the dominant absorptive contributions to the Higgs self-energies. The on-shell approximation using Breit-Wigner propagators and the $\hat{\mathbf{Z}}$ factor formalism was again found to be in good numerical agreement with the full 3×3 Higgs propagator matrix calculation. We also used the generalised narrow width approximation to calculate the asymmetry, leading to results in numerical agreement with the full squared matrix calculations. Using this method, the asymmetry, $A \equiv (\sigma_{pp\to h_i\to\tilde{\chi}_2^{0\,L}\tilde{\chi}_2^{0\,L}} - \sigma_{pp\to h_i\to\tilde{\chi}_2^{0\,R}\tilde{\chi}_2^{0\,R}})/(\sigma_{pp\to h_i\to\tilde{\chi}_2^{0\,L}\tilde{\chi}_2^{0\,L}} + \sigma_{pp\to h_i\to\tilde{\chi}_2^{0\,R}\tilde{\chi}_2^{0\,R}})$, was studied in the $M_{H^\pm}$–$\tan\beta$ plane for a modified SPS1a scenario with $\mathcal{CP}$-violating phases. It was found that the asymmetry for gluon fusion alone was resonantly enhanced to values of more than 40% for large $\tan\beta$, but this effect was suppressed in the total asymmetry due to the large $b\bar{b}$ cross section. The most promising parameter region for this scenario was for $M_{H^\pm} \gtrsim 500\,\text{GeV}$ and $\tan\beta \lesssim 10$, where gluon fusion dominates and a total asymmetry of order $10 - 20\%$ is possible.

The processes $\tilde{\chi}_i^0 \to \tilde{\chi}_j^0 h_a$ and $h_a \to \tilde{\chi}_i^0\tilde{\chi}_j^0$ are potentially interesting for the LHC as Higgs discovery channels. We have shown in this thesis that higher order effects, such as vertex corrections and interference between Higgs propagators, can be important in both the $\mathcal{CP}$-conserving and $\mathcal{CP}$-violating MSSM. We have also explored the possibility of utilising decays of Higgs bosons into neutralinos for discovering $\mathcal{CP}$-violation in the MSSM. The LHC has been built both as a Higgs discovery machine and as a discovery machine for new physics beyond the Standard Model. The crucial links between these two searches, such as those presented in this thesis, should be fully utilised in the years ahead.

Appendix A

Loop integrals

A.1 Definitions for loop integrals

Using the conventions of Ref. [75], the generalised one-loop integral in $D = 4 - \epsilon$ dimensions can be written

$$\begin{aligned} & T^N_{\mu_1 \ldots \mu_P}(k_1, \ldots k_{N-1}, m_0, m_1 \ldots m_{N-1}) \\ & = \frac{(2\pi\mu)^{4-D}}{i\pi^2} \int d^D q \frac{q_{\mu_1} \ldots q_{\mu_P}}{[q^2 - m_0^2][(q+k_1)^2 - m_1^2] \ldots [(q+k_{N-1})^2 - m_{N-1}^2]}, \end{aligned} \tag{A.1}$$

where μ is a renormalisation scale on which the resulting loop integrals will depend.[1] $T^1, T^2, T^3, \ldots$ are denoted as $A, B, C \ldots$, and the scalar integrals with $P = 0$ are denoted as $A_0, B_0, \ldots$

For example, the scalar two-point function, B_0, reads

$$\begin{aligned} B_0(p_1, m_0, m_1) &= (4\pi\mu^2)^{\frac{D-4}{2}} \Gamma\left(\frac{4-D}{2}\right) \int_0^1 dx [x^2 p_1^2 - x(p_1^2 - m_1^2 + m_0^2) + m_0^2]^{\frac{D-4}{2}} \\ &= \Delta - \int_0^1 dx \log\left[\frac{x^2 p_1^2 - x(p_1^2 - m_1^2 + m_0^2) + m_0^2}{\mu^2}\right] + \mathcal{O}(D-4), \end{aligned} \tag{A.2}$$

where the UV-divergence is contained in

$$\Delta \equiv \frac{2}{4-D} - \gamma_E + \log 4\pi. \tag{A.3}$$

[1] The dependence of the one-loop integrals on μ in the constrained differential renormalisation scheme is the same as for dimensional regularization, although it arises in a conceptually different way (see Ref. [75]).

`FormCalc` writes the tensor loop integrals in terms of tensor coefficients and Lorentz-covariant tensors as follows;

$$\begin{aligned}
B_\mu &= k_{1\mu} B_1 \\
B_{\mu\nu} &= g_{\mu\nu} B_{00} + k_{1\mu} k_{1\nu} B_{11} \\
C_\mu &= k_{1\mu} C_1 + k_{2\mu} C_2 \\
C_{\mu\nu} &= g_{\mu\nu} C_{00} + \sum_{i,j=1}^{2} k_{i\mu} k_{j\nu} C_{ij} \\
C_{\mu\nu\rho} &= \sum_{i=1}^{2} (g_{\mu\nu} k_{i\rho} + g_{\nu\rho} k_{i\mu} + g_{\mu\rho} k_{i\nu}) C_{00i} + \sum_{i,j,l=1}^{2} k_{i\mu} k_{j\nu} k_{l\rho} C_{ijl}
\end{aligned} \tag{A.4}$$

Of the A, B and C integrals, only A_0, B_0, B_1, B_{00}, B_{11}, C_{00} and C_{00i} are UV-divergent. We use `LoopTools` to evaluate the tensor coefficients of the loop integrals numerically. The UV-finiteness of a resulting expression can then be tested by varying Δ and seeing whether the numerical result changes.

A.2 The absorptive parts of loop integrals

Consider the scalar two point function, $B_0(p_1, m_0, m_1)$, in equation (A.2). This function often arises in particle self-energies. If $p_1^2 - (m_1 + m_0)^2$ is positive, then the term in the square brackets is negative, resulting in a factor of $i\pi$ from the logarithm. Thus the loop integral will have an imaginary part. This is an absorptive effect arising from the fact that the particles in the loop integral can be on-shell, since the squared four-momentum of the incoming particle is greater than the squared sum of the masses of the particles inside the loop.

Any loop-level quantity, L, can be separated into its dispersive ($\widetilde{\mathrm{Re}}$) and absorptive ($\widetilde{\mathrm{Im}}$) parts as follows;

$$L = \widetilde{\mathrm{Re}}\, L + i\, \widetilde{\mathrm{Im}}\, L \tag{A.5}$$

where $\widetilde{\mathrm{Re}}$ takes the real part of loop integrals occuring in L, but not of any parameters occuring as coefficients to those loop integrals. Thus $\widetilde{\mathrm{Re}}$ does not simply take the real part of a quantity; it can still contain imaginary parts resulting from complex parameters and mixing matrix elements ($\mathcal{CP}$-violating parameters in the theory) multiplied

by dispersive loop integrals. Conversely, $i\widetilde{\mathrm{Im}}\, L$ can contain real parts resulting from imaginary parameters multiplied by absorptive loop integrals. We can write

$$L = \mathrm{Re}\,(\widetilde{\mathrm{Re}}\, L) + i\mathrm{Im}\,(\widetilde{\mathrm{Re}}\, L) + i(\mathrm{Re}\,(\widetilde{\mathrm{Im}}\, L) + i\mathrm{Im}\,(\widetilde{\mathrm{Im}}\, L)). \tag{A.6}$$

Thus, separating $L = \mathrm{Re}\, L + i\mathrm{Im}\, L$ into its real and imaginary parts gives

$$\mathrm{Re}\, L = \mathrm{Re}\,(\widetilde{\mathrm{Re}}\, L) - \mathrm{Im}\,(\widetilde{\mathrm{Im}}\, L), \qquad \mathrm{Im}\, L = \mathrm{Im}\,(\widetilde{\mathrm{Re}}\, L) + \mathrm{Re}\,(\widetilde{\mathrm{Im}}\, L). \tag{A.7}$$

In $\mathcal{CP}$-conserving theories, $\mathrm{Im}\,(\widetilde{\mathrm{Im}}\, L)$ and $\mathrm{Im}\,(\widetilde{\mathrm{Re}}\, L)$ vanish since there are no imaginary mixing matrix elements occuring as coefficients to multiply the loop integrals. Hence $\widetilde{\mathrm{Re}} \equiv \mathrm{Re}$ and $\widetilde{\mathrm{Im}} \equiv \mathrm{Im}$. However, in $\mathcal{CP}$-violating theories, the definitions with and without the tilde remain distinct.

A.3 Self-energy relations for fermions

Fermion self-energies can be decomposed into Lorentz invariants as

$$\Sigma_{ij}(p^2) = \not{p}\omega_L\Sigma^L_{ij}(p^2) + \not{p}\omega_R\Sigma^R_{ij}(p^2) + \omega_L\Sigma^{SL}_{ij}(p^2) + \omega_L\Sigma^{SR}_{ij}(p^2). \tag{A.8}$$

The Lorentz invariant pieces of the self-energies then satisfy certain relations if the Lagrangian is invariant under various combinations of charge conjugation ($\mathcal{C}$), parity reversal ($\mathcal{P}$) and time reversal ($\mathcal{T}$) (see Ref. [94] for derivation).

If the theory is $\mathcal{CPT}$-invariant, then

$$\begin{aligned} \widetilde{\mathrm{Re}}\Sigma^{L/R}_{ij}(p^2) &= (\widetilde{\mathrm{Re}}\Sigma^{L/R}_{ji}(p^2))^* \\ \widetilde{\mathrm{Re}}\Sigma^{SL}_{ij}(p^2) &= (\widetilde{\mathrm{Re}}\Sigma^{SR}_{ji}(p^2))^*. \end{aligned} \tag{A.9}$$

Hence, we always have the following relations if the $\mathcal{CPT}$ theorem holds,

$$\begin{aligned} \mathrm{Im}(\widetilde{\mathrm{Re}}\,\Sigma^{L/R}_{ii}(p^2)) &= 0 \\ \mathrm{Im}(\widetilde{\mathrm{Re}}\,\Sigma^{SL}_{ii}(p^2)) &= -\mathrm{Im}(\widetilde{\mathrm{Re}}\,\Sigma^{SR}_{ii}(p^2)) \\ \mathrm{Re}(\widetilde{\mathrm{Re}}\,\Sigma^{SL}_{ii}(p^2)) &= \mathrm{Re}(\widetilde{\mathrm{Re}}\,\Sigma^{SR}_{ii}(p^2)) \\ \mathrm{Im}(\widetilde{\mathrm{Re}}\,\Sigma^{SL}_{ii}(p^2)) &= \frac{1}{2}\widetilde{\mathrm{Re}}\,(\Sigma^{SL}_{ii}(p^2) - \Sigma^{SR}_{ii}(p^2)). \end{aligned} \tag{A.10}$$

If the theory is $\mathcal{CP}$-invariant, then

$$\begin{aligned} \Sigma^{L/R}_{ij}(p^2) &= \Sigma^{L/R}_{ji}(p^2) \\ \Sigma^{SL}_{ij}(p^2) &= \Sigma^{SR}_{ji}(p^2). \end{aligned} \tag{A.11}$$

In most of this thesis we consider the $\mathcal{CP}$-violating MSSM, so we do not use these $\mathcal{CP}$-invariance relations unless otherwise stated.

If the theory is $\mathcal{C}$-invariant then

$$\begin{aligned} \Sigma^{L}_{ij}(p^2) &= \Sigma^{R}_{ji}(p^2) \\ \Sigma^{SL}_{ij}(p^2) &= \Sigma^{SL}_{ji}(p^2) \\ \Sigma^{SR}_{ij}(p^2) &= \Sigma^{SR}_{ji}(p^2). \end{aligned} \tag{A.12}$$

The charge conjugation invariance relations are obeyed by Majorana fermions, such as neutralinos.

We use the above relations in Chapter 4 to simplify the renormalisation constants of charginos and neutralinos.

Appendix B

Renormalised vertices

In this appendix we write down the counterterms for all the three-point vertices that involve a single Higgs or gauge boson and two charginos or neutralinos, using the definitions for the field and parameter renormalisation constants given in Chapters 3 and 4. These are implemented into our counterterm model file to supplement the MSSM model file in `FeynHiggs`. They have all been tested for UV-finiteness.

B.1 SFF vertices

The three-point vertex for a scalar and two fermions, along with its counterterm, has the following Lorentz structure;

$$\Gamma^{(3)} = \frac{i}{2}\big((C^L + \delta C^L)\omega_L + (C^R + \delta C^R)\omega_R\big), \tag{B.1}$$

where the coupling constants C^L and C^R depend on the vertex in question. Incoming fermions (F_i) and outgoing fermions ($\bar{F}_i$) are renormalised as

$$\omega_{L/R} F_2 \to \omega_{L/R}(1 + \frac{1}{2}\delta Z^{L/R})F_2 \tag{B.2}$$

$$\bar{F}_1\omega_{L/R} \to \bar{F}_1\omega_{L/R}(1 + \frac{1}{2}\delta \bar{Z}^{R/L}). \tag{B.3}$$

The chargino-chargino-neutral Higgs vertex:

For $h_k^0 = \{h, H, A, G\}$;

$$
\begin{aligned}
C^R(\tilde{\chi}_{c1}^-, \tilde{\chi}_{c2}^+, h_k^0) &= (C^L(\tilde{\chi}_{c1}^-, \tilde{\chi}_{c2}^+, h_k^0))^* = \frac{e}{\sqrt{2}s_W} c_{\tilde{\chi}_{c_1}^- \tilde{\chi}_{c_2}^+ h_k^0} \\
\delta C^{R/L}(\tilde{\chi}_{c1}^-, -\tilde{\chi}_{c2}^+, h_k^0) &= \frac{e}{\sqrt{2}s_W}\big[\delta c^{(*)}_{\tilde{\chi}_{c_1}^- \tilde{\chi}_{c_2}^+ h_k^0} + c^{(*)}_{\tilde{\chi}_{c_1}^- \tilde{\chi}_{c_2}^+ h_k^0}(\delta Z_e - \frac{\delta s_W}{s_W}) \\
&\quad + \frac{1}{2}(\delta Z^{R/L}_{-,ic_1} c^{(*)}_{\tilde{\chi}_i^- \tilde{\chi}_{c_2}^+ h_k^0} + c^{(*)}_{\tilde{\chi}_{c_1}^- \tilde{\chi}_i^+ h_k^0} \delta \bar{Z}^{L/R}_{-,c_2 i}) \\
&\quad + \frac{1}{2}(c^{(*)}_{\tilde{\chi}_{c_1}^- \tilde{\chi}_{c_2}^+ h} \delta Z_{hh} + c^{(*)}_{\tilde{\chi}_{c_1}^- \tilde{\chi}_{c_2}^+ H} \delta Z_{hH} + c^{(*)}_{\tilde{\chi}_{c_1}^- \tilde{\chi}_{c_2}^+ A} \delta Z_{hA} + c^{(*)}_{\tilde{\chi}_{c_1}^- \tilde{\chi}_{c_2}^+ G} \delta Z_{hG})\big] \\
c_{\tilde{\chi}_{c_1}^- \tilde{\chi}_{c_2}^+ h_k^0} &= (a_k s_\alpha U_{c_2 2} V_{c_1 1} + b_k c_\alpha U_{c_2 1} V_{c_1 2}) \\
a_k &= \{s_\alpha, -c_\alpha, i s_\beta, -i c_\beta\} \\
b_k &= \{-c_\alpha, -s_\alpha, i c\beta, -i s_\beta\} \\
\delta c_{\tilde{\chi}_{c_1}^- \tilde{\chi}_{c_2}^+ h_k^0} &= 0
\end{aligned}
$$

The neutralino-chargino-charged Higgs vertex:

$$
\begin{aligned}
C^{L/R}(\tilde{\chi}_{n1}^0, \tilde{\chi}_{c2}^+, H^-) &= \frac{e}{s_W} c^{L/R}_{\tilde{\chi}_{n_1}^0 \tilde{\chi}_{c_2}^+ H^-} \\
\delta C^{L/R}(\tilde{\chi}_{n1}^0, \tilde{\chi}_{c2}^+, H^-) &= \frac{e}{s_W}\big[\delta c^{L/R}_{\tilde{\chi}_{n_1}^0 \tilde{\chi}_{c_2}^+ H^-} + c^{L/R}_{\tilde{\chi}_{n_1}^0 \tilde{\chi}_{c_2}^+ H^-}(\delta Z_e - \frac{\delta s_W}{s_W}) \\
&\quad + \frac{1}{2}(\delta Z^{L/R}_{0,in_1} c^{L/R}_{\tilde{\chi}_i^0 \tilde{\chi}_{c_2}^+ H^-} + c^{L/R}_{\tilde{\chi}_{n_1}^0 \tilde{\chi}_i^+ H^-} \delta \bar{Z}^{R/L}_{-,c_2 i}) \\
&\quad + \frac{1}{2}(c^{L/R}_{\tilde{\chi}_{n_1}^0 \tilde{\chi}_{c_2}^+ H^-} \delta Z_{H^+H^+} + c^{L/R}_{\tilde{\chi}_{n_1}^0 \tilde{\chi}_{c_2}^+ G^-} \delta Z_{H^+G^+})\big] \\
C^{L(R)}(\tilde{\chi}_{c2}^-, \tilde{\chi}_{n1}^0, H^+) &= \frac{e}{s_W} c^{L(R)}_{\tilde{\chi}_{c_2}^- \tilde{\chi}_{n_1}^0 H^+} \\
\delta C^{L(R)}(\tilde{\chi}_{c2}^-, \tilde{\chi}_{n1}^0, H^+) &= \frac{e}{s_W}\big[\delta c^{L(R)}_{\tilde{\chi}_{c_2}^- \tilde{\chi}_{n_1}^0 H^+} + c^{L(R)}_{\tilde{\chi}_{c_2}^- \tilde{\chi}_{n_1}^0 H^+}(\delta Z_e - \frac{\delta s_W}{s_W}) \\
&\quad + \frac{1}{2}(\delta \bar{Z}^{R/L}_{0,n_1 i} c^{L(R)}_{\tilde{\chi}_{c_2}^- \tilde{\chi}_i^0 H^+} + c^{L(R)}_{\tilde{\chi}_i^- \tilde{\chi}_{n_1}^0 H^+} \delta Z^{L/R}_{ic_2}) \\
&\quad + \frac{1}{2}(c^{L/R}_{\tilde{\chi}_{c_2}^- \tilde{\chi}_{n_1}^0 H^+} \delta Z_{H^+H^+} + c^{L/R}_{\tilde{\chi}_{c_2}^- \tilde{\chi}_{n_1}^0 G^+} \delta Z_{H^+G^+})\big]
\end{aligned}
$$

and similarly for $G^{\pm}$ where

$$
\begin{aligned}
c^L_{\tilde{\chi}^0_{n_1}\tilde{\chi}^+_{c_2}H^-} &= (c^R_{\tilde{\chi}^-_{c_2}\tilde{\chi}^0_{n_1}H^+})^* = -c_\beta(V^*_{c_2 2}(s_W N^*_{n_1 1}/c_W + N^*_{n_1 2})/\sqrt{2} + V^*_{c_2 1}N_{n_1 4}) \\
c^R_{\tilde{\chi}^0_{n_1}\tilde{\chi}^+_{c_2}H^-} &= (c^L_{\tilde{\chi}^-_{c_2}\tilde{\chi}^0_{n_1}H^+})^* = -s_\beta(-U_{c_2 2}(s_W N_{n_1 1}/c_W + N_{n_1 2})/\sqrt{2}) + U_{c_2 1}N_{n_1 3}) \\
c^L_{\tilde{\chi}^0_{n_1}\tilde{\chi}^+_{c_2}G^-} &= (c^R_{\tilde{\chi}^-_{c_2}\tilde{\chi}^0_{n_1}G^+})^* = -s_\beta(V^*_{c_2 2}(s_W N^*_{n_1 1}/c_W + N^*_{n_1 2})/\sqrt{2} + V^*_{c_2 1}N^*_{n_1 4}) \\
c^R_{\tilde{\chi}^0_{n_1}\tilde{\chi}^+_{c_2}G^-} &= (c^L_{\tilde{\chi}^-_{c_2}\tilde{\chi}^0_{n_1}G^+})^* = c_\beta(-U_{c_2 2}(s_W N_{n_1 1}/c_W + N_{n_1 2})/\sqrt{2}) + U_{c_2 1}N_{n_1 3}) \\
\delta c^L_{\tilde{\chi}^0_{n_1}\tilde{\chi}^+_{c_2}H^-} &= -c_\beta s_W V^*_{c_2 2}N^*_{n_1 1}(\delta s_W/s_W - \delta c_W/c_W)/(\sqrt{2}c_W) \\
\delta c^R_{\tilde{\chi}^0_{n_1}\tilde{\chi}^+_{c_2}H^-} &= s_\beta s_W U_{c_2 2}N_{n_1 1}(\delta s_W/s_W - \delta c_W/c_W)/(\sqrt{2}c_W) \\
\delta c^L_{\tilde{\chi}^0_{n_1}\tilde{\chi}^+_{c_2}G^-} &= -s_\beta s_W V^*_{c_2 2}N^*_{n_1 1}(\delta s_W/s_W - \delta c_W/c_W)/(\sqrt{2}c_W) \\
\delta c^R_{\tilde{\chi}^0_{n_1}\tilde{\chi}^+_{c_2}G^-} &= -c_\beta s_W U_{c_2 2}N_{n_1 1}(\delta s_W/s_W - \delta c_W/c_W)/(\sqrt{2}c_W).
\end{aligned}
$$

The neutralino-neutralino-Higgs vertex:

For $h^0_k = \{h, H, A, G\}$;

$$
\begin{aligned}
C^R(\tilde{\chi}^0_{n2}, \tilde{\chi}^0_{n1}, h^0_k) &= = (C^L(\tilde{\chi}^0_{n2}, \tilde{\chi}^0_{n1}, h^0_k))^* = \frac{e}{2c_W s_W} c_{\tilde{\chi}^0_{n_2}\tilde{\chi}^0_{n_1}h^0_k} \\
\delta C^{L/R}(\tilde{\chi}^0_{n2}, \tilde{\chi}^0_{n1}, h^0_k) &= \frac{e}{2c_W s_W}\big[\delta c^{(*)}_{\tilde{\chi}^0_{n_2}\tilde{\chi}^0_{n_1}h^0_k} + c^{(*)}_{\tilde{\chi}^0_{n_2}\tilde{\chi}^0_{n_1}h^0_k}(\delta Z_e - \frac{\delta c_W}{c_W} - \frac{\delta s_W}{s_W}) \\
&\quad + \frac{1}{2}(\delta Z^{L/R}_{0,in_1} c^{(*)}_{\tilde{\chi}^0_{n_2}\tilde{\chi}^0_i h^0_k} + c^{(*)}_{\tilde{\chi}^0_i\tilde{\chi}^0_{n_1}h^0_k}\delta \bar{Z}^{R/L}_{0,in_2}) \\
&\quad + \frac{1}{2}(c^{(*)}_{\tilde{\chi}^0_{n_2}\tilde{\chi}^0_{n_1}h}\delta Z_{hh} + c^{(*)}_{\tilde{\chi}^0_{n_2}\tilde{\chi}^0_{n_1}H}\delta Z_{hH} + c^{(*)}_{\tilde{\chi}^0_{n_2}\tilde{\chi}^0_{n_1}A}\delta Z_{hA} + c^{(*)}_{\tilde{\chi}^0_{n_2}\tilde{\chi}^0_{n_1}G}\delta Z_{hG})\big]
\end{aligned}
$$

$$
\begin{aligned}
c_{\tilde{\chi}^0_{n_2}\tilde{\chi}^0_{n_1}h^0_k} &= [(a_k N_{i3} + b_k N_{i4})(s_W N_{j1} - c_W N_{j2}) + (a_k N_{j3} + b_k N_{j4})(s_W N_{i1} - c_W N_{i2})] \\
a_k &= \{-s_\alpha, c_\alpha, is_{\beta_n}, -ic_{\beta_n}\} \\
b_k &= \{-c_\alpha, -s_\alpha, -ic_{\beta_n}, -is_{\beta_n}\} \\
\delta c_{\tilde{\chi}^0_{n_2}\tilde{\chi}^0_{n_1}h^0_k} &= [(a_k N_{i3} + b_k N_{i4})(\delta s_W N_{j1} - \delta c_W N_{j2}) + (a_k N_{j3} + b_k N_{j4})(\delta s_W N_{i1} - \delta c_W N_{i2})]
\end{aligned}
$$

B.2 VFF vertices

The three-point vertex for a vector boson and two fermions, along with its counterterm, has the following Lorentz structure;

$$\Gamma^{(3)} = i((C^L + \delta C^L)\gamma^\mu \omega_L + (C^R + \delta C^R)\gamma^\mu \omega_R). \tag{B.4}$$

where the coupling constants C^L and C^R depend on the vertex in question. Using the relation $\omega_{L/R}\gamma^\mu = \gamma^\mu \omega_{R/L}$, we find

$$\gamma^\mu \omega_{L/R} F_2 \to \gamma^\mu \omega_{L/R}(1 + \frac{1}{2}\delta Z^{L/R})F_2 \tag{B.5}$$

$$\bar{F}_1 \gamma^\mu \omega_{L/R} \to \bar{F}_1 \gamma^\mu \omega_{L/R}(1 + \frac{1}{2}\delta \bar{Z}^{L/R}). \tag{B.6}$$

The chargino-chargino-gauge boson vertex:

$$\begin{aligned}
C^{L/R}(\tilde{\chi}^+_{c2}, \tilde{\chi}^-_{c1}, \gamma) &= e\delta_{c_1c_2} \\
\delta C^{L/R}(\tilde{\chi}^+_{c_2}, \tilde{\chi}^-_{c_1}, \gamma) &= e\big[\delta_{c_1c_2}(\delta Z_e + \frac{1}{2}\delta Z_{AA}) \\
&\quad + \frac{1}{2}\frac{1}{s_W c_W} c^{L/R}_{\tilde{\chi}^+_{c_2}\tilde{\chi}^-_{c_1}Z}\delta Z_{ZA} + \frac{1}{2}(\delta Z^{L/R}_{-,ic_1}\delta_{ic_2} + \delta_{c_1i}\delta \bar{Z}^{L/R}_{-,c_2i})\big] \\
C^{L/R}(\tilde{\chi}^+_{c2}, \tilde{\chi}^-_{c1}, Z) &= \frac{e}{c_W s_W} c^{L/R}_{\tilde{\chi}^+_{c_2}\tilde{\chi}^-_{c_1}Z} \\
\delta C^{L/R}(\tilde{\chi}^+_{c_2}, \tilde{\chi}^-_{c_1}, Z) &= \frac{e}{c_W s_W}\{\delta c^{L/R}_{\tilde{\chi}^+_{c_2}\tilde{\chi}^-_{c_1}Z} + c^{L/R}_{\tilde{\chi}^+_{c_2}\tilde{\chi}^-_{c_1}Z}(\delta Z_e - \frac{\delta c_W}{c_W} - \frac{\delta s_W}{s_W} + \frac{1}{2}\delta Z_{ZZ}) \\
&\quad - \frac{1}{2}c^{L/R}_{\tilde{\chi}^+_{c_2}\tilde{\chi}^-_{c_1}\gamma}\delta Z_{AZ} + \frac{1}{2}(\delta Z^{L/R}_{-,ic_1} c^{L/R}_{\tilde{\chi}^+_{c_2}\tilde{\chi}^+_i Z} + c^{L/R}_{\tilde{\chi}^+_i\tilde{\chi}^+_{c_1}Z}\delta \bar{Z}^{L/R}_{-,c_2i})\} \\
c^L_{\tilde{\chi}^+_{c_2}\tilde{\chi}^-_{c_1}\gamma} &= c^R_{\tilde{\chi}^+_{c_2}\tilde{\chi}^-_{c_1}\gamma} = -c_W s_W \delta_{c_1c_2} \\
c^L_{\tilde{\chi}^+_{c_2}\tilde{\chi}^-_{c_1}Z} &= s^2_W \delta_{c_1c_2} - U^*_{c_11}U_{c_21} - U^*_{c_12}U_{c_22}/2 \\
c^R_{\tilde{\chi}^+_{c_2}\tilde{\chi}^-_{c_1}Z} &= s^2_W \delta_{c_1c_2} - V^*_{c_21}V_{c_11} - (V^*_{c_22}V_{c_12})/2 \\
\delta c^L_{\tilde{\chi}^+_{c_2}\tilde{\chi}^-_{c_1}\gamma} &= \delta c^R_{\tilde{\chi}^+_{c_2}\tilde{\chi}^-_{c_1}\gamma} = -(\delta c_W s_W + \delta s_W c_W)\delta_{c_1c_2} \\
\delta c^L_{\tilde{\chi}^+_{c_2}\tilde{\chi}^-_{c_1}Z} &= \delta c^R_{\tilde{\chi}^+_{c_2}\tilde{\chi}^-_{c_1}Z} = 2\delta s_W s_W \delta_{c_1c_2}
\end{aligned}$$

The chargino-neutralino-W vertex:

$$
\begin{aligned}
C^{L/R}(\tilde{\chi}^0_{n_2},\tilde{\chi}^+_{c1},W^-) &= \frac{e}{s_W} c^{L/R}_{\tilde{\chi}^0_{n2}\tilde{\chi}^+_{c_1}W^-} \\
\delta C^{L/R}(\tilde{\chi}^0_{n_2},\tilde{\chi}^+_{c1},W^-) &= \frac{e}{s_W}\big[\delta c^{L/R}_{\tilde{\chi}^0_{n2}\tilde{\chi}^+_{c_1}W^-} + c^{L/R}_{\tilde{\chi}^0_{n2}\tilde{\chi}^+_{c_1}W^-}(\delta Z_e - \frac{\delta s_W}{s_W} + \frac{1}{2}\delta Z_{WW}) \\
&\quad + \frac{1}{2}(\delta Z^{R/L}_{in_2} c^{L/R}_{\tilde{\chi}^0_i\tilde{\chi}^+_{c_1}W^-} + c^{L/R}_{\tilde{\chi}^0_{n2}\tilde{\chi}^+_i W^-}\delta\bar{Z}^{R/L}_{c_1 i})\big] \\
C^{L/R}(\tilde{\chi}^-_{c1},\tilde{\chi}^0_{n2},W^+) &= \frac{ie}{s_W} c^{L/R}_{\tilde{\chi}^-_{c1}\tilde{\chi}^0_{n_2}W^+} \\
\delta C^{L/R}(\tilde{\chi}^-_{c1},\tilde{\chi}^0_{n2},W^+) &= \frac{ie}{s_W}\{\delta c^{L/R}_{\tilde{\chi}^-_{c1}\tilde{\chi}^0_{n_2}W^+} + c^{L/R}_{\tilde{\chi}^-_{c1}\tilde{\chi}^0_{n_2}W^+}(\delta Z_e - \frac{\delta s_W}{s_W} + \frac{1}{2}\delta Z_{WW}) \\
&\quad + \frac{1}{2}(\delta Z^{R/L)}_{-}, i c_1 c^{L/R}_{\tilde{\chi}^-_i\tilde{\chi}^0_{n_2}W^+} + c^{L/R}_{\tilde{\chi}^-_{c1}\tilde{\chi}^0_i W^+}\delta\bar{Z}^{R/L}_{0,n_2 i})\}
\end{aligned}
$$

$$
\begin{aligned}
c^L_{\tilde{\chi}^0_{n_2}\tilde{\chi}^+_{c_1}W^-} &= V^*_{c_1 1}N_{n_2 2} - V^*_{c_1 2}N_{n_2 4}/\sqrt{2}, \quad c^R_{\tilde{\chi}^0_{n_2}\tilde{\chi}^+_{c_1}W^-} = N^*_{n_2 2}U_{c_1 1} + N^*_{n_2 3}U_{c_1 2}/\sqrt{2} \\
c^L_{\tilde{\chi}^-_{c_1}\tilde{\chi}^0_{n_2}W^+} &= N^*_{n_2 2}V_{c_1 1} - N^*_{n_2 4}V_{c_1 2}/\sqrt{2}, \quad c^R_{\tilde{\chi}^-_{c_1}\tilde{\chi}^0_{n_2}W^+} = U_{c_1 1}N_{n_2 2} + U^*_{c_1 2}N_{n_2 3}/\sqrt{2} \\
\delta c^{L/R}_{\tilde{\chi}^0_{n_2}\tilde{\chi}^+_{c_1}W^-} &= 0 = \delta c^{L/R}_{\tilde{\chi}^-_{c_1}\tilde{\chi}^0_{n_2}W^+}.
\end{aligned}
$$

The neutralino-neutralino-Z vertex:

$$
\begin{aligned}
C^{L/R}(\tilde{\chi}^0_{n1},\tilde{\chi}^0_{n2},Z) &= \frac{ie}{2c_W s_W} c^{L/R}_{\tilde{\chi}^0_{n_1}\tilde{\chi}^0_{n_2}Z} \\
\delta C^{L/R}(\tilde{\chi}^0_{n_1},\tilde{\chi}^0_{n2},Z) &= \frac{e}{2c_W s_W}\big[\delta c^{L/R}_{\tilde{\chi}^0_{n_1}\tilde{\chi}^0_{n_2}Z} + c^{L/R}_{\tilde{\chi}^0_{n_1}\tilde{\chi}^0_{n_2}Z}(\delta Z_e - \frac{\delta c_W}{c_W} - \frac{\delta s_W}{s_W} + \frac{1}{2}\delta Z_{ZZ}) \\
&\quad + \frac{1}{2}(\delta Z^{L/R}_{0,n_1 i} c^{L/R}_{\tilde{\chi}^0_i\tilde{\chi}^0_{n_2}Z} + c^{L/R}_{\tilde{\chi}^0_{n_1}\tilde{\chi}^0_i Z}\delta\bar{Z}^{L/R}_{0,in_2})\big]
\end{aligned}
$$

where

$$
\begin{aligned}
c^L_{\tilde{\chi}^0_{n_1}\tilde{\chi}^0_{n_2}Z} &= -N^*_{n_2 3}N_{n_1 3} + N^*_{n_2 4}N_{n_1 4}, \quad c^R_{\tilde{\chi}^0_{n_1}\tilde{\chi}^0_{n_2}Z} = N^*_{n_1 3}N_{n_2 3} - N^*_{n_1 4}N_{n_2 4} \\
\delta c^{L/R}_{\tilde{\chi}^0_{n_1}\tilde{\chi}^0_{n_2}Z} &= 0.
\end{aligned}
$$

Appendix C

The narrow width approximation

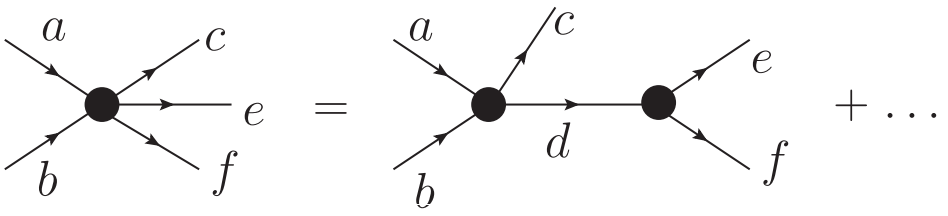

Figure C.1: Process $ab \to cef$ where the main contribution is the resonant diagram mediated by intermediate particle, d, where d can go on-shell. The ellipses represent other non-resonant diagrams which we will ignore here.

The narrow width approximation is often used to calculate a process which contains an internal propagator with a pole at $q^2 = M^2 - iM\Gamma$ by splitting the production and decay into two separate processes. To see how this is done, we consider the process, $ab \to cef$, shown in Figure C.1, where the main contribution to the amplitude is the resonant diagram mediated by the intermediate scalar particle d, with a Breit-Wigner propagator, $\frac{1}{q^2 - M^2 + iM\Gamma}$. The conditions that are required for the narrow width approximation to be valid are as follows.

- The resonant propagator should be separable from the matrix element.
- The scattering energy, $\sqrt{s}$, should be sufficiently larger than the masses, $m_c + M$, involved in the production process.
- The mass of the resonant particle, M, should be well above the sum of the masses of its decay products, $m_e + m_f$.
- The width should be small, i.e "narrow-width", compared to the mass, $\Gamma \ll M$.
- There should be no interference of the resonant diagram with other diagrams that have the same initial and final state.

For simplicity here, we further assume that other (resonant or non-resonant) diagrams do not give a large contribution to the process and can be ignored completely. Then the matrix element for the process can be written as

$$\mathcal{M}_{ab\to cef} = \mathcal{M}_{ab\to cd}\frac{1}{q^2 - M^2 + iM\Gamma}\mathcal{M}_{d\to ef} \tag{C.1}$$

so that the spin-averaged squared matrix element is given by

$$|\mathcal{M}_{ab\to cef}|^2 = |\mathcal{M}_{ab\to cd}|^2\frac{1}{(q^2 - M^2)^2 + M^2\Gamma^2}|\mathcal{M}_{d\to ef}|^2. \tag{C.2}$$

The cross section for the process is defined as

$$\sigma_{b\to cef} = \frac{1}{2\lambda^{\frac{1}{2}}(s, m_a^2, m_b^2)}\int \mathrm{dlips}(s; p_c, p_e, p_f)|\mathcal{M}_{ab\to cef}|^2 \tag{C.3}$$

where $s = (p_a + p_b)^2$, $2\lambda^{\frac{1}{2}}(s, m_a^2, m_b^2) = 4\sqrt{(p_a.p_b)^2 - m_a^2 m_b^2}$ is the flux and $\mathrm{dlips}(s; p_c, p_e, p_f)$ is the Lorentz invariant phase space element,

$$\mathrm{dlips}(s; p_c, p_e, p_f) \equiv (2\pi)^4\delta^4(s - p_c - p_e - p_f)\frac{d^3p_c}{(2\pi)^3 2E_c}\frac{d^3p_e}{(2\pi)^3 2E_e}\frac{d^3p_f}{(2\pi)^3 2E_f}. \tag{C.4}$$

Like the squared matrix element, the phase space element can be factorised into separate elements for production and decay, by inserting the phase space of the intermediate decaying particle, d, with momentum q, and using the property that

$$1 = \int d^4q\delta^4(q - p_e - p_f) = \int (2\pi)^3\frac{d^3q}{(2\pi)^3}\frac{dq^2}{2\sqrt{q^2}}\delta^4(q - p_e - p_f) \tag{C.5}$$

to give

$$\begin{aligned}\mathrm{dlips}(s; p_c, p_e, p_f) &= (2\pi)^3\frac{d^3q}{(2\pi)^3}\frac{dq^2}{2\sqrt{q^2}}\delta^4(q - p_e - p_f)(2\pi)^4\delta^4(s - p_c - p_e - p_f) \\ &\quad \frac{d^3p_c}{(2\pi)^3 2E_c}\frac{d^3p_e}{(2\pi)^3 2E_e}\frac{d^3p_f}{(2\pi)^3 2E_f} \\ &= \frac{1}{2\pi}\mathrm{dlips}(s; p_c, q)\, dq^2\, \mathrm{dlips}(q; p_e, p_f)\end{aligned} \tag{C.6}$$

where in the last line we are able to separate the terms belonging to the phase space for the production and decay as $\mathrm{dlips}(s; p_c, q)$ and $\mathrm{dlips}(q; p_e, p_f)$ respectively. This means

that our cross section can be written as

$$\begin{aligned}
\sigma_{ab\to cef} &= \frac{1}{\pi}\int dq^2 \left[\frac{1}{2\lambda^{\frac{1}{2}}(s,m_a^2,m_b^2)}\int \mathrm{dlips}(s;p_c,q)|\mathcal{M}_{ab\to cd}|^2)\right] \\
&\quad \frac{\sqrt{q^2}}{(q^2-M^2)^2+M^2\Gamma^2}\left[\frac{1}{2\sqrt{q^2}}\int \mathrm{dlips}(q;p_e,p_f)|\mathcal{M}_{d\to ef}|^2\right] \\
&= \frac{1}{\pi}\int dq^2 \sigma_{ab\to cd}(q^2)\frac{\sqrt{q^2}}{(q^2-M^2)^2+M^2\Gamma^2}\Gamma_{d\to ef}(q^2) \\
&\approx \frac{1}{\pi}\int_{q^2_{\min}}^{q^2_{\max}} dq^2 \sigma_{ab\to cd}(q^2)\frac{\sqrt{q^2}}{(q^2-M^2)^2+M^2\Gamma^2}\Gamma_{d\to ef}(q^2) \qquad \text{(C.7)}
\end{aligned}$$

where $\sigma_{ab\to cd}(q^2)$ is the off-shell cross section for the process which produces the resonant particle, d, with momentum q^2 and $\Gamma_{d\to ef}(q^2)$ is the off-shell decay width for the resonant particle, d, decaying at momentum q^2. The last line is an approximation for the full integral, where $q_{\max}$ and $q_{\min}$ are defined to be M plus or minus a few times the decay width respectively. The limit,

$$\lim_{M\Gamma\to 0}\frac{1}{(q^2-M^2)^2+M^2\Gamma^2} = \delta(M^2-q^2)\frac{\pi}{M\Gamma}, \qquad \text{(C.8)}$$

allows us to evaluate the integral in the limit of "narrow-width". The delta function means we can compute the cross-section and decay width as on-shell quantities, at $q^2 = M^2$, leaving us with

$$\sigma(ab\to cef) \approx \sigma_{ab\to cd}(M^2)\frac{\Gamma_{d\to ef}(M^2)}{\Gamma}, \qquad \text{(C.9)}$$

i.e. in the narrow width approximation, the cross-section for the full production and decay process can be simply computed by multiplying the cross section for the production part of the process with the branching ratio for the decay part of the process. The Breit-Wigner dependence of the propagator has been integrated out and replaced with the constant $\pi/M\Gamma$ and only the on-shell production and decay contribute.

Bibliography

[1] A. Pich, "The Standard Model of electroweak interactions," arXiv:hep-ph/0502010.

[2] LEP Working Group for Higgs boson searches Collaboration, R. Barate et al., "Search for the standard model Higgs boson at LEP," *Phys. Lett.* **B565** (2003) 61–75, arXiv:hep-ex/0306033.

[3] CDF Collaboration "Combined CDF and D0 Upper Limits on Standard Model Higgs Boson Production with 2.1 - 5.4 fb-1 of Data," arXiv:0911.3930 [hep-ex].

[4] CDF and D0 Collaboration, T. Aaltonen et al., "Combination of Tevatron searches for the standard model Higgs boson in the W+W- decay mode," *Phys. Rev. Lett.* **104** (2010) 061802, arXiv:1001.4162 [hep-ex].

[5] The TEVNPH Working Group of the CDF and D0 Collaboration "Combined CDF and D0 Upper Limits on Standard Model Higgs- Boson Production with up to 6.7 fb^{-1} of Data," arXiv:1007.4587 [hep-ex].

[6] A. De Roeck et al., "From the LHC to Future Colliders," *Eur. Phys. J.* **C66** (2010) 525–583, arXiv:0909.3240 [hep-ph].

[7] P. W. Higgs, "Broken Symmetries and the masses of gauge bosons," *Phys. Rev. Lett.* **13** (1964) 508–509.

[8] P. W. Higgs, "Spontaneous Symmetry Breakdown without Massless Bosons," *Phys. Rev.* **145** (1966) 1156–1163.

[9] F. Englert and R. Brout, "Broken symmetry and the mass of gauge vector mesons," *Phys. Rev. Lett.* **13** (1964) 321–322.

[10] G. S. Guralnik, C. R. Hagen, and T. W. B. Kibble, "Global conservation laws and massless particles," *Phys. Rev. Lett.* **13** (1964) 585–587.

[11] T. W. B. Kibble, "Symmetry breaking in non-Abelian gauge theories," *Phys. Rev.* **155** (1967) 1554–1561.

[12] J. F. Gunion, H. E. Haber, G. L. Kane, and S. Dawson, *The Higgs Hunter's Guide*. Addison-Wesley, Redwood City, California, 1990.

[13] A. Djouadi, "The anatomy of electro-weak symmetry breaking. I: The Higgs boson in the standard model," *Phys. Rept.* **457** (2008) 1–216, arXiv:hep-ph/0503172.

[14] T. Hambye and K. Riesselmann, "Matching conditions and Higgs mass upper bounds revisited," *Phys. Rev.* **D55** (1997) 7255–7262, arXiv:hep-ph/9610272.

[15] LEP Collaboration "A Combination of preliminary electroweak measurements and constraints on the standard model," arXiv:hep-ex/0412015.

[16] U. Baur et al., "Theoretical and experimental status of the indirect Higgs boson mass determination in the standard model," arXiv:hep-ph/0111314.

[17] D. Hooper, "TASI 2008 Lectures on Dark Matter," arXiv:0901.4090 [hep-ph].

[18] U. Amaldi, W. de Boer, and H. Furstenau, "Comparison of grand unified theories with electroweak and strong coupling constants measured at LEP," *Phys. Lett.* **B260** (1991) 447–455.

[19] A. D. Sakharov, "Violation of CP Invariance, C Asymmetry, and Baryon Asymmetry of the Universe," *Pisma Zh. Eksp. Teor. Fiz.* **5** (1967) 32–35.

[20] M. Drees, "An Introduction to Supersymmetry," arXiv:hep-ph/9611409.

[21] S. P. Martin, "A Supersymmetry Primer," arXiv:hep-ph/9709356.

[22] M. Drees, R. Godbole, and P. Roy, "Theory and phenomenology of sparticles: An account of four-dimensional N=1 supersymmetry in high energy physics,".

[23] H. Baer and X. Tata, "Weak scale supersymmetry: From superfields to scattering events,".

[24] R. Haag, J. T. Lopuszanski, and M. Sohnius, "All Possible Generators of Supersymmetries of the S Matrix," *Nucl. Phys.* **B88** (1975) 257.

[25] D. Bailin and A. Love, "Supersymmetric gauge field theory and string theory,". Bristol, UK: IOP (1994) 322 p. (Graduate student series in physics).

[26] J. R. Ellis, K. A. Olive, Y. Santoso, and V. C. Spanos, "Supersymmetric Dark Matter in Light of WMAP," *Phys. Lett.* **B565** (2003) 176–182, arXiv:hep-ph/0303043.

[27] LEP Working Group for Higgs boson searches Collaboration, S. Schael et al., "Search for neutral MSSM Higgs bosons at LEP," *Eur. Phys. J.* **C47** (2006) 547–587, arXiv:hep-ex/0602042.

[28] Particle Data Group Collaboration, C. Amsler et al., "Review of particle physics," *Phys. Lett.* **B667** (2008) 1.

[29] M. S. Carena, J. R. Ellis, A. Pilaftsis, and C. E. M. Wagner, "CP-violating MSSM Higgs bosons in the light of LEP 2," *Phys. Lett.* **B495** (2000) 155–163, arXiv:hep-ph/0009212.

[30] K. E. Williams and G. Weiglein, "Precise predictions for $h_a -> h_b h_c$ decays in the complex MSSM," *Phys. Lett.* **B660** (2008) 217–227, arXiv:0710.5320 [hep-ph].

[31] V. Buescher and K. Jakobs, "Higgs boson searches at hadron colliders," *Int. J. Mod. Phys.* **A20** (2005) 2523–2602, arXiv:hep-ph/0504099.

[32] M. Schumacher, "Investigation of the discovery potential for Higgs bosons of the minimal supersymmetric extension of the standard model (MSSM) with ATLAS," arXiv:hep-ph/0410112.

[33] E. Accomando et al., "Workshop on CP studies and non-standard Higgs physics," arXiv:hep-ph/0608079.

[34] F. Moortgat, S. Abdullin, and D. Denegri, "Observability of MSSM Higgs bosons via sparticle decay modes in CMS," arXiv:hep-ph/0112046.

[35] M. Bisset, J. Li, N. Kersting, F. Moortgat, and S. Moretti, "Four-lepton LHC events from MSSM Higgs boson decays into neutralino and chargino pairs," arXiv:0709.1029 [hep-ph].

[36] M. Bisset, J. Li, and N. Kersting, "How to Detect 'Decoupled' Heavy Supersymmetric Higgs Bosons," arXiv:0709.1031 [hep-ph].

[37] P. Huang, N. Kersting, and H. H. Yang, "Extracting MSSM masses from heavy Higgs boson decays to four leptons at the CERN LHC," *Phys. Rev.* **D77** (2008) 075011, arXiv:0801.0041 [hep-ph].

[38] M. S. Carena, S. Heinemeyer, C. E. M. Wagner, and G. Weiglein, "MSSM Higgs boson searches at the Tevatron and the LHC: Impact of different benchmark scenarios," *Eur. Phys. J.* **C45** (2006) 797–814, arXiv:hep-ph/0511023.

[39] S. Gennai et al., "Search for Heavy Neutral MSSM Higgs Bosons with CMS: Reach and Higgs-Mass Precision," *Eur. Phys. J.* **C52** (2007) 383–395, arXiv:0704.0619 [hep-ph].

[40] S. Dimopoulos and D. W. Sutter, "The supersymmetric flavor problem," *Nucl. Phys.* **B452** (1995) 496–512, arXiv:hep-ph/9504415.

[41] M. Frank, T. Hahn, S. Heinemeyer, W. Hollik, H. Rzehak, and G. Weiglein, "The Higgs boson masses and mixings of the complex MSSM in the Feynman-diagrammatic approach," *JHEP* **02** (2007) 047, arXiv:hep-ph/0611326.

[42] S. Heinemeyer, W. Hollik, and G. Weiglein, "The Masses of the neutral CP - even Higgs bosons in the MSSM: Accurate analysis at the two loop level," *Eur. Phys. J.* **C9** (1999) 343–366, arXiv:hep-ph/9812472.

[43] S. Heinemeyer, W. Hollik, and G. Weiglein, "QCD corrections to the masses of the neutral CP-even Higgs bosons in the MSSM," *Phys. Rev.* **D58** (1998) 091701, arXiv:hep-ph/9803277.

[44] S. Heinemeyer, W. Hollik, and G. Weiglein, "Precise prediction for the mass of the lightest Higgs boson in the MSSM," *Phys. Lett.* **B440** (1998) 296–304, arXiv:hep-ph/9807423.

[45] S. Ambrosanio, A. Dedes, S. Heinemeyer, S. Su, and G. Weiglein, "Implications of the Higgs boson searches on different soft SUSY breaking scenarios," *Nucl. Phys.* **B624** (2002) 3–44, arXiv:hep-ph/0106255.

[46] G. Degrassi, S. Heinemeyer, W. Hollik, P. Slavich, and G. Weiglein, "Towards high-precision predictions for the MSSM Higgs sector," *Eur. Phys. J.* **C28** (2003) 133–143, arXiv:hep-ph/0212020.

[47] D. Stoeckinger, "Einschleifenbeitraege zu schwachen Dipolmomenten und Quark-/Squarkzerfaellen im MSSM," Diploma Thesis, Karlsruhe, 1998.

[48] W. Hollik, J. I. Illana, S. Rigolin, and D. Stockinger, "One-loop MSSM contribution to the weak magnetic dipole moments of heavy fermions," *Phys. Lett.* **B416** (1998) 345–352, arXiv:hep-ph/9707437.

[49] W. Hollik, J. I. Illana, S. Rigolin, and D. Stockinger, "Weak electric dipole moments of heavy fermions in the MSSM," *Phys. Lett.* **B425** (1998) 322–328, arXiv:hep-ph/9711322.

[50] D. A. Demir, O. Lebedev, K. A. Olive, M. Pospelov, and A. Ritz, "Electric dipole moments in the MSSM at large tan(beta)," *Nucl. Phys.* **B680** (2004) 339–374, arXiv:hep-ph/0311314.

[51] D. Chang, W.-Y. Keung, and A. Pilaftsis, "New two-loop contribution to electric dipole moment in supersymmetric theories," *Phys. Rev. Lett.* **82** (1999) 900–903, arXiv:hep-ph/9811202.

[52] A. Pilaftsis, "Higgs-boson two-loop contributions to electric dipole moments in the MSSM," *Phys. Lett.* **B471** (1999) 174–181, arXiv:hep-ph/9909485.

[53] O. Lebedev, K. A. Olive, M. Pospelov, and A. Ritz, "Probing CP violation with the deuteron electric dipole moment," *Phys. Rev.* **D70** (2004) 016003, arXiv:hep-ph/0402023.

[54] S. Abel, S. Khalil, and O. Lebedev, "EDM constraints in supersymmetric theories," *Nucl. Phys.* **B606** (2001) 151–182, arXiv:hep-ph/0103320.

[55] P. Nath, "CP Violation via electroweak gauginos and the electric dipole moment of the electron," *Phys. Rev. Lett.* **66** (1991) 2565–2568.

[56] Y. Kizukuri and N. Oshimo, "The Neutron and electron electric dipole moments in supersymmetric theories," *Phys. Rev.* **D46** (1992) 3025–3033.

[57] T. Ibrahim and P. Nath, "The neutron and the electron electric dipole moment in N = 1 supergravity unification," *Phys. Rev.* **D57** (1998) 478–488, arXiv:hep-ph/9708456.

[58] M. Brhlik, G. J. Good, and G. L. Kane, "Electric dipole moments do not require the CP-violating phases of supersymmetry to be small," *Phys. Rev.* **D59** (1999) 115004, arXiv:hep-ph/9810457.

[59] J. R. Ellis, J. S. Lee, and A. Pilaftsis, "Electric Dipole Moments in the MSSM Reloaded," *JHEP* **10** (2008) 049, arXiv:0808.1819 [hep-ph].

[60] Y. Li, S. Profumo, and M. Ramsey-Musolf, "A Comprehensive Analysis of Electric Dipole Moment Constraints on CP-violating Phases in the MSSM," *JHEP* **08** (2010) 062, arXiv:1006.1440 [hep-ph].

[61] M. S. Carena, S. Heinemeyer, C. E. M. Wagner, and G. Weiglein, "Suggestions for benchmark scenarios for MSSM Higgs boson searches at hadron colliders," *Eur. Phys. J.* **C26** (2003) 601–607, arXiv:hep-ph/0202167.

[62] M. S. Carena, S. Heinemeyer, C. E. M. Wagner, and G. Weiglein, "Suggestions for improved benchmark scenarios for Higgs boson searches at LEP2," arXiv:hep-ph/9912223.

[63] B. C. Allanach et al., "The Snowmass points and slopes: Benchmarks for SUSY searches," *Eur. Phys. J.* **C25** (2002) 113–123, arXiv:hep-ph/0202233.

[64] See www.ippp.dur.ac.uk/ georg/sps/ for the low-energy MSSM parameters corresponding to the SPS points.

[65] H. K. Dreiner et al., "Mass Bounds on a Very Light Neutralino," *Eur. Phys. J.* **C62** (2009) 547–572, arXiv:0901.3485 [hep-ph].

[66] S. Heinemeyer, W. Hollik, and G. Weiglein, "Decay widths of the neutral CP-even MSSM Higgs bosons in the Feynman-diagrammatic approach," *Eur. Phys. J.* **C16** (2000) 139–153, arXiv:hep-ph/0003022.

[67] A. Denner, "Techniques for calculation of electroweak radiative corrections at the one loop level and results for W physics at LEP-200," *Fortschr. Phys.* **41** (1993) 307–420, arXiv:0709.1075 [hep-ph].

[68] M. Bohm, A. Denner, and H. Joos, *Gauge theories of the strong and electroweak interaction*. Teubner, Stuttgart, 2001.

[69] G. Passarino and M. J. G. Veltman, "One Loop Corrections for e+ e- Annihilation into mu+ mu- in the Weinberg Model," *Nucl. Phys.* **B160** (1979) 151.

[70] D. Stockinger, "Regularization by dimensional reduction: Consistency, quantum action principle, and supersymmetry," *JHEP* **03** (2005) 076, arXiv:hep-ph/0503129.

[71] W. Hollik and D. Stockinger, "MSSM Higgs-boson mass predictions and two-loop non- supersymmetric counterterms," *Phys. Lett.* **B634** (2006) 63–68, arXiv:hep-ph/0509298.

[72] J. Kublbeck, M. Bohm, and A. Denner, "FeynArts: Computer algebraic generation of Feynman graphs and amplitudes," *Comput. Phys. Commun.* **60** (1990) 165–180.

[73] T. Hahn, "Generating Feynman diagrams and amplitudes with FeynArts 3," *Comput. Phys. Commun.* **140** (2001) 418–431, arXiv:hep-ph/0012260.

[74] T. Hahn and C. Schappacher, "The implementation of the minimal supersymmetric standard model in FeynArts and FormCalc," *Comput. Phys. Commun.* **143** (2002) 54–68, arXiv:hep-ph/0105349.

[75] T. Hahn and M. Perez-Victoria, "Automatized one-loop calculations in four and D dimensions," *Comput. Phys. Commun.* **118** (1999) 153–165, arXiv:hep-ph/9807565.

[76] F. del Aguila, A. Culatti, R. Munoz Tapia, and M. Perez-Victoria, "Techniques for one-loop calculations in constrained differential renormalization," *Nucl. Phys.* **B537** (1999) 561–585, arXiv:hep-ph/9806451.

[77] M. Steinhauser, "Leptonic contribution to the effective electromagnetic coupling constant up to three loops," *Phys. Lett.* **B429** (1998) 158–161, arXiv:hep-ph/9803313.

[78] H. Burkhardt and B. Pietrzyk, "Low energy hadronic contribution to the QED vacuum polarization," *Phys. Rev.* **D72** (2005) 057501, arXiv:hep-ph/0506323.

[79] S. Heinemeyer, W. Hollik, and G. Weiglein, "FeynHiggs: A program for the calculation of the masses of the neutral CP-even Higgs bosons in the MSSM," *Comput. Phys. Commun.* **124** (2000) 76–89, arXiv:hep-ph/9812320.

[80] S. Heinemeyer, W. Hollik, and G. Weiglein, "QCD corrections to the masses of the neutral CP-even Higgs bosons in the MSSM," *Phys. Rev.* **D58** (1998) 091701, arXiv:hep-ph/9803277.

[81] S. Heinemeyer, W. Hollik, H. Rzehak, and G. Weiglein, "The Higgs sector of the complex MSSM at two-loop order: QCD contributions," *Phys. Lett.* **B652** (2007) 300–309, arXiv:0705.0746 [hep-ph].

[82] A. B. Lahanas, K. Tamvakis, and N. D. Tracas, "One loop corrections to the neutralino sector and radiative electroweak breaking in the MSSM," *Phys. Lett.* **B324** (1994) 387–396, arXiv:hep-ph/9312251.

[83] D. Pierce and A. Papadopoulos, "Radiative corrections to neutralino and chargino masses in the minimal supersymmetric model," *Phys. Rev.* **D50** (1994) 565–570, arXiv:hep-ph/9312248.

[84] D. Pierce and A. Papadopoulos, "The complete radiative corrections to the gaugino and Higgsino masses in the minimal supersymmetric model," *Nucl. Phys.* **B430** (1994) 278–294, arXiv:hep-ph/9403240.

[85] H. Eberl, M. Kincel, W. Majerotto, and Y. Yamada, "One-loop corrections to the chargino and neutralino mass matrices in the on-shell scheme," *Phys. Rev.* **D64** (2001) 115013, arXiv:hep-ph/0104109.

[86] T. Fritzsche and W. Hollik, "Complete one-loop corrections to the mass spectrum of charginos and neutralinos in the MSSM," *Eur. Phys. J.* **C24** (2002) 619–629, arXiv:hep-ph/0203159.

[87] W. Oller, H. Eberl, W. Majerotto, and C. Weber, "Analysis of the chargino and neutralino mass parameters at one-loop level," *Eur. Phys. J.* **C29** (2003) 563–572, arXiv:hep-ph/0304006.

[88] W. Oller, H. Eberl, and W. Majerotto, "Precise predictions for chargino and neutralino pair production in e+ e- annihilation," *Phys. Rev.* **D71** (2005) 115002, arXiv:hep-ph/0504109.

[89] M. Drees, W. Hollik, and Q. Xu, "One-loop calculations of the decay of the next-to-lightest in the MSSM," *JHEP* **02** (2007) 032, arXiv:hep-ph/0610267.

[90] K. Rolbiecki and J. Kalinowski, "CP violation at one loop in the polarization-independent chargino production in e+e- collisions," *Phys. Rev.* **D76** (2007) 115006, arXiv:0709.2994 [hep-ph].

[91] H. Eberl, T. Gajdosik, W. Majerotto, and B. Schrausser, "CP-violating asymmetry in chargino decay into neutralino and W boson," *Phys. Lett.* **B618** (2005) 171–181, arXiv:hep-ph/0502112.

[92] P. Osland and A. Vereshagin, "CP violation in unpolarized $e^+e^- >$ charginos at one loop level," *Phys. Rev.* **D76** (2007) 036001, arXiv:0704.2165 [hep-ph].

[93] A. Denner, E. Kraus, and M. Roth, "Physical renormalization condition for the quark-mixing matrix," *Phys. Rev.* **D70** (2004) 033002, arXiv:hep-ph/0402130.

[94] T. Fritzsche, "Berechnung von Observablen zur supersymmetrischen Teilchenerzeugung an Hochenergie-Collidern unter Einschluss hoeherer Ordnungen," PhD Thesis, Karlsruhe, 2005.

[95] D. Espriu and J. Manzano, "CP violation and family mixing in the effective electroweak Lagrangian," *Phys. Rev.* **D63** (2001) 073008, arXiv:hep-ph/0011036.

[96] D. Espriu, J. Manzano, and P. Talavera, "Flavor mixing, gauge invariance and wave-function renormalisation," *Phys. Rev.* **D66** (2002) 076002, arXiv:hep-ph/0204085.

[97] Y. Zhou, "Wave-function renormalization prescription," *Mod. Phys. Lett.* **A21** (2006) 2763, arXiv:hep-ph/0502186.

[98] B. A. Kniehl and A. Sirlin, "A Novel Formulation of Cabibbo-Kobayashi-Maskawa Matrix Renormalization," *Phys. Lett.* **B673** (2009) 208–210, arXiv:0901.0114 [hep-ph].

[99] A. C. Fowler and G. Weiglein, "Precise Predictions for Higgs Production in Neutralino Decays in the Complex MSSM," *JHEP* **01** (2010) 108, arXiv:0909.5165 [hep-ph].

[100] J. A. Aguilar-Saavedra et al., "Supersymmetry parameter analysis: SPA convention and project," *Eur. Phys. J.* **C46** (2006) 43–60, arXiv:hep-ph/0511344.

[101] R.-Y. Zhang, W.-G. Ma, L.-H. Wan, and Y. Jiang, "Supersymmetric electroweak corrections to the Higgs boson decays into chargino or neutralino pair," *Phys. Rev.* **D65** (2002) 075018, arXiv:hep-ph/0201132.

[102] H. Eberl, M. Kincel, W. Majerotto, and Y. Yamada, "One-loop corrections to neutral Higgs boson decays into neutralinos," *Nucl. Phys.* **B625** (2002) 372–388, arXiv:hep-ph/0111303.

[103] A. Datta, A. Djouadi, M. Guchait, and F. Moortgat, "Detection of MSSM Higgs bosons from supersymmetric particle cascade decays at the LHC," *Nucl. Phys.* **B681** (2004) 31–64, arXiv:hep-ph/0303095.

[104] CMS Collaboration, G. L. Bayatian et al., "CMS technical design report, Volume II: Physics performance," *CERN-LHCC-2006-021, CMS-TDR-008-2 J. Phys.* **G34** (2007) 995–1579.

[105] P. Bandyopadhyay, A. Datta, and B. Mukhopadhyaya, "Signatures of gaugino mass non-universality in cascade Higgs production at the LHC," *Phys. Lett.* **B670** (2008) 5–11, arXiv:0806.2367 [hep-ph].

[106] K. Huitu, R. Kinnunen, J. Laamanen, S. Lehti, S. Roy, and T. Salminen, "Search for Higgs Bosons in SUSY Cascades in CMS and Dark Matter with Non-universal Gaugino Masses," arXiv:0808.3094 [hep-ph].

[107] P. Bandyopadhyay, "Probing non-universal gaugino masses via Higgs boson production under SUSY cascades at the LHC: A detailed study," arXiv:0811.2537 [hep-ph].

[108] T. Hahn et al., "CP-violating Loop Effects in the Higgs Sector of the MSSM," arXiv:0711.2020 [hep-ph].

[109] T. Ibrahim, "Neutralino decay of MSSM neutral Higgs bosons," *Phys. Rev.* **D77** (2008) 065028, arXiv:0803.4134 [hep-ph].

[110] A. G. Akeroyd, "Searching for a very light Higgs boson at the Tevatron," *Phys. Rev.* **D68** (2003) 077701, arXiv:hep-ph/0306045.

[111] D. K. Ghosh, R. M. Godbole, and D. P. Roy, "Probing the CP-violating light neutral Higgs in the charged Higgs decay at the LHC," *Phys. Lett.* **B628** (2005) 131–140, arXiv:hep-ph/0412193.

[112] P. Bandyopadhyay, A. Datta, A. Datta, and B. Mukhopadhyaya, "Associated Higgs Production in CP-violating supersymmetry: probing the 'open hole' at the Large Hadron Collider," *Phys. Rev.* **D78** (2008) 015017, arXiv:0710.3016 [hep-ph].

[113] P. Bandyopadhyay, "Higgs production in CP-violating supersymmetric cascade decays: probing the 'open hole' at the Large Hadron Collider," arXiv:1008.3339 [hep-ph].

[114] LHC/LC Study Group Collaboration, G. Weiglein et al., "Physics interplay of the LHC and the ILC," *Phys. Rept.* **426** (2006) 47–358, arXiv:hep-ph/0410364.

[115] G. A. Moortgat-Pick, H. Fraas, A. Bartl, and W. Majerotto, "Polarization and spin effects in neutralino production and decay," *Eur. Phys. J.* **C9** (1999) 521–534, arXiv:hep-ph/9903220.

[116] G. Moortgat-Pick, K. Rolbiecki, J. Tattersall, and P. Wienemann, "Probing CP Violation with and without Momentum Reconstruction at the LHC," *JHEP* **01** (2010) 004, arXiv:0908.2631 [hep-ph].

[117] G. Moortgat-Pick, K. Rolbiecki, and J. Tattersall, "Momentum reconstruction at the LHC for probing CP- violation in the stop sector," arXiv:1008.2206 [hep-ph].

[118] M. A. Gigg and P. Richardson, "Simulation of Finite Width Effects in Physics Beyond the Standard Model," arXiv:0805.3037 [hep-ph].

[119] C. F. Uhlemann and N. Kauer, "Narrow-width approximation accuracy," *Nucl. Phys.* **B814** (2009) 195–211, arXiv:0807.4112 [hep-ph].

[120] D. Berdine, N. Kauer, and D. Rainwater, "Breakdown of the Narrow Width Approximation for New Physics," *Phys. Rev. Lett.* **99** (2007) 111601, arXiv:hep-ph/0703058.

[121] N. Kauer, "Narrow-width approximation limitations," *Phys. Lett.* **B649** (2007) 413–416, arXiv:hep-ph/0703077.

[122] N. Kauer, "A threshold-improved narrow-width approximation for BSM physics," *JHEP* **04** (2008) 055, arXiv:0708.1161 [hep-ph].

[123] D0 Collaboration, V. M. Abazov et al., "Search for Higgs bosons decaying to τ pairs in $p\bar{p}$ collisions with the D0 detector," *Phys. Rev. Lett.* **101** (2008) 071804, arXiv:0805.2491 [hep-ex].

[124] G. Cacciapaglia, A. Deandrea, and S. De Curtis, "Nearby resonances beyond the Breit-Wigner approximation," *Phys. Lett.* **B682** (2009) 43–49, arXiv:0906.3417 [hep-ph].

[125] CTEQ Collaboration, H. L. Lai et al., "Global QCD analysis of parton structure of the nucleon: CTEQ5 parton distributions," *Eur. Phys. J.* **C12** (2000) 375–392, arXiv:hep-ph/9903282.

[126] Tevatron New Phenomena and Higgs Working Group Collaboration, D. Benjamin et al., "Combined CDF and D0 upper limits on MSSM Higgs boson production in tau-tau final states with up to 2.2 fb-1," arXiv:1003.3363 [hep-ex].

[127] The CDF Collaboration, "CDF Note 9071: Search for Neutral MSSM Higgs Bosons Decaying to Tau Pairs with 1.8 fb^{-1} of Data," (2008) (see http://tevnphwg.fnal.gov).

[128] The D0 Collaboration, "D0 Note 5740: Search for MSSM Higgs Production in Di-tau Final States with $\mathcal{L} = 1.8$ fb^{-1} at the D0 Detector," (2007) (see www-d0.fnal.gov).

[129] The TEVNPH Working Group for the CDF and D Collaborations, "D0 Note 5980 / CDF Note 9888: Combined CDF and D upper limits on MSSM Higgs boson production in tau-tau final states with up to 2.2 fb^1 of data," (2009) (see www-d0.fnal.gov).

[130] CDF Collaboration, T. Aaltonen et al., "Search for Higgs bosons predicted in two-Higgs-doublet models via decays to tau lepton pairs in 1.96 TeV proton-antiproton collisions," *Phys. Rev. Lett.* **103** (2009) 201801, arXiv:0906.1014 [hep-ex].

[131] P. Bechtle, O. Brein, S. Heinemeyer, G. Weiglein, and K. E. Williams, "HiggsBounds: Confronting Arbitrary Higgs Sectors with Exclusion Bounds from LEP and the Tevatron," *Comput. Phys. Commun.* **181** (2010) 138–167, arXiv:0811.4169 [hep-ph].

[132] J. R. Ellis, J. S. Lee, and A. Pilaftsis, "LHC signatures of resonant CP violation in a minimal supersymmetric Higgs sector," *Phys. Rev.* **D70** (2004) 075010, arXiv:hep-ph/0404167.

[133] A. Pilaftsis, "Resonant CP violation induced by particle mixing in transition amplitudes," *Nucl. Phys.* **B504** (1997) 61–107, arXiv:hep-ph/9702393.

[134] A. Pilaftsis, "Higgs scalar-pseudoscalar mixing in the minimal supersymmetric standard model," *Phys. Lett.* **B435** (1998) 88–100, arXiv:hep-ph/9805373.

[135] J. R. Ellis, J. S. Lee, and A. Pilaftsis, "Resonant CP violation in MSSM Higgs production and decay at gamma gamma colliders," *Nucl. Phys.* **B718** (2005) 247–275, arXiv:hep-ph/0411379.

[136] J. R. Ellis, J. S. Lee, and A. Pilaftsis, "Resonant CP violation in Higgsstrahlung at an e+ e- linear collider," *Phys. Rev.* **D72** (2005) 095006, arXiv:hep-ph/0507046.

[137] J. R. Ellis, J. S. Lee, and A. Pilaftsis, "Diffraction as a CP and lineshape analyzer for MSSM Higgs bosons at the LHC," *Phys. Rev.* **D71** (2005) 075007, arXiv:hep-ph/0502251.

[138] S. Y. Choi, J. Kalinowski, Y. Liao, and P. M. Zerwas, "H / A Higgs mixing in CP-noninvariant supersymmetric theories," *Eur. Phys. J.* **C40** (2005) 555–564, arXiv:hep-ph/0407347.

[139] W. Bernreuther, A. Brandenburg, and M. Flesch, "Effects of Higgs sector CP violation in top quark pair production at the LHC," arXiv:hep-ph/9812387.

[140] J. Bernabeu, D. Binosi, and J. Papavassiliou, "CP violation through particle mixing and the H - A lineshape," *JHEP* **09** (2006) 023, arXiv:hep-ph/0604046.

[141] R. M. Godbole, S. Kraml, S. D. Rindani, and R. K. Singh, "Probing CP-violating Higgs contributions in gamma-gamma -¿ f anti-f through fermion polarization," *Phys. Rev.* **D74** (2006) 095006, arXiv:hep-ph/0609113.

[142] S. Y. Choi and J. S. Lee, "s-channel production of MSSM Higgs bosons at a muon collider with explicit CP violation," *Phys. Rev.* **D61** (2000) 111702, arXiv:hep-ph/9909315.

[143] E. Asakawa, S. Y. Choi, and J. S. Lee, "Probing the MSSM Higgs boson sector with explicit CP violation through third generation fermion pair production at muon colliders," *Phys. Rev.* **D63** (2001) 015012, arXiv:hep-ph/0005118.

[144] H. K. Dreiner, O. Kittel, and F. von der Pahlen, "Disentangling CP phases in nearly degenerate resonances: neutralino production via Higgs at a muon collider," *JHEP* **01** (2008) 017, arXiv:0711.2253 [hep-ph].

[145] O. Kittel and F. von der Pahlen, "CP-violating Higgs boson mixing in chargino production at the muon collider," *JHEP* **08** (2008) 030, arXiv:0806.4534 [hep-ph].

[146] S. Y. Choi, D. J. Miller, 2, M. M. Muhlleitner, and P. M. Zerwas, "Identifying the Higgs spin and parity in decays to Z pairs," *Phys. Lett.* **B553** (2003) 61–71, arXiv:hep-ph/0210077.

[147] R. M. Godbole et al., "CP studies of the Higgs sector," arXiv:hep-ph/0404024.

[148] R. M. Godbole, D. J. Miller, 2, and M. M. Muehlleitner, "CP Asymmetries in Higgs decays to ZZ at the LHC," *J. Phys. Conf. Ser.* **110** (2008) 072024, arXiv:0708.3612 [hep-ph].

[149] H. E. Haber, "Spin formalism and applications to new physics searches," arXiv:hep-ph/9405376.

[150] T. Hahn, S. Heinemeyer, F. Maltoni, G. Weiglein, and S. Willenbrock, "SM and MSSM Higgs boson production cross sections at the Tevatron and the LHC," arXiv:hep-ph/0607308.

[151] J. S. Lee et al., "CPsuperH: A computational tool for Higgs phenomenology in the minimal supersymmetric standard model with explicit CP violation," *Comput. Phys. Commun.* **156** (2004) 283–317, arXiv:hep-ph/0307377.

[152] A. Dedes and S. Moretti, "Effect of large supersymmetric phases on Higgs production," *Phys. Rev. Lett.* **84** (2000) 22–25, arXiv:hep-ph/9908516.

[153] S. Dawson, A. Djouadi, and M. Spira, "QCD corrections to SUSY Higgs production: The Role of squark loops," *Phys. Rev. Lett.* **77** (1996) 16–19, arXiv:hep-ph/9603423.